IRAQI JOURNAL OF APPLIED PHYSICS

The *Iraqi Journal of Applied Physics (IJAP)* is a peer reviewed journal of high quality devoted to the publication of original research papers from applied physics and their broad range of applications. IJAP publishes quality original research papers, comprehensive review articles, survey articles, book reviews, dissertation abstracts in physics and its applications in the broadest sense. It is intended that the journal may act as an interdisciplinary forum for Physics and its applications. Innovative applications and material that brings together diverse areas of Physics are particularly welcome. Review articles in selected areas are published from time to time. It aims to disseminate knowledge; provide a learned reference in the field; and establish channels of communication between academic and research experts, policy makers and executives in industry, commerce and investment institutions. IJAP is a quarterly specialized periodical dedicated to publishing original papers, letters and reviews in: Applied & Nonlinear Optics, Applied Mechanics & Thermodynamics, Digital & Optical Communications, Electronic Materials & Devices, Laser Physics & Applications, Plasma Physics & Applications, Quantum Physics & Spectroscopy, Semiconductors & Optoelectronics, Solid State Physics & Applications, Alternative & Renewable Energy, and Environmental Science & Technology. Sub-disciplines include Dielectrics, ferroelectrics, and multiferroics; Electrical discharges, plasmas, and plasma-surface interactions; Emerging, interdisciplinary, and other fields of applied physics; Energy and Sustainability; Magnetism, spintronics, and superconductivity; Organic-Inorganic systems, including organic electronics; Photonics, plasmonics, photovoltaics, optical phenomena, materials, and metamaterials; Physics of devices and sensors; Physics of materials, including electrical, thermal, mechanical and other properties; Physics of matter under extreme conditions; Physics of nanoscale, 2D materials, and low-dimensional systems; Physics of semiconductors; Quantum technology; Soft matter, fluids, and biophysics; Thin films, interfaces, and surfaces.

ISSN (Print): 1813-2065, ISSN (Online): 2309-1673

Editorial Office:
P. O. Box 88052, Baghdad 12631, IRAQ
Mobile: +964 7832 360 114 (Telegram, Viber, WhatsApp)
Website: www.ijap-iq.com
Emails: info@ijap-iq.com, editor_ijap@yahoo.co.uk, ijap.editor@gmail.com

SPONSORED AND PUBLISHED BY
AMERICAN QUALITY FOR SCIENTIFIC PUBLISHING INC.
1479 South De Gaulle Ct, Aurora, CO 80018, United States

IRAQI JOURNAL OF APPLIED PHYSICS

INSTRUCTIONS TO AUTHORS

CONTRIBUTIONS

Contributions to be published in this journal should be original research works, i.e., those not already published or submitted for publication elsewhere, individual papers or letters to editor.
Manuscripts should be submitted to the editor at the mailing address:

Iraqi Journal of Applied Physics, Editorial Board, P. O. Box 88052, Baghdad 12631, IRAQ
Mobile: +964 7832 360 114 (Telegram, Viber, WhatsApp)
Website: www.ijap-iq.com
Email: info@ijap-iq.com, editor_ijap@yahoo.co.uk, ijap.editor@gmail.com

MANUSCRIPTS

Two hard copies or a soft Word copy on a CD or DVD should be submitted to the Editor in the following configuration:

- **One-column** Double-spaced one-side A4 size with 2.5 cm margins of all sides
- Times New Roman font (16pt bold for title, 14pt bold for names, 12pt bold for headings, 12pt regular for text)
- Manuscripts presented in English only are accepted.
- English abstract not exceed 150 words
- 4 keywords (at least) should be maintained on (PACS preferred)
- Author(s) should express all quantities in SI units
- Equations should be written in equation form (*italic* and symbolic) NOT in plain text
- Tables and Figures should be separated from text and placed in new pages after the references
- Charts should be indicated by the software used for generating them (e.g., Excel, MATLAB, Grapher, etc.)
- Figures and diagrams can be submitted in original colored forms for assessment and they will be returned to authors after provide printable copies
- Only original or high-resolution scanner photos are accepted
- For electronic submission, articles should be formatted with MS-Word software
- Figures, charts, photos, images or pictures **SHOULD NOT** be grouped in Word file
- Figure caption should be written as plan text **NOT** inside a text box

AUTHOR NAMES AND AFFILIATIONS

It is IJAP policy that all those who have participated significantly in the technical aspects of a paper be recognized as co-authors or cited in the acknowledgments. In the case of a paper with more than one author, correspondence concerning the paper will be sent to the first author unless staff is advised otherwise.
Author name should consist of first name, middle initial, last name. The author affiliation should consist of the following, as applicable, in the order noted:
- Company or college (with department name or company division), Postal address, City, Governorate or State, zip code, Country name, contacting telephone number, and e-mail

REFERENCES

The references should be brought at the end of the article, and numbered in the order of their appearance in the paper. The reference list should be cited in accordance with the following examples:
[1] F.H. Al-Berkdar, D.N. Raouf and F.H. Hamza, "A Line Tuned TEM_{00} Mode CW CO_2 Laser", *Iraqi J. Appl. Phys.*, 1(1) (20025) 8-10.
[2] W. Demtröder, **"Atoms, Molecules, and Photons"**, Springer-Verlag (Berlin, 2006), Ch. 4, p. 130.
[3] Y. Lee, S.A. Korpela and R. Horne, "Structure of Multi-Cellular Natural Convection in a Tall Vertical Annulus", Proceedings of 7th International Heat Transfer Conference, U. Grigul et al., eds., Hemisphere (NY), 2 (1982) 221–226.
[5] M. Hashish, "Waterjet Technology Development", High Pressure Technology, PVP-Vol. 406 (2000) 135-140.
[6] D.W. Watson, "Thermodynamic Analysis", ASME Paper No. 97-GT-288 (1997).
[7] Z. Cheng, "Vibrational Discrete Action Theory", Ph.D. thesis, Columbia University, USA (2021).

PROOFS

Authors will receive proofs of papers and are requested to return one corrected copy as a WORD file on a compact disc (CD) or by email. New materials inserted in the original text without Editor's permission may cause rejection of paper unless the handling editor is informed.

COPYRIGHT FORM

Author(s) will be asked to sign the IJAP Copyright Form and hence transfer copyrights of the article to the Journal soon after acceptance of it. This will ensure the widest possible dissemination of information.

OFFPRINTS

Authors will receive electronic offprint free of charge and any additional reprints can be ordered.

SUBSCRIPTION AND ORDERS

Annual fees (4 issues per year) of subscription are:
50 US$ for individuals inside Iraq; **200** US$ for institutions inside Iraq; **100** US$ for individuals abroad; **300** US$ for institutions abroad.

Faten B. Mohammed Ameen
Ghazwan G. Ali
Marwan H. Younus

Department of Physics, College of Education for Pure Sciences, Mosul University, Mosul, IRAQ

Iraqi Journal of Applied Physics
Q4 Electronic, Optical and Magnetic Materials
best quartile
SJR 2022
0.19
powered by scimagojr.com

Fabrication and Characterization of Gas Sensors from ZnS/Porous Silicon Heterojunctions

ZnS-PSi heterojunction based gas sensor was fabricated in this study. ZnS thin film as the active materials over PSi substrate was synthesized by spray pyrolysis method. The effected of different concentration of ZnS (0.1M , 0.3 M and 0.5 M) on the characterization of the sensor have been investigated. The XRD results show that the ZnS has a hexagonal structure. SEM images were revealed that the ZnS as a circular grains with different sizes is synthesized over the PSi substrate. The electrical properties of the prepared sensor were proved that the sensitivity of the sensor is improved by increasing the concentration the ZnS. Furthermore, the ZnS-PSi heterojunction based gas sensor display high sensitivity and fast response and recovery times. The maximum sensitivity is found to be 5.11 when the ZnS concentration is 0.5 M compared to the sensitivity of 3.14 when the ZnS concentration is 0.1M. The ZnS-PSi heterojunction based gas sensor may be used for UV-light photo-detectors due to a valuable properties such as high sensitivity and fast response.

Keywords: Porous silicon; Zinc Sulfide; Heterojunction; Gas sensor
Received: 08 January 2024; **Revised:** 11 March 2024; **Accepted:** 18 March 2024

1. Introduction

Zinc sulfide (ZnS) is an inorganic semiconductor that has a wide direct bandgap (3.5-3.9eV). It possess a good thermal stability and high electronic mobility which is belonging to the halogen elements of the periodic table II-VI. The ZnS is attracted a lot of researchers, especially in the applications of ultraviolet light-emitting diodes (LEDs) [1], high carrier mobility, biosensors , solar cells and gas sensors [2]. The ZnS mixture shows two types of natural crystal shapes which are the cubic and the hexagonal shape. The cubic shape has a lattice constant of 0.541nm and is good match with Si. Therefore, an effective and homogeneous film of ZnS can be grown over the silicon substrate [3,4]. Moreover, an increase in the sensitivity of the gas sensor can be expected due to the increase in the absorbance of the molecules on the Porous Silicon (PSi) layer. Thus, PSi is used as bases instead of silicon wafers [5,6]. Several methods are used to synthesis the ZnS thin films such as, CVD, PECVD, sputter coater, sol-gel and spray pyrolysis [7]. Among of these methods, the spray pyrolysis method is easy to handle with, simple and inexpensive which is no need to complex devices. In addition, it is considered one of the most important methods for depositing a variety of materials in the form of a thin film [8]. Furthermore, high-quality thin film could be obtained using this method by controlling the temperature and the distance be-tween the substrate and the deposited materials. Also, the spray rate allows us to control the size of the droplets with homogeneously distribute along of heated substrate [9]. In addition, the PSi is attracted great attention due to its photoluminescence at room temperature in the visible light range [10]. Various techniques based chemical reaction are used to synthesis PSi over the surface of silicon (Si). The most widely used technique is the electrochemical etching method (ECE) because of its low cost and the possibility of obtaining high homogeneity and compatibility where alignment is required to initiate the chemical reaction [11]. The second method is photochemical reaction (PCE) via laser-induced etching which results in well-controlled light emission properties of the porous layer. The third method is photo-electrochemical etching (PECE), which is used to form and enhance the properties of the nanostructure layers for a wider PL range. The last method is spot etching of the silicon wafer in a solution based on HF:HNO_3:H_2O.The process of forming ZnS over PSi is carried out by spray pyrolysis method. This method is allow the form the particles size in nanoscale. Additionally, the concentration of the solution can be controlled easily to produce a final particle size that interested with. Using the spray pyrolysis, the process can be completed in short time just with a few seconds with high efficiency and homogeneous lattice compared to the other methods. [12,13]. The aim of this work is to fabricate the ZnS/PSi heterojunction as a sensor to detect NO_2 gas. The structural properties (XRD), surface properties (AFM and SEM), electrical for the fabricated sensor are studied.

2. Experimental Work

Porous silicon substrates were obtained by electrochemical etching of p-type (111) oriented silicon (c-Si) wafers with a resistivity of 1-10 Ω cm. Silicon wafers were cleaned with propanol and alcohol using an ultrasonic bath for 5 min. The c-Si wafers were rinsed with de-ionized water, dried with N2 flux, after that the samples immersed in mixed hydrofluoric acid (20%HF) and ethanol (99%). The anodizing cell consists of two cylinders made from Teflon with identical diameters. The upper layer contains a cylindrical cavity designated for the etching solution, while the lower layer is completely solid. The circle metal made from Stainless-steel is

placed on the lower cylinder and the Si wafer is placed on it and filled with an etching solution as shown in Figure 1a. The etching time was carried out for 5, 10, 15 min and the current density is fixed with 12 mA/cm^2 .

ZnS thin films over p-Si substrates was obtained by spray pyrolysis method. Zinc chloride ($ZnCl_2$) and sodium sulfide (Na_2S-Sigma Aldrich, reagent grade, 97% purity) were used as the source materials to produce the ZnS thin film. The $ZnCl_2$ and Na_2S were mixed in de-ionized water solutions at (0.1, 0.3 and 0.5M) as shown in table (1). The stirrer time of acetate solution was 40 min at room temperature. Next, the mixture was heated up to 85°C for one hour by magnetic stirrer. The final products were deposited over the glass substrates by chemical spray pyrolysis at 300°C and at the atmospheric pressure of 7.5 bar as shown in Fig. (1b). The reaction was investigated by the following equation [14]:

$$Na_2S(aq)+ZnCl_2(aq)\rightarrow ZnS(s)+2NaCl(aq) \quad (1)$$

Table (1) Preparation parameters of ZnS thin films

Concentration (mol)	0.1	0.3	0.5
Weight (gm) $ZnCl_2$	0.272	0.544	0.81789
Weight (gm) Na_2S	0.158	0.316	0.474

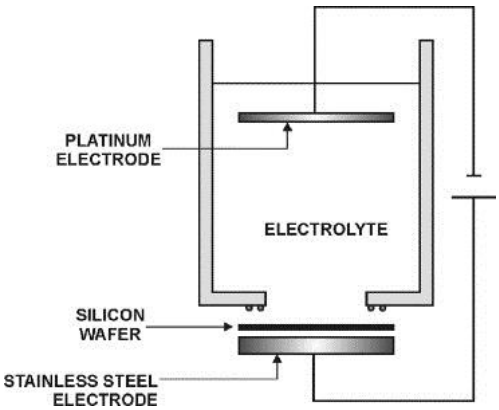

(a)

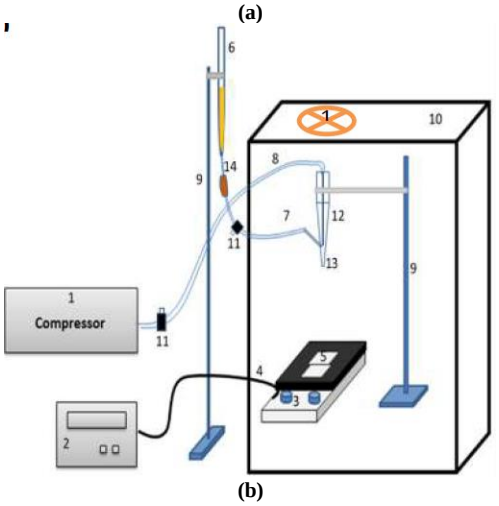

(b)

Fig. (1) (a) Electrochemical cell setup, and (b) spray pyrolysis setup

3. Results and discussion

The XRD patterns of the ZnS thin film deposited on glass substrates at concentrations of 0.1, 0.3 and 0.5M are shown in Fig. (2). It can be seen from this figure that all spectra show the peaks related to (111), (002), (110), (220) and (311) orientations corresponding to zinc-blende hexagonal structures according to JCPDS card No. 00–001–0677 wurtzite ZnS structure with an angle (2θ) equal to 31.13°, 27.32°, 38.06°, 48.31°, and 57.81°, respectively [15].

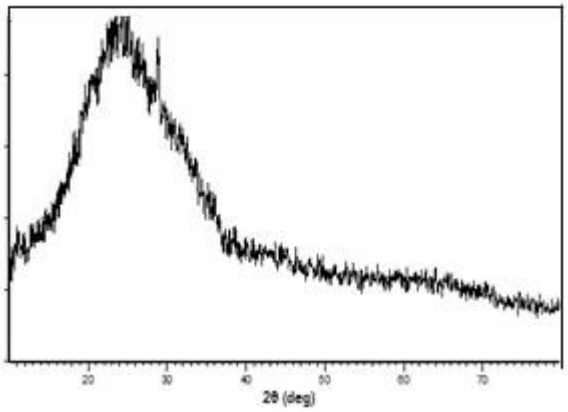

(a) 0.1 M

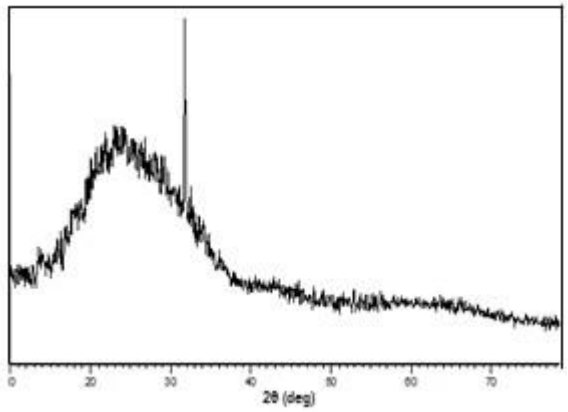

(b) 0.3 M

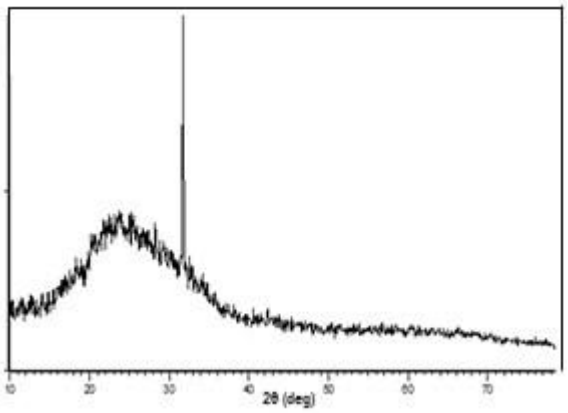

(c) 0.5 M

Fig. (2) XRD patterns of ZnS thin films deposited on glass substrate at concentrations of (a) 0.1M, (b) 0.3M and (c) 0.5M

Figure (3) shows the XRD pattern of ZnS/PSi heterojunction when the concentrations of ZnS are 0.1, 0.3 and 0.5M, respectively, at etching time of 10 min. It can be seen from Fig. (3a) that the PSi layer remains crystalline on planes of (111) and (002) with diffraction angle of 29.13° and 27.38°, respectively, which belong to wurtzite ZnS structure. Figure (3b) illustrates the peaks (002), (111) and (106) when the ZnS concentration of 0.3M which corresponding to diffraction angle 26.56°, 26.56° and 32.591°, respectively. Figure (3c) shows the diffraction angles of 30.06°, 27.27° and 38.06° belonging to (111), (002) and (110), respectively, when the ZnS concentration is 0.5M. It can be noted that the PSi peak is shifting slightly to small diffraction angle with increasing concentration. The FWHM of the peak is directly proportional to the crystallite size as shown in table (2).

The crystallite size (L) of PSi was calculated by Debye-Scherrer's formula [16,17]

$$L = \frac{k\lambda}{B\cos\theta} \qquad (2)$$

where λ is the x-ray wavelength, β is the full-width at half maximum (FWHM), and θ is the Bragg's angle

Figure (4) shows the surface morphology (2D and 3D) of porous silicon at different etching times (5 and 15 min). These images clearly show that the porous silicon with tightly branched pores has a sponge-like structure. Furthermore, the pore diameter and roughness of the surface increase with the increasing of etching time. This is attributed to extreme dissolution of PSi. Also, the porous silicon structure can be observed by uniform porosity structure with different pore diameters on the entire surface [18]. As a result, etching time may be employed to change the size and form the final pore structures. The average roughness of the pours is found to be 24.65 and 42.84 nm at etching time of 5 and 15 min, respectively. Figure (5) shows 2D and D AFM images of ZnS deposited on porous silicon substrates at concentration of 0.1M and different etching times (5 and 15 min). It is clear that the pore size expands when the ZnS heterojunction is synthesized [19]. Additionally, it can found that the PSi is completely covered by plentiful ZnS heterojunction. Subsequently, the surface distribution of the diameter values of the ZnS/PSi was randomly distributed and irregular heterojunction over the whole surface. The average roughness is found to be 83.36 and 93.32 nm at etching time of 5 and 15min, respectively. Table (3) indicates that the increasing in the etching time leads to increase the average diameter of the pores.

Figure (6) shows SEM images of ZnS deposited on glass substrates by spray pyrolysis method at concentrations of 0.1, 0.3 and 0.5 M. It indicates that the small regular grain size start to form on the glass substrate at ZnS concentration of 0.1M with circular grains as shown in Fig. (6a). When the ZnS concentration increases, the grain diameter also is increased as shown in figures (6b and 6c). The diameter of the ZnS nanoparticles it found to be 29, 37 and 58 nm at ZnS concentration of 0.1, 0.3 and 0.5 M, respectively.

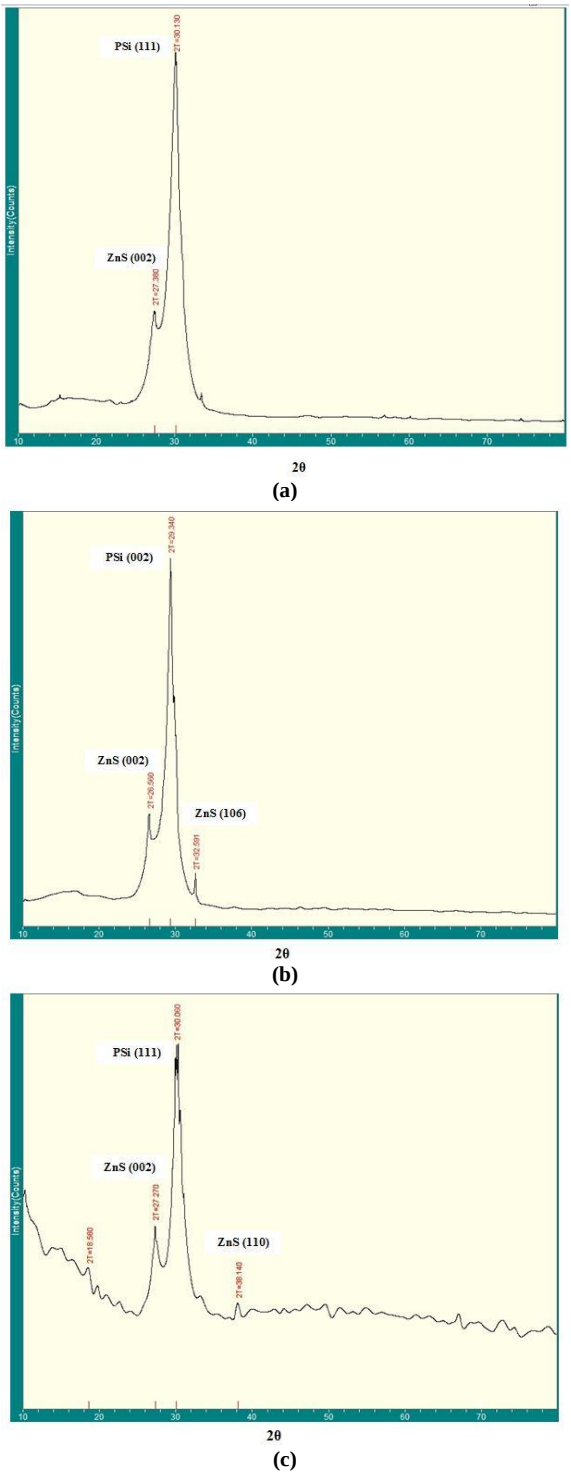

Fig. (3) XRD patterns of ZnS thin films deposited on porous silicon at concentrations of (a) 0.1M, (b) 0.3M and (c) 0.5M

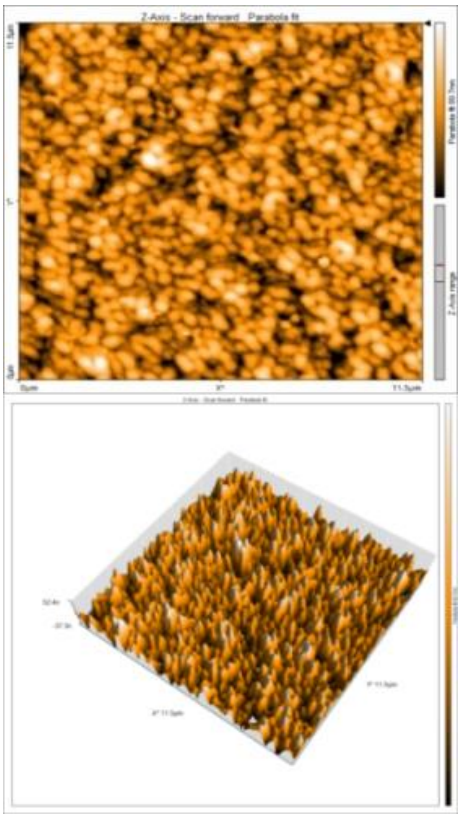

(a)

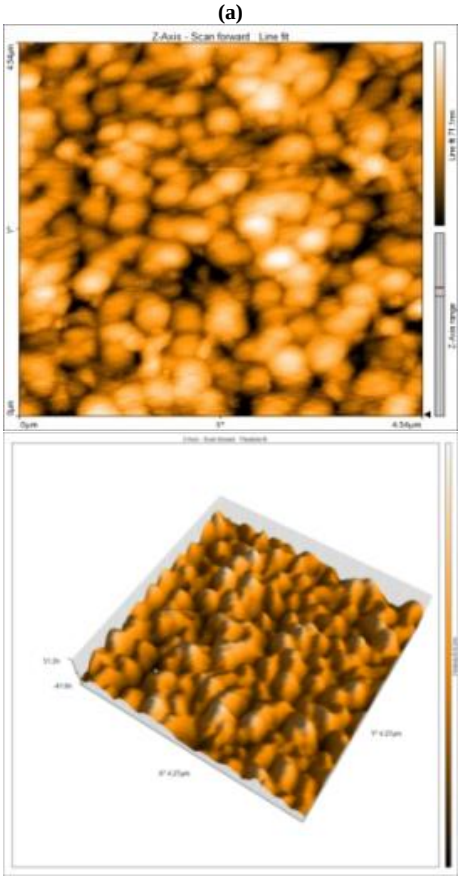

(b)

Fig. (4) AFM images for PSi at etching times of 5 and 15min

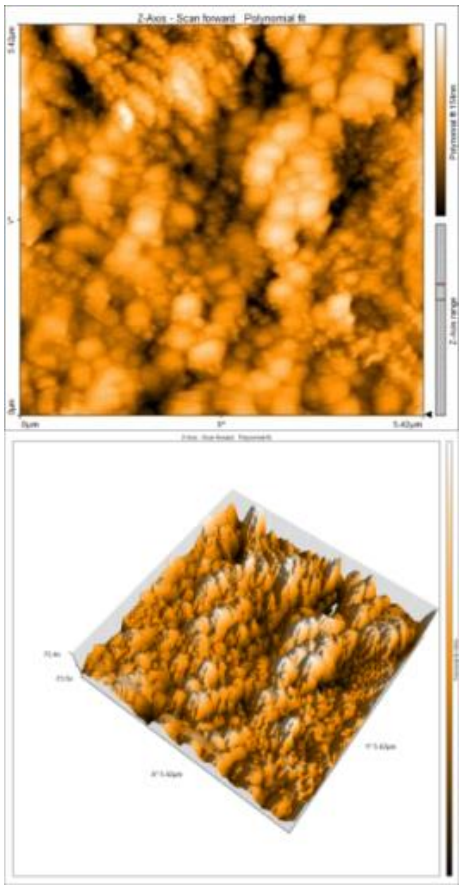

(a)

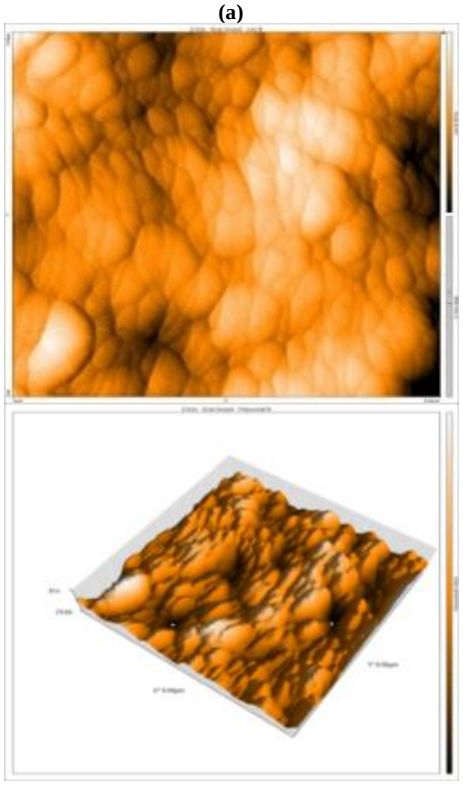

(b)

Fig. (5) AFM images of ZnS/Psi heterojunctions at etching times of 5 and 15 min when ZnS concentrations are 0.1 M and 0.5 M

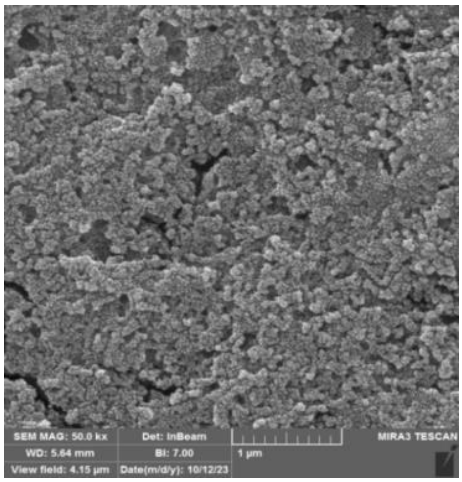

(a)

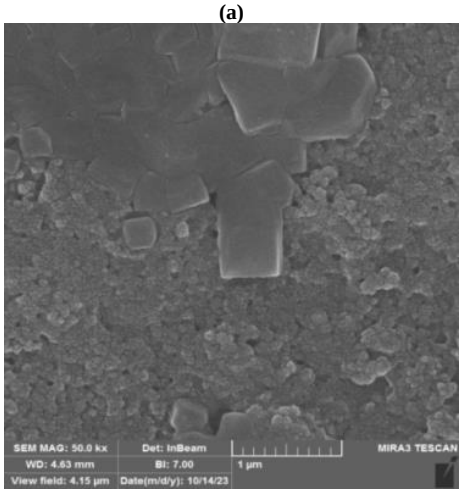

(b)

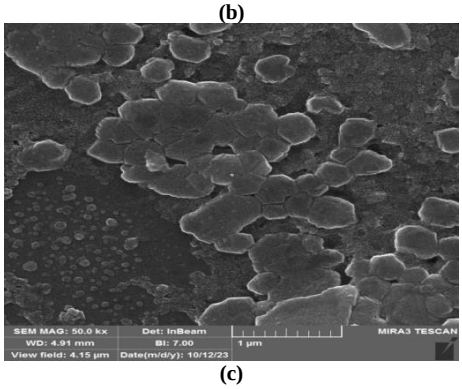

(c)

Fig. (6) SEM images of ZnS thin films on glass substrates at ZnS concentrations of (a) 0.1M, (b) 0.3M and (c) 0.5M

Figures (7a and b) show SEM images of PSi at etching time 5 and 15 min. The pore size increases with increasing the etching time due to dissolution of silicon substrate at the wall of pores. The images also approve star-like nanostructures with average diameter of 47nm. Figures (7c and d) show the SEM image of the ZnS/PSi surface at etching time 5 and 15 min respectively when the ZnS concentration is 0.3M.

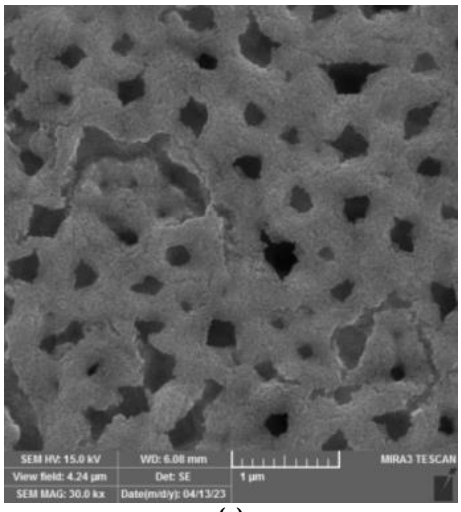

(a)

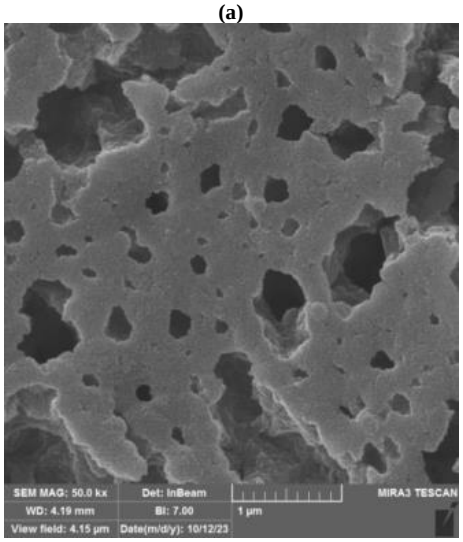

(b)

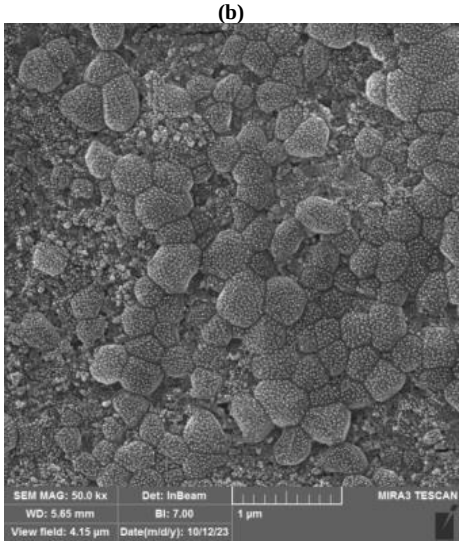

(c)

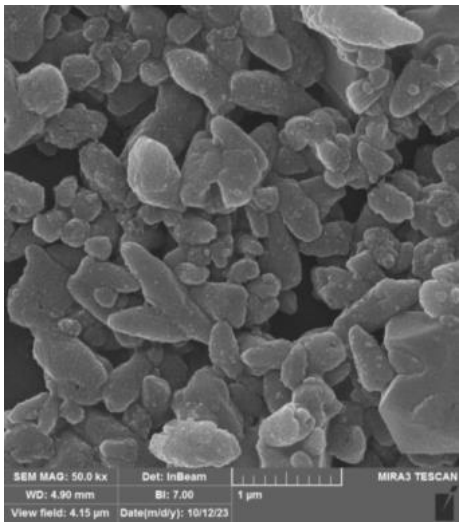

(d)

Fig. (7) SEM images (a) PSi at etching 5 min, (b) PSi at etching 15 min, (c) ZnS/PSi heterojunction of 0.3M at etching time 5 min and (d) ZnS /PSi of 0.3M at etching time 15 min

The results confirm that the agglomeration were observed with average diameter less than 100 nm [20]. Additionally, when the ZnS concentration increases, the nucleation stage of particle size is increased. We notice that there is a growth and interference between ZnS nanoparticls and the surface of the porous silicon, this interference increases with increasing etching time. The deposition of ZnS improves the structural stability of the porous silicon. Figure (8) shows the thickness of thin film as a function of the etching time. It can be notice that the thickness increases almost linearly when the etching time at all the ZnS concentration is increased. These results are agreement with previous works [21].

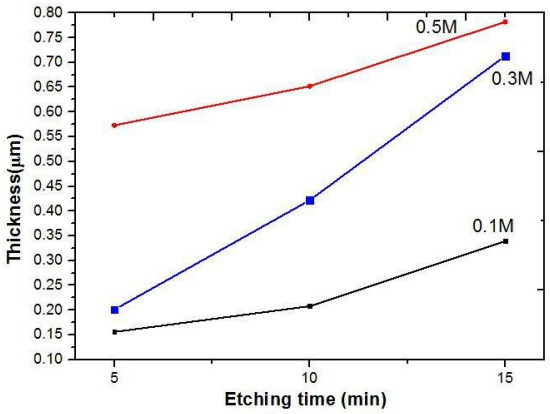

Fig. (8) Thickness of ZnS as a function of etching time with ZnS concentrations of 0.1M, 0.3M and 0.5M

Figure (9a) shows the EDS spectrum of ZnS deposited over the porous silicon at concentration of 0.1 M with etching time of 5 min. The strong spectrum shows the presence of Si, Zn and S at the appropriate energy levels. Furthermore, it is clear that the elements composition are found to be 44.10% Zn and 35.41% S at ZnS concentration of 0.5 M. In the other side, the elements mapping for Ca, Cl and Mg were presented due to aggregation and formation of ZnS nanostructure embedded porous silicon during preparation process [22] as shown in Fig. (9b). The values of all elements that appeared in the EDS spectra are shown in table (4).

Table (4) Elements values of EDS spectrum at ZnS concentration 0.1 and 0.5M with etching time 5 min

Element	0.1M	Line	0.5M
S	33.51	Ka	35.41
Ca	-	-	4.73
O	22.16	Ka	12.67
Cl	4.24	Ka	-
Mg	-	-	4.66
Zn	41.62	Ka	44.10
	100.00		100.00

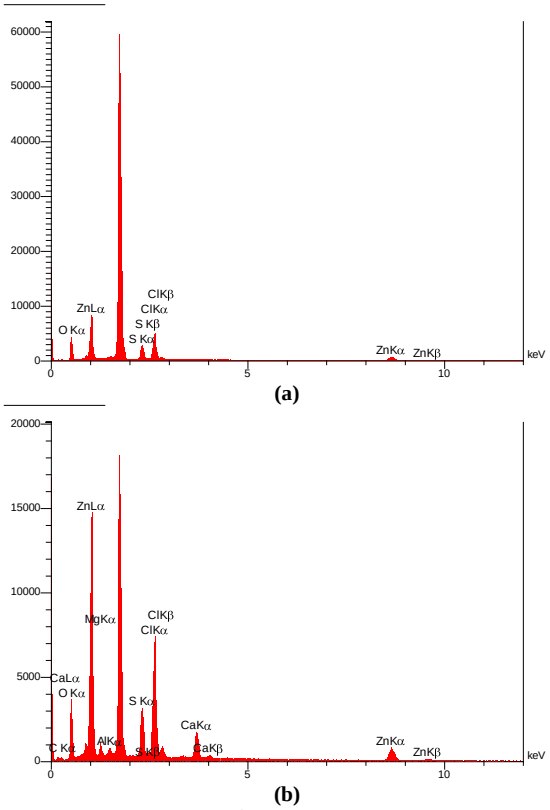

Fig. (9) EDS spectra of ZnS/PSi heterojunctions at ZnS concentrations of (a) 0.1M, and (b) 0.5M

The investigations of resistance, resistivity and conductivity were carried out for prepared gas sensor with ZnS concentrations of 0.1M and 0.5M that deposited over PSi at different etching times (5, 10 and 15 min). Figure (10) and figure (11) illustrate that the electrical conductivity increases with increasing the ZnS concentration for all samples. The obtained conductivity for the concentration of 0.5M is greater than the conductivity when the ZnS concentration is 0.1M. This is due to increase in the mobility of the charge carriers [23], and as a result, the ZnS thin films interference with the porous silicon and thus the conductivity increases. We also notice that the electrical conductivity increases with temperature.

This is attributed to improve the crystalline structure and caused a decrease in the grain boundaries due to increase in grain size [24].

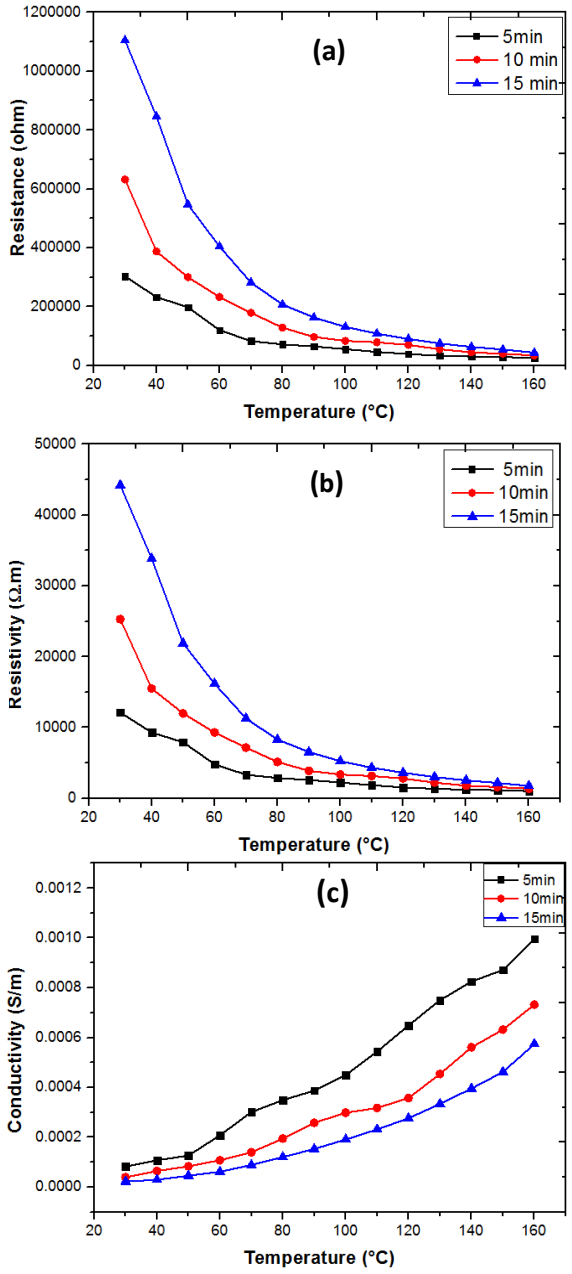

Fig. (10) Resistance, resistivity and conductivity of samples prepared at etching times of 5, 10 and 15min at concentration of 0.1M

Figure (12) shows the electrical characteristics (J-V) of ZnS/PSi heterojunction for forward and reverse bias. It can be notice that the samples have rectifier behave and the current density decreases with increasing etching time. As the dependence of the (J-V) characteristics on the etching time, is related to the formation of pores in porous silicon. When the pore diameter increases with increasing etching time, leads to an increase in resistivity of porous silicon due to the trapping of carriers at the walls of the pores. Furthermore, increasing in the etching time will also increase the thickness of the porous silicon thin film, and this leads to increase in resistivity due to a decrease in mobility with increasing etching time. We notice from these figures that there is increase in the current density with increase ZnS concentration, this is due to an increase in the carriers density that generated at the surface and the formation of additional levels, which in turn leads to an increase in electrical conductivity.

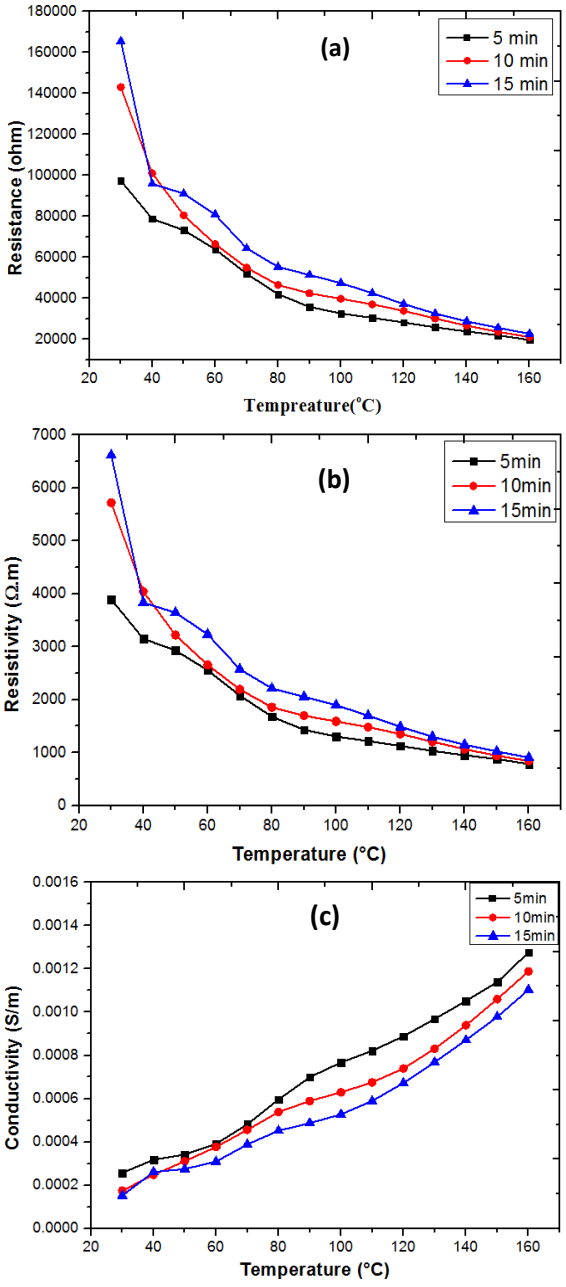

Fig. (11) Resistance, resistivity and conductivity of samples prepared at etching times of 5, 10 and 15min at concentration of 0.5M

The I-V characterization in forward bias possess two regions, the first region was found to be at low voltage ($1V < V_f$), where the current of this region is dominant because the concentration of carriers is greater than the pure state ($n_i^2 < np$). Therefore, in

order to reach a state of equilibrium, the recombination carriers process will be dominant, and this mean every electron is excited. At high voltages (V_f>1), the forward bias current increases exponentially with the applied voltages. In this case, the energy of carriers will increased with applied voltages and then it will pass through potential barrier of the ZnS-PSi heterojunction. Also, the ideality factor increases with increasing porosity due to an increase in the density of the levels at the interface between crystalline silicon and porous silicon. Table (5) shows the values of the reverse saturation cur-rent, ideality factor, barrier voltage and electrical conductivity for the ZnS/Psi heterojunction. Additionally, it can be seen that the values of the ideality factor and barrier voltage decrease with increasing concentration of ZnS [25].

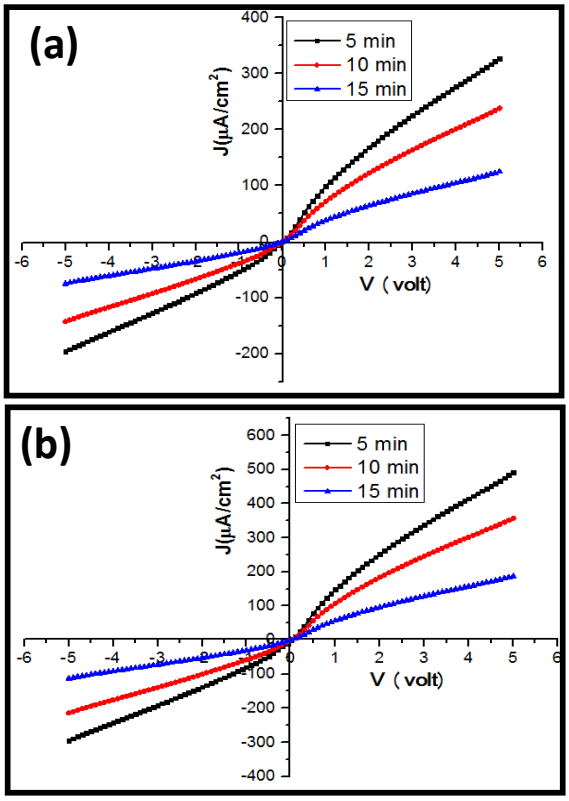

Fig. (12) J-V measurements of ZnS/PSi heterojunction with etching times of 5, 10 and 15 min at ZnS concentration (a) 0.1M and (b) 0.5M

Table (5) Parameters of Saturation current, ideality factor, barrier height and conductivity of ZnS/PSi heterojunction with etching time 5, 10 and 15 min at ZnS concentration 0.1 and 0.5 M

Etching time (min)	Concentration (M)	J_s (mA/cm²)	n	φ (eV)	σ ×10⁻³ (S/m)
5	0.1	12.27	2.43	0.635	0.997
10		6.92	2.68	0.669	0.732
15		1.64	2.79	0.72	0.575
5	0.5	17.86	2.31	0.613	1.28
10		11.21	2.48	0.632	1.19
15		6.56	2.63	0.690	1.10

Figures (13) and (14) (a-c) show the typical resistance response (kΩ) as a function to the time of gas sensor for different ZnS concentrations (0.1 M and 0.5 M). The operating temperature is selected as (RT, 100°C and 200°C) with constant NO_2 gas concentration of 75 ppm. The etching times of 5, 10 and 15 min are selected at ZnS concentration of 0.1 and 0.5M. The results illustrate that the significant variations of resistance for the gas sensor proved the synthesized ZnS over the porous silicon with higher purity and enabling their application in the manufacture of solid-state sensors for NO_2 detection. It is clear from these Figures that the resistance of ZnS/PSi heterojunction increased with increasing temperature. This can be attributed to increase the concentration which lead to increase the interactive between the surface area and the gas molecules [26]. The properties of ZnS/PSi heterojunction as a gas sensing for gases detection are examined. In order to determine the optimum operating temperature, the response of the ZnS /PSi heterojunction based gas sensors to 75 ppm of NO_2 is tested when the operating temperature varied from 50 to 250°C. Two concentrations of ZnS thin films of 0.1 M and 0.5 M are precipitated on the PSi. Figure (15) shows the sensitivity of sensor as a function of temperature for ZnS concentration of 0.1 and 0.5 M respectively when the etching time is varied from 5 to15 min with increment step of 5 min. It can be noted that the sensitivity of the sensor is varied with operating temperature. The sensitivity first is increased with increasing the temperature, up to 200°C, and then slowly decreased at 250°C. In addition, the sensitivity is improved for both concentration of ZnS when the time etching is increased. So, once size pore of PSi is changed, the sensitivity of ZnS /PSi heterojunction is change as well. Furthermore, the sensitivity is increased with increasing the ZnS concentration [27]. Figure (16) shows the comparison of the sensitivity for ZnS concentration of 0.1 and 0.5 M when the etching time is 15 min. As can be seen from this figure, the sensitivity of the ZnS/PSi heterojunction based gas sensor is increased with the increase the ZnS concentration. The maximum sensitivity is found to be 5.11 when the ZnS concentration is 0.5 M compared to the sensitivity of 3.0 at ZnS concentration of 0.1 M when the etching time of 15 min. This owing to increase the exposed surface area (increase the walls of the mesoporous structure), at this point, it is important to note that the Schottky barrier created at the ZnS/PSi interface due to the matching of the Fermi level, leading to create a depletion region and interactivity of surface area with gas molecules by the electron adsorption [28]. Tables (6-11) show response time, recovery time and sensitivity at different temperatures.

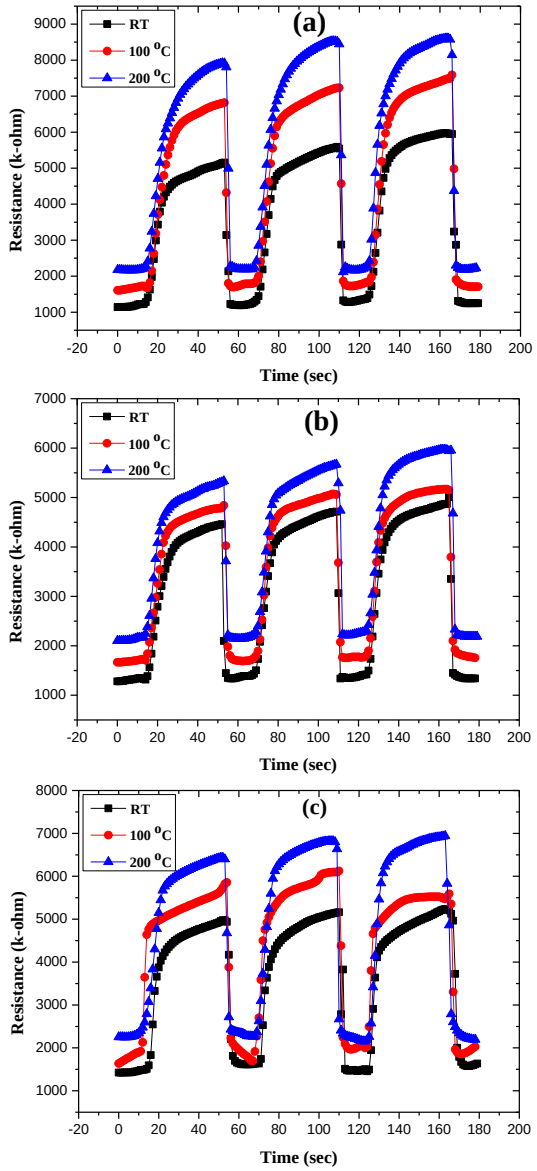

Fig. (13) Typical resistance curves of ZnS/PSi heterojunctions with ZnS concentration of 0.1M at different etching times (a) 5 min, (b) 10 min, (c) 15 min when the temperature is (RT, 100°C and 200°C) and 75 ppm of NO_2

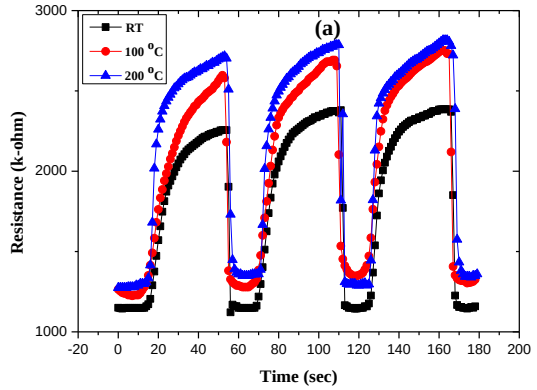

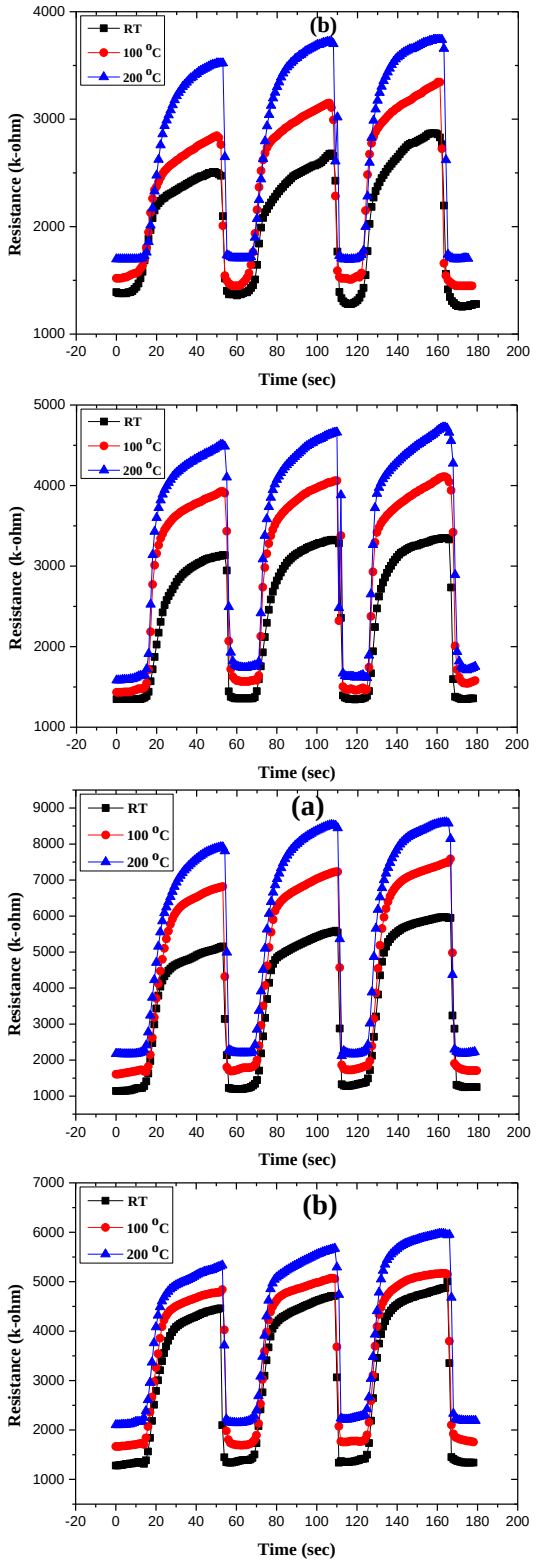

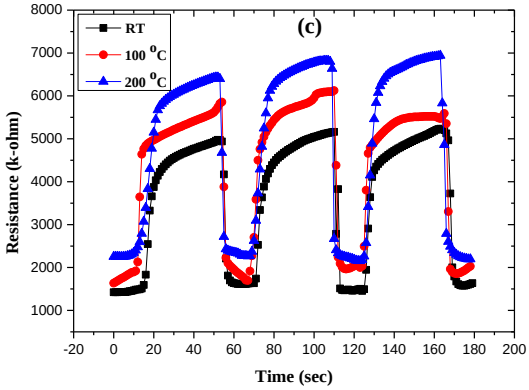

Fig. (14) Typical resistance curves of ZnS/PSi heterojunctions with ZnS concentration of 0.5M at different etching times (a) 5 min, (b) 10 min, (c) 15 min when the temperature is (RT, 100°C and 200°C) and 75 ppm of NO_2

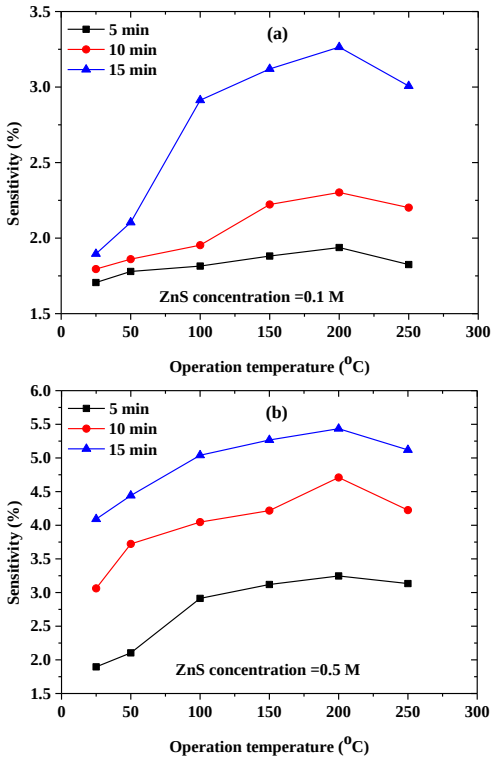

Fig. (15) Sensitivity versus operation temperature for NO_2 detection at etching times of 5, 10 and 15min and ZnS concentrations of (a) 0.1M, and (b) 0.5M

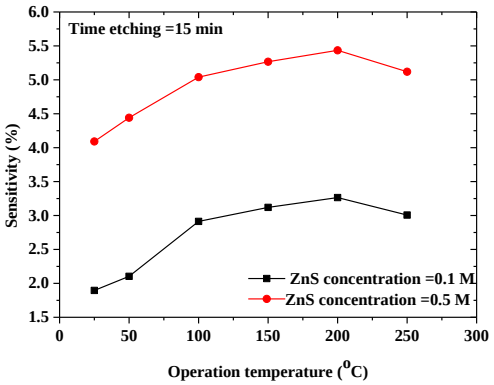

Fig. (16) The sensitivity comparison when ZnS concentrations are 0.1 and 0.5M at etching time of 15 min

4. Conclusions

In summary, good quality and high efficiency ZnS-PSi heterojunction-based gas sensors have been prepared by spray pyrolysis. The ZnS thin films are successfully grown on PSi substrates. The ZnS/PSi heterojunction-based gas sensors displayed good stability, fast response and recovery times and high sensitivity toward NO_2. The maximum sensitivity of the sensor is found to be 5.11 when the ZnS concentration is 0.5 M at operating temperatures up to 200°C. The results reveled that ZnS-PSi heterojunction is a promising candidate to use as photodetectors particularly for UV radiation.

Acknowledgements

The authors are thankful and gratitude to the Mosul University, College of Education for Pure Sciences, Department of Physics for providing all the required facilities.

References

[1] Sh.T. Hezarjaribi and N. Shahruz, "An enhanced fast ethanol sensor based on zinc oxide/nickel oxide nanocomposite in dynamic situations", *J. Inorg. Organometal. Polym. Mater.*, 30 (2020) 4072-4081.

[2] H.T. Hussein, U.M. Nayef and A.M. Hussien, "Synthesis of graphene on porous silicon for vapor organic sensor by using photoluminescence", *Optik*, 18(4) (2019) 61–70.

[3] Y.N. Al-Douri and C. Voon, "Etching time effect on optical properties of porous silicon for solar cells fabrication", *Optik*, 147(3) (2017) 343-349.

[4] O. Bisia, O. Stefano and L. Pavesi, "Porous silicon: a quantum sponge structure for silicon based optoelectronics Surface", *Sci. Rep.*, 38(12) (2000) 1-126.

[5] T. Kumeria, J.P. Steven and Sh.M. McInnes, "Porous silicon for drug delivery applications and theranostics: recent advances, critical review and perspectives", *Expert Opin. Drug Deliv.*, 14(12) (2017) 1407-1422.

[6] H. Föll et al., "New View of Silicon Electrochemistry", *phys. stat. sol. (a)*, 182(1) (2000) 7-16.

[7] A.A. Sulaiman, G.Gh. Ali and A.I. Thanon, "Synthesis and Study of ZnO Thin Films Using CVD Technique For Waveguide Sensor Applications", *J. Nanostruct.*, 12(1) (2022) 1-11.

[8] S. Mohammed, "Morphological and Optical Properties of Porous Silicon", *Eng. Technol. J.*, 37(1) (2019) 1-4.

[9] G.G. Ali, M.A. Ahmed and A.A. Sulaiman, "Structural properties of AuNPs/PSi nanostructure", *Digest J. Nanomater. Biostruct.*, 17(2) (2022) 473-480.

[10] J. Park, Y. Yanagida and T. Hatsuzawa, "Fabrication of p-type porous silicon using double tank electrochemical cell with halogen and LED light sources", *Sen. Actuat. B: Chem.*, 233(11) (2016) 136-143.

[11] E.A. Saverina, "Porous Silicon Preparation by Electrochemical Etching in Ionic Liquids", *ACS Sustain. Chem. Eng.*, 8(27) (2020) 10259-10264.
[12] J. Andrew and R. James, "Pyrite Formation via Kinetic Intermediates through Low-Temperature Solid-State Metathesis", *J. Am. Chem. Soci.*, 136(44) (2014) 15654-15659.
[13] C. Wang, "Structure and photoluminescence properties of ZnS films grown on porous Si substrates", *Opt. Laser Technol.*, 43(8) (2011) 1453-1457.
[14] I. Syahidi, B. Prayogo and K. Triyan, "Porous silicon fabrication on n-type Si (111) electrochemical anodization technique with HF: methanol solution", *Mater. Today: Proc.*, 44(7) (2021) 3430-3433.
[15] U.M. Nayef, H.T. Hussein and A.M. Abdul Hussien, "Study of photoluminescence quenching in porous silicon layers that using for chemical solvents vapor sensor", *Optik*, 172(7) (2018) 1134-1139.
[16] H.P Wang et al., "Fabrication of silicon hierarchical structures for solar cell applications", *IEEE Access*, 7(2) (2018) 19395-19400.
[17] J. Xu, "Preparation of porous silicon by electrochemical etching methods and its morphological and optical properties", *Int. J. Electrochem. Sci.*, 14(2) (2019) 5188-5199.
[18] X. Yang et al., "Porous Silicon Fabrication and Surface Cracking Behavior Research Based on Anodic Electrochemical Etching", *Fuel Cells*, 21(1) (2020) 52-57.
[19] K. Omar and K.A. Salman, "Effects of electrochemical etching time on the performance of porous silicon solar cells on crystalline n-type (100) and (111)", *J. Nano Res.*, 12(2) (2017) 123-134.
[20] R. Vercauteren, "Porous silicon membranes and their applications: Recent advances", *Sens. Actuat. A: Phys.*, 318(12) (2020) 112486.
[21] O.S. Volovlikova and P. Lazarenko, "Influence of illumination on porous silicon formed by photo-assisted etching of p-type Si with a different doping level", *Micromachines*, 11(2) (2020) 199.
[22] M.S. Akhtar, "Surfactant and template free synthesis of porous ZnS nanoparticles", *Mater. Chem. Phys.*, 189(3) (2016) 28-34.
[23] Y. Tsai, "Morphological and crystalline analysis of ZnO/ZnS nanostructures on porous silicon substrate", *Vacuum*, 178(8) (2020) 109454.
[24] D.A. Lizunkova, I.A. Shishkin and N.V. Latukhina, "Optical and photoelectric characteristics of the ZnS/porous-Si/Si structure performed by different technological routes", *IOP Publish.: Conf. Ser.*, 1 (2020) 1695.
[25] M. Mizuhata, M. Yuki and M. Hideshi, "Fabrication of ZnS/Porous silicon composite and its enhancement of photoluminescence", *Electrochimica Acta*, 201(3) (2016) 86-95.
[26] I. Sadovnikov, "Synthesis, properties and applications of semiconductor nanostructured zinc sulfide", *Russian Chem. Rev.*, 88(6) (2019) 571-582.
[27] A. Kumar, "Highly responsive and low-cost ultraviolet sensor based on ZnS/p-Si heterojunction grown by chemical bath deposition", *Sens. Actuat. A: Phys.*, 331(5) (2021) 112988.
[28] M.M. Hassan and M.A. Fakhri, "2-D of Nano Photonic Silicon Fabrication for Sensing Application", *Digest J. Nanomater. Biostruct.*, 14(4) (2019) 873-878.

Table 2: crystalline size , FWHM, inter-plane distance (d) of ZnS/PSi

Sample	Concentration (M)	2θ	hkl	L (nm)	FWHM (deg)	d (Å)
ZnS/PSi	0.1	27.38	002	37.47	0.561	3.254
		29.13	111	29.561	0.826	3.431
ZnS/PSi	0.3	26.56	002	38.615	0.436	3.174
		29.34	111	30.422	0.723	3.255
		32.591	106	22.633	0.985	3.513
ZnS/PSi	0.5	27.27	002	39.711	0.411	3.251
		29.06	111	33.622	0.633	3.122
		38.06	110	24.799	0.911	3.422

Table 3. The optimization parameters of ZnS/PSi heterojunction as a gas sensor

Sample	Concentration of ZnS (M)	Roughness Average (nm)	RMS (nm)	Diameter Average (nm)
PSi	-	1.26	1.31	24.65
	-	2.06	2.11	42.84
ZnS/PSi	0.3	2.53	1.88	83.36
	0.3	2.67	1.96	93.32

Table (6) Parameters of gas sensor for detect NO_2 gas of 75 ppm at different temperature, etching time of 5 min and ZnS concentrations of 0.1M

	RT	50°C	100°C	150°C	200°C	250°C
Air	1121.66	1224.047	1231.422	1231.422	1271.422	1251.422
Gas	3035.241	3.40E+03	3.47E+03	3548.241	3735.241	3535.241
G% (NO_2)	1.706026	1.779078	1.814822	1.881418	1.937846	1.82498
Response time (s)	4.3	5.8	8.2	11.8	13.51	15.62
Recovery time (s)	3.6	3.1	2.9	2.3	2.1	1.9

Table (7) Parameters of gas sensor for detect NO_2 gas of 75 ppm at different temperature, etching time of 10 min and ZnS concentrations of 0.1M

	RT	50°C	100°C	150°C	200°C	250°C
Air	1121.66	1224.047	1241.422	2154.084	1854.848	1322.426
Gas	3135.241	3501.723	3666.233	6941.776	6125.057	4234.195
G% (NO_2)	1.795179	1.860774	1.953254	2.222612	2.302188	2.20184
Response time (s)	8.2	9.2	6.5	8.9	9.4	10.2
Recovery time (s)	2.1	2.3	2.3	2.4	2.7	2.5

Table (8) Parameters of gas sensor for detect NO_2 gas of 75 ppm at different temperature, etching time of 15 min and ZnS concentrations of 0.1M

	RT	50°C	100°C	150°C	200°C	250°C
Air	1232.676	1665.708	1280.158	1240.158	1260.158	1250.158
Gas	3569.528	5170.168	5009.304	5109.304	5209.304	5009.304
G% (NO_2)	1.895755	2.103886	2.913035	3.11988	3.133849	3.006936
Response time (s)	4.2	5.3	4.9	6.8	6.9	7.5
Recovery time (s)	2.4	2.3	2.1	1.9	1.8	1.7

Table (9) Parameters of gas sensor for detect NO_2 gas of 75 ppm at different temperature, etching time of 5 min and ZnS concentrations of 0.5M

	RT	50°C	100°C	150°C	200°C	250°C
Air	1232.676	1665.708	1280.158	1240.158	1250.158	1260.158
Gas	3569.528	5170.168	5009.304	5109.304	5309.304	5209.304
G% (NO_2)	1.895755	2.103886	2.913035	3.11988	3.246905	3.133849
Response time (s)	6.3	7.8	11.3	13.2	15.4	17.2
Recovery time (s)	3.1	2.8	2.3	2.1	1.9	1.8

Table (10) Parameters of gas sensor for detect NO_2 gas of 75 ppm at different temperature, etching time of 10 min and ZnS concentrations of 0.5M

	RT	50°C	100°C	150°C	200°C	250°C
Air	2118.303	1606.957	1250.158	1144.121	1280.158	1380.158
Gas	8604.078	7588.949	6309.304	5969.713	7309.304	7211.304
G% (NO_2)	3.061779	3.722559	4.046804	4.21773	4.709687	4.224983
Response time (s)	6.3	7.4	11.5	12.5	13.7	15.2
Recovery time (s)	2.8	2.4	2.1	2.2	2.1	1.9

Table (11) Parameters of gas sensor for detect NO_2 gas of 75 ppm at different temperature, etching time of 15 min and ZnS concentrations of 0.5M

	RT	50°C	100°C	150°C	200°C	250°C
Air	1239.158	1244.121	1210.158	1230.158	1260.158	1231.422
Gas	6309.304	6769.713	7309.304	7709.304	8109.304	7535.241
G% (NO_2)	4.091604	4.441363	5.039957	5.26692	5.435147	5.119139
Response time (s)	7.8	8.1	8.3	8.6	9.3	9.7
Recovery time (s)	2.6	2.3	1.9	1.7	1.6	1.5

Mohammed A. Anaz [1]
Israa F. Al-sharuee [2]

[1] *Department of Physics, College of Science, Al-Anbar University, Al-Anbar, IRAQ*
[2] *Department of Physics, College of Science, Mustansiriyah University, Baghdad, IRAQ*

Spectroscopic and Compositional Analysis of Hydrophobic Silica Aerogels and Their Applications in Crude Oil Adsorption

The experiments studied the oil adsorption and doping effects of silica aerogels; doped with small percentages of silver and copper chloride, coumarin, and fluorescein dyes, were produced using a two-step acid-base catalyzed via sol-gel procedure. Tetraethoxysilicat (TEOS), methanol (MeOH), acid catalysis (0.1M), base catalysis NH_4OH:NH_4F (1:4), and modified solution trimethylchlorosilane (TMCS): n-hexane (1:10). Raman spectroscopy and Fourier transform infrared spectroscopy are utilized to indicate the molecular bonds and their regions, and field emission scanning electron microscopy to investigate the morphological properties. The hydrophobic aerogel particles showed a very high uptake capacity. The desorption of oil by keeping the liquid-absorbed aerogel. From FTIR examination, the aerogel structure was not significantly altered by the solvent absorption but shrank as a consequence of the oil absorption; the homogenous structure is dominant. The doping gives a strongly skeleton network that gives a bearing to the produced samples to re-use in the mentioned application.

Keywords: Laser dyes; Doped aerogel; Oil adsorption; Hydrophobicity
Received: 26 December 2023; **Revised:** 05 February; **Accepted:** 12 February 2024

1. Introduction

Silica aerogel, as a result of its high porosity and large specific surface area, is a new porous material that has been used and put to good use. Silica aerogels, on the other hand, don't have very good mechanical properties. Because of the drying steps involved in their manufacture, aerogels are notoriously weak, inflexible, and brittle [1]. This severely restricts silica aerogels' potential uses. Two of the most common ways to produce silica aerogels are through sol-gel and hydrothermal processes. Removing the solvent from a solution containing hydrolyzed inorganic compounds leaves behind a gel with a spatial network structure, which can be used to create porous structural materials. This process is known as the sol-gel technique [2]. There are several potential uses for silica aerogels, including thermal insulation, optics, medicine, power, and more. Silica aerogel is often utilized in environmental applications, including wastewater treatment, air purification, and more, because of its high porosity and vast surface area. Aerogels are the most buoyant solids known, with a density lower than water and a surface area higher than that of any other solid. These benefits have led to much research on the sorption of oil and other organics from water using various hydrophobic aerogels [3,4]. Hydrophobic silica aerogels were discovered to adsorb miscible and immiscible organic contaminants, including ethanol, toluene, chlorobenzene, and trichloroethylene. The tiny particles that make up silica aerogel provide the material its unique properties, including a low density that allows it to float on water [5]. Several conventional separation techniques have their limits when it comes to treating offshore crude oil leakages: Oil tanker treatment recycles a huge quantity of oil, but its treatment range is restricted by volume limitations and the spread area of oil slicks, the recovered oil includes a high amount of water, and the separation efficiency is poor. The silica aerogel is very soft had been researched for this project is a good way to solve this problem because it is cheap, good at separating oil and water, easy to use, good for the environment, and has many other benefits [6]. When dealing with offshore crude oil leaks, using aerogel eliminates the drawbacks of secondary separation on oil tankers as well as the drawbacks the combustion treatment and treatment with chemical reagents, all of which contribute to environmental contamination. It effectively separates oil from water and has zero environmental impact. It is distinguished by its low energy use and concern for the environment [7,8]. In this work the parameters that influence the efficiency with which aerogels separate oil and water was investigated. the superhydrophobic aerogels are a potential sorbent for cleaning up crude oil spills [9]. Zhang et al. have proposed that excellent adsorption capacity and high repeated utilization rate of RGO/REMO aerogels indicated the composite adsorbent's prospective application in the remediation of RhB-containing effluent [10]. Liu et al. have shown that the SGA beads exhibited excellent elasticity (rebounding at 70% strain) and oil/water selectivity. A continuous absorption-combustion process could be used to recover the adsorbed organic solvents. Therefore, because of the simplicity of their fabrication and their superior properties, SGA beads have great potential for use in oil spill and organic waste cleaning [11]. Parale et al. have shown that both the absorption capacity and the uptake rate of the

hydrophobic aerogel granules were very high. Aerogel granules soaked in liquid were weighed at set intervals until all the absorbed liquid had been completely desorbed in order to study the desorption of solvents and oils. Examination Fourier transform infrared spectroscopy indicated that solvent absorption did not substantially change the aerogel structure, but oil absorption caused the shrinkage that ultimately resulted in a thick structure following desorption [12]. Reynold et al. suggested that powdered CF3-functionalized aerogel may be able to efficiently separate oil from oil-water mixtures up to 14 times the aerogel's weight [13]. The findings of Nguyen et al. verified the superior efficacy of the modified silica aerogel nanoparticles over water in cleaning up the oil spill [14].

In the present study, the prepared hydrophobic aerogel was doped with metal ions and laser dyes. The doping gives a strong skeleton network, which gives a bearing of the produced samples to re-use in the application. The motivation for the prepared hydrophobic silica aerogel was utilized for oil adsorption to contribute to water environmental cleanup; spilled oil poses a danger to living organisms and humans in particular, and to protect fish health and living organisms from water pollution caused by crude oil spills.

2. Experimental Part

The chemicals used in this work includes tetraethylorthosilicat (TEOS, 98%) from Sigma-Aldrich (Germany), trimethylchlorosilane (TMCS, >98%) from TCI (Japan), hexane (>98%) from CHem-LAB (Belgium), ethanol (>99%) from Schariau (Spain), hydrochloric acid (35-38% strength) from Thomas Baker (India), ammonia solution from CDH (India), and silver chloride (AgCl) and copper chloride (CuCl). Both fluorescein ($C_20H_{12}O_5$) laser dye (146.145 g/ml molecular weight), and Coumarin ($C_6H_6O_2$) laser dye (332.31 g/ml molecular weight) were used as doping materials.

Metal ions and laser dyes doping of silica at a concentration of 10^{-2} g/cm^3, yields a variety of silica aerogel. Amounts of 0.71 of AgCl and 0.85 g of CuCl were dissolved in 50 ml ethanol. Fluorescein and Coumarin should be mixed into 50 ml of ethanol, respectively. A 2:40 molar ratio of ethanol was used to dilute TEOS (a precursor). By stirring on a magnetic stirrer for 10 minutes as well as incorporating 2 ml of 0.1M HCL as an acidic catalyst, condensed silica (CS) was successfully produced. First, the dopant materials (10 ml) were mixed with the concentrated and then stirred for 15 minutes using a magnetic stirrer. Finally, a 0.5M NH_4OH base catalyst was added to accelerate the transformation of the sol into a gel. After being prepared for 15 minutes, this gel is aged for 2 hours before being soaked three times every 24 hours, immerse in ethanol. The gel's surface was treated with TMCS (7.5ml) in 30 ml hexane drop by drop, and after baking it for 24 hours at 60°C, it was let to settle at room temperature for 24 hours before being replaced in the oven with pure hexane for 4 hours to modify the surface. After being washed in hexane, the holders were coated with salophen that had tiny holes drilled into it, and the whole thing was let dry at room temperature. Remove moisture from the gel by gradually raising the oven temperature from 80 to 180° degrees with a step of 20°. The application was surveyed via spraying a known quantity of aerogel on the surface of water onto which a quantity of crude oil of known weight was spilled, and after a while an isolated layer was formed on the surface. The layer was scraped off, weighed, and the weight of the aerogel was subtracted from the total weight. This quantity represents what was adsorbed from the crude oil spilled on the surface of the water.

Raman spectroscopy is a kind of spectroscopy used for structural analysis and the observation of rotational, vibrational, and other low-frequency modes. Photoluminescence is an extremely potent, contactless, and nondestructive optical phenomenon that is used to probe the electronic structure of materials. The external source was used to excite the electronic state. Fourier-transform infrared (FTIR) spectroscopy with a scanning wavenumber range of 4000-400 cm^{-1} confirmed the hydrophobicity and surface modification. Field-emission scanning electron microscopy (FE-SEM) analysis validated the porous morphology of silica aerogels, which has drawn a lot of interest due to its unusual features, such as its low density was examined depended on the ratio between mass to volume. To evaluate the practical crude oil adsorption performance by the aerogel. The oil absorption capacity (Q_a) of the aerogels can calculate by weighted it before (M_w) and after (M_d) adsorbed, using the following formula [15]

$$Q_a = \frac{M_w - M_d}{M_d} \quad (1)$$

3. Results and Discussion

Figures (1) and (2), the Raman spectra, demonstrate the presence of the metal ions copper chloride and silver chloride; the highest intensity of silver chloride is seen at a wavelength of 183.255nm in the case of the aerogel generated via surface modification using TMCS/hexane, the weakest peaks emerged at wavelengths 3630.433 and 4330.878nm; the highest peaks appeared at the wavelengths 666.097 and 2113.214 nm in the copper chloride, where the symmetric stretching vibration constituted the sole form of vibration [16]. The vibration of two symmetrical expansion distinct kinds of atoms is responsible for the formation of these lower-amplitude peaks. The vibration of two symmetrical expansion distinct kinds of atoms is responsible for the formation of these lower-amplitude peaks.

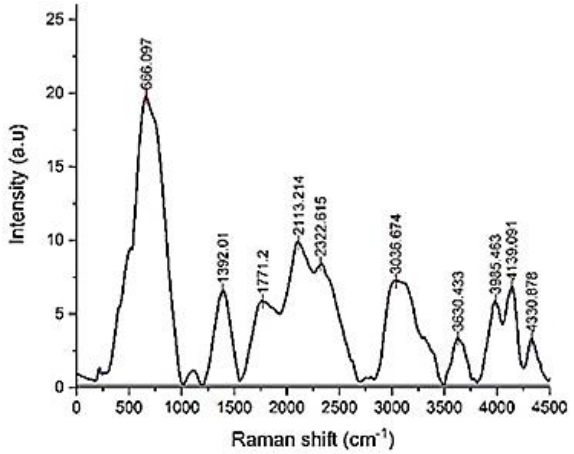

Fig. (1) Raman spectrum of silica aerogel doped with copper chloride (CuCl)

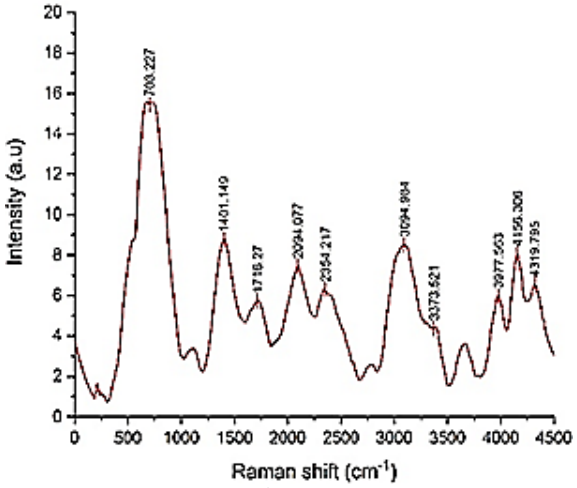

Fig. (2) Raman spectrum of silica aerogel doped with silver chloride (AgCl)

Figures (3) and (4) show the Raman spectra of silica aerogel doped with laser dyes (Coumarin and fluorescein, respectively). They show a shift and regarding the aerogel generated via surface modification utilizing TMCS/hexane, the highest intensity of coumarin emerged at wavelengths of 85.324 and 595.598 nm, while the maximum intensity of fluorescein appeared at wavelengths of 479.627 and 1415.129 nm. This is because one sort of vibration, denoted by the symmetrical stretching vibration, is responsible for the phenomenon, while it manifested itself at the next wavelength for the less powerful peaks at 3630.433 and 4330.878 nm. It is because of the similar stretching vibration that two different kinds of atoms produce that these peaks may be seen with a lesser intensity [17,18]. There are many peaks appeared in Raman spectrum for all produced samples signified in table (1).

Figures (5) and (6) refer to the presence of the metal ions copper chloride and silver chloride. The surface groups react during drying to form Si-O-Si bonds by condensation at ambient pressure. As a result of the increased capillary pressures caused by the creation of Si-O-Si bonds, the wet gel's pore network collapses. A total of 38 Si-O-Si stretching vibrations are reflected in the bands at 1096 cm^{-1}, whereas Si-O vibrations produce the characteristics around 798 cm^{-1}. Bands of adsorption at 3435 cm^{-1} have been identified as belonging to hydroxyls, -H, and CH_3 bands, the primary source of hydrophobicity, peaked at roughly 2981-2900 cm^{-1}.

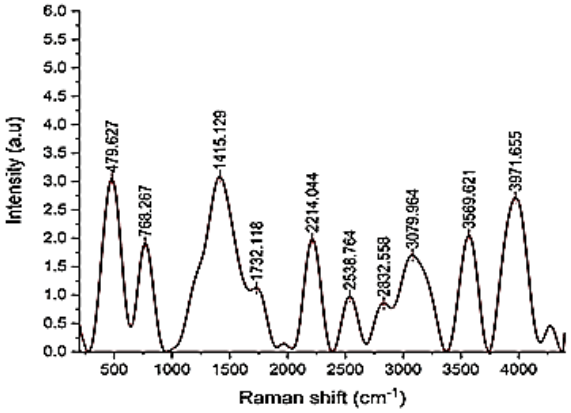

Fig. (3) Raman spectrum of silica aerogel doped with Fluorescein

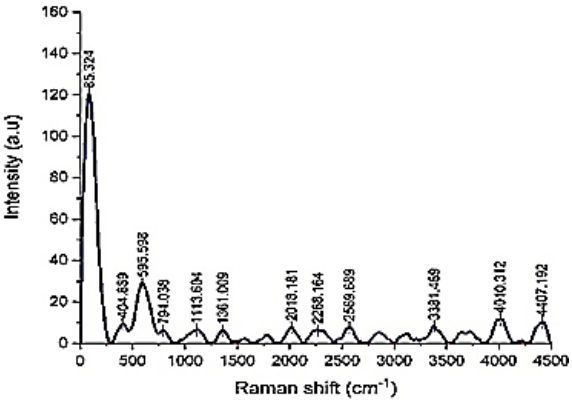

Fig. (4) Raman spectrum of silica aerogel doped with Coumarin

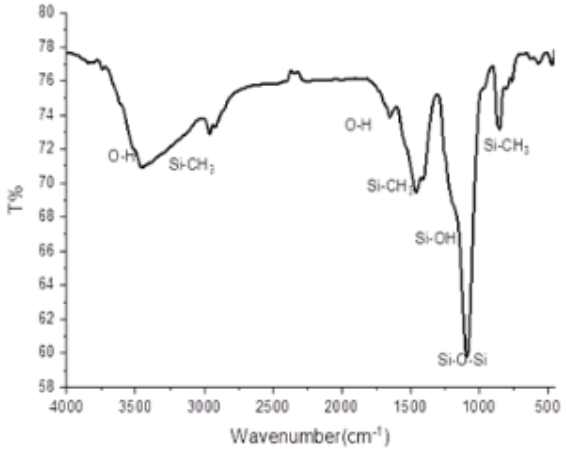

Fig. (5) FTIR spectrum of doped silica aerogel with CuCl

The infrared spectra of modified SiO_2 aerogel show the H-OH peaks at 3425 and 1633 cm^{-1}, which is CO insistent with the aerogel's altered structure. After TMCS modification, hydroxyl groups are replaced by -CH_3 groups, enhancing the compound's

hydrophobicity. Diffusion via the wet gel's porous structure ensures that surface reactions take place uniformly throughout the material. The thermogram analysis confirmed that the aerogel's surface hydroxyl (-OH) and alkoxy (-OR) groups were converted to the more stable Si-R group [12].

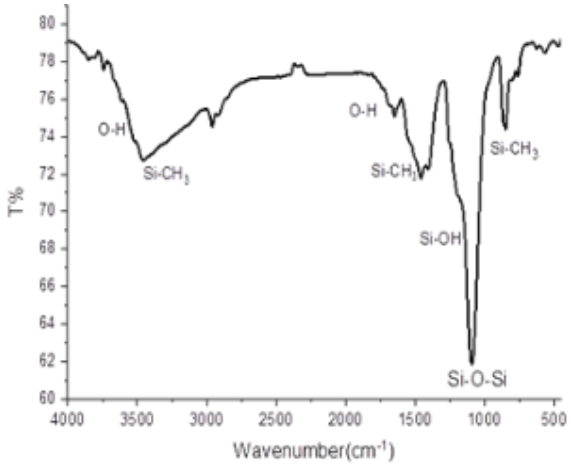

Fig. (6) FTIR spectrum of doped silica aerogel with AgCl

In figures (7) and (8) for Coumarin and fluorescein dyes, the FTIR bands were used to study the chemical bonds of the (SA) changed by TMCS. At 3480 and 1610 cm^{-1}, vigorous absorption peaks are observed are caused by the stretching vibration of hydroxyl (-OH). This shows that these hybrid aerogels can take in water from the air and have strong hydrophilicity. In contrast, Weak absorption peaks for Si-OH at 980 cm^{-1} were observed in the hydrophobic sample (TMCS).

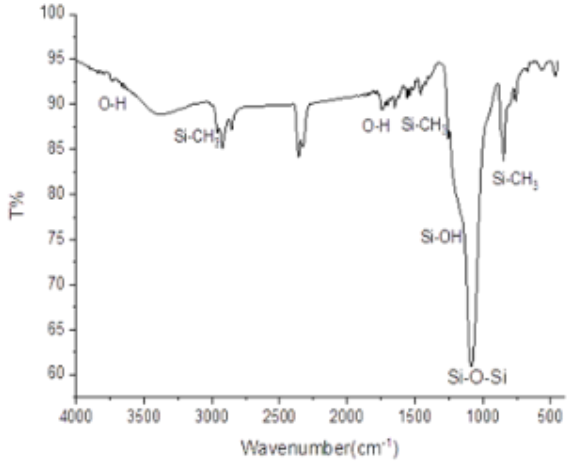

Fig. (7) FTIR spectrum of doped silica aerogel with Coumarin

They appeared Si-O-Si bonds in the silica network exhibit prominent absorption peaks at approximately 1100 cm^{-1}, which meant in which TEOS was effectively hydrolyzed and cross-links were formed, which are attributes characteristic of (SA). At 2990 cm^{-1}, the sample had an absorption peak related to the terminal $–CH_3$ group. At 1280, 840, and 766 cm^{-1}, vibration peaks of Si-C were seen, which were caused by the TMCS surface modification. Furthermore, the TMCS-based hybrid aerogel showed good hydrophobicity and a lowlight weight [19,20].

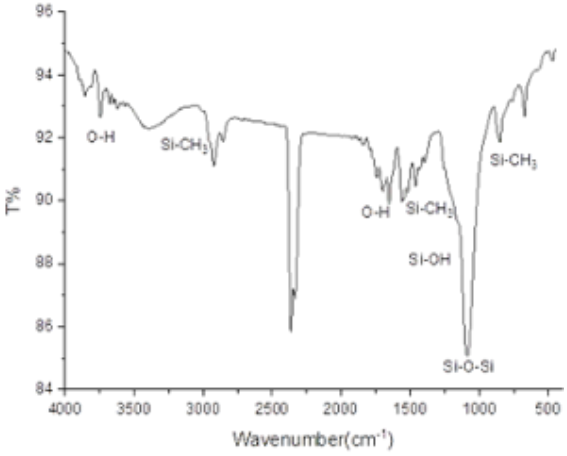

Fig. (8) FTIR spectrum of doped silica aerogel with fluorescein

Figure (9) shows FE-SEM results for copper chloride and silver chloride ions. The aerogel had a porous morphology, with pores of varying sizes spread out randomly throughout the material. Previous research has shown that the pore size of aerogels used in oil/water separation applications should be below 200 m [21] and employed to make the nanocomposite aerogels in this research. Various magnification photos of the created aerogel composite aerogel should be shown. Aerogel pores ranged in size 29.43 nm as determined by an image analysis program (ImageJ). Pores in the aerogels have a rough appearance in the high-resolution SEM picture. The creation of an internal phase transition is responsible for the aerogel's enlarged pores. From figures it cleared the morphological study of the as-prepared aerogels for Coumarin and fluorescein dyes was done using FE-SEM analysis, and images were analyzed for their quality.

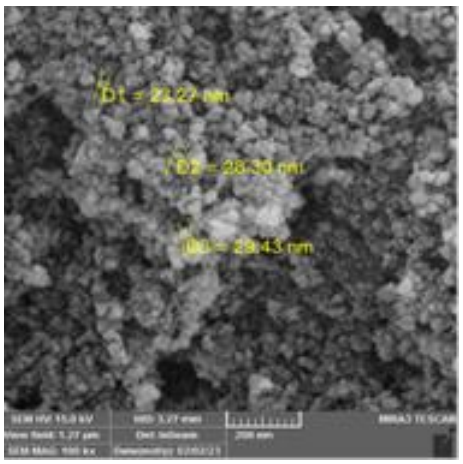

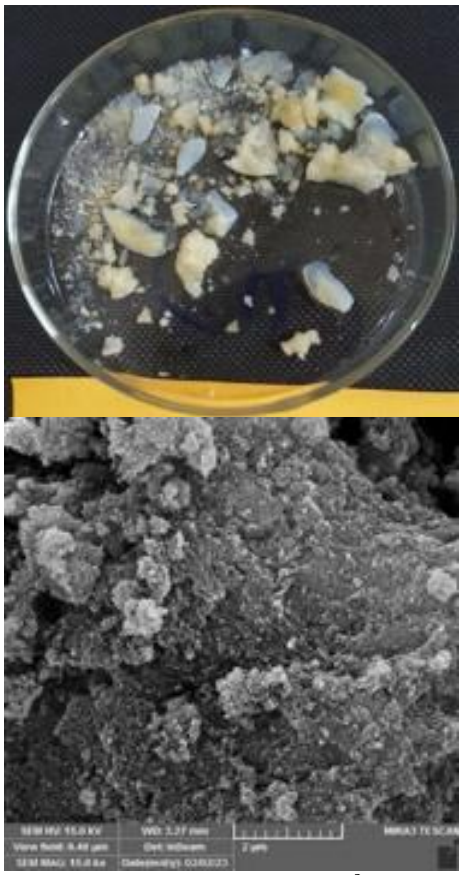

(a) CuCl density 0.219 g/cm^3

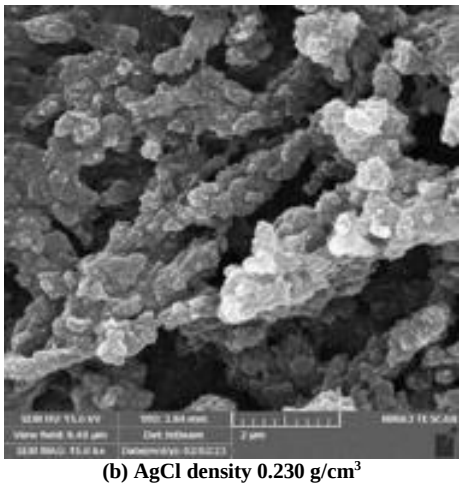

(b) AgCl density 0.230 g/cm^3

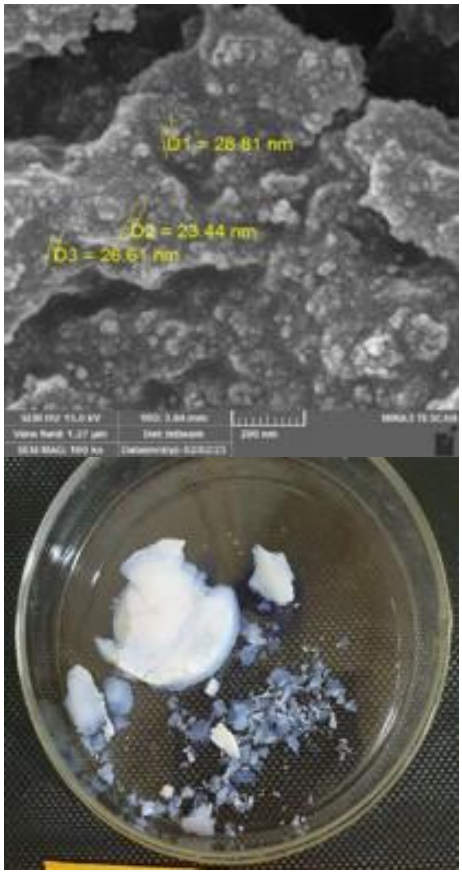

(c) Fluorescein density 0.221 g/cm^3

(d) Coumarin density 0.20 g/cm^3

Fig. (9) FE-SEM images of doped silica aerogel with (a) copper chloride, (b) silver chloride, (c) fluorescein, and (d) Coumarin with different magnifications

All aerogels seen in the photographs, regardless of magnification, have a porous 3D structure that is well linked. Aerogels are of particular interest due to their unusual features, such as their low density, which results from the tight packing of primary particles in the agglomerates, which is themselves porous. Because of the aerogel's porous, networked interior, it is possible to use gravity to drive a high-flux oil/water separation process using aerogels with superoleophobicity characteristics [22,23].

Figure (10) illustrates the mechanism of absorption during the first few minutes. The aerogel rapidly assimilated the crude oil on the surface of the mixture in about 30 minutes. A 0.053 g of aerogel powder were sprayed over the surface of the oil. The aerogel powder absorbed 4.75 g of oil after 30 minutes. The absorption capacity may be quantified using Eq. (1):

$$Q_a = \frac{4.75 - 0.053}{0.053} = 88.623\% \quad (1)$$

Fig. (10) Photographs before and after the absorption of crude oil by the hydrophobic aerogel

4. Conclusion

Hydroxyl groups are replaced by -CH_3 groups, enhancing the compound's hydrophobicity, in the Raman spectrum, more peaks are different because of the vibration that two different kinds of atoms were produced. These peaks may be seen with a lesser intensity. The aerogel had a porous morphology and a porous 3D structure, with pores of varying sizes spread out randomly throughout the material. The FTIR spectrum shows that the TMCS silylating agents were effective in making the surface of the aerogel hydrophobic by replacing the polar bond -OH with nonpolar bonds like Si-C and C-H. Aerogel materials are gaining a lot of interest because of their peculiar properties, such as their low density. Because of the assumed packing of primary particles in agglomerates, they are very porous. The homogenous structure is dominate for all samples. Using aerogel as an adsorbent medium for oil gave good results through the adsorption of 88% of the oil spilled on the water's surface. The doping gives a strong skeleton network, which gives a bearing of the produced samples to re-use in the mentioned application.

References

[1] L. Li et al., "Preparation of Super-Flexible Silica Aerogel and Its Application in Oil–Water Separation", *Gels*. 9 (2023) 739.

[2] X. Li et al., "Preparation of La1. 89Ce0. 11CuO4 superconducting film by sol-gel method", *Physica C: Supercond. Appl*., 603 (2022) 1354153.

[3] D. Wang et al., "Removal of emulsified oil from water by inverse fluidization of hydrophobic aerogels", *Powder Technol*., 203 (2010) 298-309.

[4] W.H. Al-Husseny, I.F. Al-Sharuee and B.R. Ali, "Sspectral and structural analysis for sodium silicate-based aerogel via normal drying pressure", *Malaysian J. Sci*., 42 (2023) 47-55.

[5] Z. Xue et al., "A novel superhydrophilic and underwater superoleophobic hydrogel- coated mesh for oil/water separation", *Adv. Mater*., 23 (2011) 4270-4273.

[6] J. Ge et al., "Joule-heated graphene-wrapped sponge enables fast clean-up of viscous crude-oil spill", *Nature Nanotech*., 12 (2017) 434-440.

[7] P. Renjith et al., "Micro-cellular polymer foam supported silica aerogel: Eco-friendly tool for petroleum oil spill cleanup", *J. Hazard. Mater*., 415 (2021) 125548.

[8] A. Iranitalab, A. Khattak and E. Thompson, "Statistical modeling of types and consequences of rail-based crude oil release incidents in the United States", *Reliab. Eng. Syst. Safe.*, 185 (2019) 232-239.

[9] I.F. Al-sharuee and F.H. Mohammed, "Investigation study the ability of superhydrophobic silica to adsorb the Iraqi crude oil leaked in water", *IOP Conf. Ser.: Mater. Sci. Eng.*, 571 (2019) 012116.

[10] H. Cai et al., "Preparation of silica aerogels with high temperature resistance and low thermal conductivity by monodispersed silica sol", *Mater. Design*, 191 (2020) 108640.

[11] L. Liu et al., "Superhydrophobic graphene aerogel beads for adsorption of oil and organic solvents via a convenient in situ sol-gel method", *Coll. Interface Sci. Commun*., 45 (2021) 100518.

[12] V.G. Parale et al., "Potential application of silica aerogel granules for cleanup of accidental spillage of various organic liquids", *Soft Nanosci. Lett.*, 1 (2011) 97-104.

[13] J.G. Reynolds, P.R. Coronado and L.W. Hrubesh, "Hydrophobic aerogels for oil-spill cleanup Intrinsic absorbing properties", *Ener. Sourc*., 23 (2001) 831-843.

[14] H.K. Nguyen, P.T. Hoang and N.T. Dinh, "Synthesis of modified silica aerogel nanoparticles for remediation of vietnamese crude oil spilled on water", *J. Brazil. Chem. Soc*., 29 (2018) 1714-1720.

[15] S.T. Nguyen et al., "Advanced thermal insulation and absorption properties of recycled cellulose aerogels", *Coll. Surf. A: Physicochem. Eng. Aspects*, 445 (2014) 128-134.

[16] R. Nasi et al., "Application of reverse micelle sol–gel synthesis for bulk doping and heteroatoms surface enrichment in mo-doped TiO_2 nanoparticles", *Materials*, 12 (2019) 937.

[17] Á. Lakatos and I. Csarnovics, "Influence of thermal annealing on structural properties of silica aerogel super insulation material", *J. Therm. Anal. Calorim.*, 142 (2020) 321-329.

[18] S.S. Ahmed and I.F. Al-Sharuee, "Comparison of the properties of silica aerogel doped with two different laser dyes: Crystal violet and Rhodamine B", *Kuwait J. Sci*., 50 (2023) 10.48129/kjs.20549.

[19] P.B. Sarawade et al., "High specific surface area TEOS-based aerogels with large pore volume prepared at an ambient pressure", *Appl. Surf. Sci*., 254 (2007) 574-579.

[20] S.S. Ahmed and I.F. Al-Sharuee, "Superhydrophobic silica monolithic doped with crystal violet dye under ambient pressure: preparation and characterization", *New Mater. Comp. Appl*., 6 (2022) 282-293.

[21] F. Akhter, S.A. Soomro and V.J. Inglezakis, "Silica aerogels; a review of synthesis, applications and fabrication of hybrid composites", *J. Porous Mater*., 28 (2021) 1387-1400.

[22] B. Merillas et al., "Silica-Based Aerogel Composites Reinforced with Reticulated Polyurethane Foams: Thermal and Mechanical Properties", *Gels*, 8 (2022) 392.

[23] W.H. Al-Husseny, I.F. Al-Sharuee and B.R. Ali, "Water glass based superhydrophobic silica aerogel in different environmental of preparation", *New Mater. Comp. Appli.*, 6 (2022) 127-139.

Table (1) The main peaks of Raman CuCl spectrum

Aerogel doped with CuCl				Aerogel doped with AgCl			
Wavenumber (cm^{-1})	Intensity (a.u)	Wavenumber (cm^{-1})	Intensity (a.u)	Wavenumber (cm^{-1})	Intensity (a.u)	Wavenumber (cm^{-1})	Intensity (a.u)
666.097	20.001	3036.674	7.11	703.227	15.501	3094.984	8.5298
1392.01	6.531	3630.433	3.197	1401.149	8.800	3373.521	4.3790
1771.2	6.12	3985.463	6.10	1716.27	6.77	3977.563	6.130
2113.214	10.002	4139.091	7.009	2094.077	7.09	4156.306	8.2001
2322.615	8.50	4330.878	3.21	2354.217	5.999	4319.795	6.5.1
Aerogel doped with fluorescein				Aerogel doped with Coumarin			
479.627	3.0469	2538.764	1.002	85.324	120.24	2018.181	8.110
768.267	2.109	2832.558	0.988	404.889	9.4384	2268.164	5.449
1415.129	3.0850	3079.964	1.7009	595.598	28.944	2569.689	8.110
1732.118	1.132	3569.621	2.0511	794.038	6.1615	3381.489	8.009
2214.044	1.980	3971.655	2.7151	1113.604	6.42	4010.312	12.220
				1361.009	6.2368	4407.192	10.249

Aveen S. Abdulhamed
Qusay A. Abbas

Department of Physics, College of Science, University of Baghdad, Baghdad, IRAQ

Effect of Magnetic Field on Characteristics of Micro-Discharges Generated by Dielectric Barrier Discharge Actuator

The present work studied the influence of a parallel magnetic field on the properties of micro-discharges generated in a DBD actuator under atmospheric pressure. The micro-discharge is formed when the Ac high voltage with frequency of 9 kHz was applied. As well as, the magnetic parallel field was present when the magnetic permanent was putting behind the powered electrode. The micro-discharge characteristics were measured at various horizontal distance that varying for 0 to 5 cm. Magnetic field effects on micro-discharge properties at different horizontal distances were examined. The results indicated that the influence of the powered electrode area affect the micro-discharge. The presence of the parallel magnetic field shown inverse behavior on the micro-discharge characteristics.

Keywords: Micro-discharge; Optical Emission Spectra; Magnetized DBD; Actuators
Received: 29 January 2024; **Revised:** 06 March; **Accepted:** 13 March 2024

1. Introduction

The dielectric barrier discharge (DBD) is considered to be one of the most economically efficient non-thermal plasma sources among the different options available. This discharge is recognized for its efficacy in initiating chemical and physical processes that take place in gases [1]. In past few years, DBD has been extensively studied due to its application in many different areas. This type of discharge covers many applications such as material surface processing [2,3] and also applications in the environment and energy field, water treatment [4-8], agriculture [9-11], surface modification [12,13], biomedical sterilization [14-16], pollution control [17] and medicine [18,19]. The ability of these DBD applications lies in their capacity to produce highly reactive plasma using a simple reactor system, requiring low energy consumption, and operating at room temperature and atmospheric pressure [20,21]. DBD reactor is fundamentally composed of a series of electrodes, separated by at least one dielectric barrier. To generate the breakdown in gases between the electrodes, a high enough electric field must be applied. Therefore, this feature represents the advantage of DBD than the other conventional plasma generator sources [22]. Anyway, in various industrial applications, active flow control is necessary to improve efficiency of system efficiency or to less the environmental load [23]. Therefore, the mechanical actuators were used to achieve flow control [24]. In 1990, Roth et. al. [24] developed a new device for flow control. The DBD device was utilized as a plasma actuator. The non-thermal plasma actuator functions at air pressure and has various advantages over traditional flow control actuators. These include compact size, straightforward design, lightweight construction, rapid response, and the absence of mechanical components [25-27]. For decades plasma actuators have received attention for the barrier discharge of the AC surface [28-31]. Basic plasma properties of AC-SDBDPAs have been studied [27]. Non-thermal plasma actuators for flow control were illustrated in many applications for separation flow control [32–35] and noise reduction [36,37]. The Based operating principle of plasma actuator is the electrohydrodynamic phenomenon that formed due to the transfer of the ions momentum to neutral molecules by impact process. DBD and corona discharges represent the most common discharge that occurs in the plasma actuators [38]. Moreover, numerous endeavors have been made to enhance the control authority and reduce the power demands of DBD actuators. The range is from 2 to 4. In these studies, several parameter trends have been examined, such as the characteristics of the input alternating current voltage (e.g., amplitude, frequency, and waveform shape), material properties, and the design of the DBD device. The amplitude of the sinusoidal input voltage increases as the electrical power consumed by the DBD actuators increases, as 3.5 PV. Moreover, the dielectric barrier discharge actuators make a wall jet with speed range from 1to 6 m/s occurring at distance range from 0.5 to 1 mm above the dielectric surface. According to experimental results, the maximum produced velocities was approximately 8 m/s2, while according to numerical predictions indicate velocities approximately up to10 m/s2 [39]. Recently, different researchers were studied the influence of the magnetic field on the characteristics of the DBD actuator and the researchers observed that the permanent magnetic field gives an impression of the movement of electrons after the release of DBD in the gaseous insulation [40]. The influence of the magnetic field that produced by permanent magnet in

the normal direction of the electric field on DBD performance was investigated in reference [41]. Furthermore, another study examined the contrast between the behavior of DBD with and without a magnetic field in the air. The findings demonstrated distinct variations in various DBD characteristics, including; DBD plasma, discharge current, power dissipation, and more, when the magnetic field was present compared to when it was absent [42,43]. When the pulse repetition frequency of unipolar positive nanosecond pulsed DBD lowers from 1200 to 100 Hz, the discharge becomes more homogeneous. Furthermore, an equivalent outcome can be attained in presence of a parallel magnetic field [44].

Present work characterizes micro-discharges that formed in single DBD actuator with two AC frequency and at different horizontal distances. The characterization encompassed many parameters such as micro discharge volume, I-V curve, Debye length, electron number density, electron temperature, plasma parameter, and plasma frequency.

2. Methodology

This section describes the theoretical description of some plasma parameters of micro discharge that formed in the DBD actuator, like; electron number density (n_e), electron temperature (T_e), Debye length (λ_D), plasma parameter. (N_D), and plasma frequency. (ω_p). The electron temperature (T_e) is the fundamental plasma parameters which used to describe the plasma state. In this work, the Boltzmann plot was utilized to calculate electron temperature, as [45-46]:

$$\ln\left(\frac{I_Z\lambda_{ki,z}}{g_{k,z}A_{ki,z}}\right) = -\frac{1}{kT_e}E_{k,z} + ln\left(\frac{hcL_{nz}}{4\pi P_z}\right) \qquad (1)$$

where Z is the species-related ionization state, C is speed of light, k is Boltzmann constant, L is characteristic length of the plasma, h is Planck's constant, E_k is energy of the upper energy level k, g_k is degeneracy of the upper energy level k, P_Z species partition function in ionization stage Z, and I_Z is optically measured integrated intensity of a species in ionization stage Z are all included. By graphing the left-hand side of equation (1) against the upper-level energy of the species in the Z ionization phase, a linear relationship is observed. The slope of this line corresponds to electron temperature in electron volts.

There are many methods adjusted to calculated the electron number density, the Stark broadening method is used in this work. The electron number density was determined using the Stark broadening method [47-50]:

$$n_e(cm^{-3}) = \left[\frac{\Delta\lambda}{2\omega_s}\right] N_r \qquad (2)$$

where ω_s is the electron impact, $\Delta\lambda$ denotes the full width at half maximum of the line, N_r is the reference electron number density, that equal of 10^{16} cm^{-3} for neutral atoms and 10^{17} cm^{-3} for singly charged ions.

Debye length (λ_D) is a fundamental quantity of the plasma that represents its ability to shield out electric potentials that are applied to it. λ_D is determine of the sheath thickness or shielding distance which can determined as [45,46,50,51]:

$$\lambda_D = 7430(kT/n)^{1/2} \quad m, T \ in \ eV \qquad (3)$$

The plasma parameter (N_D) represent the number of charged particles in the Debye sphere which can calculated as [52,53]:

$$N_D = \frac{4\pi}{3}n\lambda_D^3 = 1.38\times10^6\frac{T_e^{\frac{3}{2}}}{\sqrt{n}} \qquad (4)$$

where T_e is the electron temperature (in K) and n is the plasma number density (in cm^{-3})

Plasma frequency (ω_p) can define as the electrons oscillation around the original positions inside the plasma as a results of the electric force that built up due to the electrons displacement. This parameter was calculated from [49,46]:

$$\omega_p = \left(\frac{n_0e^2}{\epsilon_0 m_e}\right)^{1/2} (rad/s) \qquad (5)$$

where ε_0 is vacuum permittivity, e is the electronic charged, n_0 is the electron number density and m_e is the electron mass

3. Experimental Part

Figure (1) displays the experimental arrangement of magnetized DBD actuator system. The system consists of two circular disc aluminum electrodes with diameter 9 cm and thickness of 1 cm. Both electric electrodes are submerged in a circular Teflon container to preclude electrical sparks at edges of the electrodes.

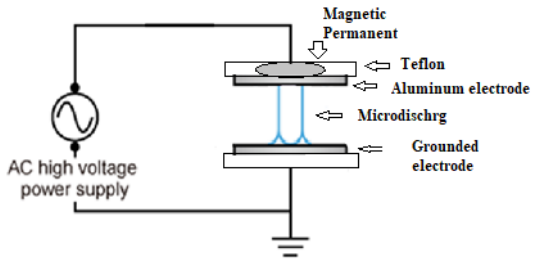

Fig. (1) Typical DBD actuator system

An AC high voltage (r.m.s is 22 kV) power supply with AC frequency of 9 kHz was supplied of one electrode, while the other electrode was connected to the ground. The distance between the two electrodes is 1cm and filled by air at atmospheric pressure at room temperature. One circular magnetic permanent (diameter of 7 cm and thickness of 1cm) was located inside the Teflon under the powered electrode in the parallel direction of the applied electric field. When the AC high voltage was supplied between two electrodes, a micro a discharge was established in the air gap between two electrodes in the absence and presence of the magnetic field. The micro-discharge generated in the DBD actuator is found by a high-resolution digital camera at various horizontal distances ranging from 0 to 5 cm. The emission spectra of the micro-discharge are recorded

using the THOR LAB model CCS100 optical emission spectrometer, manufactured in Germany. The measurements are conducted in two scenarios: one with the presence of a magnetic field and one without. The wavelength range for the recorded spectra is 320-740 nm. The magnetic field was measured by Leybold Tesla meter and has the value of 18.7 mT. The spectrometer was placed at an angle 45° from the direction of the magnetic field. The results of the emission spectra of the micro-discharge were adjusted with NIST database to determine the micro-discharge characteristics in the electrodes gap.

4. Results and Discussion

Figure (2) shows a photograph of such micro-discharges in air gap between electrodes at different horizontal distance in the lack of the magnetic field. Many features can be noted from this figure; the photographs display that the micro-discharge current is characterized by one distinct period of pulse, corresponding to the micro-discharge which due to streamer propagation.

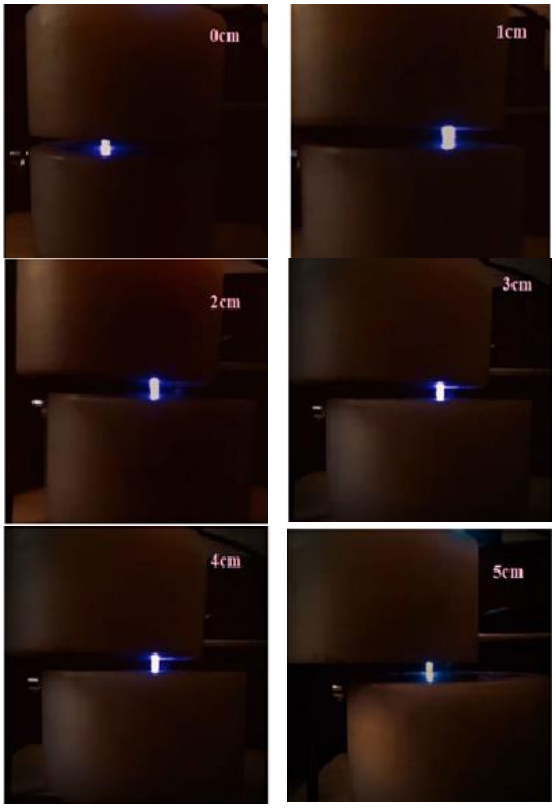

Fig. (2) Influence of horizontal distance on the micro-discharge that formed in DBD actuator in the absence of the magnetic field

Micro-discharges (sometimes called current filaments) generated from gases breakdown that occur at atmospheric pressure in DBD. These independent current filaments represent the most interesting property of DBDs. The temporal progression of the discharge current is significantly affected by multiple factors, which encompass the actuator's geometry, the electrical properties of the power supply, environmental conditions (such as humidity, pressure, temperature, and ambient gas), and the physicochemical attributes of the dielectric material. The second half of the paper will further explore the impact of geometry and electricity on the generated body force and subsequent electric wind [30].

The intensity of this micro- discharge depends strongly on the characteristics of AC power supply source. Increasing the horizontal distance from D equal 0 to 5 cm, the micro-discharge intensity increases. On the other hand, the effect of the magnetic field on the micro-discharge that formed in DBD actuator at different horizontal distances was demonstrated in Fig. (3). The illustration demonstrates the visible confirmation of the micro-discharge that takes place at the air gap between the electrodes. The magnetic field's presence influences the formation of micro-discharge in the air gap between the electrodes.

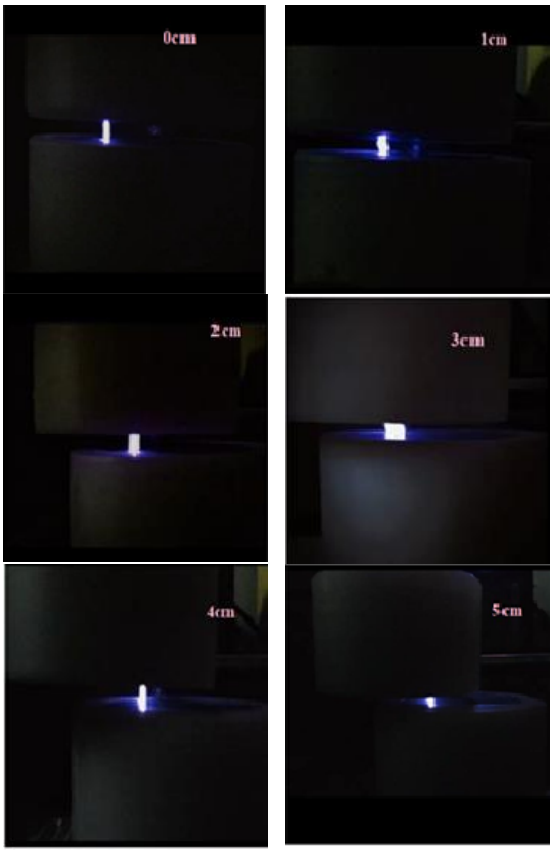

Fig. (3) Influence of horizontal distance on the micro-discharge that formed in DBD actuator in the Presence of the magnetic field

Plasma images of three models are depicted in Fig. (4). Upon comparing figures (2) and (3), it was seen that the micro-discharge created in the presence of the magnetic field exhibited a higher density compared to the micro-discharge formed in the absence of the magnetic field. The radiation emitted from plasma provides further information about

plasma characteristics [54,55]. Therefore, the optical emission spectroscopy (OES) technique is commonly employed for diagnosing of several types of laboratory plasma.

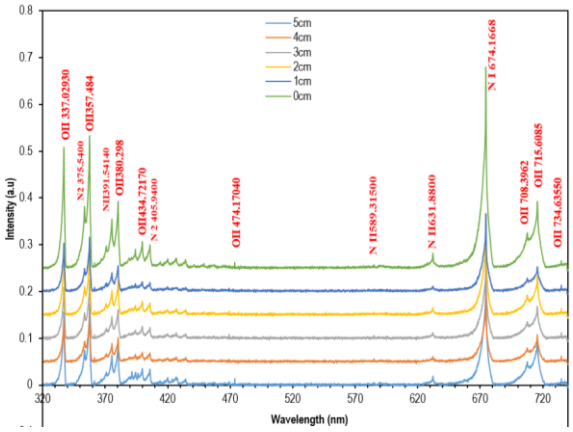

Fig. (4) Influence of horizontal distance on the emission spectra of micro-discharge in DBD actuator in the absence of the magnetic field

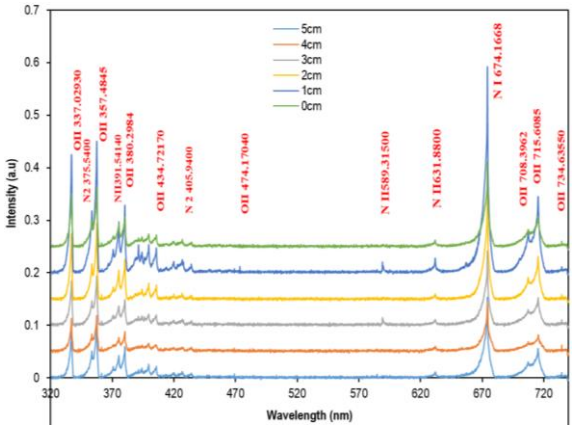

Fig. (5) Influence of horizontal distance on the emission spectra of micro-discharge in DBD actuator in the presence of the magnetic field

In the present work, OES approach was used to determine the characteristics of DBD actuator with and without magnetic field. The emission spectra of the micro- discharge that produced in the distance between the electrodes at normal atmospheric air pressure at wavelength range 320-740 nm in the presence and absence of the magnetic field is illustrated in figures (4) and (5), respectively. One can observed from these figures that there are many peaks of the ionic emission peaks of oxygen (OII) that appears at the wavelengths 337.029, 357.484, 380.298, 434.2003, 474.170, 708.3962, 715.608, and 734.635 nm. One atomic emission peak of nitrogen (NI) appear of wavelength of 674.167 nm and two ionic emission peaks of nitrogen (NII) detected at wavelengths of 391.541 and 631.880 nm. As well as, there are two molecular emission peaks of nitrogen (N2I) corresponding to wavelengths 375.540 and 405.940 nm. When moving the electrodes horizontally from 0 to 5cm, the results detected that intensity decreases as distance increases. This result agree with references [46,56]. Finally, the comparison of figures (4) and (5) shown that the emission lines intensity are increases in the presence of the magnetic field. This behavior can be explained as; when a magnetic field it is expected that the acting magnetic force on the electron particle motion in the parallel direction of the electric field increases and consequently its kinetic energy increases the discharge current. Therefore, the micro-discharge presented more homogeneous in space between the electrodes. Consequently, the excitation and photo emission processes becomes higher than that of ionization case, which lead to a more luminous zone higher than that without the magnetic field [42,57]. T_e is the most plasma characteristic that described the plasma state. Anyway, if we assumed that the local thermodynamic equilibrium is established in the plasma, then the number of excited atoms follows the Boltzmann distribution to determine of T_e.

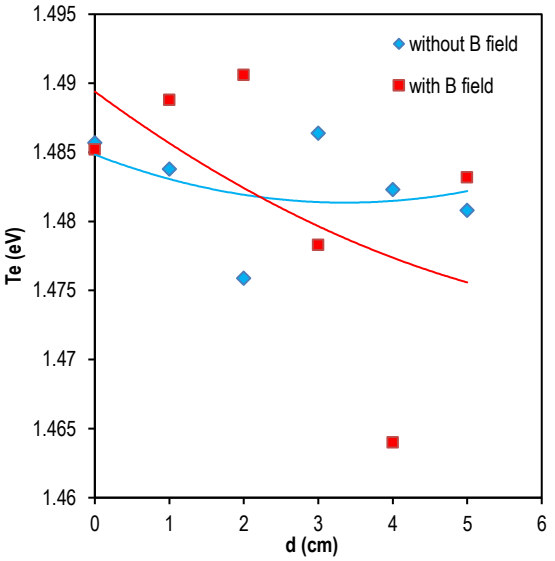

Fig. (6) The variation of electron temperature with moving distance (D) in two cases with and without magnetic field

Table (1) O II standard emission lines that used to calculate electron temperature, and their characteristics

λ (nm)	$A_{ki}g_k$ (S^{-1})	E_i (eV)	E_k (eV)
337.714	2.66E+08	25.28562	28.95584
380.2984	1.36E+08	26.56109	29.82035
734.6895	1.72E+07	29.06224	30.74935
357.3763	2.01E+05	30.74935	34.21765

Using Eq. (1) with the data that listed in table (1), the electron temperature was evaluated in the presence and absence of the magnetic field as shown in Fig. (6). From this figure one can observed that, the variation of T_e with distance D shown inverse behavior when the magnetic field was applied. The variation of T_e behavior with the distance D was due to the variation of the surface area of the powered electrode with the changing of the distance D. this

result means that the characteristics of micro-discharge changed in the presence of the parallel magnetic field. In addition, the data shown also because of the magnetic confinement, the electron temperature decreases with increase of the distance D. Anyway, the spectroscopic atomic lines that emitted from the plasma represent the most reliable technique for determining of the electron number density (n_e). Using stark effect based for λ=380.298nm and Eq. (2) can be calculated electron number density at various horizontal distance utilized the values (ω_m =0.418Å for peak λ=380.298nm) [58]. Figure (7) displays the variation of n_e with horizontal distance in two cases with and without magnetic field. It is pointed out from this figure, without magnetic field the electron number density increased with increases of the horizontal distance. This result agree with reference [56]. While when the magnetic field was applied in the parallel direction of electric field, the data detected the reduction in the electron number density with increases of the horizontal distance (i.e. reduces of the surface area of powered electrode).

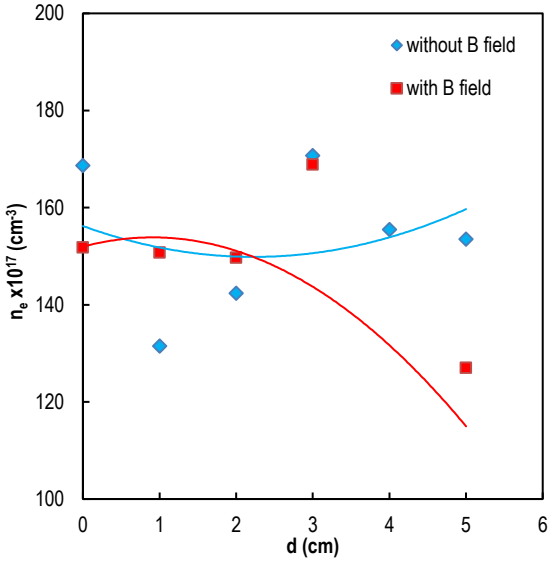

Fig. (7) Variation of electron number density with moving distance for with and without magnetic field at 9kHz frequency

Since the presence of the magnetic field has much effect on the surface electrons, the electron diffusion was increases which cause to reduce in the electron number density. As well as, the decrease in the electron surface dissipation is revealed in the phenomenon that the intensity of reverse discharges was significantly enhanced by the parallel magnetic field. The dissipation of energetic electrons in the heads of the avalanche was reduced by the parallel magnetic field [44]. Figure (8) illustrated the effect of the magnetic field on the variation of Debye length (λ_D) with the horizontal distance at atmospheric pressure. One can noticed from this figure, the presence of the magnetic field causes to change the behavior of the Debye length with increases of horizontal distance (D). One can detected that the micro-discharge channel becomes wider in the present of the magnetic field.

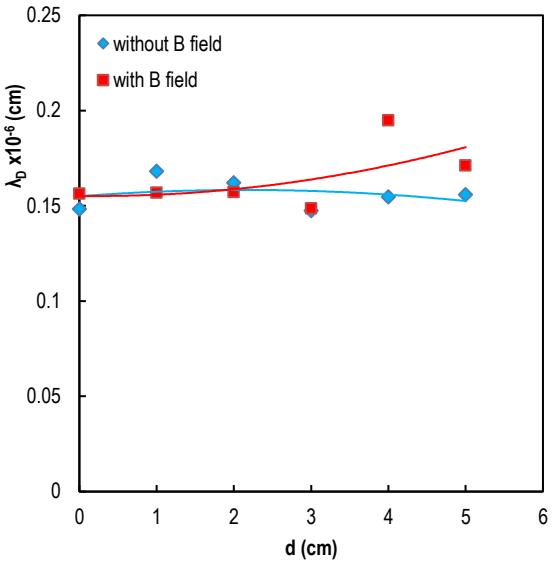

Fig. (8) The effect of the magnetic field on the variation of λ_D as function of horizontal distance at atmospheric pressure

Finally, figure (9) demonstrated the influence of the magnetic field on the number of charged particles in the Debye sphere (N_D) versus the horizontal distance. On can observe that, when the magnetic field is not exist, the plasma parameter is approximately not affect by varying of the horizontal distance. On the other hand, when the magnetic field is applied the experimental curve of N_D display that there is slightly increase of N_D when the horizontal distance increases greater than 3 cm. this behavior of N_D means that the magnetic field causes the variation of micro-discharge structure and the structure of the micro-discharge also variation with horizontal distance.

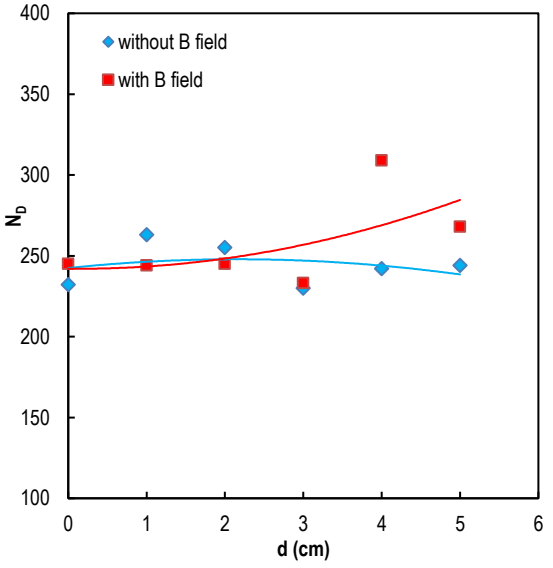

Fig. (9) Influence of the magnetic field on the variation of the plasma parameter as function of the horizontal distance at

atmospheric pressure

5. Conclusion

In the current work, the experimental data investigated that there is a significant effect of electrode area on the properties of the micro-discharge that formed in the DBD actuator in the presence and absence of the magnetic field. The presence of parallel magnetic field will effect on the micro-discharge characteristics in all horizontal distance. There is a significant the impact of the parallel magnetic field on the surface electrons.

References

[1] [1] A. Kumar et al., "Plasma Polymerization: Electronics and Biomedical Application", in "Plasma Science and Technology for Emerging Economies", Springer (2017) 593-657.

[2] [2] A.K. Abd and Q.A. Abbas, "Surface Treatment of Epoxy/Al Composite by Dielectric Barrier Discharge (DBD) at Atmospheric Pressure", *Iraqi J. Sci.*, 64(6) (2023) 2867-2876.

[3] [3] S.F. Khaleel and Q.A. Abbas, "Effect of dielectric barrier discharge on conductive properties for epoxy/copper composite", *J. Phys.: Conf. Ser.*, 2114(1) (2021) 012042.

[4] [4] D.P. Subedi et al., "Treatment of water by dielectric barrier discharge", *J. Sci. Technol. Tropics*, 5(2) (2009) 117-123.

[5] [5] U. Kogelschatz, B. Eliasson and W. Egli, "Dielectric-barrier discharges. Principle and applications", *Le J. de Phys. IV*, 7(C4) (1997) C4-47.

[6] [6] L.R. Grabowski, "Pulsed corona in air for water treatment", PhD thesis, Eindhoven University of Technology, Netherlands (2006).

[7] [7] H. Ukhtiyah, K. Kusumandari and T.E. Saraswati, "Effect of Dielectric Barrier Discharge (DBD) plasma treatment in drinking water on physical, chemical, and biological parameters", *J. Phys.: Conf. Ser.*, 2498(1) (2023) 012017.

[8] [8] T. Shibata and H. Nishiyama, "Water treatment by dielectric barrier discharge tube with vapor flow", *Int. J. Plasma Enviro. Sci. Technol.*, 11(1) (2017) 112-117.

[9] [9] S.-H. Ji et al., "Effects of high voltage nanosecond pulsed plasma and micro DBD plasma on seed germination, growth development and physiological activities in spinach", *Archiv. Biochem. Biophys.*, 605 (2016) 117-128.

[10] [10] A. Gómez-Ramírez et al., "Surface chemistry and germination improvement of Quinoa seeds subjected to plasma activation", *Sci. Rep.*, 7(1) (2017) 5924.

[11] [11] L. Sivachandiran and A. Khacef, "Enhanced seed germination and plant growth by atmospheric pressure cold air plasma: combined effect of seed and water treatment", *RSC Adv.*, 7(4) (2017) 1822-1832.

[12] [12] Y. Liu, Z. Fang and L. Cai, "Improving hydrophilicity of polypropylene film using atmospheric pressure plasma jet in argon", *High Voltage Eng.*, 38(5) (2012) 1141-1149.

[13] [13] T. Shao et al., "Surface modification of polyimide films using unipolar nanosecond-pulse DBD in atmospheric air", *Appl. Surf. Sci.*, 256(12) (2010) 3888-3894.

[14] [14] N.Y. Babaeva, W. Tian and M.J. Kushner, "The interaction between plasma filaments in dielectric barrier discharges and liquid covered wounds: electric fields delivered to model platelets and cells", *J. Phys. D: Appl. Phys.*, 47(23) (2014) 235201.

[15] [15] A.V. Nastuta et al., "Stimulation of wound healing by helium atmospheric pressure plasma treatment", *J. Phys. D: Appl. Phys.*, 44(10) (2011) 105204.

[16] [16] A. Yang et al., "Characteristics of the atmospheric pressure argon plasma jet", *High Voltage Eng.*, 38(7) (2012) 1763-1769.

[17] [17] B. Jiang et al., "Review on electrical discharge plasma technology for wastewater remediation", *Chem. Eng. J.*, 236 (2014) 348-368.

[18] [18] A.Z. Zain et al., "Development of ozone reactor for medicine base on dielectric barrier discharge (DBD) plasma", *J. Phys.: Conf. Ser.*, 1153(1) (2019).

[19] [19] M. Restiwijaya et al., "New development of double dielectric barrier discharge (DBD) plasma reactor for medical", *J. Phys.: Conf. Ser.*, 1170(1) (2019).

[20] [20] J. Hu et al., "Dielectric barrier discharge in analytical spectrometry", *Appl. Spectro. Rev.*, 46(5) (2011) 368-387.

[21] [21] P. Vanraes et al., "Study of an AC dielectric barrier single micro-discharge filament over a water film", *Sci. Rep.*, 8(1) (2018) 10919.

[22] [22] U. Kogelschatz, "Dielectric-barrier discharges: their history, discharge physics, and industrial applications", *Plasma Chem. Plasma Process.*, 23 (2003) 1-46.

[23] [23] M. Gad-el-Hak, "Flow control", Cambridge University Press (1989) 261-293.

[24] [24] J.R. Roth and X. Dai, "Optimization of the aerodynamic plasma actuator as an electrohydrodynamic (EHD) electrical device", *44th AIAA Aerospace Sci. Meet. Exhibit* 9-12 January 2006, Reno, Nevada (AIAA 2006-1203).

[25] [25] K.P. Singh and S. Roy, "Impedance matching for an asymmetric dielectric barrier discharge plasma actuator", *Appl. Phys. Lett.*, 91(8) (2007) 081504.

[26] [26] M. Neumann et al., "Determination of the phase-resolved body force produced by a dielectric barrier discharge plasma actuator", *J. Phys. D: Appl. Phys.*, 46(4) (2012) 042001.
[27] [27] Q. Sun et al., "Study on Characteristics of an AC Sliding Discharge Plasma Actuator Operating at Different Pressures", *MDPI Actuators*, 12(1) (2023) 34.
[28] [28] J. Roth, D. Sherman and S. Wilkinson, "Boundary layer flow control with a one atmosphere uniform glow discharge surface plasma", *36th AIAA Aerospace Sci. Meet. Exhibit*, 12-15 January 1998, Reno, Nevada (AIAA 98-0328).
[29] [29] T.C. Corke, M.L. Post and D.M. Orlov, "Single dielectric barrier discharge plasma enhanced aerodynamics: Physics, modeling and applications", *Exper. Fluids*, 46 (2009) 1–26.
[30] [30] N. Benard and E. Moreau, "Electrical and mechanical characteristics of surface AC dielectric barrier discharge plasma actuators applied to airflow control", *Exper. Fluids*, 55 (2014) 1-43.
[31] [31] M. Kotsonis, "Diagnostics for characterisation of plasma actuators", *Measur. Sci. Technol.*, 26(9) (2015) 092001.
[32] [32] N. Benard and E. Moreau, "Role of the electric waveform supplying a dielectric barrier discharge plasma actuator", *Appl. Phys. Lett.*, 100(19) (2012) 193503.
[33] [33] T. Abe et al., "Experimental study for momentum transfer in a dielectric barrier discharge plasma actuator", *AIAA J.*, 46(9) (2008) 2248-2256.
[34] [34] J. Soni and S. Roy, "Low pressure characterization of dielectric barrier discharge actuators", *Appl. Phys. Lett.*, 102(11) (2013) 112908.
[35] [35] A. Debien, N. Benard and E. Moreau, "Streamer inhibition for improving force and electric wind produced by DBD actuators", *J. Phys. D: Appl. Phys.*, 45(21) (2012): 215201.
[36] [36] F.O. Thomas, A. Kozlov and T.C. Corke, "Plasma actuators for cylinder flow control and noise reduction", *AIAA J.*, 46(8) (2008) 1921-1931.
[37] [37] Y. Li, X. Zhang and X. Huang, "The use of plasma actuators for bluff body broadband noise control", *Exper. Fluids*, 49 (2010) 367-377.
[38] [38] K. Shimizu and M. Blajan, "Dielectric barrier discharge microplasma actuator for flow control", Actuators, IntechOpen (London, 2018), doi: 10.5772/intechopen.75802.
[39] [39] J. Zito et al., "Microscale dielectric barrier discharge plasma actuators: Performance characterization and numerical comparison", *43rd AIAA Plasma Dynam. Lasers Conf.*, 25-28 June 2012, New Orleans, Louisiana (AIAA 2012-3091)
[40] [40] S. Pekárek, "Experimental study of nitrogen oxides and ozone generation by corona-like dielectric barrier discharge with airflow in a magnetic field", *Plasma Chem. Plasma Process.*, 37(5) (2017) 1313-1330.
[41] [41] J.Y. Park et al., "NO_x removal using DC corona discharge with magnetic field", *Combus. Sci. Technol.*, 133(1-3) (1998) 65-77.
[42] [42] Y. Liu et al., "The impacts of magnetic field on repetitive nanosecond pulsed dielectric barrier discharge in air", *Phys. Plasmas*, 23(11) (2016) 113508.
[43] [43] C. Wang et al., "Surface treatment of polypropylene films using dielectric barrier discharge with magnetic field", *Plasma Sci. Technol.*, 14(10) (2012) 891.
[44] [44] Y. Liu et al., "Effect of parallel magnetic field on repetitively unipolar nanosecond pulsed dielectric barrier discharge under different pulse repetition frequencies", *Phys. Plasmas*, 25(3) (2018) 033519.
[45] [45] A.K. Bard and Q.A. Abbas, "Influence of Cylindrical Electrode Configuration on Plasma Parameters in a Sputtering System", *Iraqi J. Sci.*, 63(8) (2022) 3412-3423.
[46] [46] A.K. Abd and Q.A. Abbas, "Spectral Analysis of the Effects of Variation in Electrodes' Area for Dielectric Barrier Discharge Actuator", *Iraqi J. Sci.*, 64(4) (2023) 1691-1703.
[47] [47] A.M. El Sherbini et al., "Measurements of plasma electron temperature utilizing magnesium lines appeared in laser produced aluminum plasma in air", *Opt. Photon. J.*, 2(04) (2012) 278.
[48] [48] M.M. Kahim, Q.A. Abbas and M.R. Abdulameer, "Study of Some Plasma Characteristics in Dielectric Barrier Discharge (DBD) System", *Iraqi J. Sci.*, 63(5) (2022) 2048-2056.
[49] [49] M.U. Hussein and T.H. Khalaf, "The effect of Dielectric Thickness on Dielectric Barrier Discharge properties at Atmospheric Pressure", *Eng. Technol. J.*, 33(6B) (2015) 1102-1109.
[50] [50] F.F. Chen, **"Introduction to Plasma Physics and Controlled Fusion"**, Springer (2016).
[51] [51] Q.A. Abbas, F.Y. Hadi and S.S. AL-Awadi, "Modified Bohm Diffusion equation in Q-Machine", *Baghdad Sci. J.*, 8 (2011) 339-344.
[52] [52] H.Q. Farag and S.J. Kadhem, "Study the Effect of Dielectric Barrier Discharge (DBD) Plasma on the Decomposition of Volatile Organic Compounds", *Iraqi J. Phys.*, 20(4) (2022) 45-53.
[53] [53] R.S. Mohammed, K.A. Aadim and K.A. Ahmed, "Spectroscopy diagnostic of laser intensity effect on Zn plasma parameters generated by Nd: YAG laser", *Iraqi J. Sci.*, 63(9) (2022) 3711-3718.

[54] [54] S. Iordanova and I. Koleva, "Optical emission spectroscopy diagnostics of inductively-driven plasmas in argon gas at low pressures", *Spectrochimica Acta B: Atom. Spectro.*, 62(4) (2007) 344-356.
[55] [55] B.M. Ahmed, "Plasma parameters generated from iron spectral lines by using LIBS technique", *IOP Conf. Ser.: Mater. Sci. Eng.*, 928(7) (2020) 072096.
[56] [56] S.F. Khaleel and Q.A. Abbas, "Influence of Dielectric Media on the Plasma Characteristics in DBD Discharge", *Iraqi J. Sci.*, 63(6) (2022) 2470-2481.
[57] [57] A. El-Zein et al., "The Characteristics of Dielectric Barrier Discharge Plasma under the Effect of Parallel Magnetic Field", *IEEE Trans. Plasma Sci.*, 48(4) (2020) 1022-1029.
[58] [58] N. Konjević et al., "Experimental Stark widths and shifts for spectral lines of neutral and ionized atoms (a critical review of selected data for the period 1989 through 2000)", *J. Phys. Chem. Ref. Data*, 31(3) (2002) 819-927.

Photosensitivity of Nb_2O_5/Si Thin Films Produced via DC Reactive Sputtering at Different Substrate Temperatures

Yahya R. Hathal [1]
Isam M. Ibrahim [1]
Mohammed K. Khalaf [2]

[1] *Department to Physics, College of Science, University of Baghdad, Baghdad, IRAQ*
[2] *Department of Materials Research, Ministry of Science and Technology, Baghdad, IRAQ*

This study thoroughly investigates the potential of niobium oxide (Nb_2O_5) thin films as UV-A photodetectors. The films were precisely fabricated using dc reactive magnetron sputtering on Si(100) and quartz substrates, maintaining a consistent power output of 50W while varying substrate temperatures. The dominant presence of hexagonal crystal structure Nb_2O_5 in the films was confirmed. An increased particle diameter at 150°C substrate temperature and a reduced Nb content at higher substrate temperatures were revealed. A distinct band gap with high UV sensitivity at 350 nm was determined. Remarkably, films sputtered using 50W displayed the highest photosensitivity at 514.89%. These outstanding optoelectronic properties highlight Nb_2O_5 thin films' potential for use in optoelectronic circuits and UV-A sensors, especially in the visible-blind range. These findings underscore Nb_2O_5 thin films' promise in advancing UV-A photodetector technology.

Keywords: Nb_2O_5 thin film; Substrate temperatures; Sputtering; Photosensitivity
Received: 23 January 2024; **Revised:** 27 February; **Accepted:** 05 March 2024

1. Introduction

Metal oxide thin films have gained significant prominence across various fields, including optics and microelectronics. Among these materials, niobium oxide (Nb_2O_5) stands out as a highly sought-after transparent conducting oxide. Its distinct electronic and optical properties render it a compelling choice for a wide range of electronic and optical applications [1]. Nb_2O_5, classified as an n-type transition material, has undergone extensive exploration due to its versatility in applications such as gas sensors, catalysts, dye-sensitized solar cells (DSSCs), displays, and optical coatings. Its appeal lies in its favorable attributes, including remarkable thermal stability, corrosion resistance, high refractive index, and notably, a wide band gap [2-4]. In the electromagnetic spectrum, UV light encompasses higher frequencies beyond the human eye's visible range. UV radiation spans from 200 to 400 nm, with the sun serving as a primary source. While a significant portion of the UV spectrum, particularly the ultraviolet-C (UV-C) region (200-290 nm), and a substantial part of the UV-B region (290-320 nm), are absorbed by atmospheric molecules and sunscreens, the longer wavelengths in the UV-A band (320-400 nm) penetrate the Earth's surface. Prolonged exposure to UV-A radiation poses health risks, including an increased the possibility of skin cancer [5]. Therefore, efficient techniques for monitoring UV-A radiation are essential. Numerous methods have been employed to produce Nb_2O_5 thin films, encompassing dc magnetron sputtering, ion beam sputtering, electron beam evaporation, thermal oxidation, photochemical vapor deposition, plasma-enhanced chemical vapor deposition, spray pyrolysis, sol-gel techniques, and pulsed laser deposition [6-10]. Among these methods, sputtering stands out for its ability to produce thin films of diverse materials, including oxides [11-15]. Renowned for its capacity to deposit thin films with exceptional uniformity, homogeneity, density, purity, adhesion, and reproducibility at a high deposition rate, sputtering is highly regarded in the thin film deposition realm [16-21]. This technique facilitates consistent film thickness over extensive substrate areas and is readily accessible through commercially available sputtering systems [22-26]. The resultant thin films exhibit remarkable transparency and conductivity [27-30].

The present investigation endeavors to pinpoint the optimal substrate temperature for producing Nb_2O_5/Si thin films exhibiting maximum photosensitivity. The study scrutinizes the influence of substrate temperatures on various film properties, including structural, morphological, optical characteristics, and sensing capabilities. The insights gleaned from this research hold the potential to enhance the efficacy of photosensitive devices, unlocking new possibilities in the realm of UV-A radiation monitoring.

2. Experimental Work

This study aimed to investigate the substrate temperature impact on the microstructure, optical and electrical properties of niobium oxide (Nb_2O_5) thin films. This material was deposited on quartz substrate to evaluate their structural, morphological, optical, and electrical characteristics. The deposition process was carried out using a dc reactive magnetron technique with a consistent power output of 50W. The

sputtering target utilized 99.95% pure niobium disk with a 5 cm diameter and 3 mm thickness.

Firstly, the quartz substrates have been cleaned by soaking them in ultrasonic bath of isopropanol and deionized water, followed by drying with nitrogen gas. The sputtering process involved argon (Ar) gas (99.99%) as the sputtering gas and oxygen gas as the reactive gas. The vacuum chamber was evacuated at $4.2x10^{-5}$ mbar using a diffusion pump. The flow rate of the Ar gas during sputtering process was maintained at a constant 50 sccm. While the O_2 flow rate was 5 sccm. The deposition process performed for 120 minutes. Subsequently, the deposited thin films annealed at 800°C for one hour in an ambient air.

The x-ray diffraction (XRD) patterns were analyzed using a Shimadzu XRD-6000 x-ray diffractometer with CuK_α radiation (0.154 nm) in the 2θ range from 10° to 90°. The samples' crystal structure and surface morphology were observed using field-emission scanning electron microscopy (FE-SEM), and statistical and image analyses were conducted using Image J and Origin LAB. The optical absorption spectra and optical energy gap of the deposited thin films in the 300-1100 nm wavelength range were determined using a Shimadzu UV-1650 PC UV-Visible spectrophotometer. Light sensitivity measurements were performed using Sensible Fluke 8846A digital electrometers.

3. Results and Discussion

The XRD patterns of Nb_2O_5 thin film samples that fabricated under a constant dc power of 50W with variant substrate temperatures (room temperature, 100°C and 150°C), are illustrated in Fig. (1). The result shows that all samples exhibited the presence of a hexagonal Nb_2O_5 structure. Elevating the substrate temperature notably enhanced the crystallinity of the samples. Such as, the sample fabricated with 50W DC power and substrate temperature of 150°C displayed the highest degree of crystallinity. This is an evidence of presence four distinct peaks corresponding to the (001), (100), (101), and (002) lattice planes, discernible at 2θ= 22.38°, 28.52°, 36.76° and 46.11°, respectively [31]. These observed peaks were found to align with JCPDS card no. 00-028-0317. Furthermore, the elevation of substrate temperature resulted in narrower diffraction lines, signifying larger crystallite sizes. This phenomenon can be attributed to the increased thermal energy at higher temperature, allowing atoms to arrange themselves more effectively during the thin film growth process and reducing the grain boundaries [32-34]. The increase of substrate temperature also reduced crystal defects, dislocations and lattice strain caused by the nano-size effect. The assessment of crystallite size was performed using the Scherrer's formula, with focus on the (001) crystal plane. The results revealed that crystallite size ranged from 21.7 to 26.0 nm, with an increase in substrate temperature from room temperature to 150°C. Table (1) provides comprehensive data on the measured crystallite sizes corresponding to the most prominent peaks, including peak positions, Miller indices and full-width at half maximum (FWHM) values [35]. These XRD findings underscore the significant influence of substrate temperature on the crystalline properties of Nb_2O_5 thin films, offering valuable insights into the structural characteristics of the materials under investigation.

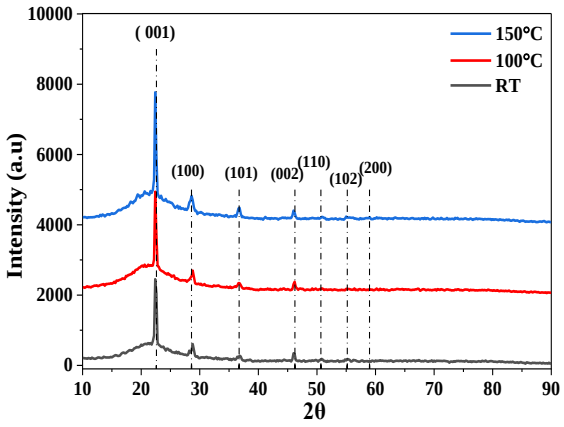

Fig. (1) XRD patterns of Nb_2O_5 thin films deposited at various substrate temperatures using 50W DC power

Equation (1) can be used to compute the absorption coefficient for the frequency associated with the highly absorbent region. This involves using the values of absorption (A) and thickness (t) to derive the coefficient:

$$\alpha = 2.303\frac{A}{t} \quad (1)$$

Both crystalline and amorphous materials exhibit distinct and noticeable characteristics in their fundamental absorption edges. Before determining the band gap of the material, it is crucial to understand the transition from the valence band to the conduction band. The energy band gap (E_g) can be calculated using Eq. (2) [36]

$$\alpha h\nu = B(h\nu - E_g)^r \quad (2)$$

The optical absorption coefficient (α) is determined by various factors, including the optical energy gap (E_g), the material structure (β) and the index (r) that describes the optical absorption process, according to the provided equation [37,38]. The absorption-causing electronic transition's r-coefficient was 0.5

Our results show good agreements with previous studies, demonstrating direct optical transitions [39]. The optical absorbance curves of Nb_2O_5 thin films fabricated using a constant dc power of 50W at various substrate temperatures (RT, 100, and 150 °C) in the wavelength range of 200–800 nm are presented in Fig. (2). It can be observed that the films exhibit high transparency in the visible region. As the substrate temperature increased, there was a decrease in absorbance, which can be attributed to the reduction of defects. This improvement in

crystallinity and reduction in optical scattering at grain boundaries contributed to the reduced absorbance [40].

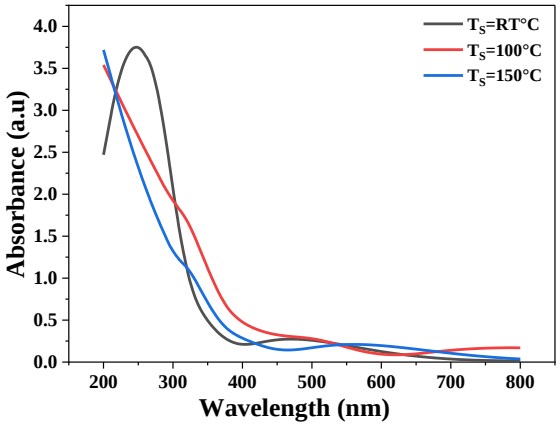

Fig. (2) UV-visible spectra of Nb_2O_5 thin films fabricated using 50W DC power at different substrate temperatures

Usually, the optical band gap variations are attributed to the Moss-Burstein shift, a phenomenon commonly referred to as a blue shift. This shift is typically a result of an increased carrier concentration stemming from the filling of the optical band. Conversely, a redshift, characterized by a decrease in the optical band gap, is believed to be induced by many-body effects, including interactions between electrons and electrons or impurities, leading to an excessive density of donors surpassing a certain threshold [41].

Figure (3) presents the relationship between the square of the product of the optical absorption coefficient (α) and photon energy (hν) for Nb_2O_5 thin films generated using a 50W dc power source at various substrate temperatures. The outcomes revealed an escalation in the energy gap from 3.93 to 4.60 eV as the substrate temperature increased from room temperature to 150°C. This increase in substrate temperature corresponds to a rise in the oxygen content within the deposited thin film. As the oxygen content increases, the presence of oxygen vacancies within the film decreases. The variation in oxygen content with changing substrate temperature directly influences the energy band gap of the thin film. Specifically, an increase in oxygen content can lead to an expansion of the energy bandgap. This effect is attributed to the role of oxygen atoms as electron acceptors, contributing to the widening of the energy gap between the valence and conduction bands [42].

In summary, the observed changes in the optical band gap of Nb_2O_5 thin films can be attributed to alterations in oxygen content induced by varying substrate temperatures. These findings shed light on the connection between material composition and optical properties, offering insights into the potential applications of these thin films in optoelectronic devices.

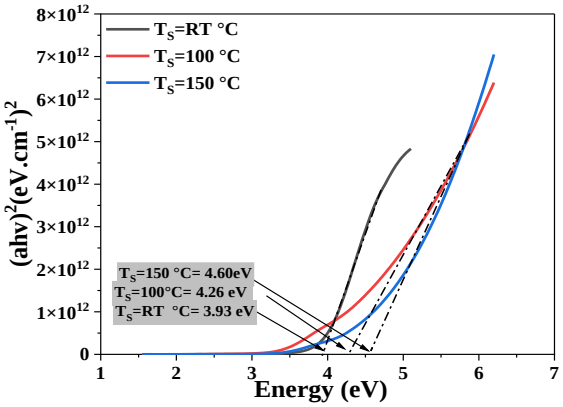

Fig. (3) Variation of $(\alpha h\nu)^2$ with $(h\nu)$ for Nb_2O_5 thin films deposited using 50W dc power at different substrate temperatures

The FE-SEM images presented in Fig. (4) provide a comprehensive view of the surface morphology of Nb_2O_5 thin films. These films were meticulously deposited onto quartz slide substrates under controlled temperatures, namely room temperature (RT), 100°C and 150°C, while maintaining a constant sputtering power of 50W. Examination these images reveal a distinct trend highlighting the influence of substrate temperature on the structural characteristics of the thin films.

The substrate temperature significantly influences thin film deposition and particle size distribution from a physics perspective. As substrate temperatures rise, the thermal energy of atoms on the substrate surface increases significantly. According to statistical mechanics, the elevated thermal energy enhances atomic diffusion, allowing atoms from the sputtered material to move more freely across the substrate surface. This enhanced atomic mobility that plays a pivotal role in the formation of smaller particles during thin film deposition, as atoms have a higher probability of encountering each other and forming bonds at shorter distances. These principles are governed by Fick's laws of diffusion, which describes the particles dispersion through a medium over time [43]. Additionally, substrate temperature impacts the nucleation and growth processes of thin films. Nucleation refers to the initial formation of particles, while growth involves their subsequent increase in size [44].

The increased thermal energy promotes the mobility of atoms, leading to a higher rate of nucleation. Importantly, the growth rate remains moderate, resulting in the formation of smaller and more uniform size of particles.

However, at higher substrate temperatures, such as 150°C, the elevated thermal energy not only boosts nucleation but also accelerates growth. This behavior aligns with classical nucleation and growth theory and is consistent with the principles of statistical physics [45].

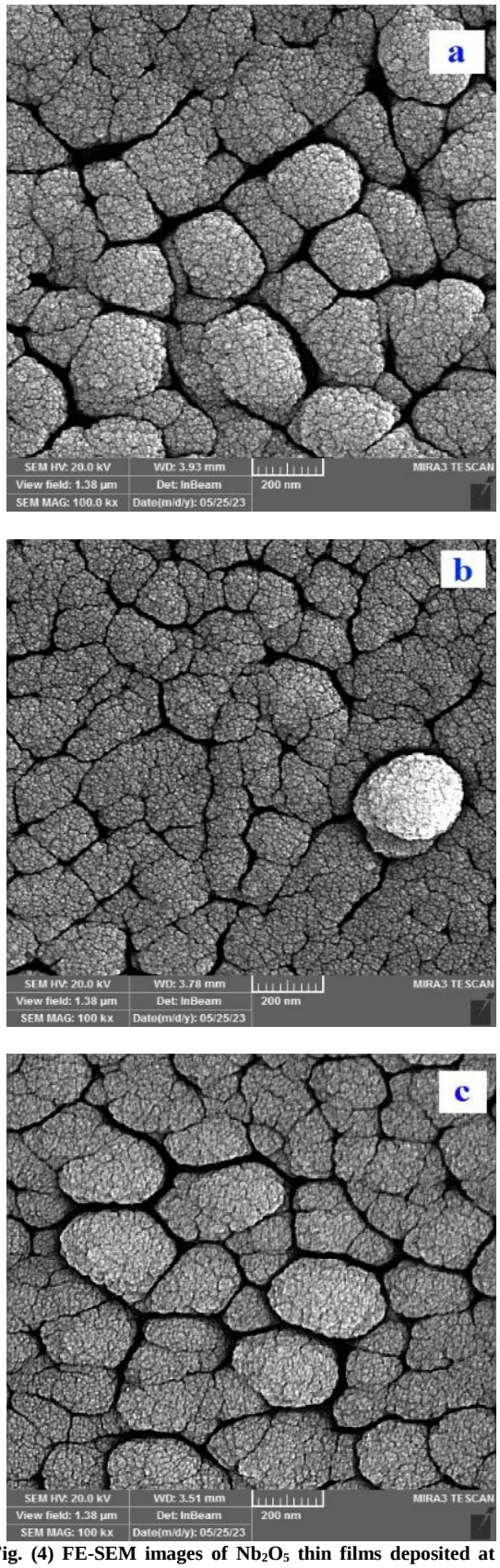

Fig. (4) FE-SEM images of Nb_2O_5 thin films deposited at a constant dc power of 50W and different substrate temperatures: (a) RT, (b) 100°C, and (b) 150°C

Figure (5) illustrates the EDX spectra of Nb_2O_5 thin films deposited on quartz slide substrates at various temperatures (RT, 100, and 150°C) using a dc sputtering power of 50W. These spectra exhibit multiple peaks corresponding to the emission lines of oxygen (O) and niobium (Nb). Notably, an increase in substrate temperature leads to higher oxidation levels, resulting in an elevated oxygen concentration from 80.5 at.% to 94.2 at.% and a decrease in Nb concentration from 19.5 at.% to 5.8 at.%. This process potentially reduces the number of electron vacancies, leading to a decline in the concentration of charge carriers [46]. Excess oxygen beyond its stoichiometric ratio on the surface of nanoparticles can be attributed to the presence of adsorbed oxygen species originating from the surrounding environment. Additionally, the EDX spectrum displays a distinct peak at 1.75 eV, corresponding to silicon emissions. This peak serves as an indicator of the quartz (SiO_2) substrate employed in the deposition process, highlighting the thoroughness of the elemental analysis.

The I-V characteristics are important parameter for assessing heterojunctions, representing the current response under different forward and reverse biases in both dark and light conditions. Figure (6) illustrates the typical I-V characteristics of Nb_2O_5 thin films fabricated on p-type Si (100) substrates at a constant power of 50 W at RT, 100°C, and 150°C. The I-V measurements were performed under various light intensities showing an increase of photocurrent with higher light intensity. The experiment involved a voltage sweep from -1 to 1 V. The I-V characteristics exhibit two types of currents: the forward dark current which driven by majority carriers and the recombination current which occurring at lower voltages due to the concentrations of majority and minority carriers exceeding the intrinsic carrier concentration ($n_i^2<np$). Additionally, a small increase of recombination current observed at low voltage regions which attributed to electron excitations from the valence band (V.B) to the conduction band (C.B). As voltage increases, the diffusion current dominates, resulting in an exponential increase in current magnitude [47]. On the other hand, the decrease of reverse bias current with increasing substrate temperature in Nb_2O_5 thin films which can be attributed to the reduction of interface states and trap levels at the metal/semiconductor interface that leading to improve Schottky barrier height (SBH) and ideality factor (IF) of the metal/Nb_2O_5 contact. This reduction in trap levels and interface states at higher temperatures can be attributed to improve crystallinity, reduced oxygen vacancies in the Nb_2O_5 thin films and decreased roughness of the Nb_2O_5 surface. Consequently, more uniform and defect-free Nb_2O_5/Si interface is achieved, resulting in a decrease in reverse bias current.

Figure (7) illustrates the time-dependent photosensitivity characteristics of Nb_2O_5 thin films excited with UV light of 350 nm wavelength and an intensity of 0.0004 W/cm². The samples were fabricated at RT, 100°C and 150°C. The dark current

values the films were measured at 0.038, 0.028, and 0.013 μA, respectively. Upon UV illumination, the photocurrent significantly exceeded the dark current, surpassing it by a factor of over ten. The light sensitivity of Nb_2O_5 thin films was assessed using Eq. (3):

$$S = \frac{I_{PH}-I_d}{I_d} \times 100\% \quad (3)$$

where I_{ph} represents the photocurrent and I_d represents the dark current. This evaluation yielded a sensitivity of 514.89% at a substrate temperature of RT

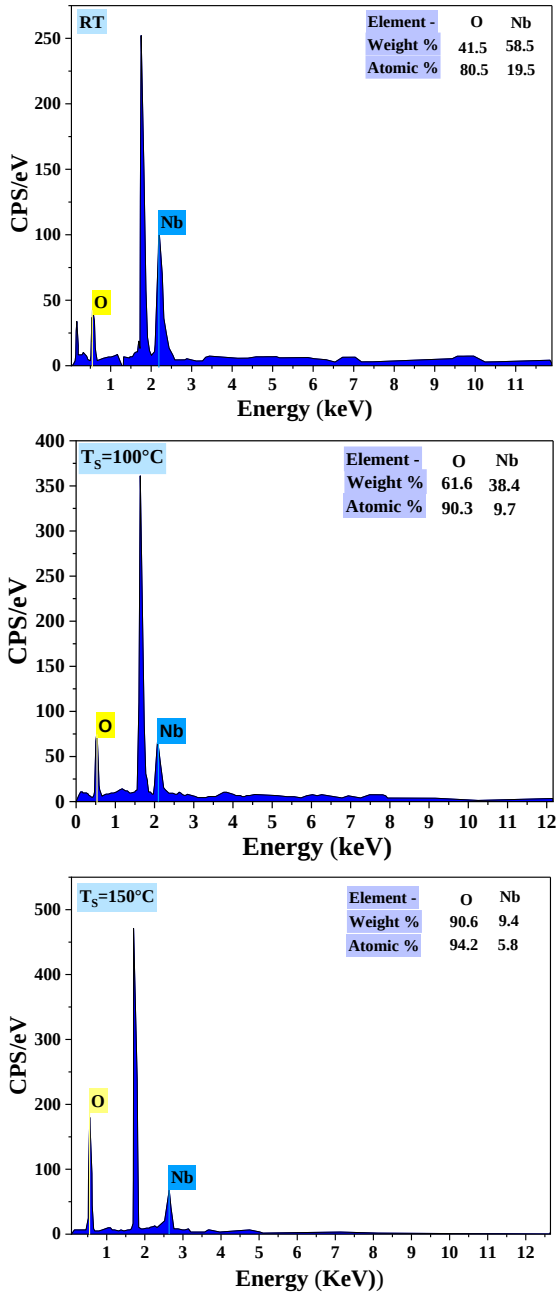

Fig. (5) EDX spectra of Nb_2O_5 thin films fabricated using 50W dc power at different substrate temperatures

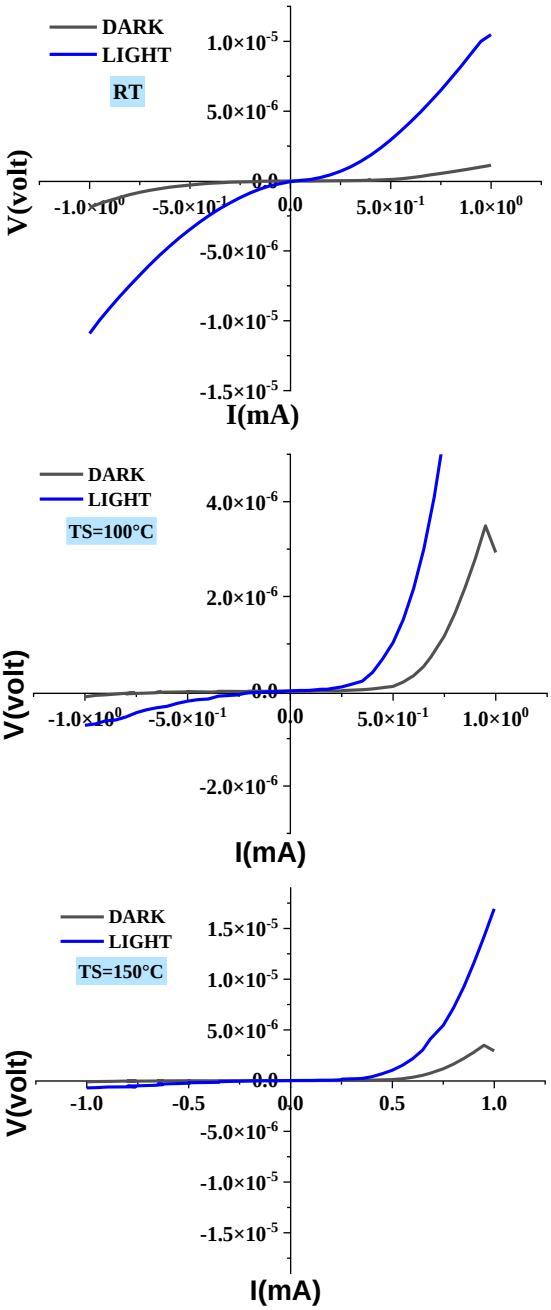

Fig. (2) Dark and illumination I-V characteristics of Nb_2O_5 thin films fabricated using 50W dc power at different substrate temperatures (RT, 100 °C, and 150 °C)

Interestingly, as the substrate temperature was gradually increased from RT to 100°C, light sensitivity exhibited a consistent decrease, reaching its maximum value of 244.71% at 100°C. However, at a substrate temperature of 150°C, the sensitivity experienced a decline to 67.63%.

The primary observation of significant importance is the notably heightened level of photosensitivity demonstrated by the UV sensor when employing the sample growth under constant sputtering power conditions of 50W and a substrate temperature at RT. This enhanced performance can be attributed to the distinct attributes inherent to the film produced under RT conditions. The film displays reduced reflectance

spectra in the UV range, a quality that holds considerable advantages in the domain of photodetection devices.

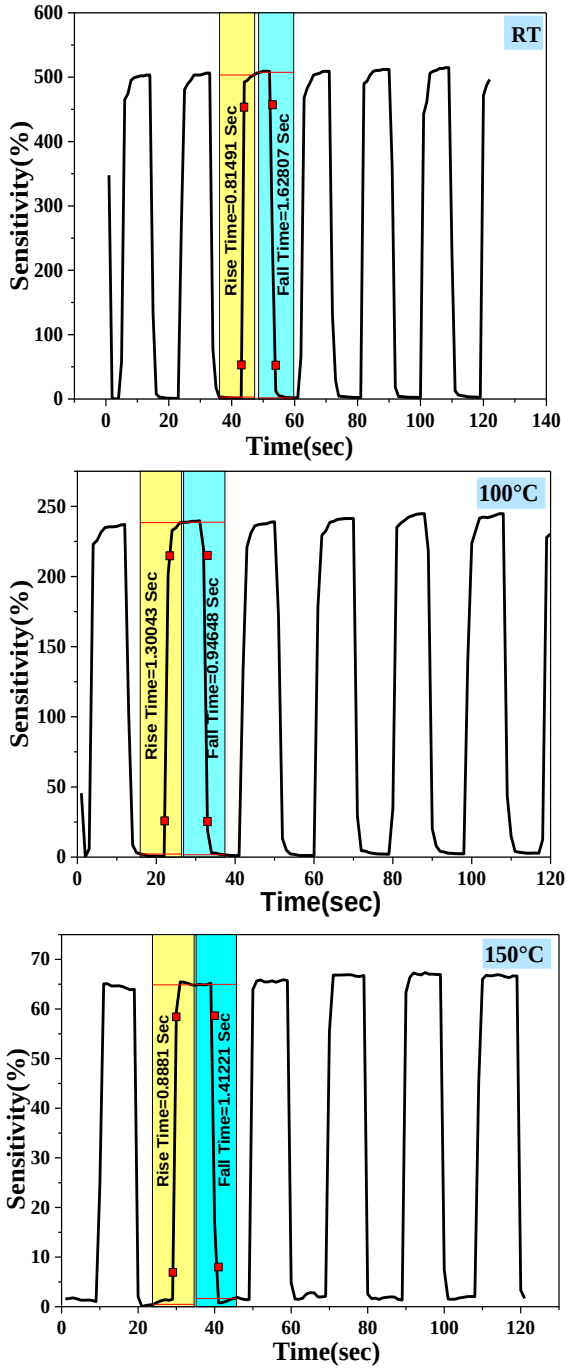

Fig. (7) Time-dependent photosensitivity of Nb_2O_5 thin films deposited using dc power of 50W at RT, 100 °C, and 150 °C

The reduction in sensitivity as the deposition temperature increases is not an arbitrary outcome. Instead, it can be rationalized by the elevated temperatures' ability to induce a heightened degree of reflectivity within the film, particularly in the UV spectrum. This amplified reflectance phenomenon functions to restrict the amount of UV radiation absorbed by the film, consequently resulting in the reduction of photo-induced charge carrier generation, the very essence of photosensitivity [48].

4. Conclusions

This research achieved a successful deposition of high-quality Nb_2O_5 thin films onto quartz substrates. Well-defined polycrystalline hexagonal structures in the Nb_2O_5 thin films were confirmed, a finding consistently observed across varying substrate temperatures. Moreover, a noticeable increase in particle size and stronger inter-particle connectivity of substrate temperature at 150°C was revealed. Notably, an escalation in dc power correlated with an increase in the direct optical energy gap. Furthermore, a decrease in Nb content with rising substrate temperature was observed. This investigation extended to the deposition of Nb_2O_5 thin films on silicon wafers and results demonstrated a swift and substantial response to UV light at 350nm, showcasing an impressive photosensitivity rating of 514.89% upon exposure.

References

[1] N.C. Emeka, P.E. Imoisili and T.C. Jen, "Preparation and Characterization of Nb_xO_y Thin Films: A Review", *Coatings*, 10(12) (2020) 1246.

[2] M. Mazur et al., "Determination of optical and mechanical properties of Nb_2O_5 thin films for solar cells application", *Appl. Surf. Sci.*, 301 (2014) 63-69.

[3] R.A. Rani et al., "Nanoporous Nb_2O_5 hydrogen gas sensor", *Sens. Actuat. B: Chem.*, 176 (2013) 149-156.

[4] Ö.D. Coşkun and S. Demirela, "The optical and structural properties of amorphous Nb_2O_5 thin films prepared by RF magnetron sputtering", *Appl. Surf. Sci.*, 277 (2013) 35-39.

[5] X. Fang et al., "New ultraviolet photodetector based on individual Nb_2O_5 nanobelts", *Adv. Func. Mater.*, 21(20) (2011) 3907-3915.

[6] R. Panetta et al., "Synthesis and characterization of Nb_2O_5 mesostructures with tunable morphology and their application in dye-sensitized solar cells", *Mater. Chem. Phys.*, 202 (2017) 289-301.

[7] R. Chandrasekharan et al., "Thermal oxidation of tantalum films at various oxidation states from 300 to 700°C", *J. Appl. Phys.*, 98(11) (2005).

[8] J.P. Masse et al., "Stability and effect of annealing on the optical properties of plasma-deposited Ta_2O_5 and Nb_2O_5 films", *Thin Solid Films*, 515(4) (2006) 1674-1682.

[9] H. Szymanowski et al., "Optical properties and microstructure of plasma deposited Ta_2O_5 and Nb_2O_5 films", *J. Vac. Sci. Technol. A: Vac. Surf. Films*, 23(2) (2005) 241-247.

[10] S.H. Mujawar et al., "Electrochromic properties of spray-deposited niobium oxide thin films", *Solid Stat. Ion.*, 177(37-38) (2006) 3333-3338.

[11] M.K. Khalaf et al., "Operation Characteristics of a Closed-Field Unbalanced Dual-Magnetrons Plasma Sputtering System", *Bulg. J. Phys.*, 41(1) (2014) 24-33.
[12] M.K. Khalaf et al., "Effect of Adding Nitrogen to the Gas Mixture on Plasma Characteristics of a Closed-Field Unbalanced DC Magnetron Sputtering System", *Iraqi J. Appl. Phys.*, 10(1) (2014) 27-31.
[13] M.K. Khalaf et al., "Fabrication of UV Photodetector from Nickel Oxide Nanoparticles Deposited on Silicon Substrate by Closed-Field Unbalanced Dual Magnetron Sputtering Techniques", *Opt. Quant. Electron.*, 47(12) (2015) 3805-3813.
[14] M.K. Khalaf et al., "Fabrication and Characterization of UV Photodetectors Based on Silicon Nitride Nanostructures Prepared by Magnetron Sputtering", *Proc. IMechE, Part N, J. Nanomater. Nanoeng. Nanosys.*, 230(1) (2016) 32-36.
[15] M.K. Khalaf et al., "Silicon Nitride Nanostructures Prepared by Reactive Sputtering Using Closed-Field Unbalanced Dual Magnetrons", *Proc. IMechE, Part L, J. Mater.: Design & Appl.*, 231(5) (2017) 479-487.
[16] M.A. Hameed and Z.M. Jabbar, "Preparation and Characterization of Silicon Dioxide Nanostructures by DC Reactive Closed-Field Unbalanced Magnetron Sputtering", *Iraqi J. Appl. Phys.*, 12(4) (2016) 13-18.
[17] F.J. Al-Maliki and E.A. Al-Oubidy, "Effect of gas mixing ratio on structural characteristics of titanium dioxide nanostructures synthesized by DC reactive magnetron sputtering", *Physica B: Cond. Matter*, 555 (2019) 18-20
[18] B.K. Nasser and M.A. Hameed, "Structural Characteristics of Silicon Nitride Nanostructures Synthesized by DC Reactive Magnetron Sputtering", *Iraqi J. Appl. Phys.*, 15(4) (2019) 33-36.
[19] S.H. Faisal and M.A. Hameed, "Heterojunction Solar Cell Based on Highly-Pure Nanopowders Prepared by DC Reactive Magnetron Sputtering", *Iraqi J. Appl. Phys.*, 16(3) (2020) 27-32.
[20] R.H. Turki and M.A. Hameed, "Spectral and Electrical Characteristics of Nanostructured NiO/TiO_2 Heterojunction Fabricated by DC Reactive Magnetron Sputtering", *Iraqi J. Appl. Phys.*, 16(3) (2020) 39-42.
[21] M.A. Hameed, S.H. Faisal, R.H. Turki, "Characterization of Multilayer Highly-Pure Metal Oxide Structures Prepared by DC Reactive Magnetron Sputtering Technique", *Iraqi J. Appl. Phys.*, 16(4) (2020) 25-30.
[22] N.H. Mutesher and F.J. Kadhim, "Comparative Study of Structural and Optical Properties of Silicon Dioxide Nanoparticles Prepared by DC Reactive Sputtering and Sol-Gel Route", *Iraqi J. Appl. Phys.*, 17(1) (2021) 17-20.
[23] A.M. Hameed and M.A. Hameed, "Highly-Pure Nanostructured Metal Oxide Multilayer Structure Prepared by DC Reactive Magnetron Sputtering Technique", *Iraqi J. Appl. Phys.*, 18(4) (2022) 9-14.
[24] N.A.H. Hashim and F.J. Kadhim, "Structural and Optical Characteristics of Co_3O_4 Nanostructures Prepared by DC Reactive Magnetron Sputtering", *Iraqi J. Appl. Phys.*, 18(4) (2022) 31-36.
[25] A.M. Hameed and M.A. Hameed, "Spectroscopic characteristics of highly pure metal oxide nanostructures prepared by DC reactive magnetron sputtering technique", *Emerg. Mater.*, 6 (2022) 627-633.
[26] N.A.H. Hashim, F.J. Kadhim and Z.S. Abdulsattar, "Characterization of Electrochromism and Photoelectrochromism of N-Doped TiO_2 and Co_3O_4 Thin Films Prepared by DC Reactive Magnetron Sputtering: Comparative Study", *Iraqi J. Appl. Phys.*, 19(1) (2023) 5-12.
[27] S. Saipriya, M. Sultan and R. Singh, "Effect of environment and heat treatment on the optical properties of RF-sputtered SnO_2 thin films", *Physica B: Cond. Matter*, 406(4) (2011) 812-817.
[28] Y. Huang, Y. Zhang and X. Hu, "Structural, morphological and electrochromic properties of Nb_2O_5 films deposited by reactive sputtering", *Sol. Ener. Mater. Sol. Cells*, 77(2) (2003) 155-162.
[29] S.B. Ogale, T.V. Venkatesan and M. Blamire, eds., "Functional metal oxides: new science and novel applications", John Wiley & Sons (2013).
[30] K. Wasa, I. Kanno and H. Kotera, eds., "Handbook of sputter deposition technology: fundamentals and applications for functional thin films", Nano-materials and MEMS, William Andrew (2012).
[31] A.A. Atta et al., "Effect of thermal annealing on structural, optical and electrical properties of transparent Nb_2O_5 thin films", *Mater. Today Commun.*, 13 (2017) 112-118.
[32] K. Huang et al., "Nanoscale conductive niobium oxides made through low temperature phase transformation for electrocatalyst support", *RSC Adv.*, 4(19) (2014) 9701-9708.
[33] M.K. Ali and F.J. Kadhim, "Structural Characteristics of TiO_2/TiN Nanocomposites Synthesized by DC Reactive Magnetron Sputtering Technique", *Iraqi J. Appl. Phys.*, 19(3A) (2023) 49-54.
[34] D.A. Taher and M.A. Hameed, "Spectroscopic Characteristics of Silicon Nitride Thin Films Prepared by DC Reactive Sputtering Using Silicon targets with Different Types of Conductivity", *Iraqi J. Appl. Phys.*, 19(4A) (2023) 73-76.

[35] M. Manzoor et al., "Structural, optical, and magnetic study of Ni-doped TiO_2 nanoparticles synthesized by sol–gel method", *Int. Nano Lett.*, 8 (2018) 1-8.
[36] E.A. Davis and N. Mott, "Conduction in non-crystalline systems V. Conductivity, optical absorption and photoconductivity in amorphous semiconductors", *Philos. Mag.*, 22(179) (1970) 0903-0922.
[37] Z. Li and C. Wang, "One-dimensional nanostructures: electrospinning technique and unique nanofibers", Springer Berlin Heidelberg (NY, 2013).
[38] C.J. Thompson et al., "Effects of parameters on nanofiber diameter determined from electrospinning model", *Polymer*, 48(23) (2007) 6913-6922.
[39] M. Afzali, A. Mostafavi and T. Shamspur, "Electrospun composite nanofibers of poly vinyl pyrrolidone and zinc oxide nanoparticles modified carbon paste electrode for electrochemical detection of curcumin", *Mater. Sci. Eng. C*, 68 (2016) 789-797.
[40] E.T. Salim and H.T. Halboos, "Synthesis and physical properties of Ag doped niobium pentoxide thin films for Ag–Nb_2O_5/Si heterojunction device", Materi. Res. Exp., 6(6) (2019) 066401.
[41] N. Usha et al., "Niobium pentoxide (Nb_2O_5) thin films: rf Power and substrate temperature induced changes in physical properties", *Optik*, 126(19) (2015) 1945-1950.
[42] R. Dangi et al., "Effect of Oxygen Vacancy on the Crystallinity and Optical Band Gap in Tin Oxide Thin Film", *Energies*, 16(6) (2023) 2653.
[43] J. Crank, "The mathematics of diffusion", Oxford University Press (Oxford, 1975).
[44] J. Venables, "Introduction to surface and thin film processes", Cambridge University Press (2000).
[45] D.A. Taher and M.A. Hameed, "Structural and Hardness Characteristics of Silicon Nitride Thin Films Deposited on Metallic Substrates by DC Reactive Sputtering Technique", *Silicon*, 15 (2023) 7855-7864.E.T. Salim et al., "Electrical conductivity inversion for Nb_2O_5 nanostructure thin films at different temperatures", *Mater. Res. Exp.*, 6(12) (2020) 126459.
[46] N. Usha et al., "Effect of substrate temperature on the properties of Nb_2O_5:MoO_3 (90:10) thin films prepared by rf magnetron sputtering technique", *J. Alloys Comp.*, 649 (2015) 112-121.
[47] S.A. Hamdan, "Synthesized pure cobalt oxide nanostructure and doped with yttrium by hydrothermal method for photodetector applications", *Iraqi J. Phys.*, 17(40) (2019) 77-87.
[48] Z. Zhang et al., "Electrospinning of Ag Nanowires/polyvinyl alcohol hybrid nanofibers for their antibacterial properties", *Mater. Sci. Eng. C*, 78 (2017) 706-714.

Table (1) XRD parameters for Nb_2O_5 thin films deposited by different substrate temperatures

T_S (°C)	2θ (Deg.)	FWHM (Deg.)	Relative Int.	d_{hkl} Exp.(Å)	D (nm)	d_{hkl} Std.(Å)	hkl
RT	22.4312	0.3727	100.0	3.9604	21.7	3.9300	(001)
	28.8199	0.4259	10.6	3.0953	19.3	3.1200	(100)
	36.8057	0.6110	5.6	2.4400	13.7	2.4460	(101)
	46.0958	0.4259	11.3	1.9676	20.3	1.9620	(002)
100	22.3834	0.3368	100.0	3.9687	24.0	3.9300	(001)
	28.8083	0.4182	6.9	3.0966	19.6	3.1200	(100)
	36.7358	0.4922	4.4	2.4445	17.0	2.4460	(101)
	46.1917	0.4145	11.2	1.9637	20.8	1.9620	(002)
150	22.3834	0.3109	100.0	3.9687	26.0	3.9300	(001)
	28.5233	0.3959	11.0	3.1268	20.7	3.1200	(100)
	36.7617	0.4440	7.6	2.4428	18.9	2.4460	(101)
	46.1140	0.4100	9.3	1.9668	21.1	1.9620	(002)

Doigu M. Ezzat
Ali I. Salih

Department of Physics, College of Science, University of Kirkuk, Kirkuk, IRAQ

Effect of Annealing Temperatures on the Color Properties of Copper Oxide Films Prepared by the Sol-Gel Technique

Sol-gel spin coating was employed to produce thin films on the glass substrate, which were subsequently heated to 300,400, 500, and 600 degrees for annealing. The effect of annealing temps on some physical features of the prepared films, such as XRD, AFM, FESEM, and UV-visible spectrophotometer, was studied. X-ray diffraction patterns showed the coexistence of two phases, Cu2O and CuO. According to the AFM findings, the root mean square (RMS) for thin films has been found to increase from 50.72nm at 300°C annealing temp to 122.0nm at 600°C and surface roughness and grain size rate increase with increasing annealing temp. Experimental findings indicated that the transmittance of films increases with increasing annealing temp. The viewable region's transmittance was 88% at 500°C. In this work, the color coordinates of copper oxide were determined. Three critical color attributes were measured utilizing CIE1931 technology to monitor color values: brightness, color purity, and dominant wavelength. The findings illustrated that the color purity and the dominant wavelength decrease with increasing annealing temp, and these values ranged between (0.7-0.51) and (563-556), respectively, when the temp increased from 300°C to 500°C, in contrast to the brightness values, which increased with increasing annealing temps.

Keywords: Thin films; Copper oxide; Atomic fprce microscopy; CIE1931
Received: 04 November; **Revised:** 05 December; **Accepted:** 12 December 2023

1. Introduction

Copper oxide, as a metal oxide, is a semiconductor widely utilized in photovoltaic devices, including the absorption layer, electron transport layer, transparent electrodes, and photo anode [1]. Copper oxide exhibits p-type conductivity and has a monoclinic crystal structure [2]. Copper oxide has three various phase structures: the monoclinic tenorite (CuO) phase, in which the band gap value ranges from 1.3 to 2.1 eV, and sometimes it has a larger band gap of about 3 eV [3,4]. Moreover, the cuprite phase (Cu_2O) has A cubic structure and a band gap between 2.0 and 2.6 eV in addition to the parameclonide phase (Cu_3O_4) [5]. The development of thin film technology began to increase when the world urgently needed to manufacture integrated circuits. The most crucial feature of thin films is their low cost and small size compared to matter in its volumetric state [6]. Numerous deposition techniques involving spray pyrolysis, vacuum evaporation, chemical vapor deposition (CVD), and molecular beam epitaxy have been utilized to prepared Copper oxide thin films [7]. Among the techniques for preparing thin films is the spin coating technique due to its low cost and the possibility of obtaining a homogeneous film with a large area. In addition to controlling the features of the thin film depending on the concentration and type of material and the annealing temp [8]. Sol-gel technique is ideal for preparing thin films of one thickness on solid, flat substrates [9,10]. In general, the principle of sol-gel synthesis is based on chemical colloidal materials, representing solid raw materials that dissolve in specific solvents and transform into homogeneous solutions under controlled conditions, for example temp and pressure. The dispersed phase is then converted into a gel under the same controlled conditions [11]. In general, the gelation process includes the transformation of the system from the liquid state (sol) to the gel state (gel) [12].

In this research, color was studied in order to control the color and its intensity, because thin films are used in many applications that may need to remove the color or control it according to what is required. It was found that the best color removal was at a temperature of 500°C.

2. Experimental detail

Thin films of copper oxide were prepared at various annealing temperatures. A 0.2 g of copper acetate was dissolved in 50 ml isopropanol alcohol. The mixture was stirred on a magnetic mixer for 20 minutes. The temperature of the solution was gradually raised until it reached 60°C and maintained at this temp. A 1 mL diethanolamine was added drop by drop to the solution with continuous stirring until the solution was homogeneous and became a clear, dark blue color. The solution was removed from the magnetic mixer and kept in an airtight glass bottle for one day. After one day, the solution was filtered with filter paper and deposited on the glass bases. The glass bases were cleaned with water and detergent and then washed with distilled water. The glass bases were placed in acetone and ethanol for ten minutes. The bases were dried in an oven at 250°C for ten minutes. The glass base was placed in the middle of the rotary coating device, and the solution was dropped onto the base in drops. The device was

rotated at a speed of 3000 rpm for 30 minutes, and then the deposited film was dried at a temperature of 250°C. The process was repeated ten times. Finally, it was annealed at temperatures ranging in 300-600°C. The morphological and optical features have been investigated utilizing x-ray diffraction (XRD) patterns, atomic force microscopy (AFM), field-emission scanning electron microscopy (FE-SEM), and UV-visible spectrophotometry in the spectral range of 300-1100 nm.

3. Results and Discussion

Figure (1) illustrates the XRD patterns of CuO and Cu_2O thin films prepared by sol gel spin coating method at different annealing temperatures. The results of XRD examination of copper oxide films prepared using the gel solution technique and at temperatures of 300, 400, 500, and 600°C showed that they have a polycrystalline structure. They confirm the coexistence of two phases: the cubic copper oxide phase (Cu_2O) at a temperature of 300 °C and it turns into a monocrystalline copper oxide phase, inclination (CuO) when temperatures increase. They are detected by JCPDS standard card number 00-005-0667 and 00-045-0937, respectively.

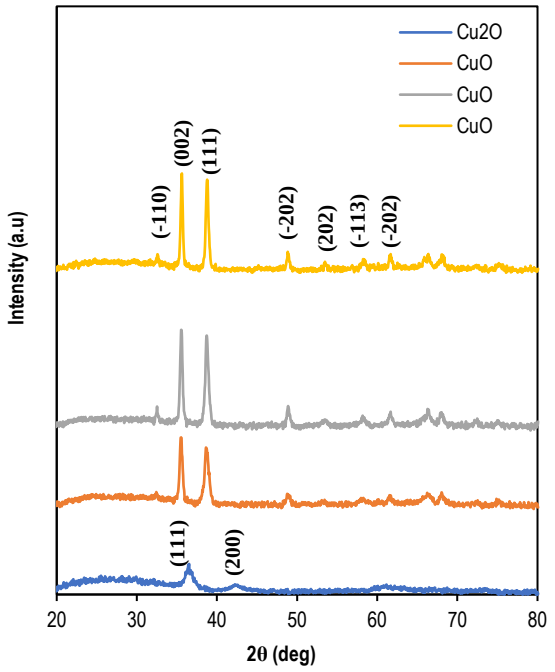

Fig. (1) XRD patterns of CuO and Cu_2O thin films prepared by sol gel spin coating method at different annealing temperatures

As for the Cu_2O phase, peaks 36.436° and 42.151° appeared at levels (111) and (200), and these results are consistent with the results of researchers [13]. As the annealing temperature increases, the CuO phase begins to appear with peaks at 32.47°, 35.48°, 38.60°, 48.70°, 53.29°, 58.34°, 61.52°, 66.35°, 68.07°, 72.49°, and 75.14° for levels (-110), (002), (111), (-202), (020), (202), (-113), (-311), (-220), (311), and (004), respectively, and with the prevailing trend of growth (002), these results are consistent with the results of researchers [14-16].

Atomic force microscopy (AFM) was utilized to study the topography of the surfaces of deposited films and the extent of the effect of annealing on them. Figure (2) illustrates AFM images. From table (1) and Fig. (3), it was found that the root-mean-square (R.M.S.) roughness, the surface roughness, and the grain size increase with increasing annealing temperature; it has been detected that all surfaces of the films are regular and homogeneously distributed in the form of a horizontal matrix with low peaks facing upward, separated by nanoscale spaces and that the films possess a large number of crystals that are aligned and connected regularly on the, without interstitial cracks or voids, and holes in the structures.

The topography of the surfaces of the prepared Cu_2O films and annealed at temperatures of 300, 400, 500, 600°C was studied utilizing the FE-SEM, which depicts the surfaces with high resolution and magnification. Figure (4) illustrates the FE-SEM images of the prepared copper oxide films with magnification of 50kX and 100kX.

Table (1) Results of the AFM examination

A-T (°C)	R.M.S. S_q (nm)	Surface Roughness S_a (nm)	Average Grain Size (nm)
300	50.72	39.26	142.8
400	91.21	68.68	146.4
500	417.8	343.2	197.4
600	122.0	99.82	100.6

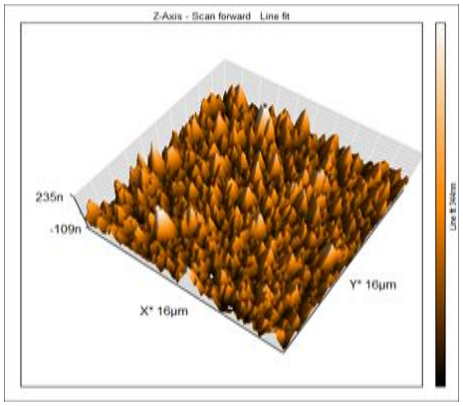

300°C

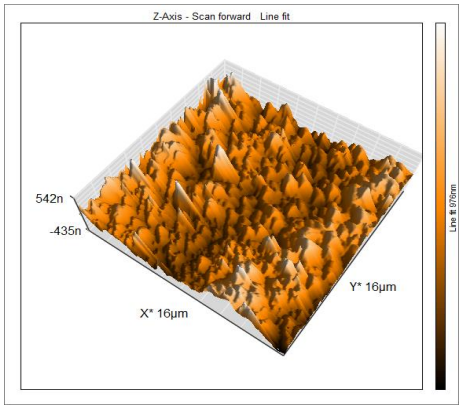

400°C

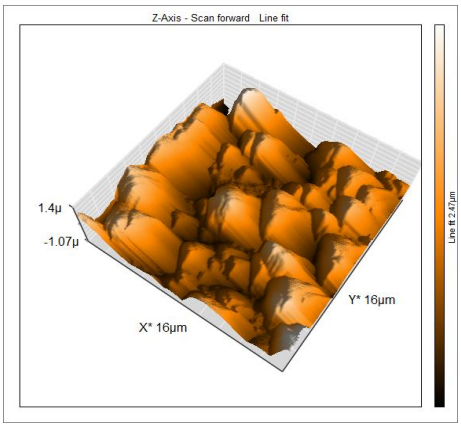

500°C

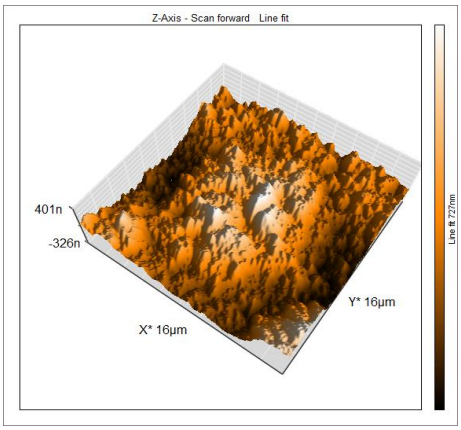

600°C

Fig. (2) 3D AFM images at various annealing temperatures for the prepared Cu_2O and CuO thin films

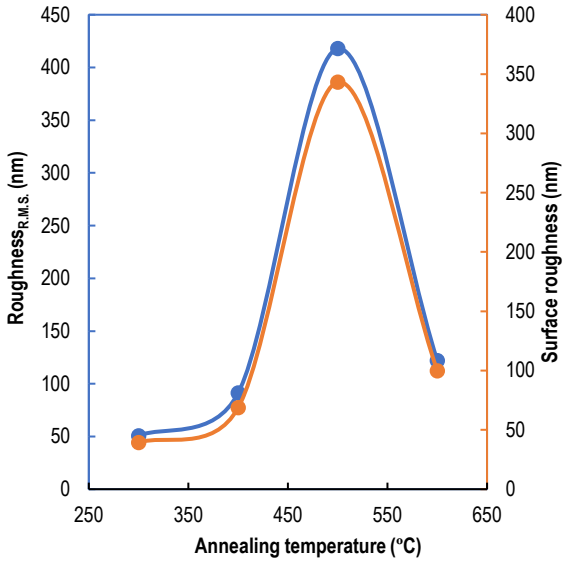

Fig. (3) Variation of the RMS roughness and surface roughness with annealing temperature

It is noted from the figure that the surface composition of the films consists of cauliflower-like shapes, with an apparent increase in the particle size composition with increasing temp due to increased granular growth. It was observed through energy-dispersive x-ray spectroscopy (EDS) examination that the copper oxide films consist of copper and oxygen concentrations only, and there are no concentrations of other elements, indicating the purity of the copper oxide films deposited on the substrate. Table (2) illustrates the percentages of oxygen and copper, and figure (5) illustrates images of EDS analysis.

Table (2) Approximate percentages of elements present in the thin films prepared at various annealing temperatures

T (°C)	Element	Atomic %	Weight %
300	O	49.28	19.65
	Cu	50.72	80.35
400	O	4.43	1.15
	Cu	95.57	98.85
500	O	37.28	13.02
	Cu	62.72	86.98
600	O	43.93	16.48
	Cu	56.07	83.52

The transmission spectra as a function of wavelength for films made of CuO and Cu_2O that were prepared and annealed for one hour at annealing temperatures of 300, 400, 500, and 600°C are displayed in Fig. (6). It has been observed that as the wavelength and annealing temperature rise, the transmittance also rises. The transmittance of the film annealed at 600°C is an exception to this rule, as its transmittance drops. The cause is that the glass utilized in the deposition process distorted due to the high annealing temperature, which reduced the glass's transmittance. The coordinates and color values can be found in the CIE 1931 system from the transmittance measurements.

After obtaining the transmittance spectrum curve for copper oxide utilizing a UV-visible spectrophotometer, some mathematical conversions can be made on the transmittance or absorbance values, which will yield a table of T_λ values for light with equal gradations of wavelengths for the range 380-770nm. The transmitting light's tristimulus values (XT, YT, ZT) and color coordinates (x, y, z) can be computed by applying successive steps to the transmittance values T_λ, which were ascertained by CIE [17,18].

$$X_T = k \sum P_\lambda \; T_\lambda \; X_\lambda \quad (1)$$

$$Y_T = k \sum P_\lambda \; T_\lambda \; Y_\lambda \quad (2)$$

$$Z_T = k \sum P_\lambda \; T_\lambda \; Z_\lambda \quad (3)$$

$$k = \frac{100}{\sum P_\lambda \; Y_\lambda} \quad (4)$$

P_λ represents the power distribution curve of the employed light source, and (X_λ ،Y_λ،Z_λ) represents the distribution coefficient values of the light source. The color coordinate magnitudes for the CIE system are determined utilizing the specimen's Tristimulus values of X_T, Y_T, and Z_T.

$$x = \frac{X}{X+Y+Z} \quad (5)$$

$$y = \frac{Y}{X+Y+Z} \quad (6)$$

$$z = \frac{Z}{X+Y+Z} \quad (7)$$

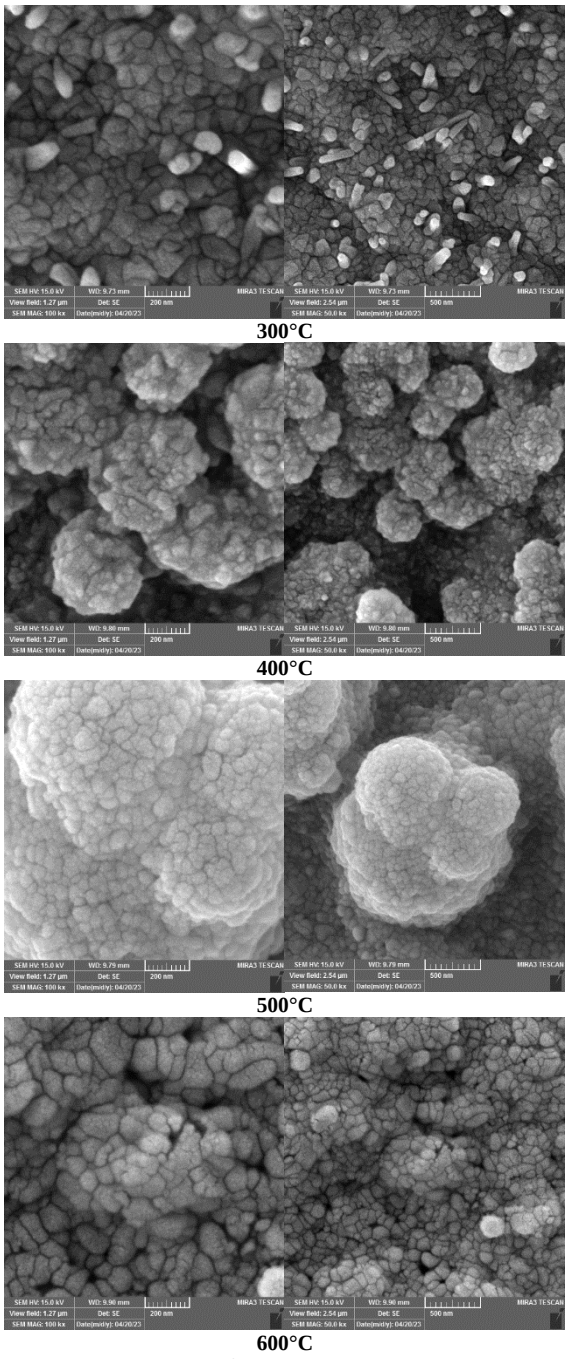

Fig. (4) FE-SEM images for the prepared Cu_2O and CuO thin films at various annealing temperatures

Tables (3) illustrate the color coordinate value (x, y, and z) of the CIE color system, which is utilized to find three other critical color value: dominant wavelength, color purity, and brightness.

The color purity change at various annealing temps is depicted in Fig. (7). A sample with a lower color purity values implies that it contains less color; hence, a sample with a purity of 0% indicates that all color has been removed. Figure (8) illustrates the brightness of thin films. A perfect white diffuser is represented by a thin film when its brightness value reaches 100%.

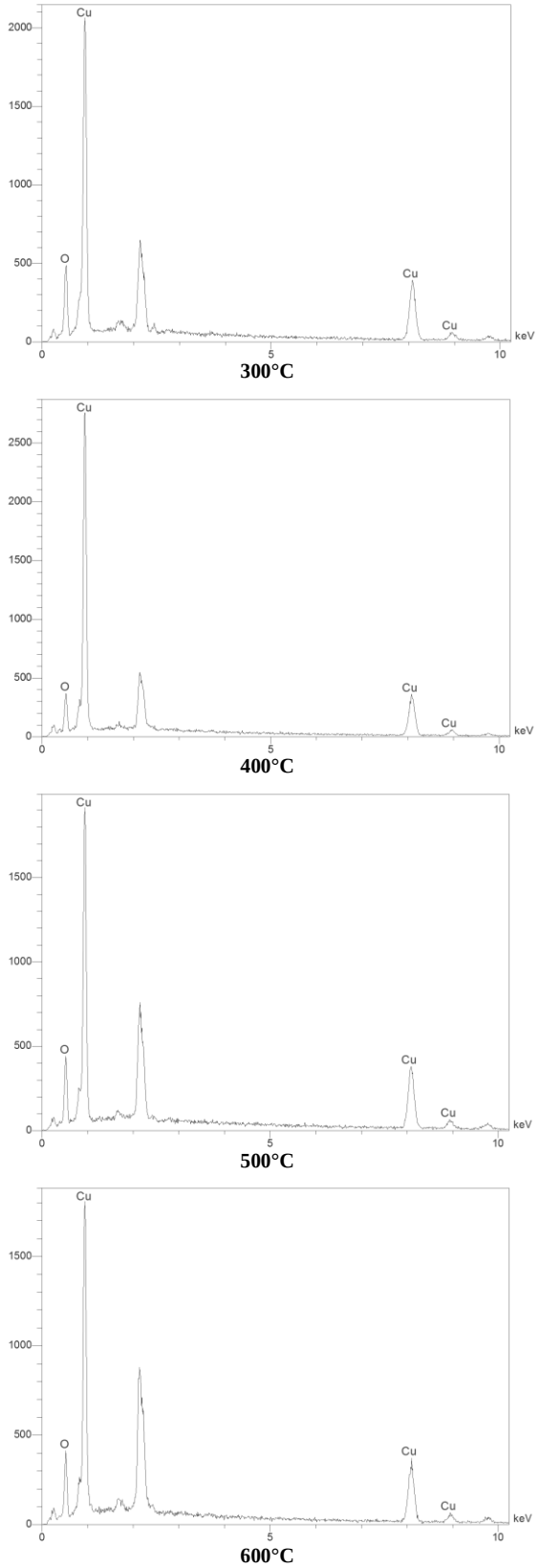

Fig. (5) EDS analysis results for the prepared Cu_2O and CuO thin films at various annealing temperatures

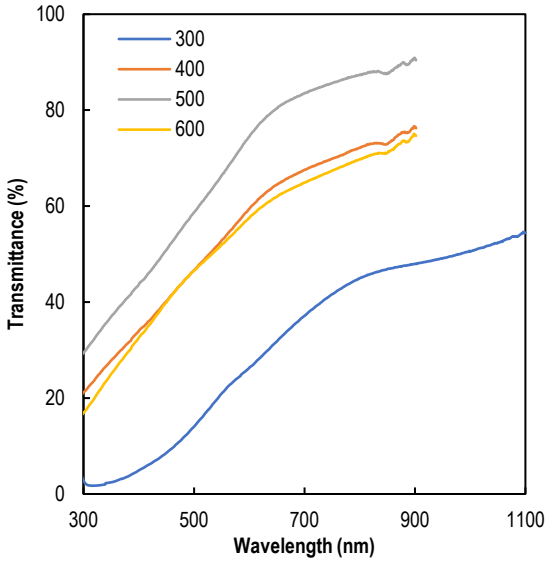

Fig. (6) Transmittance as a function of wavelength for the Cu_2O and CuO thin films prepared at various annealing temperatures

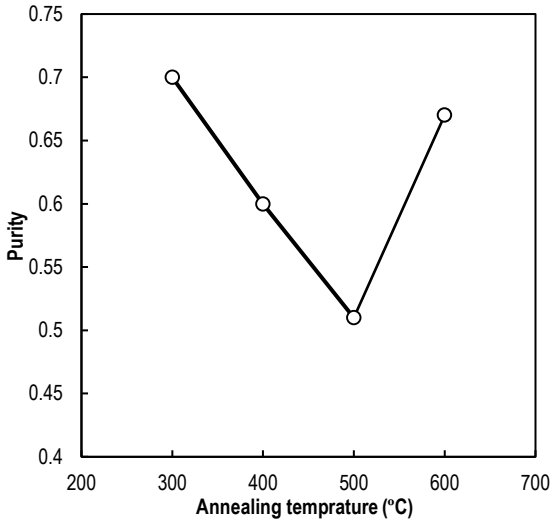

Fig. (7) The color purity of Cu_2O and CuO thin films prepared at various annealing temperatures

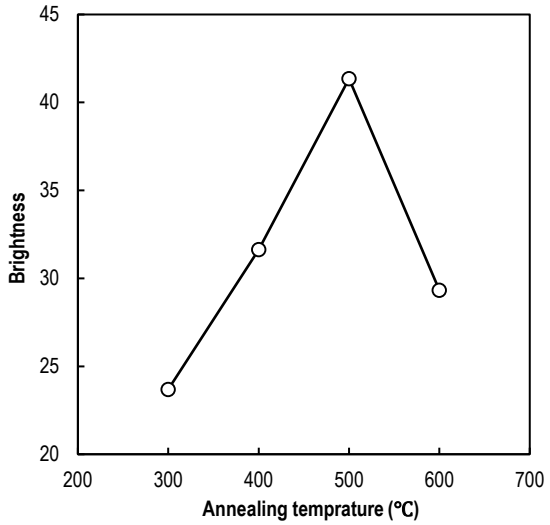

Fig. (8) The brightness of Cu_2O and CuO thin films prepared at various annealing temperatures

4. Conclusions

Thin films of copper oxide have been prepared on glass substrates utilizing the sol-gel spin coating technique, and the impact of annealing temp on the morphological, optical features, and color coordinates was studied. The coexistence of Cu_2O and CuO phases was confirmed. The results confirmed that the grain size and surface roughness increased with increasing annealing temperature. The highest transmittance of 88% has been gained at the annealing temperature of 500°C in the visible region. The best color removal was at temperature of 500°C.

References

[1] S.S. Parui et al., "Zinc oxide and cupric oxide based thin films for solar cell applications", *Mater. Today Proc.*, 41 (2021) 233-236.

[2] K. Chopra, **"Thin Film Device Applications"**, Springer Science & Business Media (2012).

[3] S. Aroussi et al., "Characterization of Some Physical and Photocatalytic Properties of CuO Nanofilms Synthesized by a Gentle Chemical Technique", *Cond. Matter.*, 7(2) (2022) 37.

[4] A.M. Koshy et al., "Effect of substrate temperature on the optical properties of DC magnetron sputtered copper oxide thin films", *Physica B: Cond. Matter.*, 32 (2023) 650 414452.

[5] A. Prakash et al., "Spectroscopic and electrical analysis of spray deposited copper oxide thin films", *Mater. Today Commun.*, 32 (2022) 103926.

[6] M.A. Green, "Third generation photovoltaics: Ultra-high conversion efficiency at low cost", *Prog. Photovolt.: Res. Appl.*, 9(2) (2001) 123-135.

[7] K.I. Mohammed, F.M. Jasim and M.I. Azawe, "Influence of thickness and crystalline structure on thermal and optical properties of ZnO thin films", *Curr. Appl. Phys.*, 14(9) (2014) 1318-1324.

[8] J.E. Greene, "Tracing the recorded history of thin-film sputter deposition: From the 1800s to 2017", *J. Vac. Sci. Technol. A*, 35(5) (2017).

[9] J. Danglad-Flores, S. Eickelmann and H. Riegler, "Deposition of polymer films by spin casting: A quantitative analysis", *Chem. Eng. Sci.*, 179 (2018) 257-264.

[10] R.A. Munef, B.A. Omar and S.J. Fathi, "Preparation and synthesis of the nanoferrite $Ni_{0.3}Co_{0.2}Zn_{0.5}Al_xFe_{2-x}O_4$ utilizing sol-gel auto-combustion approach", *J. Ovonic Res.*, 18(2) (2022) 213-218.

[11] Y.C. Ke and P. Stroeve, **"Polymer-layered silicate and silica nanocomposites"**, Elsevier (2005).

[12] J. Livage, M. Henry and C. Sanchez, "Sol-gel chemistry of transition metal oxides", *Prog. Solid State Chem.*, 18(4) (1988) 259-341.

[13] S.C. Ray, "Preparation of copper oxide thin film by the sol–gel-like dip technique and study of their structural and optical properties", *Sol. Ener. Mater. Solar Cells*, 68(3-4) (2001) 307-312.
[14] M. Dhaouadi et al., "Physical properties of copper oxide thin films prepared by sol–gel spin–coating method", *Am. J. Phys. Appl.*, 6(2) (2018) 43-50.
[15] H. Absike et al., "Synthesis of CuO thin films based on Taguchi design for solar absorber", *Opt. Mater.*, 118 (2021) 111224.
[16] H. Absike et al., "Influence of spinning speed on the physical properties of sol-gel spin coated CuO films", *Mol. Cryst. Liq. Cryst.*, 711(1) (2020) 18-31.
[17] K. Nassau, **"Color for Science, Art and Technology"**, Elsevier (1997).
[18] A.I. Salih, "Color Characterizations of Pure ZnO and ZnO/SeO_2 Thin Films Annealed at Different Temperatures", *Kirkuk Univ. J. Sci. Stud.*, 15(4) (2021) 107-124.

Table (3) Results of the coordinates and color value copper oxide prepared at various annealing temperatures

T (°C)	Color coordinates CIE			Dominant wavelength (nm)	Brightness	Purity
	x	Y	Z			
300	0.5495	0.3363	8.04	563	23.69	0.7
400	0.5197	0.3261	14.95	562	31.63	0.6
500	0.5052	0.3239	21.80	556	41.35	0.51
600	0.5488	0.3310	10.63	569	29.32	0.67

Saleem H. Trier

Department of Medical Physics, College of Science, University of Al- Qadisiyah, Diwaniyah, IRAQ

Study of Optical, Electrical, and Structural Properties of Zinc-Doped CdTe Films by Chemical Bath Deposition

Thin layer coatings of CdZnTe were prepared using a non-aqueous chemical bath deposition method. X-ray diffraction (XRD), scanning electron microscopy (SEM), field-emission scanning electron microscopy (FE-SEM), Fourier-transform infrared spectroscopy (FTIR), photoluminescence (PL), UV-visible spectroscopy, Raman spectroscopy, and Hall effect analysis were used to examine the deposited films. Results indicates that the deposited films exhibit polycrystalline characteristics of cubic zinc-blende. Evaluations were conducted on the structural characteristics, including dislocation density, lattice constant, micro-strain, and crystallite size. The as deposited films are smooth, uniformly sized, spherical grains that are dispersed in both single-state and cluster form, according to FE-SEM and SEM results. It was found that the average crystallite size of the film was 12.33 nm and the energy gap was 2.2 eV, which is responsible for the large transmittance, and that the resistivity of the film deposited at room temperature was 5×10^3 Ω.m.

Keywords: CdZnTe; Thin films; Chemical bath deposition, Structural characteristics
Received: 04 November; **Revised:** 05 December; **Accepted:** 12 December 2023

1. Introduction

CdZnTe is a direct energy gap semiconductor with outstanding properties and is from the most suitable materials for ambient temperature detectors for X-rays and gamma rays due to its short leakage currents as well as high quantum efficiency in detector sensors [1]. CdZnTe is an interesting subject for imparting exotic electrical and optical properties. CdZnTe has a triplet energy gap which is constant for all alloy compounds and can be estimated at approximately (1.5-2.3) eV at ambient temperature [2]. It has been shown that several physical features are required to operate the detector, for example increased atomic number (2) to achieve the good atomic radioactive conductivity, and a sufficiently large energy gap is required. To achieve a high magnitude resistivity to keep the noise associated with the short external flux current in the sensor. The broad cross-sectional area of photoelectric absorption of gamma rays allows for efficient conversion of gamma ray energy into electrical energy, a large intrinsic mobility lifetime (μτ) product, and a reduction in electronic interference. The cubic zinc hybrid lattice of this ternary compound has an atomic number that is extremely similar to that of CdTe. CdZnTe has been applied to solid-state devices such solar cells, photodetectors or sensors, and light-emitting diodes [3]. The application of CdZnTe technology has expanded in recent years, particularly in the domains of space science, nuclear medicine, and national security. It is related to imaging techniques like x-ray or gamma-ray tomography, x-ray fluorescence, etc. in the field of nuclear medicine. Implementing national security mostly entails finding, following, or detecting radioactive elements. Examples of this include tracking nuclear power plants for environmental change and welfare, as well as inspecting nuclear weapons. The high energy focusing telescope is connected to implementation in space science (HEFT) [2]. Recently, a range of thin film deposition techniques, including as electrodeposition[4,5], thermal evaporation [6], magnetron sputtering [7], closed space sublimation [8], and chemical bath deposition [9], have been developed to create CdZnTe thin film layers.

Chemical bath deposition (CBD) technology is the most straightforward and cost-effective of all operating techniques. In comparison to other methods, it also offers vast area deposition and high deposition rates [10,11]. As a result, it satisfies the standards for the production of solar devices [9]. Since the non-aqueous mode allows greater flexibility and is more convenient than the aqueous mode, so in this study, CdZnTe films deposited on nickel substrates were prepared using chemical bath deposition in a non-aqueous medium. Working at high temperatures can be done using non-aqueous techniques, giving a wide range of substrates. Of course, no hydrogen gas is produced, unlike the water-based concept, leaving a hole-free layer. Detectable and post-infrared optical transmission, X-ray diffraction, and field emission scanning electron microscopy (FE-SEM) were used to analyze the deposited layers.

2. Experimental Techniques

0.05M TeO_2, 0.05M cadmium acetate ($Cd(CH_3CO_2)$), 0.125M $NaBH_4$, and 0.5M $ZnCl_2$ deliquesced in 40ml ethylene glycol were used to aggregate the osmolality. First, fill a beaker with 40 mol of ethylene glycol. Stir the mixture moderately for two hours using a magnetic stirrer, and maintain the temperature of the combined solution at 160°C. 0.05M TeO_2 is added and stirred for 10min., followed

by 0.05M Cadmium acetate and 5min. of stirring. After the compound reaches 160°C, 0.125M $NaBH_4$ is added and stirred for 2hours ,Finally, 0.5 M ZnC_{l2} was introduced into the solution and stirred for the next 2 hours. With the help of a rigid support, a Ni plate of size 2.5×1.5cm was immersed in the electrolyte and the film was continuously deposited for 15min.

The color of the sediment is black. The films were washed with distilled water and dried at room temperature. Examine the structural form and composition as well as optical properties of the deposited film to observe its solid-state properties.

3 .Results and Discussion

Figure (1) displays the x-ray diffraction pattern of the CdZnTe film that was deposited on a Ni substrate. The final film has good physical stability and adhesion. The range of the XRD spectra is still (20-90)°. The figure illustrates the indicated peaks present in the CdZnTe film at 2θ = 23.01°, 40.45°, 51.27°, 56.9°, 67.7°, and 81.4°. These peaks are recognized as (111), (220), diffraction planes of (222), (400), (331), (420), and (511) cubic zinc whisk structures [12]. It was discovered that the sphalerite structure's cubic phase with thin CdZnTe coatings was a feasible polycrystalline phase with a (111) preferred orientation [8]. Additionally, phase exclusion, or two aspects (ZnTe and CdTe) with ZnTe having (012) preferred orientation and CdTe having (222) and (331) preferred orientations, was detected in the deposited CdZnTe films. It displays, among other things, peaks for Cd and Te, where the optimal orientations for Cd are (101) and (110) and Te is (220). Scherrer's formula was used to get the average crystallite size (D), as indicated in Eq. (1) [13,14]. While the 2θ value of the (111) peak and the Bragg equation of the cubic arrangement both of which are given in table (1) are used to compute the lattice constant (a) and inter-planar spacing (d_{hkl}) of the cubic state.

$$D = \frac{K\lambda}{\beta\cos\theta} \quad (1)$$

To estimate the micro-strain in the film, use the following equation [15]

$$\epsilon = \frac{\beta\cos\theta}{4} \quad (2)$$

The deposited CdZnTe has an average particle size of about 68 nm. The cast film's CdZnTe lattice invariance coefficient is 6.7Å. It is well known that atoms' elimination discrepancies with respect to their reference lattice positions can alter the lattice tension in thin coatings that have been applied [8]. The dislocation density of the CdZnTe film that was deposited was determined by applying the Williamson-Smallman formula.

$$\sigma = \frac{1}{D^2} \quad (3)$$

The calculated 2θ, d_{hkl}, and Miller indices for the deposited CdZnTe thin film are provided in table (2). Table (3) lists dislocation density and the micro-strain of the CdZnTe thin films that were deposited.

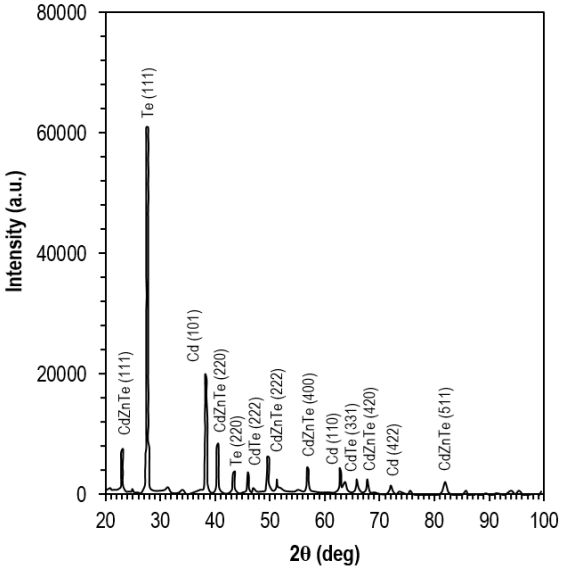

Fig. (1) XRD spectrum of the prepared CdZnTe thin film

Table (1) The inter-planer spacing (ISP), lattice constant (a), and crystalline size (D) of the deposited CdZnTe thin film

Sample	$d_{(hkl)}$ (Å)	Lattice Constant (a) (Å)	Average Crystalline Size (D) (nm)
1	3.854	6.692	67.87

Table (2) Values of 2θ, d_{hkl} , and Miller indices of the deposited CdZnTe thin film

Measured values			Standard values		
2θ (deg)	d_{hkl}	Miller indices	2θ (deg)	d_{hkl}	Miller indices
23.10	3.840	(111)	23.74	3.743	(111)
40.55	2.207	(220)	40.60	2.218	(220)
51.37	1.760	(222)	50.50	1.805	(222)
56.98	1.600	(400)	56.83	1.618	(400)
67.80	1.362	(420)	66.83	1.398	(420)
81.50	1.160	(511)	80.91	1.197	(511)

Table (3) Micro-strain and dislocation density of the CdZnTe thin film that were deposited

Micro-strain (×10^{-3})	Dislocation density (×10^{10}cm^{-2})
29.39	2.163

Surface diagnostics of deposited CdZnTe films using FESEM and SEM are displayed in Fig. (2). 25kX and 50kX magnifications were used for FE-SEM and SEM photography, respectively. The deposited layer shows smooth, consistently sized spherical particles, as the figure illustrates. The spherical particles are dispersed both single states and in clusters on the whole upper surface of the films. This demonstrates the CdZnTe film's crystallite nature. Agglomeration of CdZnTe elemental particles was seen in the FE-SEM and SEM of the formed films, leading to the formation of nanoclusters [16]. The film comparison also shows that the deposited

film contains thick grains with an average grain size of 12.33 nm and no holes or pits.

Figure (3) shows how the elements composition of the as-cast CdZnTe the film is analyzed. EDS signals were captured between 0 and 20 keV in binding energies. The as-deposited CdZnTe film contains zinc (Zn), tellurium (Te), and cadmium (Cd), as seen by the peaks in Fig. (3).

Table (4) shows the percentage weight and atomic content of the deposited film. It was found that the average atomic percentages of Cd, Zn, and Te were 17.64%, 1.44%, and 80.92%, respectively. As stated in the research [17], zinc's share of the element ratio in the CdZnTe film is significantly less than that of tellurium and cadmium. The deposition of stoichiometric films was revealed by EDS analysis of the as-deposited CdZnTe films.

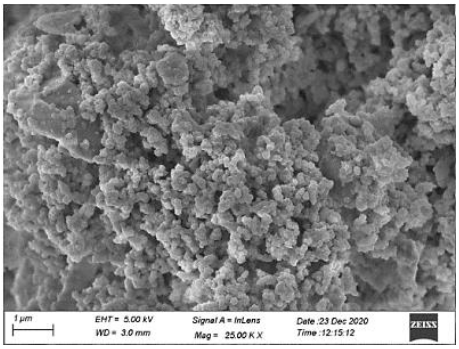

(1)

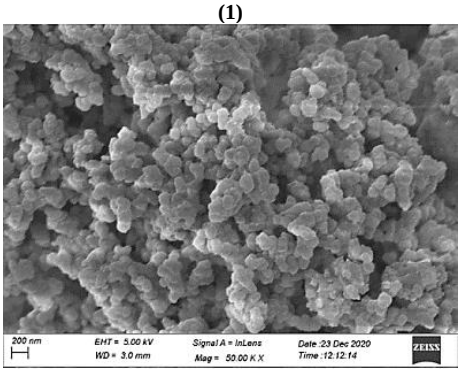

(2)

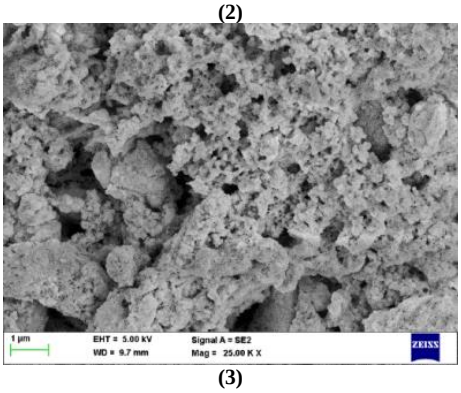

(3)

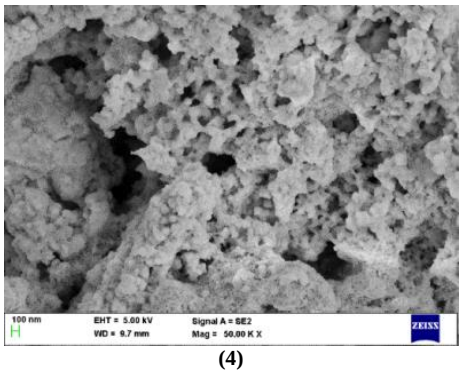

(4)

Fig. (2) FE-SEM and SEM images of the deposited CdZnTe film (1,2) FE-SEM at 25 and 50kX, (3,4) SEM at 25 and 50kX

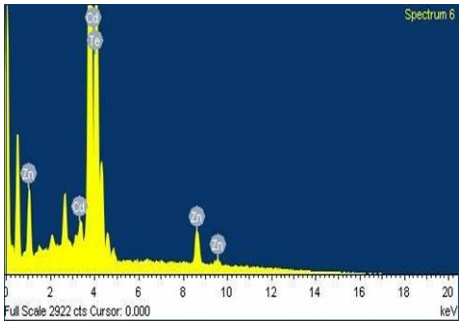

Fig. (3) EDS spectrum of the deposited CdZnTe film

Table (4) Elemental analysis of the deposited CdZnTe film

Element	Atomic (%)	Weight (%)
Cd	17.64	9.91
Zn	1.44	1.39
Te	80.29	88.71

The FTIR spectrum of the CdZnTe film as prepared is shown in Fig. (4). The CdZnTe sample demonstrates the existence of C-H, carboxyl, and hydroxyl groups. It also exhibits C-O stretching. The presence of OH stretching as a result of air pressure is shown by the large peak 3278.99 cm^{-1} [18]. The alkane functional group's C-H bent bond structure is thought to be represented by the tiny peak 1330.88 cm^{-1} [19]. Alkene (=C-H) bending vibration is present as indicated by the peak 921.97 cm^{-1} [20]. The stretching mode of aliphatic amines was identified as the peak 1072.42 cm^{-1} [21]. It is believed that the bending mode of aromatic C-H functional groups is responsible for the peak 682.80 cm^{-1} [22]. The appearing absorption band is associated with wave 856.39 cm^{-1} and can be ascribed to the CdZnTe thin-layer coating's stretching vibration [8]. Table (5) displays various functional groups found in the deposited CdZnTe films.

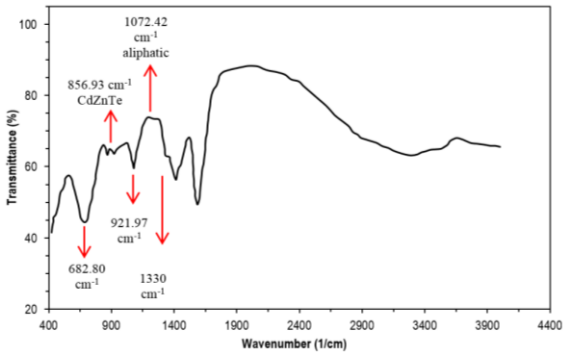

Fig. (4) FTIR spectrum of the deposited CdZnTe film

Table (5) Assignments of molecular vibrations of deposited CdZnTe film

Positions(cm^{-1})	Assignments
3278.99	O-H
1330.88	C-H
921.97	=C-H
1072.42	Aliphatic amines
682.80	C-H
856.39	CdZnTe

At room temperature, the optical absorption spectrum of the deposited CdZnTe thin film was recorded in the spectral range 200-800nm. The energy gap of CdZnTe film may be determined using the Tauc equation $(\alpha h\upsilon)^2=A(h\upsilon-E_g)^{1/2}$, which confirms that the material is a direct energy gap semiconductor [6]. In this equation, the absorption coefficient is α, the band gap is E_g, the frequency is υ, the proportionality constant is A, and the Planck's constant is h

Plotting $(\alpha h\upsilon)^2$ versus energy (hυ) and energy gap (E_g) of deposited CdZnTe thin film, as seen by extrapolating the curve of $(\alpha h\upsilon)^2=0$, illustrates the optical absorption extension of a CdZnTe film in Fig. (5). It was discovered that the as-deposited CdZnTe film had an energy band width of 2.2eV. The outcomes agree with the published research [8,23,24]. The Tauc plot's roughly linear behavior suggests that CdZnTe is a direct energy gap semiconductor.

It has been stated that there is a greater energy gap between pure and doped CdTe nanocrystals. The two primary causes of an increase in band gap are (1) alloying with materials that have a greater band gap, and (2) quantum confinement of energy levels within nanocrystals [25].

The photoluminescence spectrum of deposited CdZnTe is depicted in Fig. (6). The non-destructive photoluminescence (PL) spectroscopy is frequently used to investigate the inherent and external characteristics of bulk semiconductors and nanostructures. This PL intensity and spectral content provide precise measures of a range of superior material characteristics. This method uses laser light with accompanying energy far bigger than the optical band gap to produce excitation. It is clear that the deposited CdZnTe film has a broad emission spectrum at 448 and 469 nm, respectively, and a fluorescence peak at 374 nm as shown in Fig. (6). The particle size dispersion of CdZnTe nanocrystal films is the cause of this widespread emission [26-28].

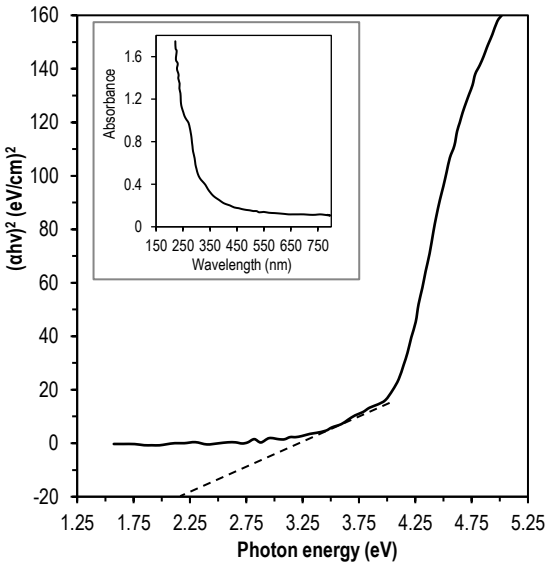

Fig. (5) Determination of energy gap and absorbance of the deposited CdZnTe film

The spectrum also shows that the bulk CdZnTe crystals are responsible for the higher wavelengths, whereas the lesser wavelengths are related to the smaller size of CdZnTe quantum dots. A widening of the emission peak at 469 nm, an indication of CdZnTe nanocrystalline layer formation and deep trap emission, was seen when Zn was doped with CdTe films [29].

An additional practical technique for identifying material phases and assessing the crystallinity of films is Raman spectroscopy. This method uses the inelastic scattering of monochromatic photons to monitor vibrations, rotations, and other low-frequency modes in molecules. Transverse optics (TO) and longitudinal optics (LO) of deposited phonon mode CdTe were stated in Ref. [30] as well as a clear peak of Raman at 166, 139 and 332 cm^{-1} in the Raman spectra produced for the sample using a wavelength of 785 nm, an exposure duration of 10 s, and a power of 0.1 mW. Common Te inclusions in crystalline CdTe have been effectively detected using Raman spectroscopy. There is a difference between the Raman longitudinal optics of the LO mode of crystalline CdTe and the A1 mode of crystalline tellurium. For these reasons, x-ray techniques may not always be able to see Te inclusions in CdTe that are discovered by Raman scattering. Crystalline materials' Raman spectrum can only display modes where ω deviates from zero at $q \approx 0$. An amorphous material's Raman spectrum is frequency dependent and typically broadens to match its whole vibrational dynamic density (DOS). The term "modulation" refers to the local atomic environment's symmetry. This is because, in theory, all Raman and infrared

vibration modes become active when the momentum conservation selection criteria for Raman scattering is applied to the amorphous state [31].

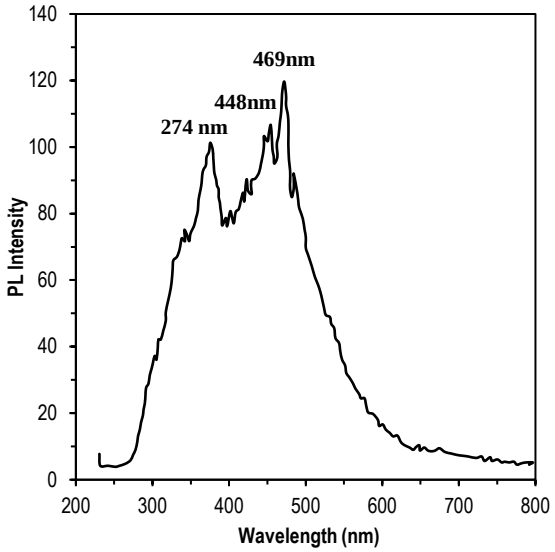

Fig. (6) PL spectrum of the deposited CdZnTe film

Other semiconductors have been subjected to this study. The peak characteristics of CdTe are shown in Fig. (7), where A1 is represented by the first peak seen at 119 cm^{-1}, the second at 139 cm^{-1}, the third at 166 cm^{-1}, and the fourth at 332 cm^{-1} (LO). The longitudinal optical phonon vibration mode (LO) of Te and the transverse optical phonon vibration mode (2LO) of CdTe are the corresponding E modes. It is noteworthy that Te/Raman modes are frequently found in CdTe samples, which may be the result of trace amounts of Te precipitates [32,33].

CdZnTe film resistivity was calculated using Hall effect technique. Equation (4) is used to compute resistivity (ρ).

$$\rho = \frac{V}{I} \times 2\pi S \qquad (4)$$

where I is the current flowing into and out of the outer probe, V is the potential difference between the inner probes, and S is the probe distance (0.2cm). The temperature range in which CdZnTe resistivity is estimated is 303-363K. It was discovered that the resistivity of CdZnTe at room temperature was 5×10^3 Ω.m. Resistivity for semiconductors diminishes with temperature. The resistivity of CdZnTe as deposited is displayed in Fig. (8). The figure illustrates how resistivity falls with temperature because excited electrons in the valence band hop to the conduction band, increasing conductance and resulting in a decrease in resistivity. Resistivity will likewise decrease since resistance is proportionate to resistivity [34,35]. The plot of $\log_{10}\rho$ versus 1/T yields a linear curve at higher temperatures. As a result, the width of the energy gap can be estimated from the slope of the linear section of the experimental curve.

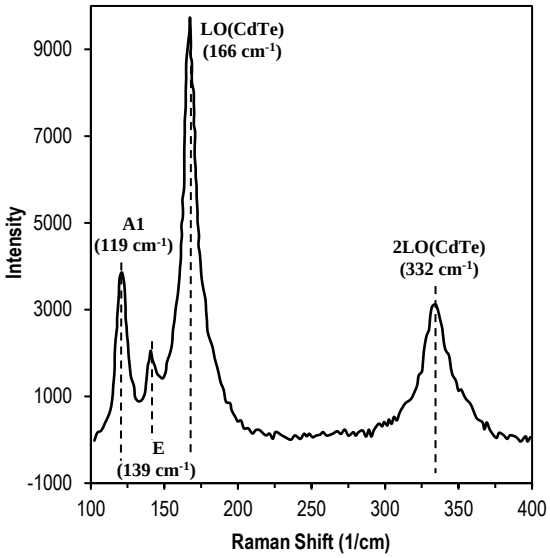

Fig. (7) Raman spectrum of the deposited CdZnTe film

The formula for calculating the energy gap is $E_g=2.3\times2k_B\Delta\log_{10}\rho/\Delta T^{-1}$, where k_B is Boltzmann's constant. The band gap was discovered to be 1.98 eV, which agrees with the band gap determined using reported work and Tauc's formula (band gap variation is roughly 1.4-2.2eV) [8,23,24].

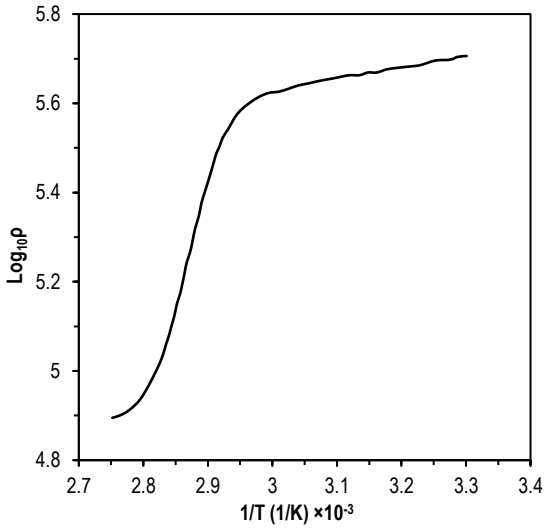

Fig. (8) Variation of $\log_{10}\rho$ with reciprocal temperature (1/T) for the deposited CdZnTe films

4. Conclusion

A non-aqueous mode chemical bath deposition approach was used to easily produce cubic zinc stirred CdZnTe films on Ni substrates. Using various methods, the solid-state and as well as optical characteristics of deposited CdZnTe films were investigated. Cubic zincblende phase of CdZnTe was confirmed. The surface is uniform, dense, and devoid of voids. With some Te still present, the deposited film's stoichiometry is precisely observed. Based on the light absorption extension, a pre-designed band gap of 2.2eV was assigned. CdZnTe has a resistivity of 5×10^3 Ω.m. Photoluminescence reveals emission

from deep traps. The LO and 2LO modes of CdTe phonon vibration were observed at 166 and 332cm^{-1}, respectively, according to Raman analysis. These features make CdZnTe films suitable for use in sensor, photovoltaic, and photoelectrochemical cells.

References

[1] N. Manez et al., "Material optimization for X-ray imaging detectors", *Nucl. Instrum. Methods Phys. Res. A*, 567(1) (2006) 281-284.

[2] S. Jain, "Photoluminescence study of cadmium zinc telluride", MSc thesis, West Virginia University (USA, 2001).

[3] S.D. Sordo et al., "Progress in the Development of CdTe and CdZnTe Semiconductor Radiation Detectors for Astrophysical and Medical Applications", *Sensors*, 9(5) (2009) 3491-3526.

[4] K.R. Murali et al., "Properties of CdTe films deposited by electron beam evaporation", *Surf. Coat. Technol.*, 41(2) (1990) 211-219.

[5] A. Bansal and P. Rajaram, "Electrochemical growth of CdZnTe thin films", *Mater. Lett.*, 59(28) (2005) 3666-3671.

[6] G. Zha et al., "The growth and the interfacial layer of CdZnTe nano-crystalline films by vacuum evaporation", *Vacuum*, 86(3) (2011) 242-245.

[7] P. Banerjee, R. Ganguly and B. Ghosh, "Optical properties of $Cd_{1-x}Zn_xTe$ thin films fabricated through sputtering of compound semiconductors", *Appl. Surf. Sci.*, 256(1) (2009) 213-216.

[8] H. Xu et al., *Appl. Surf. Sci.*, "The dependence of Zn content on thermal treatments for $Cd_{1-x}Zn_xTe$ thin films deposited by close-spaced sublimation" 305 (2014) 477-480.

[9] T. Yamaguchi et al., "Preparation and characterization of (Cd,Zn)S thin films by chemical bath deposition for photovoltaic devices", *Thin Solid Films*, 343-344 (1999) 516-519.

[10] J. Zhou et al., "CBD-$Cd_{1-x}Zn_xS$ thin films and their application in CdTe solar cells", *phys. stat. sol. (b)*, 241(3) (2004) 775-778.

[11] N. Gaewdang and T. Gaewdang, "Investigations on chemically deposited $Cd_{1-x}Zn_xS$ thin films with low Zn content" *Mater. Lett.*, 59(28) (2005) 3577-3584.

[12] S. Chander and M.S. Dhaka, "Thermal annealing induced physical properties of electron beam vacuum evaporated CdZnTe thin films", *Thin Solid Films*, 625 (2017) 131-137.

[13] S. Chander and M.S. Dhaka, "Effect of thickness on physical properties of electron beam vacuum evaporated CdZnTe thin films for tandem solar cells" *Physica E: Low-Dim. Sys. Nanostruct.*, 84 (2016) 112-117.

[14] S.H. Trier, "The Study of $Mg_{1-x}Co_xFe_2O_4$ Ferrite Physical Properties and its Applications", *NeuroQuantology*, 18(2) (2020) 143-156.

[15] M.K. Ashok and S. Muthukumaran, Phys. Proced., 49 (2013) 137-???.

[16] G. Rajesh et al., "Photoinduced electrical bistability of sputter deposited CdZnTe thin films", *Mater. Res. Exp.*, 5 (2018) 026412.

[17] S. Chander and M.S. Dhaka, "Optimization of structural, optical and electrical properties of CdZnTe thin films with the application of thermal treatment", *Mater. Lett.*, 182 (2016) 98-101.

[18] S. R. Kumar et al., "Structure, Composition and Optical Properties of Non Aqueous Deposited ZnCdS Nanocrystalline Film", *Mater. Today: Proc.*, 2(9A) (2015) 4563-4568.

[19] M.K. Bin Bakri and E. Jayamani, **"Science, Humanities, and Technology"**, 1st ed., Tro India (2016) Ch. 30, p. 167.

[20] E. Al-Shareefi, A.H. Abdual Sahib and I.H. Hameed, *Indian J. Public Health Res. Develop.*, 10(1) (2019) 994.

[21] N. Janakiraman and M. Johnson, "Functional Groups of Tree Ferns (Cyathea) Using FT-IR: Chemotaxonomic Implications", *Romanian J. Biophys.*, 25(2) (2015) 131-141.

[22] K. Banerjee, N. Thiagarajan and P. Thiagarajan, "Azadirachta indica A. Juss Based Emollient Cream for Potential Dermatological Applications", *Indian J. Pharmaceut. Sci.*, 78(3) (2016) 320-325.

[23] E. Yilmaz, "An Investigation of CdZnTe Thin Films for Photovoltaics", *Ener. Sour. A*, 34(4) (2011) 332-335

[24] M. Dammak et al., "Optical spectroscopy of titanium-doped CdZnTe", *Semicond. Sci. Technol.*, 13(7) (1998) 762-768.

[25] A. Al-Rasheedi et al., "Structural and optical properties of CdZnTe quantum dots capped with a bifunctional Molecule", J. Mater. Sci.: Mater. Electron., 28(12) (2017) 9114.

[26] A. Khare, "Effects of the Zn concentration on electro-optical properties of $Zn_xCd_{1-x}S$ films", *Chalcogen. Lett.*, 6(12) (2009) 661-671.

[27] M.A. Mahdi et al., "Structural and optical properties of nanocrystalline CdS thin films prepared using microwave-assisted chemical bath deposition", *Thin Solid Films*, 520(9) (2012) 3477-3484.

[28] C.S. Tiwary et al., "Synthesis of wurtzite-phase ZnS nanocrystal and its optical properties", *J. Lumines.*, 129(11) (2009) 1366-1370.

[29] C. Jin et al., "Synthesis and Wavelength-Tunable Luminescence Property of Wurtzite $Zn_xCd_{1-x}S$ Nanostructures", *Cryst. Growth Des.*, 9(11) (2009) 4602-4606.

[30] H. Park et al., "CdTe microwire-based ultraviolet photodetectors aligned by a non-uniform electric field ", *Appl. Phys. Lett.*, 103 (2013) 051906.

[31] Z. Bai and D. Wang, "Oxidation of CdTe thin film in air coated with and without a CdCl2 layer", *phys. stat. sol. (a)*, 209(10) (2012) 1982-1987.

[32] E. Campos-González et al., "Structural and optical properties of CdTe-nanocrystals thin films grown by chemical synthesis", *Mater. Sci. Semicond. Process.*, 35 (2015) 144-148.

[33] Y. Xu et al., "Study on temperature dependent resistivity of indium-doped cadmium zinc telluride", *J. Phys. D: Appl. Phys.*, 42(3) (2009) 035105.

[34] S. Rajpal and S.R. Kumar, "Annealing temperature dependent structural and optical properties of nanocrystalline ZnTe thin films developed by electrodeposition technique", *Solid State Sci.*, 108 (2020) 106424.

[35] G. Morell, A. Reynes-Figueroa and R.S. Katiyar, "Raman spectroscopy of oxygenated amorphous CdTe films", *J. Raman Spectro.*, 25(3) (1994) 203-207.

Hassan A. Ashoor
Awattif A. Mohammed

Department of Physics, College of Science, University of Baghdad, Baghdad, IRAQ

Effect of Metal Oxide Nanoparticles on Mechanical and Optical Properties of Bioblend (PLA/PCL)

An important development in the plastics industry involves the production of bio-nanocomposites through the combination of metal oxide nanoparticles with polylacticacid (PLA) and polycaprolactone (PCL). Various quantities of nanoparticles, such as zirconium dioxide (ZrO_2) and magnesium oxide (MgO), were employed to fabricate and analyze different combinations of the PLA/PCL blend. The blend contains 60% PLA and 40% PCL, with different concentrations of nanoparticles ranging between 0%, 0.75%, 1.5%, and 2.5%. The FTIR and mechanical properties study showed a direct correlation between the increase in nano-oxide fraction and the enhancement of tensile strength, tear resistance, elongation at break, and modulus of elasticity. UV-VIS transmission test confirmed that the impact of ZrO2 and MgO NPs have reduced the permeability in contrast to the pure PLA/PCL blend. The increased opacity caused by reinforcement which is responsible for the decrease in permeability. Also, we conducted contact angle measurements for both the reinforced and the pure (PLA/PCL) films. As oxides are hydrophobic, our findings show an obvious connection between the percentage of reinforcements and the rise in contact angle.

Keywords: Polylacticacid; Polycaprolactone; Food Packing; Nanoparticles
Received: 27 December 2023; **Revised:** 08 February; **Accepted:** 15 February 2024

1. Introduction

A lack of petroleum resources and rising environmental concerns have led to a large increase in the need for biodegradable materials. Examples of natural polymers include starch, protein, and cellulose, and polymers created from natural monomers include (PLA). Also, (PCL) is produced from petroleum [1,2]. The increased use of non-biodegradable plastics that aren't petroleum-based has caused an important rise in pollution of the environment [3]. The packaging industry is significantly liable for the substantial quantities of plastic waste that end up in certain landfills [4]. Using bio-based polymers is an option for solving these issues. The manufacturing of environmentally friendly plastics includes several processes, such as the polymerization of bio-based monomers, the extraction of natural polymers from biomass, and the extraction of micropolymers [5].

PLA is now the most effective biodegradable polymer in use. However, the fragility and low resistance to heat of the material limit its use. By mixing PLA with other biodegradable polymers, it can modify the way it behaves, ensuring its natural degradation [6-9]. PCL exhibits the features of being flexible and available, and it may be mixed evenly with a wide range of polymers [10-13].

The aim of this work is to create mixtures of PLA and PCL that can increase the tensile strength of PCL and improve the ductility and toughness of PLA. PLA/PCL blends are widely used in biomedical applications due to their biocompatibility and biodegradability. These include scaffolds, managed delivery systems, and implants. An advantage of using PLA/PCL mixes is being able to control the usefulness of products due to the relatively slow degradation rate of PCL compared to PLA. A full study has been done over the past twenty years on the preparation and evaluation of PLA/PCL blends [14].

Adding the nanofiller to the matrix changes the biopolymer's physical and chemical properties, as well as its mechanical, thermal, and barrier properties [15-17].

Zirconium oxide (ZrO_2) has advantages that include great thermal stability, resistance to friction and chemicals, as well as unique mechanical strength, hardness, and fracture toughness [18,19]. Magnesium-based nanoparticles (Mg-based NPs) have become popular in biomedical applications due to their antimicrobial abilities, unique mechanical qualities, and ability to enhance bone cell proliferation [20-22].

Previous studies have demonstrated that the production of Zinc oxide nanoparticles was successfully shown by the analysis of FTIR patterns. The production of ZnO-NPs was carried out using hydrothermal methods. Subsequently, a blend of polylactic acid and polycaprolactone (PLA/PCL, 80/20 wt/wt) was prepared by melt mixing. The blend was then loaded with 2, 4, and 6 wt.% of ZnO-NPs. The mechanical examination of the Bio Nano composites reveals that the tensile modulus experiences an increase of around 5.4%, 11.1%, and 24% with the addition of 2, 4, and 6 wt.% of ZnO-NPs to the blend sample, respectively [23].

Enhancing the strength of wood powder (WP) by using polycaprolactone (PCL) and polylactic acid (PLA) composites. The strength impact of PLA/PCL bioblend and PLA/PCL/WP composites exhibited superior performance compared to pure PLA, as its mechanical properties such as tensile strength, Shore D hardness, and impact resistance. Moreover, the elongation at break and Shore D hardness exhibited similarity to PLA, indicating that these traits were not

substantially influenced by high WP concentrations. The water interaction of the PLA/PCL/WP composites was boosted, as shown by the contact angle, whereas the elastic modulus and tensile strength were seen to decrease [24].

2. Experimental Part

The PLA with density of 1.25 g/cm^3 was supplied from BASF India. The PCL was supplied from Sigma-Aldrich. The THF solution was purchased from HiMedia Laboratories (India). The ZrO_2 and MgO nanoparticles were supplied from SkySpring Nanomaterials (USA).

The PLA was weighed (2.1g) using an electron scale and then dissolved in THF to obtain a viscous solution. The dissolution process was carried out by slowly warming the solution to 55°C for 2 hours using a magnetic stirrer. The PCL is prepared using the same method. Then, mix the solutions of PLA and PCL. After that, pour the mixture into a petri dish and allow it to evaporate at room temperature for a day to ensure the complete removal of the solvent. The preparation involved creating film samples of PLA/PCL with varying filler quantities (0.75, 1.5, and 2.25%) of MgO and ZrO_2 with similar experiments and the same technique. The thickness of PLA/PCL/MgO and PLA/PCL/ZrO_2 nanocomposites was found to be 110 micrometers using a digital micrometer.

The spectroscopic studies were carried out using a Shimadzu UV-1900 UV-visible spectrophotometer in the wavelength range of 200-800 nm. The material's infrared spectra were obtained using a Shimadzu 8400S Fourier-transform infrared (FTIR) spectrometer in the wavenumber range of 400-4000 cm^{-1}.

As per the ASTM D-882 standard, the modulus of elasticity, tensile strength, and elongation are measured using a 10 N load cell in tensile mode. The tested films were divided into strips of 1 cm in width and 10 cm in length. The starting gauge length and speed were both set at 10 mm/min. The equation used to calculate the tensile strength (σ_s) and Young's modulus (E) is as follows:

$$\sigma_s = \frac{F}{A} \quad (1)$$

$$E = \frac{FL_0}{A\Delta L} \quad (2)$$

where F is the force exerted on an object under tension, L_0 is the original length, A is the cross-section area, ΔL is the length of the object changes [25]

The tear strengths of the films were assessed using the trouser tear method, following the guidelines of ASTM D-1922, with the same Universal Electronic Dinamometer. A 50 mm cut was made in the center of one end of the 7 cm long and 3 cm wide sample. An impact pendulum tester is used to determine the amount of force required to displace a slit a certain distance from the edge of the sample.

Contact angle analysis of distilled water generated by each sample was recorded using a Firsttenangstroms FTA32 goniometer. Each sample has a distinct droplet image.

3. Results and Discussion

The chemical formula of PCL is $C_6H_{10}O_2$, while that of PLA is $C_3H_4O_2$. The unique peaks observed in PCL and PLA can be attributed to the existence of CH bonds and CO double bonds. The presence of a peak at 1768 cm^{-1} in PLA and a peak at 1730 cm^{-1} in PCL indicates the presence of bond vibration [6]. The peaks at 2939.5 and 2866.2 cm^{-1} in Fig. (1) indicate the stretching of C-H bonds in PCL.

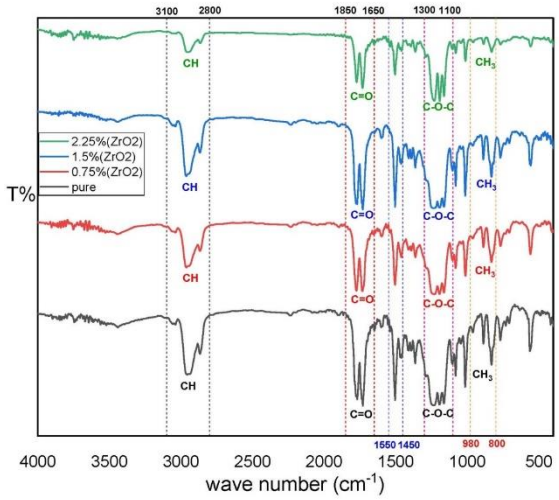

(a)

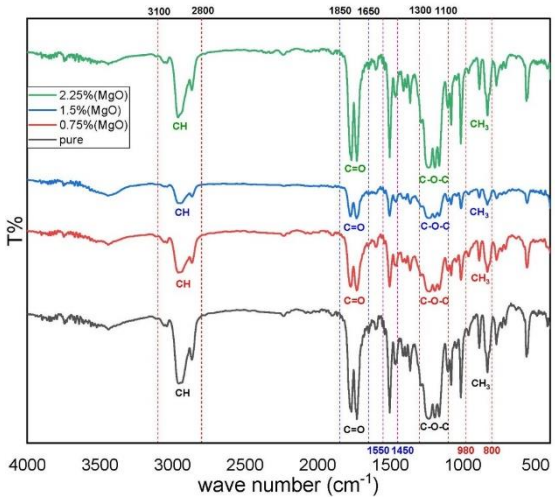

(b)

Fig. (1) FTIR of bioblend PLA/PCL with nanoparticles (a) ZrO_2 (b) MgO

The presence of the aliphatic C-O-C ether group was observed within the frequency range of 1163-1236 cm^{-1} in PCL, while it was observed in PLA. The range of 962-831 cm^{-1} showed the stretching of the carbonate chain in PCL and PLA, which was caused by the oscillation band of the CH_3 methyl group [8]. There is no evidence of any new interaction between PLA/PCL and MgONPs, while PLA/PCL/MgO films have infrared bands that are similar to those of PLA/PCL film. The proof of creation of the

PLA/PCL/MgO nanocomposites has been verified [26]. Similarly, this concept can be applied to films that are made of a nanocomposite material containing PLA, PCL, and ZrO_2 [27].

Figure (2) shows stress-strain curves obtained from the tensile testing of the produced films. The statistical data for film elongation at break (EAB), tensile strength (TS), and elastic modulus (EM) can be found in Table (1).

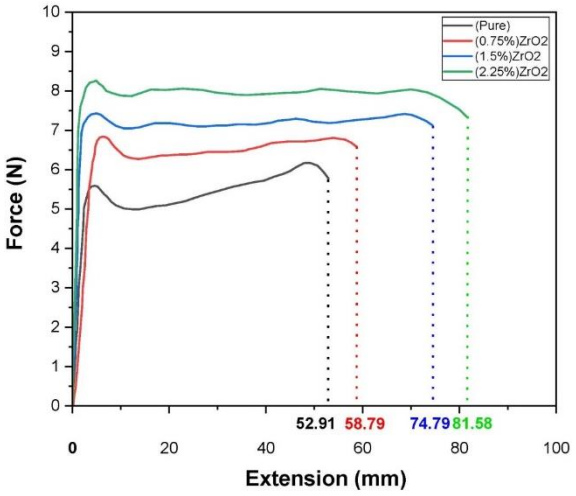

(a)

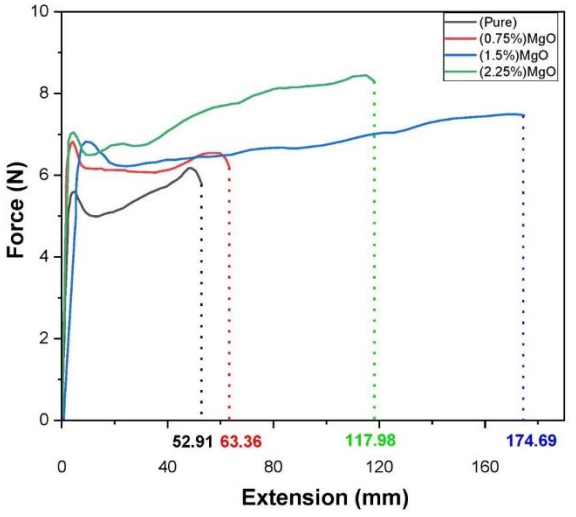

(b)

Fig. (2) Mechanical properties stress-strain curve of bioblend PLA/PCL with nanoparticles (a) ZrO_2 (b) MgO

Studies suggest that films made only from PLA/PCL exhibit a notable increased tensile strength (TS) of about 31.09 MPa. The addition of nano-MgO at a maximum concentration of 2.25% improves the TS and EM of the films compared to PLA/PCL films. The increased stiffness (elastic modulus) of the reinforced MgO NPs occurs by reducing the mobility of the chains. Also, the efficient transfer of stress from the nanoparticles to the PLA/PCL chains results in an enhancement of the tensile strength. The inclusion of MgO NPs significantly enhances the elastic modulus of PLA/PCL films compared to basic PLA/PCL sheets. Nano-fillers tend to accumulate in particular regions due to their high surface energy, while the mix content remains in the background. The mechanical properties get worse as the number of nanoparticles increases, which means that MgO NPs are less effective at strengthening. The presence of agglomerated nano-fillers in the matrix reduces the efficacy of filler material. The aggregated nanofillers behave as flaws, leading to increased stress on the film and finally fracture. The behavior of ZrO_2 particles showed an identical characteristic to that of MgO particles [28-30].

The tear resistance of the pure PLA/PCL film was found to be 11.41 mN/mm. The addition of ZrO_2 and MgO nanoparticles improves a material's tear resistance by modifying the path of tear propagation, effectively reducing or preventing the risk of fractures. By using ZrO_2 with a range of 12.30 to 15.93 mN/mm and MgO with a range of 11.82 to 15.45 mN/mm, the tear resistance is greatly enhanced. The nanoparticles exhibited a strong interaction with the PLA/PCL matrix at the interface, resulting in improved tear strength for the samples containing 2.25% ZrO_2 and MgO nanoparticles.

The water wettability of PLA/PCL, PLA/PCL/MgO, and PLA/PCL/ZrO_2 films was determined by measuring the interfacial contact angles as shown in Fig. (3). Table (2) presents the measured contact angles. The contact angle likely increased with the addition of ZrO_2 and MgO nanoparticles due to the combined effect of the higher surface area and hydrophobic nature of the nanoparticles [31].

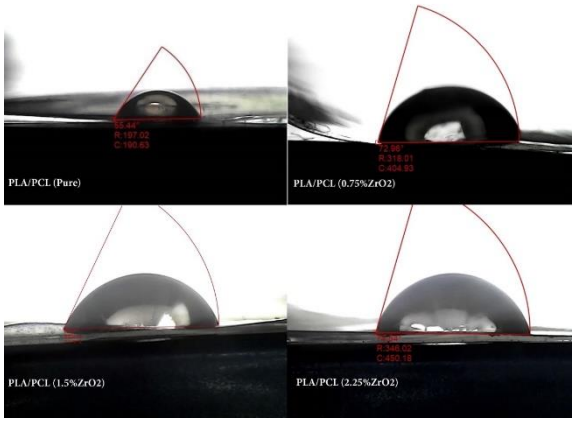

(a)

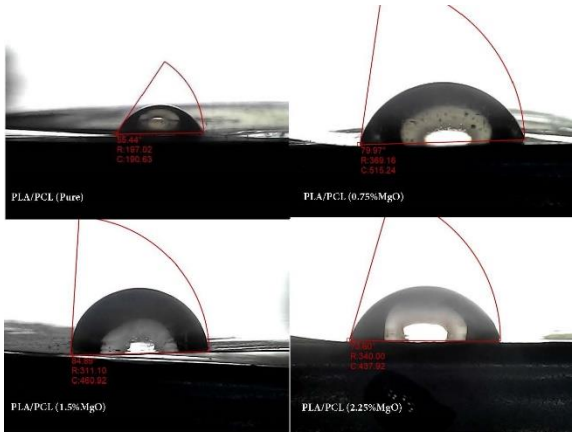

(b)

Fig. (3) Contact angle of bioblend PLA/PCL with nanoparticles (a) ZrO_2 (b) MgO

Table (2) Contact angle for bioblend PLA/PCL with nanoparticles

Sample	Contact Angle (θ)
Pure	55.29
ZrO_2 (0.75%)	72.96
ZrO_2 (1.5%)	63.57
ZrO_2 (2.25%)	74.54
MgO (0.75%)	79.97
MgO (1.5%)	84.89
MgO (2.25%)	73.80

Figure (4) shows the UV-visible transmission spectra of the pure PLA/PCL films and the (PLA/PCL) films with (ZrO_2 and MgO) NPs. The results indicated that the transparent PLA/PCL films showed the best degree of visibility compared to the other films.

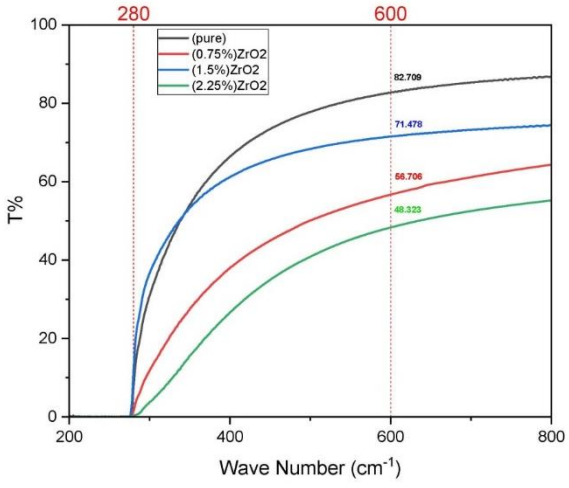

(a)

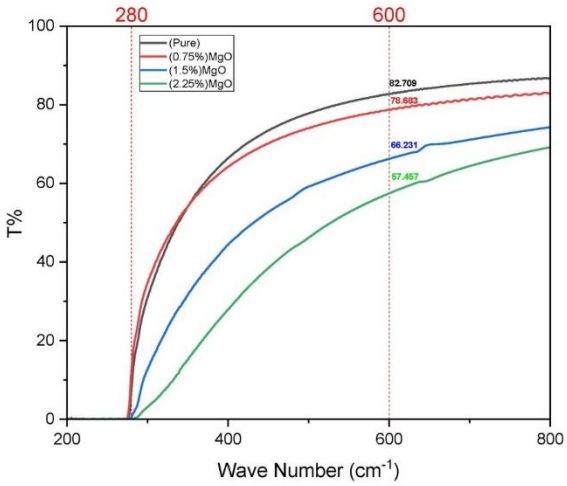

(b)

Fig. (4) UV-visible transmission of bioblend PLA/PCL with nanoparticles (a) ZrO_2 (b) MgO

The dispersion of nanoparticles mostly limits the expected improvement in UV protection when using increasing amounts of MgO. Also, the ZrO_2 particles had similar features to the MgO particles. Protecting oneself from UV radiation is important, and this study provides evidence to support this claim. There is a high need for films with excellent UV-preventing abilities and excellent transparency, as they are used in food packaging [28,32].

4. Conclusion

The effective formation of nanocomposite films containing (PLA/PCL/MgO) and (PLA/PCL/ZrO_2) was confirmed. The enhanced ductility upon the addition of ZrO_2 and MgO nanoparticles was shown. The incorporation of ZrO_2 and MgO led to better tensile strength and elongation at break and an obvious rise in elastic modulus and tear resistance as compared to pure PLA/PCL bio-blend films. Also, it led to a large rise in the contact angle, enhancing the hydrophobicity of the surface. The pure films exhibited the highest level of transparency when compared to films supported by nanoparticles such as ZrO_2 and MgO.

References

[1] R.M. Rasal, A.V. Janorkar and D.E. Hirt, "Poly (lactic acid) modifications", *Prog. Polym. Sci.*, 35(3) (2010) 338-356.

[2] A.A. Hasan and A.A. Mohammed, "Optical and ac electrical properties of PMMA/CB, PMMA/G and PMMA/(CB+G) composites", *Digest J. Nanomater. Biostruct.*, 15(3) (2020) 923-930.

[3] M. Dadras Chomachayi et al., "Biodegradable nanocomposites developed from PLA/PCL blends and silk fibroin nanoparticles: study on the microstructure, thermal behavior, crystallinity and performance", J. Polym. Enviro., 28 (2020) 1252-1264.

[4] J. Muller, C. González-Martínez and A. Chiralt, "Combination of poly (lactic) acid and starch for

biodegradable food packaging", *Materials*, 10(8) (2017) 952.
[5] A.N. Obaid and N. Ali, "Wettability, thermal stability, and antibacterial properties of polycaprolactone/ZnO nanocomposites in packaging", *Iraqi J. Phys.*, 18(47) (2020) 1-10.
[6] Y.Y. Chen et al., "Analysis of the mechanical properties of solvent cast blends of PLA/PCL", *Appl. Mech. Mater.*, 679 (2014) 50-56.
[7] I. Fortelny et al., "Phase structure, compatibility, and toughness of PLA/PCL blends: A review", *Front. Mater.*, 6 (2019) 206.
[8] N.A. Ali, "Characterization of biochar (bio carbon) on the properties of plasticized polylactic acid composites for antistatic packaging", *Iraqi J. Phys.*, 17(42) (2019) 13-26.
[9] M. Petousis et al., "The Effect of Nano Zirconium Dioxide (ZrO_2)-Optimized Content in Polyamide 12 (PA12) and Polylactic Acid (PLA) Matrices on Their Thermomechanical Response in 3D Printing", *Nanomater.*, 13(13) (2023) 1906.
[10] J.I. Castro et al., "Synthesis, Characterization, and Optimization Studies of Polycaprolactone/Polylactic Acid/Titanium Dioxide Nanoparticle/Orange Essential Oil Membranes for Biomedical Applications", *Polymers*, 15(1) (2022) 135.
[11] A.H. Mohsen and N.A. Ali, "Improve Wettability of Polycaprolactone (PCL)/Chitosan of Wound Dressings by Plasma Jet", *Iraqi J. Sci.*, 63(11) (2022) 4761-4770.
[12] R. Karimian et al., "Poly (ε-Caprolactone)/cellulose nanofiber blend nanocomposites containing ZrO_2 nanoparticles: A new biocompatible wound dressing bandage with antimicrobial activity", *Adv. Pharmaceut. Bull.*, 10(4) (2020) 577.
[13] K. del Ángel-Sánchez et al., "Development, fabrication, and characterization of composite polycaprolactone membranes reinforced with TiO_2 nanoparticles", *Polymers*, 11(12) (2019) 1955.
[14] M.K. Fong, "Polycaprolactone (PCL)/polylactice acid (PLA) reinforced with polyethlene gylcol (PEG) and nano-hydroxyapatite (n-HA) for fused deposition modeling (FDM) composite filament", Dissertation, Universiti Tun Hussein Malaysia (2021).
[15] P. Bazan et al., "Bio-based polyethylene composites with natural fiber: Mechanical, thermal, and ageing properties", *Materials*, 13(11) (2020) 2595.
[16] O. Okolie et al., "Bio-Based Sustainable Polymers and Materials: From Processing to Biodegradation", *J. Compos. Sci.*, 7(6) (2023) 213.
[17] E.d.S.B. Ferreira et al., "Production of eco-sustainable materials: Compatibilizing action in poly (lactic acid)/high-density biopolyethylene bioblends", *Sustainabil.*, 13(21) (2021) 12157.
[18] M. Topuz, "Effect of ZrO_2 on morphological and adhesion properties of hydroxyapatite reinforced poly–(lactic) acid matrix hybrid coatings on Mg substrates", *Res. Eng. Struct. Mater.*, 8 (2022) 721-733.
[19] R. Osorio-Arciniega et al., "Composite fiber spun mat synthesis and in vitro biocompatibility for guide tissue engineering", *Molecules*, 26(24) (2021) 7597.
[20] A. Leonés et al., "Potential applications of magnesium-based polymeric nanocomposites obtained by electrospinning technique", *Nanomater.*, 10(8) (2020) 1524.
[21] A. Ferrández-Montero et al., "Development of biocompatible and fully bioabsorbable PLA/Mg films for tissue regeneration applications", *Acta biomaterialia*, 98 (2019) 114-124.
[22] Y. Zhao et al., "Effects of magnesium oxide (MgO) shapes on *in vitro* and *in vivo* degradation behaviors of PLA/MgO composites in long term", *Polymers*, 12(5) (2020) 1074.
[23] A. Babaei, M.H. Abdolrasouli and A. Rostami, "Polylactic acid/polycaprolactone bionanocomposites containing zinc oxide nanoparticles: Structure, characterization and cytotoxicity assay", *J. Thermoplast. Compos. Mater.*, 36(7) (2023) 2998-3020.
[24] W.A. da Silva et al., "Feasibility of manufacturing disposable cups using PLA/PCL composites reinforced with wood powder", *J. Polym. Enviro.*, 29 (2021) 2932-2951.
[25] B.M. Al-Shabander, A.A. Mohammed and H.I. Jaffer, "Effect of Fiber Volume on The Flexural Strenght of Steel Fiber Reinfored Polyester Resin Composite", *Iraqi J. Sci.*, 54(1) (2013) 105-109.
[26] C. Swaroop and M. Shukla, "Mechanical, optical and antibacterial properties of polylactic acid/polyethylene glycol films reinforced with MgO nanoparticles", *Mater. Today: Proc.*, 5(9) (2018) 20711-20718.
[27] B. Joseph et al., "Processing and evaluation of the structure-properties of electrospun PCL/zirconium nanoparticle scaffolds", *Mater. Today Commun.*, 34 (2023) 104961.
[28] C. Swaroop and M. Shukla, "Development of blown polylactic acid-MgO nanocomposite films for food packaging", *Compos. A: Appl. Sci. Manufact.*, 124 (2019) 105482.
[29] M.I. Mohammed, "Controlling the optical properties and analyzing mechanical, dielectric characteristics of MgO doped (PVA–PVP) blend by altering the doping content for multifunctional microelectronic devices", *Opt. Mater.*, 133 (2022) 112916.
[30] I.M. Ali, A.A. Mohammed and A.H. Ajil, "A study of the characterization of CdS/PMMA

nanocomposite thin film", *Iraqi J. Phys.*, 14(29) (2016) 191-197.

[31] N.A. Ali, "Zinc oxide on Polymethyl Methacrylate prepared by Pulsed Laser Deposition in Artistic and Aesthetic application", *Egyptian J. Chem.*, 64(9) (2021) 4791-4795.

[32] A. Khalil et al., "Study UV-visible and FTIR Characterization of ZnPc Dye using double solvent", *J. Global Pharma. Technol.*, 12(6) (2020) 210-216.

Table (1) Mechanical properties of bioblend PLA/PCL with nanoparticles

Sample	Tensile strength (MPa)	Elongation (%)	E-Modulus (MPa)	Tear/Thickness (mN/mm)
Pure	31.09	74.9	701	11.4113
ZrO_2 (0.75)	34	87	796	12.3084
ZrO_2 (1.5)	37	122.3	1041	13.5941
ZrO_2 (2.25)	41.75	129	1358	15.9305
MgO (0.75)	33.5	86.12	887	11.8244
MgO (1.5)	36	248.6	1098	13.4434
MgO (2.25)	42.25	168.6	1689	15.4543

Photoresponse Characteristics of Ppy/Ag_2O Nanocomposites Synthesized by Hydrothermal Method

Zainab S. Ali [1,2]
Najat A. Dahham [2]

[1] *Department of Physics, College of Science, University of Tikrit, Tikrit, IRAQ*
[2] *Department of Physics, College of Education, Tuzkhurmatu, University of Tikrit, Tuzkhurmatu, IRAQ*

Polypyrrole (Ppy) and Ppy/silver oxide (Ag_2O) nanoparticles (NPs) have been synthesized utilizing hydrothermal method. Then, the pure Ppy and its nanocomposites films with various volume percentages of Ag_2O (10, 30 and 50 vol.%) films were deposited successfully using drop-coat method on glass and Si substrate. The morphology, structural and optical properties of the as-prepared films were measured and characterized utilizing FE-SEM/EDX, XRD, FTIR, and UV. further, these Ppy/Ag_2O nanocomposites were tested to study their influence of Photoresponse properties The photo-detector fabricated employing the Ppy/ Ag_2O-50% showed a good photo-sensitivity of 265.45% and a high responsivity of 243.33 mA/W under the light (532 nm) illumination at bias voltage 5 volt with the rise/decay times of 0.81 sec and 0.85 sec, respectively. The obtained results are proposing that the Ppy/ Ag_2O nanocomposite is a promising material for optoelectronic applications.

Keywords: Ppy/Ag_2O; Hydrothermal method; Drop casting; Photoresponse
Received: 17 January 2024; **Revised:** 15 February, **Accepted:** 22 February 2024

1. Introduction

In today's world, there is a high request for developed opto-electronic devices for everyday life, research organizations, industries, and education field, etc. [1-3]. As significant devices, photodetector (PDs) are fundamental tools in optoelectronic circuits and memory storage, as well as in light-wave communications, and high resolution imaging methods [4]. In the last few years, aromatic conducting polymers (CP) , particularly electro-active polymers, have gotten much explore thought for utilize as advance materials due to their special physical characteristics, However, Conducting polymers, excite an wide interest among researchers due to their interesting optical, electronic, magnetic properties[5-7]. The detection of conducting polymers led to their wide range of applications are in photo-detectors , batteries , solar cells, acoustic wave devices, , nano-generator, UV-nanolaser, varistors, etc. [8]. Among conductive polymers, Polypyrrole (PPy), is one of most extensively investigated polymers, possessing a wide potential application due to its facile, low-cost synthesis, thermal and air stability, good environmental stability, high conductivity [9-11]. In recent years, various types of photo-sensors have been developed by mixing inorganic nano-materials (semi-conductor type) with Conducting polymer, such as PPy/semiconductor -based nano-composites photodetectors, Ppy/TiO_2 [12], Ppy/WO_3 [13], Ppy/CdS [14] Ppy/SnO_2 , etc [15]. silver oxide (Ag_2O) as a perfect p-type has narrow band gap (1.2eV) semiconductor material, is a suitable candidate [16]. Recently, Ag_2O nano-particles have received great attention because of their use for most industrial applications such as for photodetector, photovoltaic cells, storage devices, photodiodes, antibacterial coatings and so on [17]. Here, the advantage of this work is the synthesis of Ppy/Ag_2O nanocomposites for photo-sensing application. The optical, morphological, structural, and photoresponse properties of prepared thin films of Ppy nanotubes and Ppy/Ag_2O nanocomposites have been investigated.

2. Experimental:

Pure Ppy was synthesized employed by hydrothermal method. In this procedure, 0.167g of pyrrole solution and 0.041g of methyl orange acid were dissolved in 50 ml of DI water. Then, 0.675 g of iron (III) chloride was dispersed in 50 ml of DI water and then added it into the above solution with continuous stirring for 10 min in RT. After that, this mixture was transferred into a Teflon lined (autoclave) with heated for 5 h at 150 °C. Then precipitated solution was filtered and the remains obtained was washed several times by DI water and ethanol, alternatively. Further, the definitive product was dried for 3 h in the oven at 70 °C to get Ppy powder. The Ppy powder was dispersed in 15 ml of ethanol utilized the ultrasonic curing for 3 h and it's deposited via drop-casting technique on cleaned glass and Si substrate to make of Ppy thin film.

Ag_2O NPs was synthesized utilized via hydrothermal method. In this step, 0.849 g of silver nitrate was dissolved in 50 ml of DI water. Thereafter, 50 mL of a sodium hydroxide (0.5M) aqueous solution was added drop-wise, with continuous

stirring for 10 min in RT. Then, the mixture solution was moved into a Teflon lined (autoclave) with heated for 5 h at 150 °C. After that, precipitated solution was filtered and the remains obtained was washed several times by DI water and ethanol, alternatively. Further, the definitive product was dried for 3 h in the oven at 100 °C to get Ag_2O NPs. The Ag_2O powder was dispersed in 15 ml of ethanol utilized the ultrasonic curing for 3 h and it's mixed with Ppy solution to form Ppy /Ag_2O Nano-composites with various volume percentages of Ag_2O (10,30 and 50Vol.%), and deposited successfully using drop-coating method on glass and Si substrate to form of Ppy /Ag_2O thin films and labeled as PA-10, PA-30 and PA-50 respectively. The prepared films were examined using Fourier transform-infrared spectroscopy (FT-IR), X-ray diffraction (XRD) Field emission-scanning electron microscopy (FE-SEM), Energy-dispersive X-ray spectroscopy (EDX) and optical spectroscopy. For photodetector measurements, two Al electrodes were thermally-evaporated onto a thin film. the current–voltage (I–V) measurements and visible photo-response were recorded under laser light (532 nm) of power density 5 mW/cm^2 employing Source Measure Unit (UT81B).

3. Results and Discussion

The structural investigations of Ppy /Ag_2O thin films were performed by X-ray diffraction and the obtained results were compared with that of PPy film. XRD plot of pure Ppy and Ppy /Ag_2O films with 10, 30 and 50 Vol% of Ag_2O NPs was showed in Fig. 1. For Ppy film, it is clearly noted that the existence of wide peak at 2θ = 22°, referencing the amorphous nature of the polymer. The wide peak produces by X-ray scattering of Ppy chain [18]. in the state of Ppy/Ag_2O thin films, The sharp peaks of Ag_2O NPs were discovered at 2θ=26°, 32°,38°,44°,55°,57°,64°,68°and 77°, which are assigned to the diffraction from (110), (111), (200), (211), (220), (221), (311), (222), and (123) planes of Cubic Ag_2O [19-20]. These peaks are agreed with the JCPDS card no. 76-1393 for Cubic Ag_2O. The difference in average crystallite size of the as-prepared samples were calculated with utilizing Scherer's relation [21]

$$D_{av} = \frac{0.9\,\lambda}{\beta \cos\theta} \qquad (1)$$

where λ is X-ray wavelength(Cu Kα-1.54056 Aº), θ is the diffraction angle, and β is full-width at half-maxima respectively. The measurements showed that the values of average size for PA-10, PA-30 and PA-50 nanocomposites are 35, 37 and 41 nm respectively.

The characteristics of the FTIR spectroscopy for Ppy and their nanocomposites films are demonstrated in the Fig. 2. The main peaks for pure Ppy were observed at 1543, 1483, 1319, 1184, 1037, 964, and 918 cm^{-1}. The peaks at 1543 and 1483cm^{-1} may be ascribed to the C-C and C-N stretching-vibrations in the pyrrole rings, respectively [22]. The band assigned at 1319 cm^{-1} was related of C–H or C–N in-plane deformation modes [23], while the peaks at 1184 and 1037cm^{-1} were related to the breathing-vibrations of the pyrrole rings[24]. In also, the peak related at 964 cm^{-1} correspond to the C–H and N–H in-plane deformation-vibrations [25]. The out-plane bending-vibration of the C-H is assigned at about 918 cm^{-1}[26]. However, some changes of characteristic peaks are observed in Ppy-Ag_2O samples. This shift can be occurred due to the incorporation of Ag_2O within the Ppy structure.

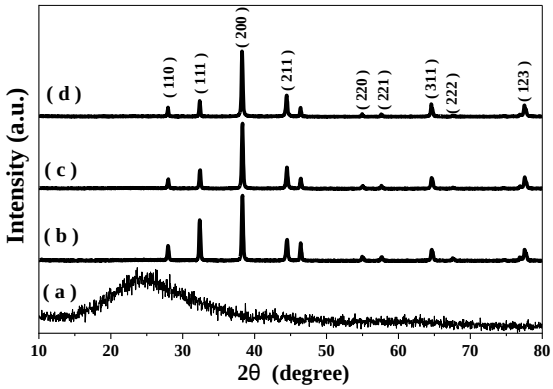

Fig. (1) XRD patterns of (a) Ppy, (b) PA-10, (c) PA-30 and (d) PA-50

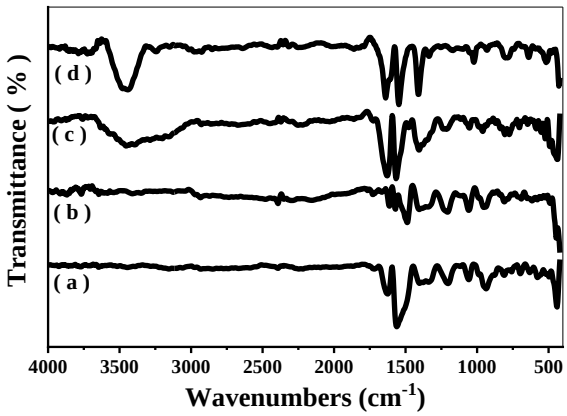

Fig. (2) FTIR spectra of (a) Ppy, (b) PA-10, (c) PA-30 and (d) PA-50

Figure (3) displays the FE-SEM pictures of Ppy and Ppy /Ag_2O nanocomposites films. The FE-SEM picture of pure PANI has a mixture of nanotubular morphology with some irregular globular. Dye-free polypyrrole possess a characteristic spherical shape. However, the presence of Methyl Orange into the polymerization medium leaded to the formation of nanotubular morphology having average particle diameter approximately 100–200 nm, because it works as a morphology-directing factor [27]. The FESEM pictures of Ppy /Ag_2O nanocomposites films Fig. 3(b) to (d) confirmed that Ag_2O NPs were implanted almost fully in the polymer form with average particle diameters approximately 200–400 nm, confirming the preparation of nano-composites, and it's observed that improvement in the

incorporation of Ag_2O NPs to the Ppy form with increasing concentration of Ag_2O. Thus, the outcomes obtained from FESEM analyses which would ease good electrical-conductivity [28].

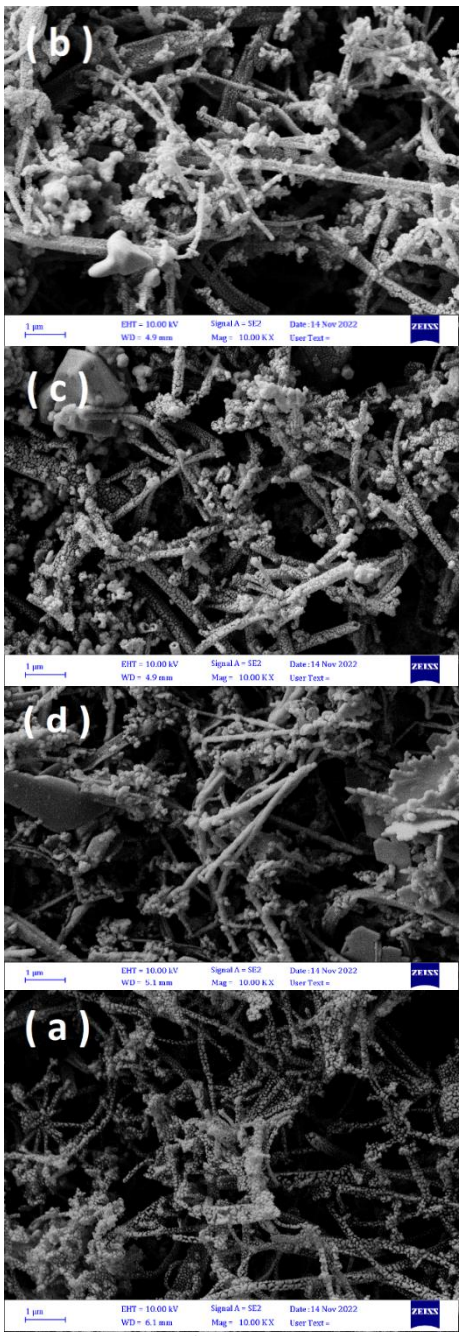

Fig. (3) FE-SEM images of (a) Ppy, (b) PA-10, (c) PA-30 and (d) PA-50

In addition, an elemental analysis of all films was tested via EDX analysis. Figure (4) displays the EDX image of the as-deposited films that confirms the presence of S, C and N in the Ppy film, and also it revealed the existence of Ag and O elements in Ppy/Ag_2O nanocomposites films. The existence of sulfur(S) confirms that MO was integrated in films [29]. The outcomes obtained that confirms in the incorporation of Ag_2O NPs in polymer structure without forming any impurities.

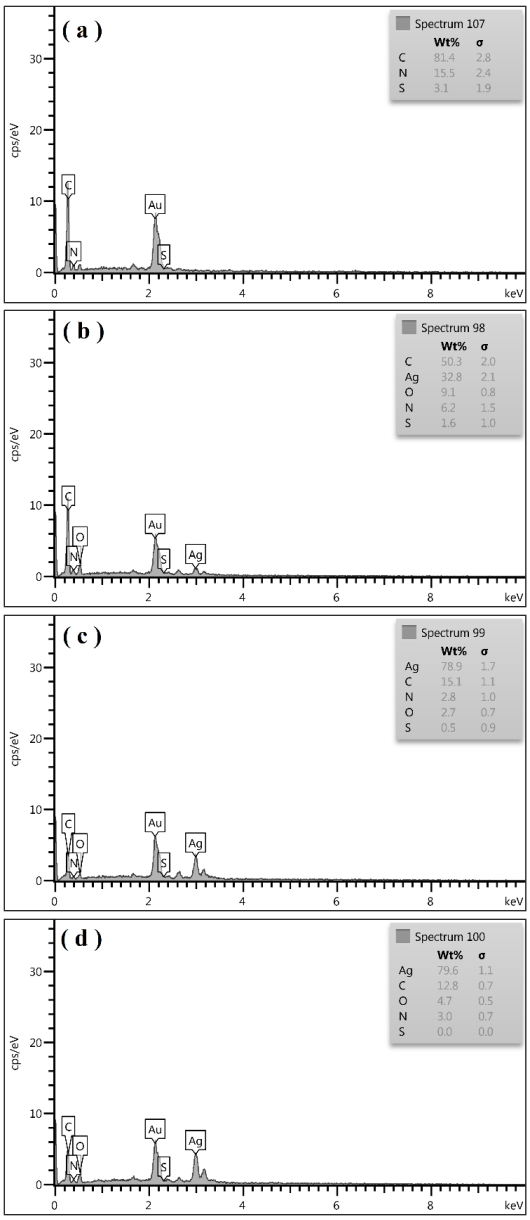

Fig. (4) EDX images of (a) Ppy, (b) PA-10, (c) PA-30 and (d) PA-50

In order that discuss the optical properties of all samples, the UV–Visible absorption spectra and (αhv)2 with hv plots are displayed in Fig. 5 and 6. As is obvious from Fig. 5, the absorbance spectra of Ppy film showed absorption peak at 463 nm associated as being a π–π* transition, with the bi-polaron peak at 970 nm. Compared by Pure Ppy, the nanocomposites films exhibits the π–π* peak is expanded, and red shifted due to the incorporation of Ag_2O NPs in polymer structure with increasing concentration of Ag_2O and also, the bi-polaron peak is expanded, that indicates a change in the conjugation length [30-32].

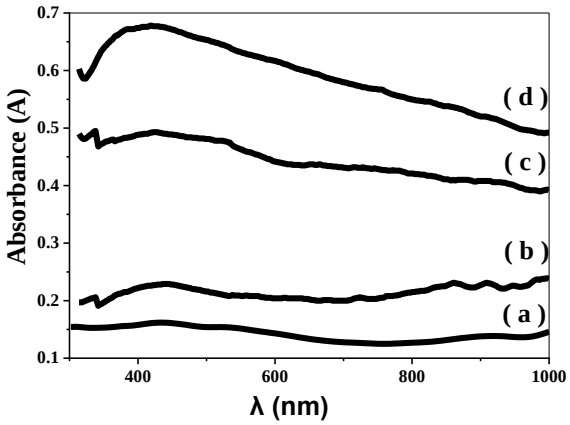

Fig. (5) Absorption spectra of (a) Ppy, (b) PA-10, (c) PA-30 and (d) PA-50

The direct band gap (Eg) of the as-prepared films were obtained by the following relation [33]:

$$(\alpha h\upsilon) = A(h\upsilon - Eg)^{\frac{1}{2}} \quad (2)$$

where A, α, ν and h indicate for the constant

A gradual fall of E_g value from 1.63 to 1.46 eV is observed with adding Ag_2O NPs as illustrated in Fig. (6). This decrease in E_g may be due to the increasing in the crystallite size, with increase in Ag_2O NPs.

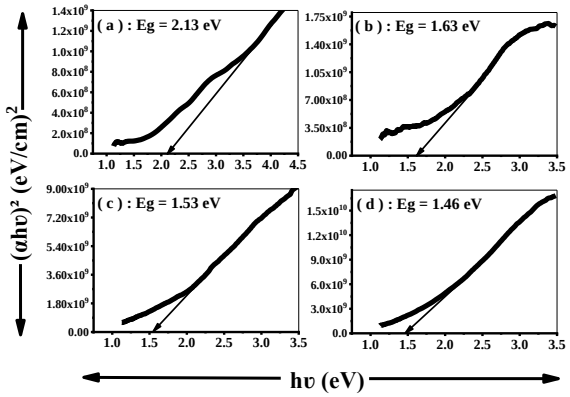

Fig. (6) Plots of $(\alpha h\upsilon)^2$ with $h\upsilon$ for (a) Ppy, (b) PA-10, (c) PA-30 and (d) PA-50

The current-voltage (I-V) test of as-fabricated photodetectors were studied in the existence and non-existence of laser light (532 nm) of power density of 5 mW/cm^2 for the potential range between 5V and –5V. Figure (7) displays the I-V plots of the devices measured under dark and visible-light of 5 mW/cm^2 intensity. In light state the value of photocurrent increases significantly when compared to the dark state, due to the generation of an electron-hole pair under illumination.

Figure (8) shows that the Photo-current verses time of all photo-detector. Obviously, all films display higher photocurrent compared to the corresponding dark current under the existence of illumination, which implies the generation of phot-induced electron-hole pair in the films.

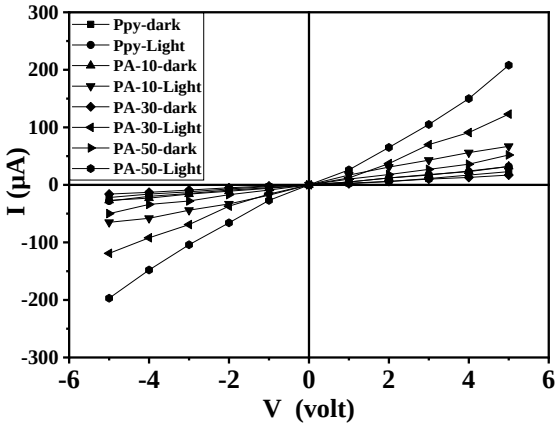

Fig. (7) I-V characteristics of as-fabricated photodetectors

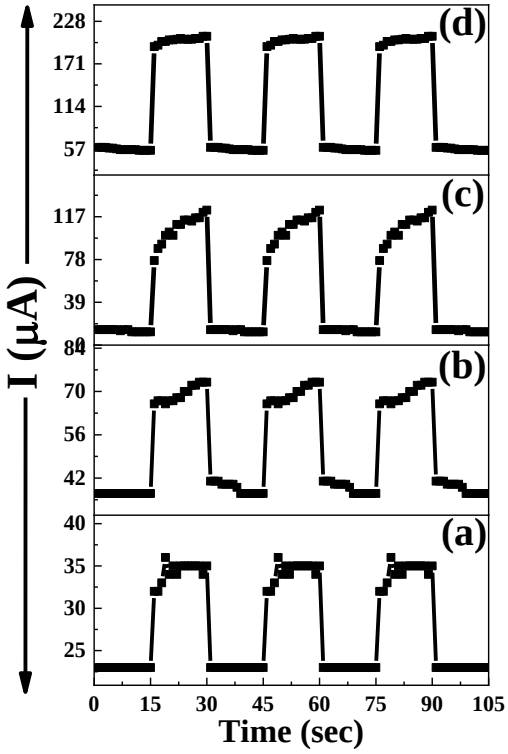

Fig. (8) Variation of photo-current with time for (a) Ppy, (b) PA-10, (c) PA-30 and (d) PA-50.

The three parameters, i.e., sensitivity (S), responsivity (R), and specific detectivity (D*), of the photodetectors are evaluated by the relations [34]:

$$S(\%) = \frac{I_{ph}}{I_{dark}} \times 100 \quad (3)$$

$$R = \frac{I_{ph}}{A.P} \quad (4)$$

$$D = \frac{R.A^{1/2}}{(2 \times e \times I_{dark})^{1/2}} \times 100 \quad (5)$$

where I_{ph} is the photocurrent (I_{ph}=I_{light}−I_{dark}), P is the power of light, A is lighting area and e is electronic-charge

The estimated photodetectors parameters are tabulated in table (1). The as-fabricated device of pure Ppy display a sensitivity of 39.13%, R of 15 mA/W and detectivity of 1.92×10^9 Jones for the illumination intensity of 5 mW/cm^2. The as-fabricated device based on PA-50 exhibits sensitivity as high as,

265.45%, R of 243.33 mA/W and detectivity of 20.09×10^9 Jones. Clearly, the performance of PA-(10, 30 and 50) device enhanced several times with compared to pure Ppy. A compare of the photo-detector performance of the current paper with past photodetectors for Ppy/ metal oxide nanostructures are displayed in table (1). Obviously, these results that the performance of Ppy/Ag_2O photodetector is excellent in several asides of previously reported papers.

The rise time and decay time of as-fabricated photodetectors were evaluated for 1 cycle from Fig. (8). The rise time and fall time of Ppy, PA-10, PA-30 and PA-50 photodetectors are (0.88, 0.85, 1.51 and 0.85 s) and (0.8, 0.83, 0.79 and 0.81 s) respectively. The values of rise/decay time are less than 2 s. Comparison of rise /decay times of as-fabricated photodetectors with other previous works are tabulated in Table 1. From the results, it is shown that Ppy/$Ag_2$0 nanocomposite are a promising component for next-generation visible-light photodetection devices.

4. Conclusions

In this article, Polypyrrole NTs and Ag_2O NPs have been successfully prepared employing hydrothermal method, Also, it studied the effect of adding Ag_2O NPs with different mixing ratios (10, 30, and 50 vol.%) on the physical properties of Ppy thin films prepared employing drop-casting. The XRD analysis displayed the amorphous structure of Ppy film and the formation of cubic structure of Ppy /Ag_2O films. FE-SEM analysis showed the nanocrystalline nature by formation of a mixture of nanotubular and globular morphology. The improvement in the direct band-gap value from 2.13 eV for pure Ppy to 1.46 eV for Ppy/Ag_2O-50%. The photo-detector fabricated of Ppy/Ag_2O-50% showed a good photo-sensitivity of 265.45% and high responsivity of 243.33 mA/W at 5 V applied bias with rise time and decay times < 2s.

References

[1] I.L.P. Raj et al., "Enhancement of photo-sensing properties of CdS thin films by changing spray solution volume", *Sens. Actuat. A: Phys.*, 315 (2020) 112306.

[2] C.M. Lieber, "Nanoscale science and technology: building a big future from small things", *MRS Bull.*, 28(7) (2003) 486-491.

[3] Y. Jung, D.K. Ko and R. Agarwal, "Synthesis and structural characterization of single-crystalline branched nanowire heterostructures", *Nano Lett.*, 7(2) (2007) 264-268.

[4] T. Zhai et al., "Fabrication of high-quality In_2Se_3 nanowire arrays toward high-performance visible-light photodetectors", *ACS Nano*, 4(3) (2010)1596-1602.

[5] B.H. Kim et al., "Synthesis, characteristics, and field emission of doped and de-doped polypyrrole, polyaniline, poly (3,4-ethylenedioxythiophene) nanotubes and nanowires", *Synth. Met.*, 150(3) (2005) 279-284.

[6] M.R. Mahmoudian, Y. Alias and W.J. Basirun, "Electrodeposition of (pyrrole-co-phenol) on steel surfaces in mixed electrolytes of oxalic acid and DBSA", *Mater. Chem. Phys.*, 124(2-3) (2010) 1022-1028.

[7] A. Asan, M. Kabasakaloglu and M.L. Aksu, "The role of oxalate ions in the coverage of mild steel with polypyrrole", *Russian J. Electrochem.*, 41(2) (2005) 154-158.

[8] F. Kanwal et al., "Synthesis of polypyrrole–ferric oxide (Ppy–Fe_2O_3) composites and study of their structural and conducting properties", *Synth. Met.*, 161(3-4) (2011) 335-339.

[9] Y. Li et al., "Polypyrrole prepared in the presence of methyl orange and ethyl orange: nanotubes versus globules in conductivity enhancement", *J. Mater. Chem. C*, 5(17) (2017) 4236-4245.

[10] J. Huang et al., "Ultrasound assisted polymerization for synthesis of ZnO/Polypyrrole composites for zinc/nickel rechargeable battery", *J. Power Sourc.*, 271 (2014) 143-151.

[11] E. Alekseeva et al., "The composites of silver with globular or nanotubular polypyrrole: the control of silver content", *Synth. Met.*, 209 (2015) 105-111.

[12] W. Zheng et al., "Fabrication of a visible light detector based on a coaxial polypyrrole/TiO_2 nanorod heterojunction", *RSC Adv.*, 4(85) (2014) 44868-44871.

[13] B. Gowtham et al., "Upliftment the rectification behavior of PPy-WO_3 nanocomposites for photodetector applications", *Inorg. Chem. Commun.*, 135 (2022) 109105.

[14] M. Amiri and N. Alizadeh, "Mid-infrared photoconductivity of polypyrrole doped with cadmium sulfide quantum dots", *J. Phys. Chem. Solids*, 141 (2020) 109383.

[15] S. Fu et al., "Deep Ultraviolet Photodetector with Ultrahigh Responsivity based on a Nitrogen-Doped Graphene-Modified Polypyrrole/SnO_2 Organic/Inorganic p–n Heterojunction", *Adv. Mater. Interfac.*, 10 (2023) 2202488.

[16] A.C. Nwanya et al., "Structural and optical properties of chemical bath deposited silver oxide thin films: Role of deposition time", *Adv. Mater. Sci. Eng.*, 2013 (2013) 1-8.

[17] A. Umar et al., "Enhanced NO_2 gas sensor device based on supramolecularly assembled polyaniline/silver oxide/graphene oxide composites", *Ceram. Int.*, 47(18) (2021) 25696-25707.

[18] A. Elahi et al., "Polypyrrole and its nanocomposites with $Zn_{0.5}Ni_{0.4}Cr_{0.1}Fe_2O_4$ ferrite: preparation and electromagnetic properties", *J. Mater. Sci.: Mater. Electron.*, 27 (2016) 6964-6973.

[19] J. Fowsiya and G. Madhumitha, "Biomolecules derived from Carissa edulis for the microwave assisted synthesis of Ag_2O nanoparticles: A study against *S. incertulas*, *C. medinalis* and *S. Mauritia*", *J. Cluster Sci.*, 30 (2019) 1243-1252.

[20] A. Ananth, R.H. Jeong and J.H. Boo, "Preparation, characterization and CO oxidation performance of Ag_2O/γ-Al_2O_3 and (Ag_2O+ RuO_2)/γ-Al_2O_3 catalysts", *Surfaces*, 3(2) (2020) 251-264.

[21] B.D. Cullity, **"Elements of X-ray Diffraction"**, Addison-Wesley Publishing (Boston, 1956), Ch. 9, p. 259.

[22] R. Moučka et al., "One-dimensional nanostructures of polypyrrole for shielding of electromagnetic interference in the microwave region", *Int. J. Mol. Sci.*, 21(22) (2020) 8814.
[23] J. Stejskal et al., "Polypyrrole salts and bases: superior conductivity of nanotubes and their stability towards the loss of conductivity by deprotonation", *RSC Adv.*, 6(91) (2016) 88382-88391.
[24] J. Kopecká et al., "Polypyrrole nanotubes: mechanism of formation", *RSC Adv.*, 4(4) (2014) 1551-1558.
[25] A. Munteanu et al., "Bidisperse magnetorheological fluids utilizing composite polypyrrole nanotubes/magnetite nanoparticles and carbonyl iron microspheres", *Rheologica Acta*, 62(9) (2023) 461-472.
[26] D. Kopecký et al., "Optimization routes for high electrical conductivity of polypyrrole nanotubes prepared in presence of methyl orange", *Synth. Met.*, 230 (2017) 89-96.
[27] M. Varga et al., "The ageing of polypyrrole nanotubes synthesized with methyl orange", *Euro. Polym. J.*, 96 (2017) 176-189.
[28] I. Sapurina et al., "Polypyrrole nanotubes: the tuning of morphology and conductivity", *Polymer*, 113 (2017) 247-258.
[29] Y. Li et al., "Polypyrrole prepared in the presence of methyl orange and ethyl orange: nanotubes versus globules in conductivity enhancement", *J. Mater. Chem. C*, 5(17) (2017) 4236-4245.
[30] Y. Liu et al., "Preparation of PPy/TiO_2 core-shell nanorods film and its photocathodic protection for 304 stainless steel under visible light", *Mater. Res. Bull.*, 124 (2020) 110751.
[31] M. Rahaman et al., "Chemical and electrochemical synthesis of polypyrrole using carrageenan as a dopant: Polypyrrole/MWCNT nanocomposites", *Polymers*, 10(6) (2018) 632.
[32] M. Trchová and J. Stejskal, "Resonance Raman spectroscopy of conducting polypyrrole nanotubes: disordered surface versus ordered body", *J. Phys. Chem. A*, 122(48) (2018) 9298-9306.
[33] O. Stenz, **"The Physics of Thin Film Optical Spectra"**, Springer (2005), Ch. 6, p. 301.
[34] S. Pyshkin and J. Ballato, **"Optoelectronics: Advanced Device Structures"**, BoD–Books on Demand .l, (2017), Ch. 12, p.257.
[35] S.K. Singh and R.K. Shukla, "Optical and photoconductivity properties of pure Polypyrrole and titanium dioxide-doped Polypyrrole nanocomposites", *Mater. Sci. Semicond. Process.*, 31 (2015) 245-250.
[36] L. Zheng et al., "Scalable-production, self-powered TiO_2 nanowell–organic hybrid UV photodetectors with tunable performances", *ACS Appl. Mater. Interfaces*, 8(49) (2016) 33924-33932.
[37] H. Chen et al., "Ultrasensitive self-powered solar-blind deep-ultraviolet photodetector based on all-solid-state polyaniline/MgZnO bilayer", *Small*, 12(42) (2016) 5809-5816.
[38] M. Amiri and N. Alizadeh, "Highly photosensitive near infrared photodetector based on polypyrrole nanoparticle incorporated with CdS quantum dots", *Mater. Sci. Semicond. Process.*, 111 (2020) 104964.
[39] O.A. Kareem, I.M. Ibrahim and S.J. Mohameed, "Optimizing the optical response of polypyrrol nanofibers by decoration with ZnO nanoparticles", *AIP Conf. Proc.*, 2400(1) (2022) 030008.
[40] A.M. Elsayed et al., "Highly Uniform Spherical MoO_2-MoO_3/Polypyrrole Core-Shell Nanocomposite as an Optoelectronic Photodetector in UV, Vis, and IR Domains", *Micromachines*, 14(9) (2023) 1694.
[41] A. Ben Gouider Trabelsi et al., "Photodetector-Based Material from a Highly Sensitive Free-Standing Graphene Oxide/Polypyrrole Nanocomposite", *Coatings*, 13(7) (2023) 1198.
[42] M. Rabia et al., "Porous-Spherical Cr_2O_3-Cr (OH) 3-Polypyrrole/Polypyrrole Nanocomposite Thin-Film Photodetector and Solar Cell Applications", *Coatings*, 13(7) (2023) 1240.

Table (1) The Photodetector parameters of Ppy and Ppy/Ag_2O nanocomposites thin films when compared to other previous works

Photodetector	Wavelength (nm)	Bias (V)	S (%)	R (mA/W)	D (Jones)	Rise Time (s)	Fall Time (s)	Refs
Ppy/TiO_2	365	-	1.17	-	-	273	253	[35]
Polyaniline/ TiO_2	320	5	-	3×10^{-3}	-	-	-	[36]
Polyaniline/ MgZnO	250	5	-	0.1	-	-	-	[37]
Ppy/CdS	850	10	120	3.8	2.1×10^{16}	-	-	[38]
Ppy/ZnO	720	-	167.4	-	-	2.5	3	[39]
Ppy/ MoO_2, MoO_3	540	2	-	4	5.85×10^{8}	-	-	[40]
Ppy/GO	540	2	-	0.31	6.9×10^{7}	-	-	[41]
Ppy/Cr_2O_3	540	3	-	0.0143	3.21×10^{6}	-	-	[42]
Ppy	532	5		39.13	15	0.8	0.88	This work
PA-10				83.78	51.67	0.83	0.85	
PA-30				733.33	146.67	0.79	1.51	
PA-50				265.45	243.33	0.81	0.85	

Doha M. Challoob [1]
Mohammed Y. Khdiar [1]
Oday A. Hammadi [2]

[1] *Department of Biology, College of Education, Al-Iraqia University, Baghdad, IRAQ*
[2] *Department of Physics, College of Education, Al-Iraqia University, Baghdad, IRAQ*

Highly-Pure Titanium Dioxide nanopowders Synthesized by Eco-Friendly Solvothermal Method

In this study, titanium dioxide nanopowders were synthesized by solvothermal method using banana peels as a source for plant extract and titanium isopropoxide as a precursor. The structural characteristics confirmed that the synthesized nanopowders have tetragonal crystalline structure containing both anatase and rutile phases of titanium dioxide. These nanopowders showed high structural purity as no materials other than titanium dioxide was found according to the x-ray diffraction (XRD) patterns and Fourier-transform infrared (FTIR) spectroscopy. As well, no elements other than titanium and oxygen were found according to the energy-dispersive x-ray spectroscopy (EDX). The minimum particle size in the synthesized samples was 53.48nm. The spectroscopic characteristics showed that the prepared nanopowders have reasonable absorption in the UV region of electromagnetic spectrum (<375nm) and very low absorption in the visible region. The solvothermal method used in this work can be described by low complexity, simple assembly, low cost and high purity production.

Keywords: Titanium dioxide; Nanoparticles; Solvothermal method; Green synthesis
Received: 13 January 2024; **Revised:** 19 February, **Accepted:** 26 February 2024

1. Introduction

Nanomaterials are at the leading edge of the rapidly developing field of nanotechnology. Their unique size-dependent properties make these materials superior and indispensable in many areas of human activity [1]. Nanomaterials could be defined as a set of materials where at least one dimension is less than approximately 100 nanometers [2]. Nanomaterials are of interest because at this scale, unique optical, magnetic, electrical, and other properties emerge. These properties have the potential for reasonable impacts in photonics, electronics, medicine, and many other fields [2]. Two approaches; bottom–up and top–down, are generally used to synthesize the nanopowders. The bulk materials are divided into small particles by top–down methods. Small particles are aggregates and form nanoscale range crystals throughout bottom–up methods [3]. Top-down methods include high-energy wet ball milling, electron beam lithography, atomic force manipulation, gas-phase condensation, aerosol spray, etc. [4]. The bottom–up approach starts from the atomic level and leads to the formation of nanostructures with further self-assembly of the atoms/molecules, whose growth and self-assembly as building blocks leads to the formation of nanomaterials with well-defined size, morphology, and chemical composition. This approach includes chemical, physical and biological methods [5,6]. Chemical methods often allow synthesis of nanoparticles in large quantities. Moreover the possibility of controlling particle size even at nanometer scale is also possible during chemical synthesis of nanoparticles [7]. The chemical methods include oraganometallic chemical route, revere-micelle route, sol-gel synthesis, colloidal precipitation, and hydrothermal synthesis. Physical route or mechanism includes different methods, e.g., gas-phase deposition, electron beam lithography, pulsed-laser deposition or ablation, laser-induced pyrolysis, powder ball milling, reactive sputtering, thermal evaporation, electrodeposition, and aerosol [6]. The biological route includes different methods, e.g., fungi mediated, algae, bacteria mediated, yeast mediated, etc. Nanoparticles made by a biogenic enzymatic process are significantly superior to those made by chemical methods in various aspects. Even though the latter methods can produce large quantities of nanoparticles with a defined size and shape during short time, they are complicated, outdated, expensive, and inefficient, and they generate hazardous toxic wastes that are harmful not only to the environment but also to human health [6] .

Among the many semiconductor materials, titanium dioxide or titania (TiO_2) has been regarded as one of the most relevant for photocatalytic purposes, owing to its exceptional optical and electronic properties. Its high level of photoconductivity, ready availability, low toxicity, inertness (biologically and chemically) and low cost, resistance to photocorrosion, high photocatalytic activity, and biological compatibility [8]. However, the effectiveness of TiO_2 as photocatalyst depends on its crystal phase, impurities, particle size, surface area, crystallinity and other physicochemical parameters that strongly influence charge recombination and electron/hole trapping [9].

Green synthesis employs a clean, safe, cost effective and environmentally friendly process of synthesizing nanomaterials. Microorganisms such as bacteria, yeast, fungi, algae species and certain plants act as substrates for the green synthesis of nanomaterials [10]. Molecules in plants and microorganisms, such as proteins, enzymes, phenolic

compounds, amines, alkaloids and pigments perform nanoparticle synthesis by reduction [11-17]. The plant extracts including leaves, roots, flowers, and parks are said to contain many secondary metabolites which act as reducing, stabilizing, and capping agents for the bioreduction reactions in the synthesis of nanomaterials [18-21].

In traditional chemical and physical methods; reducing agents involved in the reduction of metal ions, and stabilizing agents used to prevent undesired agglomeration of the produced nanoparticles carry a risk of toxicity to the environment and to the cell. Besides, the contents of the produced nanoparticles are thought to be toxic in terms of shape, size and surface chemistry. In the green synthesis method in which nanoparticles with biocompatibility are produced, these agents are naturally present in the employed biological organisms [22].

In this work, titanium dioxide nanopowders were synthesized by an eco-friendly solvothermal method using a plant extract (banana peels) and titanium isopropoxide as a precursor. The structural and spectroscopic characteristics of the synthesized nanopowders were determined.

2. Experimental Part

The banana peels and titanium isopropoxide were used as a reference for the plant extract and precursors, respectively. Fresh bananas were taken from the local market and banana peels were cut into small pieces, washed three times with distilled water to remove any contaminants and excrement and dried with drying paper. Then, an 80g of the dried peels were put in a beaker containing 150 mL of deionized water. The mixture was heated up to boiling temperature (100°C) for 20 min. Then, the boiled mixture was filtered twice using filter paper (Whatman No. 1).

An aqueous solution was prepared by solving 1ml of titanium isopropoxide ($C_{12}H_{28}O_4Ti$) in 10ml of deionized water. The aqueous solution is placed on the hotplate stirrer (40°C) for 10 min. Then, 50 ml of the extracted solution of banana peels was added to the aqueous solution as drops while keeping stirring for one hour. The mixture was filtered twice using filter paper (Whatman No. 1) to separate the formed nanopowder. These filtered nanopowder were washed twice with distilled water to remove any residuals from the previous mixing process and reaction step. The separated nanopowder was dried by heating up to 100 °C for 24 hours and bleaching by using (KOH) to remove organic residues stuck on the nanopowders during the preparation process. Figure (1) shows schematically the experimental procedure.

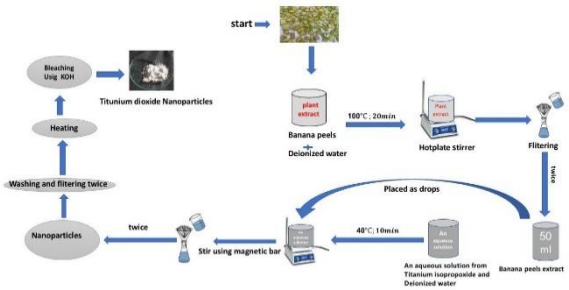

Fig. (1) The experimental procedure used in this work to synthesize TiO_2 nanopowder

The structural characteristics of the synthesized nanopowders were determined by x-ray diffraction (XRD) patterns using a Bruker D2 PHASER XRD system (Cu-Kα x-ray tube with λ=1.54056Å), the surface morphology was determined by an Inspect F50 field-emission scanning electron microscope (FE-SEM), the elemental constitution was determined by energy-dispersive x-ray spectroscopy (EDX), the formation of molecular bonds and their vibrations were determined by Fourier-transform infrared (FTIR) spectroscopy using a SHIMADZU FTIR-8400S instrument, and the absorption spectra were recorded using a K-MAC Spectra Academy SV2100 spectrophotometer in the range of 300-800 nm as the synthesized nanopowder was immersed in a transparent viscous host as a reference.

3. Results and Discussion

Figure (2) shows a photograph of TiO_2 nanopowder sample synthesized in this work by solvothermal method and figure (3) shows the XRD pattern of this sample. Obviously, 21 peaks are seen, which belong all to the TiO_2; 15 of them for anatase (A) phase and 6 for rutile (R) phase. This is why the TiO_2 nanopowder referred to as mixed-phase and tetragonal crystalline structure [23,24]. The formation of rutile phase cannot be avoided even much more care is considered during the formation of nanopowder as heating steps are necessarily required. The crystallite size (D) was determined for all peaks, as shown in table (1), by Scherrer's equation as [24]:

$$D = \frac{0.9\lambda}{\beta cos\theta}$$

where λ is the wavelength of x-rays (1.54Å), 0.9 is a constant, β is the full width at half-maximum (FWHM), which was given by the software of the XRD instrument

Fig. (2) Photograph of TiO_2 nanopowder synthesized by solvothermal method

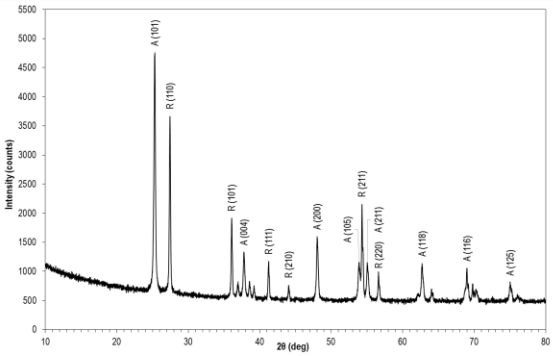

Fig. (3) XRD pattern of synthesized TiO_2 nanopowder

Table (1) Determination of crystallite size for the synthesized mixed-phase TiO_2 nanopowder

Peak no.	2θ (deg)	D (nm)	Phase
1	25.2723	1.23	A
2	27.4066	1.71	R
3	36.0501	1.91	A
4	36.9171	1.29	R
5	37.7662	1.22	A
6	38.5467	1.6	A
7	39.1683	1.85	A
8	41.2124	1.94	A
9	44.0255	2.05	R
10	48.016	1.32	R
11	53.8677	1.11	A
12	54.2986	2.11	R
13	55.0386	1.33	A
14	56.6053	18.6	R
15	62.681	1.23	A
16	64.0264	2.07	A
17	68.9473	1.21	A
18	69.7733	1.99	A
19	70.254	1.06	A
20	75.0219	1.19	A
21	76.0538	0.96	A

Figure (4) shows the FE-SEM image of TiO_2 nanopowder synthesized in this work. The nanopowder sample clearly contains different sizes and the smallest particle size is 53.48 nm, but the difference is not big enough. The sample is considered to be non-uniform. As well, aggregation is apparent, which is unavoidable in any preparation method or technique that includes formation processes based on thermally-activated chemical reactions [23].

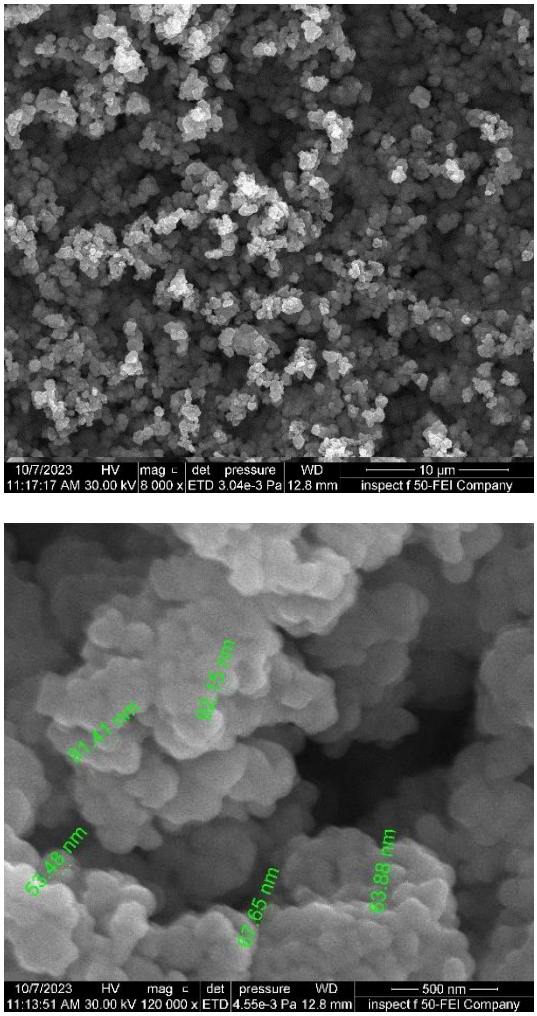

Fig. (4) FE-SEM images of synthesized TiO_2 nanopowder with two different magnification powers

Figure (5) shows the EDX results of the TiO_2 nanopowder synthesized in this work. The color mapping images (Fig. 3a) show that the volume density of Ti atoms is higher than that of O, which is confirmed by the elemental weight analysis (56.7% Ti vs 34.7% O). This can be attributed to the difference in atomic radius between titanium and oxygen. Furthermore, the atomic percentages of both elements (Ti and O) are comparable (29% and 53%, respectively). These results show that the synthesized nanopowder certainly contains stoichiometric TiO_2 compound.

Figure (6) shows the FTIR spectrum of the TiO_2 nanopowder synthesized in this work. There are three distinct peaks centered at 409, 447 and 667 cm^{-1} belonging to the vibrations of the TiO_2 molecules in the TiO_2 lattice; bending, asymmetric and symmetric modes, respectively [25]. As well, two bands at 1620 and 3450 cm^{-1} are clearly seen and they are attributed to the vibration modes of O-H bond. The two possible

sources for the OH molecules are (1) the aqueous solution included in the synthesis route, and (2) adsorption of water molecules from the environment when the synthesized sample is exposed to the atmosphere [24,26].

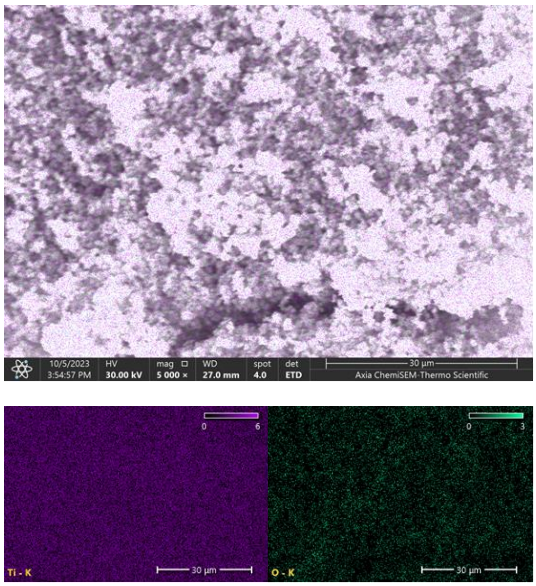

(a)

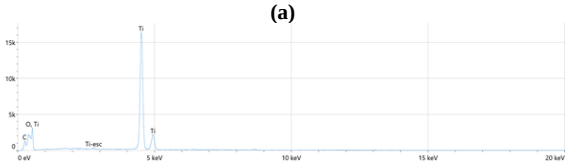

(b)

Element	Atomic %	Atomic % Error	Weight %	Weight % Error
O	53.2	1.9	34.7	1.2
Ti	29.0	0.1	56.7	0.2
C	17.7	0.4	8.7	0.2

Fig. (5) EDX result of synthesized TiO_2 nanopowder (a) color map distribution, (b) EDX spectrum and elemental analysis table

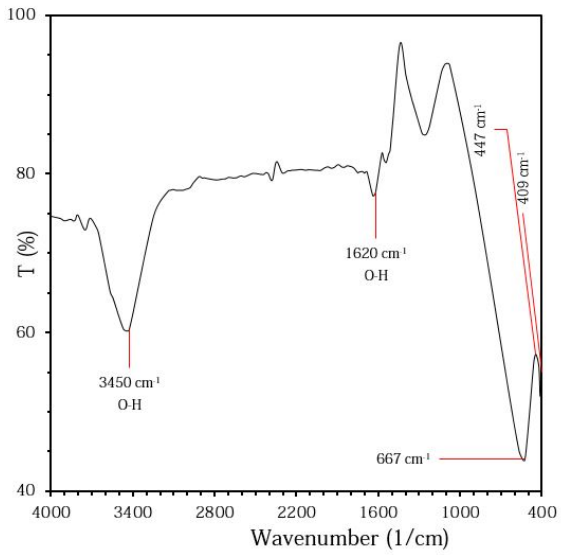

Fig. (6) FTIR spectrum of synthesized TiO_2 nanopowder

Figure (7) shows the UV-visible spectrum of the synthesized TiO_2 nanopowder in the spectral range of 300-800 nm. It is clear that the sample exhibits high absorption in the UV region (<375nm) and very low absorption in the visible and near-infrared (NIR) regions. Such behavior is a characteristic of TiO_2 as its photocatalytic activity is induced by the absorption of UV radiation. Figure (8) shows the determination of energy band gap (E_g) of the TiO_2 nanopowder sample synthesized in this work. The value is about 3.14 eV, which lies in the range of energy band gap of mixed TiO_2 structures (3.0-3.2eV).

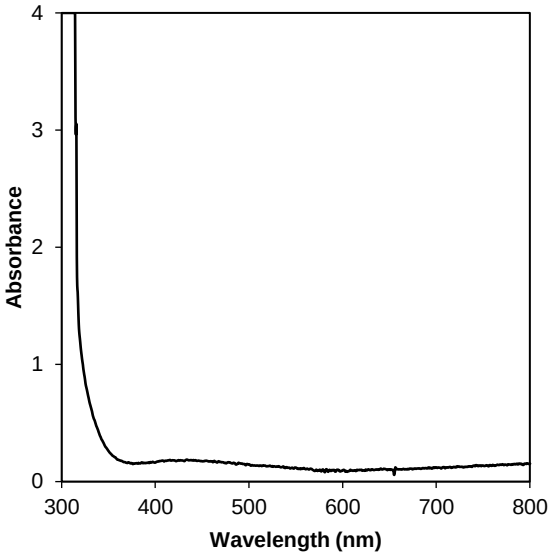

Fig. (7) UV-visible spectrum of synthesized TiO_2 nanopowder

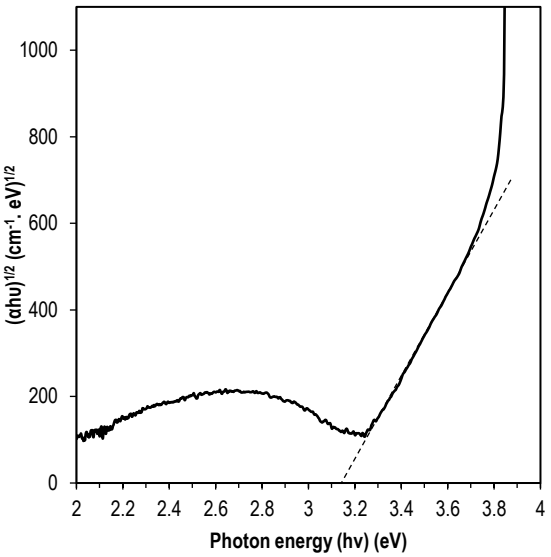

Fig. (8) Determination of energy band gap of the synthesized TiO_2 nanopowder sample

4. Conclusions

The mixed-phase titanium dioxide nanopowders were synthesized by an eco-friendly solvothermal method. The structural characteristics confirmed that the synthesized nanopowders have tetragonal crystalline and contains anatase and rutile phases of

titanium dioxide. The minimum particle size is 53.48nm with inevitable aggregation of the nanoparticles. The prepared nanopowders have reasonable absorption in the UV region of electromagnetic spectrum (<375nm) and very low absorption in the visible region. The energy band gap of the synthesized samples was determined to be 3.14eV, which agrees with the standard range of energy band gap of mixed-phase TiO_2 structures (3.0-3.2eV). The solvothermal method used in this work can be described by low complexity, simple assembly, low cost and high purity production.

References

[1] O. V Salata, "Applications of nanoparticles in biology and medicine," *J. Nanobiotechnology*, vol. 2, no. 1, pp. 1–6, 2004.

[2] H. H. M. Darweesh, "Nanomaterials: classification and properties-Part I," *Nanoscience*, vol. 1, no. 1, pp. 1–11, 2018.

[3] P. Nikolaidis, *Analysis of green methods to synthesize nanomaterials*, no. September 2020. 2020. doi: 10.1002/9781119576785.ch5.

[4] N. Baig, I. Kammakakam, and W. Falath, "Nanomaterials: A review of synthesis methods, properties, recent progress, and challenges," *Mater. Adv.*, vol. 2, no. 6, pp. 1821–1871, 2021.

[5] Z. Vaseghi and A. Nematollahzadeh, "Nanomaterials: types, synthesis, and characterization," *Green Synth. Nanomater. bioenergy Appl.*, pp. 23–82, 2020.

[6] S. S. Salem, E. N. Hammad, A. A. Mohamed, and W. El-Dougdoug, "A comprehensive review of nanomaterials: Types, synthesis, characterization, and applications," *Biointerface Res. Appl. Chem*, vol. 13, no. 1, p. 41, 2022.

[7] A. Mageswari, R. Srinivasan, P. Subramanian, N. Ramesh, and K. M. Gothandam, "Nanomaterials: classification, biological synthesis and characterization," *Nanosci. Food Agric. 3*, pp. 31–71, 2016.

[8] Y. A. Shaban, M. A. El Sayed, A. A. El Maradny, R. K. Al Farawati, and M. I. Al Zobidi, "Photocatalytic degradation of phenol in natural seawater using visible light active carbon modified (CM)-n-TiO_2 nanoparticles under UV light and natural sunlight illuminations," *Chemosphere*, vol. 91, no. 3, pp. 307–313, 2013.

[9] M. Tomás-Gamasa and J. L. Mascareñas, "TiO_2-Based Photocatalysis at the Interface with Biology and Biomedicine," *ChemBioChem*, vol. 21, no. 3, pp. 294–309, 2020.

[10] M. Huston, M. DeBella, M. DiBella, and A. Gupta, "Green synthesis of nanomaterials," *Nanomaterials*, vol. 11, no. 8, p. 2130, 2021.

[11] M. Shah, D. Fawcett, S. Sharma, S. K. Tripathy, and G. E. J. Poinern, "Green synthesis of metallic nanoparticles via biological entities," *Materials (Basel).*, vol. 8, no. 11, pp. 7278–7308, 2015.

[12] H. Nadaroglu, H. Onem, and A. Alayli Gungor, "Green synthesis of Ce_2O_3 NPs and determination of its antioxidant activity," *IET nanobiotechnology*, vol. 11, no. 4, pp. 411–419, 2017.

[13] H. Nadaroglu, A. A. Gungor, S. Ince, and A. Babagil, "Green synthesis and characterisation of platinum nanoparticles using quail egg yolk," *Spectrochim. Acta Part A Mol. Biomol. Spectrosc.*, vol. 172, pp. 43–47, 2017.

[14] S. Cicek, A. A. Gungor, A. Adiguzel, and H. Nadaroglu, "Biochemical evaluation and green synthesis of nano silver using peroxidase from Euphorbia (Euphorbia amygdaloides) and its antibacterial activity," *J. Chem.*, vol. 2015, 2015.

[15] K. B. Narayanan and N. Sakthivel, "Biological synthesis of metal nanoparticles by microbes," *Adv. Colloid Interface Sci.*, vol. 156, no. 1–2, pp. 1–13, 2010.

[15] Z.H. Zaidan, K.H. Mahmood and O.A. Hammadi, "Using Banana Peels for Green Synthesis of Mixed-Phase Titanium Dioxide Nanopowders", Iraqi J. Appl. Phys., 18(4) (2022) 27-30

[17] N. K. Mukhopadhyay and T. P. Yadav, "Some aspects of stability and nanophase formation in quasicrystals during mechanical milling," *Isr. J. Chem.*, vol. 51, no. 11-12, pp. 1185–1196, 2011.

[18] N. M. Noah and P. M. Ndangili, "Green synthesis of nanomaterials from sustainable materials for biosensors and drug delivery," *Sensors Int.*, vol. 3, p. 100166, 2022.

[19] S. Rajeshkumar and L. V Bharath, "Mechanism of plant-mediated synthesis of silver nanoparticles–a review on biomolecules involved, characterisation and antibacterial activity," *Chem. Biol. Interact.*, vol. 273, pp. 219–227, 2017.

[20] K. Vijayaraghavan and T. Ashokkumar, "Plant-mediated biosynthesis of metallic nanoparticles: A review of literature, factors affecting synthesis, characterization techniques and applications," *J. Environ. Chem. Eng.*, vol. 5, no. 5, pp. 4866–4883, 2017.

[21] Z.H. Zaidan, O.A. Hammadi and K.H. Mahmood, "Effect of Preparation Method on Crystalline Structure of Titanium Dioxide Nanoparticles", Iraqi J. Appl. Phys. Lett, 6(2) (2023) 11-14.

[22] I. Hussain, N. B. Singh, A. Singh, H. Singh, and S. C. Singh, "Green synthesis of nanoparticles and its potential application," *Biotechnol. Lett.*, vol. 38, pp. 545–560, 2016.

[23] H. E. Swanson, *Standard X-ray diffraction powder patterns*, vol. 25. US Department of Commerce, National Bureau of Standards, 1953.

[23] Z.H. Zaidan, O.A. Hammadi and K.H. Mahmood, "Effect of Structural Phase on Photocatalytic Activity of Titanium Dioxide Nanoparticles" Iraqi J. Appl. Phys., 19(3A) (2023) 55-58.

[22] A. Monshi, M. R. Foroughi, and M. R. Monshi, "Modified Scherrer equation to estimate more accurately nano-crystallite size using XRD," *World J. nano Sci. Eng.*, vol. 2, no. 3, pp. 154–160, 2012.

[23] N. N. Greenwood, E. J. F. Ross, and B. P. Straughan, "Index of vibrational spectra of inorganic and organometallic compounds," *(No Title)*, 1972.

[24] Y. Bouachiba, A. Bouabellou, F. Hanini, F. Kermiche, A. Taabouche, and K. Boukheddaden, "Structural and optical properties of TiO_2 thin films grown by sol-gel dip coating process," *Mater. Sci.*, vol. 32, pp. 1–6, 2014.

[25] F. J. Al-Maliki and N. H. Al-Lamey, "Synthesis of Tb-doped titanium dioxide nanostructures by sol–gel method for environmental photocatalysis applications," *J. Sol-Gel Sci. Technol.*, vol. 81, pp. 276–283, 2017.

[26] Z.H. Zaidan, O.A. Hammadi and K.H. Mahmood, "Plant-Extracted Preparation of Crystalline Titanium Dioxide Nanoparticles", Iraqi J. Appl. Phys. Lett, 6(4) (2023) 23-26.

Ayad A. Salih [1]
Asmaa H. Mohammed [2]
Shaymaa H. Aneed [2]
Bushra H. Hussein [1]

[1] *Department of Physics, College of Education for Pure Science / Ibn Al-Haitham, University of Baghdad, Baghdad, IRAQ*
[2] *Department of Physics, College of Science, Al Nahrain University Baghdad, IRAQ*

Fabrication and Optoelectronic Properties of Bismuth Oxide Thin Films Prepared by Thermal Evaporation

This work shows the fabrication of Bi_2O_3/Si heterojunctions for solar cell applications. Bi_2O_3 nanoparticles were deposited on quartz, n- and p-type silicon substrates by thermal evaporation method. The structural and optical characteristics of the prepared Bi_2O_3 thin films were studied. The polycrystalline structure of these thin films was revealed with (111) direction. These Bi_2O_3 thin film has direct energy gap of 2.6 eV. The electrical measurements under dark and light conditions indicate a significant improvement conversion efficiency values for Al/n-Bi_2O_3/n-Si/Al heterojunction. The growth of the depletion layer width with the built-in potential was the cause of the decrease in device capacitance. The photovoltaic measurements were determined and the results showed that the Bi_2O_3/n-Si sample was the best.

Keywords: Thin films; Bismuth oxide; Silicon conductivity type; Solar cells
Received: 19 January 2024; **Revised:** 13 March 2024, **Accepted:** 20 March 2024

1. Introduction

One of the most promising components of a new era in technology and science are nanoparticles (NPs), which are chemical structures with a size between 1 and 100 nm. The market for NPs-based goods is expanding quickly in a number of industries, including biomedical applications, home and garden, electronics and computers, health and fitness, photo cell and photodetector [1-3]. Because of their distinctive and varied physicochemical characteristics, metal oxide nanoparticles have drawn interest from researchers in a variety of fields and one of the important metal oxides that have gained attention recently is Bi_2O_3 [4,5]. Nanostructured Bi_2O_3 thin films have attracted the interest of many researches due to the values of some their characteristics parameters, e.g., available and easy to manufacture, refractive index, photoconductivity, transparency and mechanical strength [3-6]. Also, the energy gap is wide (1.73-3.98eV), it is close to CdS, which is considered a prominent filter for solar cells application [1,6,7]. Although Bi_2O_3-NPs are widely used and purposeful or incidental exposure is rising, nothing is known regarding their toxicity [8]. Different method was used to prepare Bi_2O_3 such as sol-gel [1], pulsed-laser deposition (PLD) [2], green synthesis [4], reactive sputtering [7], spray pyrolysis [9], and magnetron reaction [10]. In order to produce thin films and study their characterization for solar cell applications, bismuth oxide nanoparticles were prepared in this paper using a simple physical method. This is one of the simplest ways to prepare nanoparticles with very perfect crystallinity and deposit them on quartz and other silicon type substrates.

2. Experimental Part

As substrates, test quartz slides with an area of 2x2 cm^2 were used. Alcohol and ultrasonic waves were used to clean them, removing residue and contaminants from their surfaces.

Using a wire-cut machine, square-shaped n & p type silicon samples were created, each measuring 1 cm^2 in area and having resistivities between 1.5 and 4 Ω.cm. For the purpose of removing oxides, the samples were etched using a CP4 solution made up of HNO_3, CH_3COOH and HF in the ratios (3:3:5). After 15 minutes of cleaning with alcohol and ultrasonic waves (using a Berry PUL 125 device), they underwent another 15 minutes of cleaning with water and ultrasonic waves. Ohmic contacts are made on both Bi_2O_3 film and Si substrate by depositing of Al thick films through certain mask using an Edwards thermal evaporation system followed by rapid thermal oxidation. Four-point probe (FPP) technique was used to assess the silicon substrate's resistivity and kind of conductivity. For the TCO's/Si heterojunction, the silicon sample serves as the substrate. The cross-sectional view of Bi_2O_3/Si heterojunction is shown in Fig. (1a).

An Edwards thermal evaporation system was employed to vaporize extreme purity (99.99 %) Bi on quartz slides and Si substrates (n-type and p-type) at room temperature under low pressure (~10^{-6} torr).

Rapid thermal oxidation (RTO) for Bi films was employed to prepare Bi_2O_3 films at different temperature and oxidation time. Figure (1b) depicts

the apparatus used to create the oxide film. To ensure that air (a source of dry oxygen) flowed through it, a quartz cylinder measuring 0.03 m in diameters and having two open ends were employed. Light and heat were radiated by a 650W halogen lamp, and the output power was managed by a variable power supply. Temperature measurements of the sample were made using a k-type thermocouple.

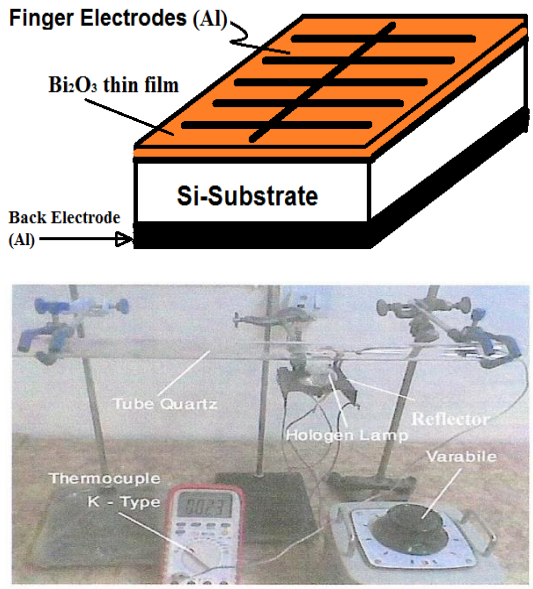

Fig. (1) Cross-sectional view of Bi_2O_3/Si heterojunction (upper), and rapid thermal oxidation (R.T.O) setup (lower)

After being cleaned, the samples were fixed on the quartz tube irradiated by halogen lamp directly. The position of the lamp was fixed to maintain certain temperature, and the distance between the lamp and the tube was 0.5 cm. Thermal oxidation process took place at temperatures between 373 and 973 K, and at different oxidation times in order to obtain the best oxidation of Bi thin films.

3. Results and Discussion

Figure (2) illustrates how to compute the crystalline lattice of inert fixed crystals coordination of single crystal and the preferred trend of polycrystalline crystal using the experimental method of x-ray diffraction (XRD) [11]. XRD pattern of film deposited on the quartz subsurface displays a multicolor construction with a bismuth metal peak at 27.59°, 32.40° and 48.20°, respectively, in the (111), (200) and (116) planes. The conforming d-values have been associated with the JCPDS card, plane (Alpha Order): Bi_2O_3:00-041-1449. The average crystallite size of Bi_2O_3 thin films equal to 29.154 nm was calculated from the Scherrer's formula [12]:

$$C.S = \frac{0.94\,\lambda}{\beta\cos(\theta)} \qquad (1)$$

where $\lambda_{x\text{-ray}}$=1.5406Å, β is (FWHM) of the preferential plane (111)= 0.2932° at 2θ=27.58°

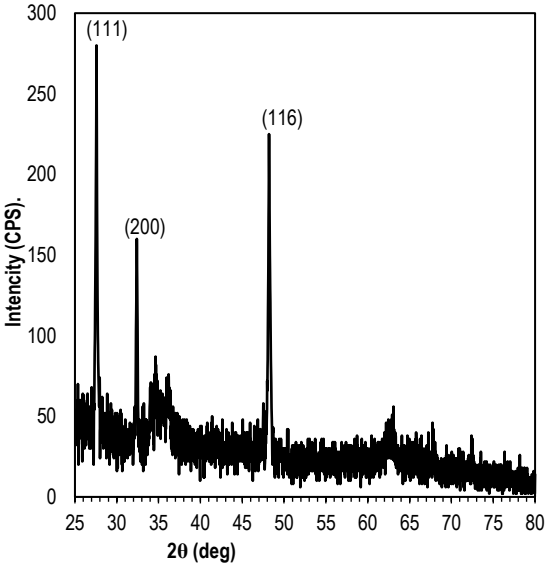

Fig. (2) XRD pattern of the Bi_2O_3 thin film

The SEM microimage of the thin Bi_2O_3 layer on the quartz bottom layer is shown in Fig. (3) at 20 KX magnification. The prepared film has regular distribution granules with uniform and homogeneous surface, thus improving the quality of the prepared films. Additionally, nanostructured grains ranged between 50-90 nm are evenly distributed across the film's surface.

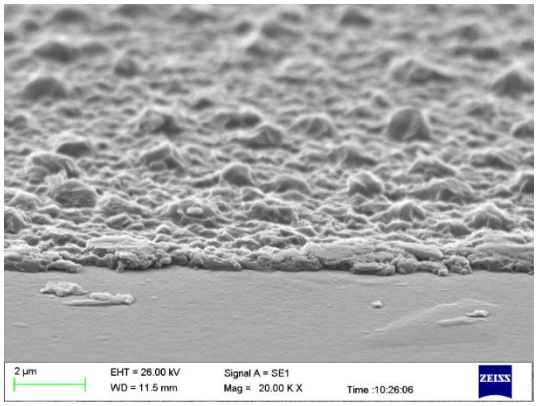

Fig. (3) SEM microimage of the Bi_2O_3 thin film

The UV-visible spectroscopy established the occurrence of nanoparticles by in Fig. (4). The Bi_2O_3 nanoparticles were observed for wavelength scanning between 250-700nm. The characteristic absorption peak of bismuth was detected at 290nm [13]. The energy band gap can be determined using the absorption coefficients with Tauc's equation [14]:

$$(\alpha h\nu) = B(h\nu - E_g)^{n} \qquad (2)$$

where α is the absorption coefficient, ν is the photon frequency, E_g denotes the optical band gap, and B is constant

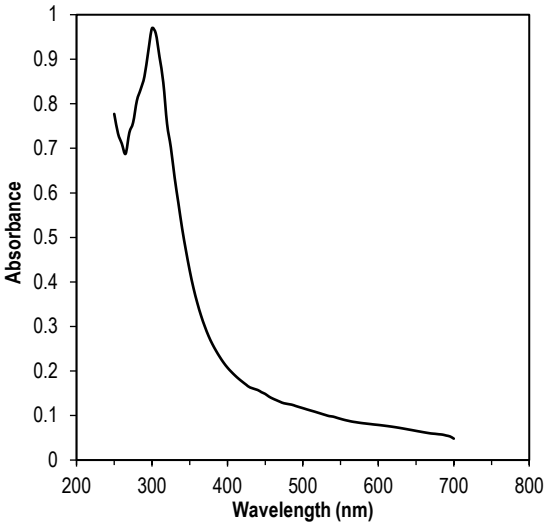

Fig. (4) Absorption spectrum of Bi_2O_3 thin film

The parameter (η) is an index associated with the material's characteristics and determined by the optical transition influencing the absorption process. It dictates the allowed (η = 1/2 and 2) direct and indirect transitions within the electronic band structure. The optical band gap energy (E_g) was obtained from the straight line intersection of the curve as shown in Fig. (5). The band gap is 2.6 eV direct transitions for Bi_2O_3, which is an important characteristic for photovoltaic applications. This value is good agreement with [11].

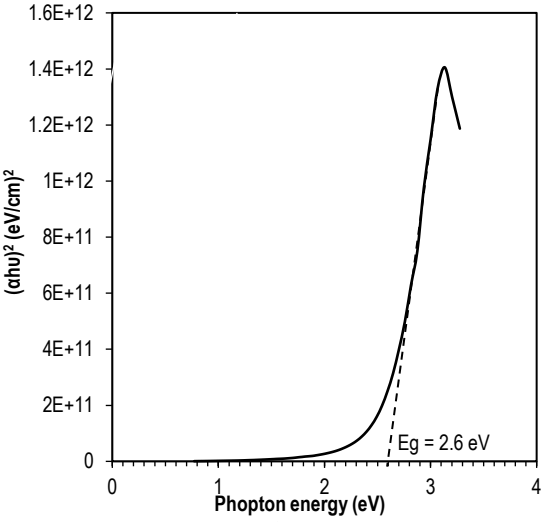

Fig. (5) Variation of $(\alpha h\nu)^2$ with $h\nu$ of Bi_2O_3 thin film

The FTIR absorption spectrum, shown in Fig. (6), was recorded within the range of 400–4000 cm^{-1} to analyze the formation of Bi_2O_3 nanoparticles and identify functional groups. O-H stretching vibrations were evident at 3363~3414 cm^{-1}, while C-O vibrations linked to environmental CO_2 were observed at 2330 cm^{-1}. A peak with 1629 cm^{-1} corresponded to H_2O, and the 542 cm^{-1} peak originated from the metal oxygen (Bi-O) vibration.

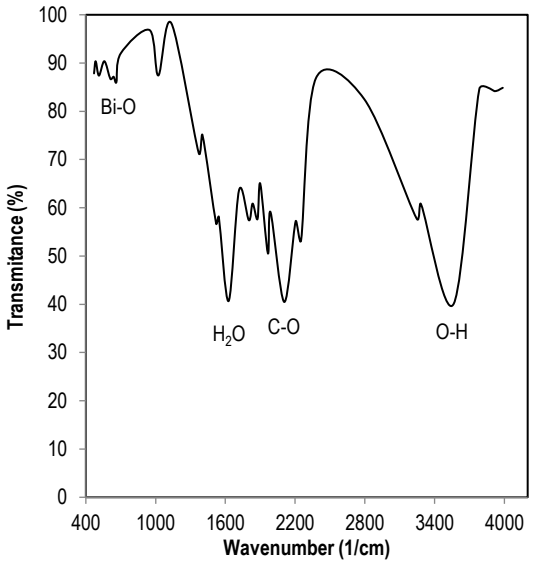

Fig. (6) FTIR spectrum of Bi_2O_3 thin film

Figure (7) displays the outcomes of the electrical measurements (J-V curve) for the devices made from n-Bi_2O_3/SiO_2/n-Si and n-Bi_2O_3/SiO_2/p-Si under ideal conditions at forward and reverse biasing in the dark and illumination. These qualities are crucial for describing the performance of the device and any parameters that depend on it [11]. For two devices operating optimally with reverse bias, the J-V characteristics were given. It has obtained a trace with two distinct sections. The first region is the produced zone, at which the reverse current modestly increases with the related voltage to form pairs of electron-hole at the case of low biasing. Significantly more reverse bias may be seen in the second section. In this instance, diffusion of minority carrier through the connection produced the current. It is evident from the results that n-Bi_2O_3/SiO_2/p-Si produces less current than n-Bi_2O_3/SiO_2/n-Si, that is connected to the substantial junction resistance that lowers leakage current. The improvement in the junction structure is connected to the improvement in the reverse current, which reduces a sum of faults at the semiconductor insulators semiconductor interface of the two junctions. Those flaws are the outcome of strain brought on by mismatched thermal expansion, crystal structure, and lattice parameters. The potential barrier is lowered by the forward voltage in the forward bias, which allows majority carriers to pass it much more easily than they could at zero bias. As a result, the diffusion current exceeds the drift current. The ultimate result is that figure (7) shows how both the n-Bi_2O_3/SiO_2/n-Si and n-Bi_2O_3/SiO_2/p-Si devices behave in terms of J-V characteristics when biased forward. There are two distinct zones; the first one is a recombination current that forms when the generated carrier concentration ($n.p>n_i^2$), or when the produced carrier concentrations are greater than the intrinsic carrier's concentration (n_i), leads to the recombination process.

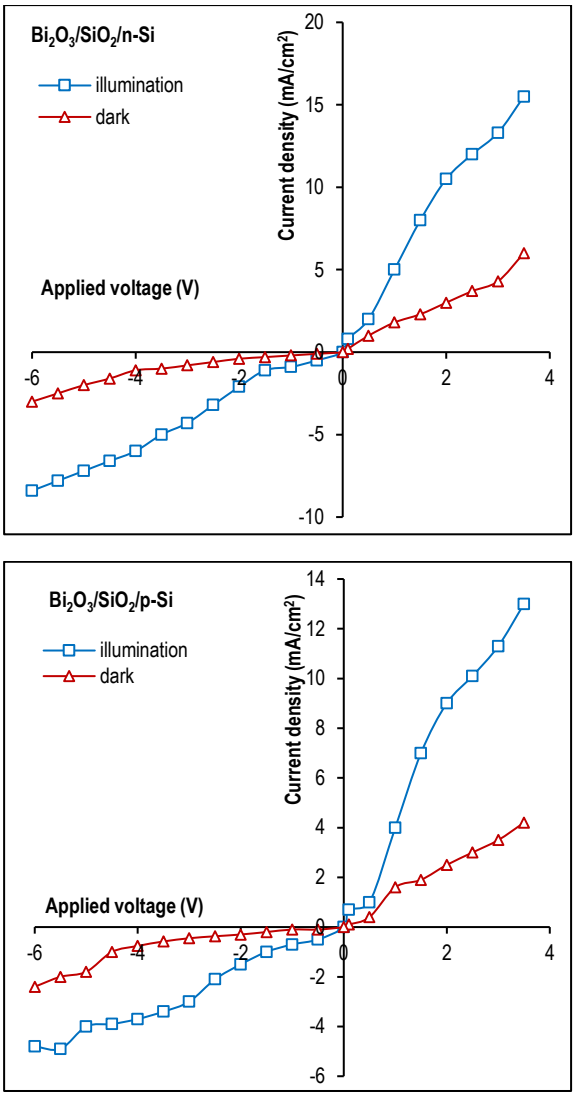

Fig. (7) J-V characteristics for both MIS devices under forward and reverse bias

Depending on the series resistance, second zone when high voltages indicated the diffusion and bending regions, which in the case of MIS characterized the tunneling regions. It is clear from a contrast of the results of the two devices created under ideal conditions that the value of the current enhanced for n-Bi_2O_3/SiO_2/n-Si because a reduction in resistivity of n-type silicon leads to a growth in the electron concentrations. Because of the thicker SiO_2 layer used in the n-Bi_2O_3/SiO_2/n-Si device, this results in a decrease the holes concentrations, hence a corresponding fall in I_s. Being able to determine several factors, including built-in potential (V_{bi}), device capacitance (C_o), and device kind, makes it one of the most crucial measures. The measurements for C-V and $1/C^2$-V for each device are shown in Fig. (8).

The findings indicate that the devices capacitances are inverse related to the bias voltage. The growth of the depletion layers (W) with the built-in potential (V_{bi}) caused the device capacitance to decrease with the related bias voltage. The capacitance of depletion layers is increased with increasing the applied voltage. The action of charge transfer from donor to the acceptor zone, was discovered to be abrupt is accurately indicated with this, and is further verified by the fact that the relationship between $1/C^2$ and reverse bias are straight lines. Given that band bending occurs mainly on the silicon side, the small-single capacitance-volt characteristic can be used to measure the potential barrier for the junction. The point where the curve intersects the x-axis corresponds to the diffusion potential of silicon as shown in table (1), and its values are anticipated to be solely dependent on the Fermi level within the conduction band at elevated carrier concentration. Donor concentration (N_D) is determined by the straight line's slope, and its value closely matches the silicon substrate's well-known resistivity.

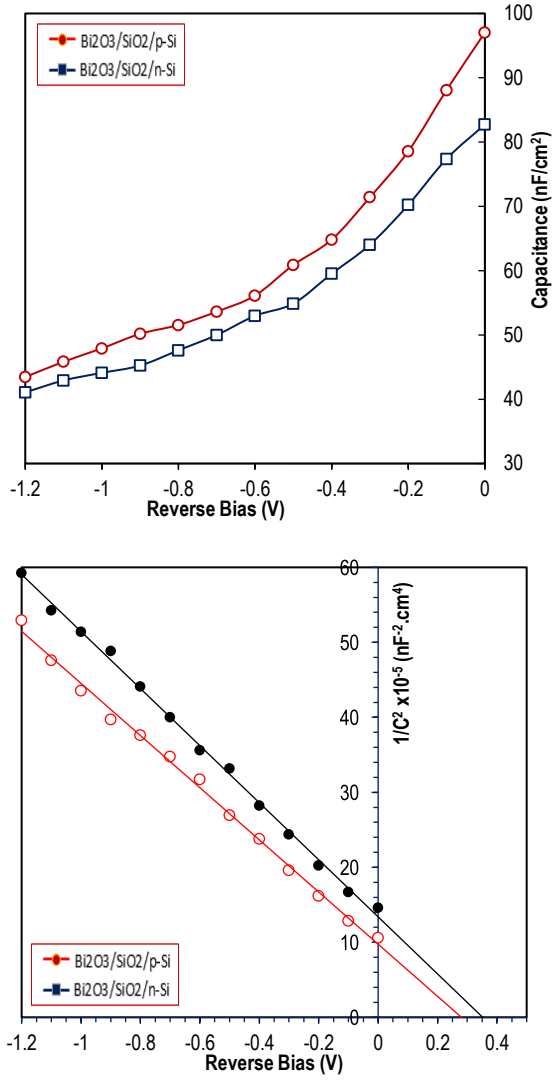

Fig. (8) The relationship between junction capacitance and applied voltage for both MIS devices, at f=100 kHz

Table (1) Values of C-V diagram for Bi_2O_3/SiO_2/Si heterojunctions

Si substrate type	V_{bi} (V)	C_o (nf/cm²)	$W=\varepsilon_s/C_o$ (μm)	$N_D x10^{+15}$ (cm^{-3})
n-Bi_2O_3/SiO_2/ p-Si	0.27	100.00	7.303	2.37978
n-Bi_2O_3/SiO_2/ n-Si	0.35	91.29	7.999	2.39564

In Fig. (9), the relationship between the incidence photons power of the halogen lamp and the short circuit current (I_{SC}) and open circuit voltage (V_{OC}) for both devices is depicted. According to the results, there is a linear relationship between I_{SC} and V_{OC}, by the photo powers incident having a maximum value beyond with both values for the two devices tending for becoming saturated and constant. This is brought on by the complete separations of the electron-hole pairs produced by the photons. It is evident that there is a significant disparity between the values of the obtained results. The increased performance of the n-Bi_2O_3/SiO_2/n-Si device was due to widening of the depletion layer (*W*) caused by addition of the interfacial thickness (SiO_2), which results in large areas for the separation of electron-hole pair and hence a significant photocurrent.

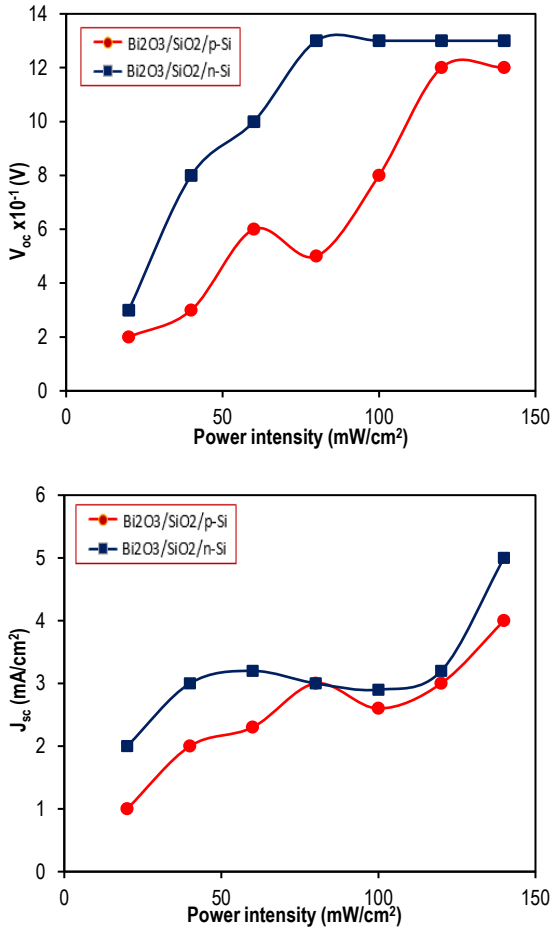

Fig. (9) Variation of open-circuit voltage and short-circuit current density with incident power intensity for both MIS devices

Figure (10) represents J-V characteristics of both n-Bi_2O_3/SiO_2/n-Si and n-Bi_2O_3/SiO_2/p-Si solar cells, the short-circuit current value (I_{SC}) determined at V=0, while the open-circuit voltage (V_{OC}) was determined at I=0, as shown in table (2), where the value of fill factor (F.F) and the photovoltaic conversion solar cell efficiency (η) are calculated from the following equations [14]:

$$\eta = \frac{P_m}{P_{in}} \times 100\% = \frac{I_m \cdot V_m}{P_{in}} \times 100\% \quad (3)$$

$$\text{F.F.} = \frac{J_m \cdot V_m}{J_{sc} \cdot V_{oc}} \quad (4)$$

Table (2) Electrical parameters for (a) n-Bi_2O_3/SiO_2/n-Si and (b) n-Bi_2O_3/SiO_2/p-Si heterojunction solar cells

Si substrate type	V_{oc} (V)	J_{sc} (mA/cm²)	V_{max}, V_m (V)	J_{max}, J_m (mA/cm²)	F.F	η %
(a)	1.3	2.9	0.84	1.9	0.423	1.6
(b)	0.8	2.6	0.52	1.6	0.400	0.83

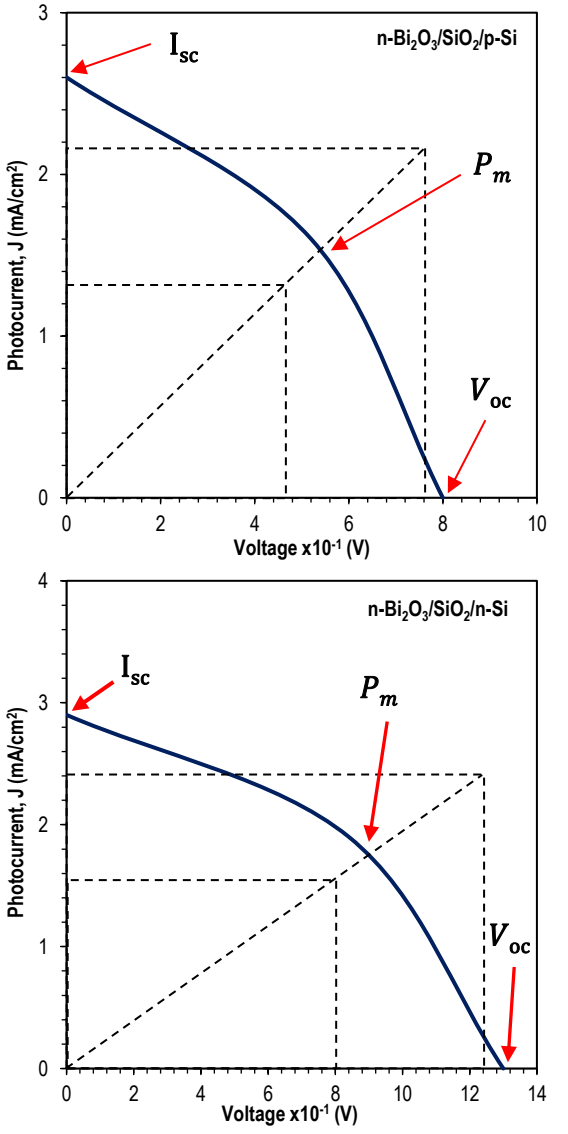

Fig. (10) J-V curves of n-Bi_2O_3/SiO_2/p-Si and n-Bi_2O_3/SiO_2/n-Si heterojunction solar cells

4. Conclusions

The Bi_2O_3 thin films prepared in this work were polycrystalline with grain size of 15-29nm and uniform surface. The direct optical energy gap was found to be 2.6 eV. The photovoltaic outcome for the n-Bi_2O_3/(n,p)Si heterojunction was found to be a linear relationship between I_{SC} and V_{OC}. The I-V and C-V measurements of the heterojunctions depends on the silicon substrate type. The efficiency of solar cell fabricated on n-type silicon substrate is higher than that fabricated on p-type silicon substrate due to less light-induced degradation.

References

[1] W. He et al., "Thin bismuth oxide films prepared through the sol–gel method", *Mater. Lett.*, 61(19) (2007) 4100-4102.

[2] E.T. Salim et al., "Optical properties of Cauliflower like Bi_2O_3 nanostructures by reactive pulsed laser deposition (PLD) technique", *Sol. Ener.*, 107 (2014) 523-529.

[3] E. Hashemi, R. Poursalehi and H. Delavari, "Formation mechanisms, structural and optical properties of Bi/Bi_2O_3 One dimensional nanostructures prepared via oriented aggregation of bismuth based nanoparticles synthesized by DC arc discharge in water", *Mater. Sci. Semicond. Process.*, 89 (2019) 51-58.

[4] N. Motakef-Kazemi and M. Yaqoubi, "Green Synthesis and Characterization of Bismuth Oxide Nanoparticle Using Mentha Pulegium Extract", *Iranian J. Pharmaceut. Res.*, 19(2) (2020) 70-79.

[5] C.M. Hincapie et al., "Physical-Chemical Properties of Bismuth and Bismuth Oxides: synthesis, characterization and applications", *DYNA*, 176 (2012) 139-148.

[6] R.A. Ismail, "Fabrication and Characteristics Study of n-Bi_2O_3/n-Si Heterojunction", *J. Semicond. Technol. Sci.*, 6(2) (2006) 119-123.

[7] H.T. Fan et al., "δ-Bi_2O_3 thin films prepared by reactive sputtering Fabrication and characterization", *Thin Solid Films*, 513 (2006) 142–147.

[8] E. Öztaş et al., "Bismuth oxide nanoparticles induced oxidative stress-related inflammation in SH-SY5Y cell line", *Istanbul J. Pharm.*, 49(3) (2019) 173-179.

[9] T.P. Gujar, V.R. Shinde and C.D. Lokhande, "Spray pyrolysis bismuth oxide thin films and their characterization", *Mater. Res. Bull.*, 41 (2006) 1558-1564.

[10] J. Morasch et al., "Reactively magnetron sputtered Bi_2O_3 thin films: Analysis of structure, optoelectronic, interface, and photovoltaic properties", *phys. stat. sol. (a) Appl. Mater.*, 211(1) (2014) 342.

[11] B.K. Hasson and N.I. Najm, "The Influence of Aluminum Doping on Structural and Optical Properties of (Bi_2O_3) Thin Films", *Ibn Al-Haitham J. Pure Appl. Sci.*, 29(2) (2016) 387-396.

[12] B.D. Dullity, **"Elements of X-Ray Diffraction"**, Addison-Wesley Publishing Co., Inc. (USA, 1956), p. 99.

[13] L. Leontie et al., "Structural and Optical Characteristics of Bismuth Oxide Thin Films", *Surf. Sci.*, 507 (2002) 480-485.

[14] S.M. Sze, **"Physics of Semiconductor Devices"**, 3rd ed., John-Wiley & Sons, Inc. (Canada, 2007).

Mohammed A. Mohammed [1]
Khansaa N. Aklo [2]
Anaam W. Watan [2]
Kareem A. Jasim [2]
Ebtisam M-T. Salman [2]

[1] *Department of Remote Sensing and GIS, College of Science, University of Baghdad, Baghdad, IRAQ*
[2] *Department of Physics, College of Education for Pure Sciences / Ibn Al-Haitham, University of Baghdad, Baghdad, IRAQ*

Effect of Thermal Neutron Radiation Dose on Density of Local and Extended Energy States in $Se_{55}S_{20}Sb_{15}Sn_{10}$ Alloy

Four samples of the $Se_{55}S_{20}Sb_{15}Sn_{10}$ alloy were prepared using the melting point method. Samples B, C and D were irradiated with (6.04×10^{10}, 12.08×10^{10} and 18.12×10^{10} ($n.cm^{-2}s^{-1}$) of thermal neutron beam from a neutron source (241Am-9Be) respectively, while sample A was left not irradiated. The electrical properties were assessed both before and after the radiation. All irradiated and non-irradiated samples show three conduction mechanisms, at low temperatures, electrical conductivity is achieved by electron hopping between local states near the Fermi level. At intermediate temperatures, conduction occurs by the jumping of electrons between local states at band tails. At high temperatures, electrons transfer between extended states in bands. The results show that the local and extended state densities above the Fermi level are affected by exposure to thermal neutron radiation.

Keywords: Melt quenching; Thermal neutron beam; Electron hopping
Received: 03 January 2024; **Revised:** 02 March; **Accepted:** 09 March 2024

1. Introduction

Studies on the properties of amorphous chalcogenide semiconductors have shown that, due to the presence of local states close to the Fermi level and in the energy gap, where the Fermi level was pinned, they generally behave as doping-insensitive P-type semiconductors [1-3]. It was found that the amorphous chalcogenides might be improved for use in device applications by substituting certain chemical components entirely or with metallic impurities [4]. This increased their conductivity and greatly lowered the conduction activation energy [5]. According to Mott, any element may satisfy the valence criterion in chalcogenides applying the 8-N rule [6]. The electrical and optical properties of doped chalcogenides don't vary much because this rule holds for doped elements. The researchers demonstrated that adding atoms of some chemical elements (such as bismuth) to chalcogenide glass causes a significant change in the p-type electrical conductivity of more than 7% compared to that of the n-type [7]. In contrast, the addition of other elements (like In, Sb, Sn) always indicates a p-type compound [8,9]. Since not all impurities can be electroactive, the concentration of the impurities is undoubtedly a key element in such situations [10,11]. It is therefore important, both from the point of view of basic research and applied research, to investigate the influence of impurities on the properties of chalcogenide glass [12,13].

The electrical characteristics of the chalcogenide glass are significantly altered when impurity atoms are added to the Se-Te-Sn and Ge-Te-Sb binary systems, according to the findings of multiple experimental investigations [14]. In addition, the composition of the glass, the chemistry of the impurities, and the doping technique have a significant impact on the behavior of the chalcogenide glass [15]. This study investigated the density of the extended, local, and Fermi levels of In and their effects of indium on the $Se_{85}Te_{10}Sn_{5-x}In_x$. These include changes to the activation energy, tail width, and distance between states in addition to a decrease in the density of extended and local states, also known as Fermi states [14]. When the Sb element in the $Ge_{30}Te_{70-x}Sb_x$ alloy was partially exchanged, the density of local and extended states, as well as the Fermi level, were examined, and it was discovered that all energy states, including activation energy, tail width, interatomic distances, and transition distance, changed [15]. The studies [10-13] focused on examining the electrical characteristics of $Se_6Te_{4-x}Sb_x$ and $Se_6Te_{4-x}Sn_x$ alloys by partially replacing Te with Sb and the energy density was calculated for several energy states, including electron hopping distance, Fermi level, localization, and tail width. They concluded that the states of energy density increase along with the concentration of Sb. One of the distinctive characteristics of amorphous chalcogenide semiconductors is their susceptibility to the effects of external factors, notably ionizing radiation with an average energy of more than 1 MeV [16,17].

To gain additional knowledge regarding how radiation affects dc conductivity measurements at various temperatures and to exploit amorphous chalcogenides in electrical device applications. We

will investigate the impact of thermal neutron irradiation on the random energy level and crystal regularity of $Se_{55}S_{20}Sb_{15}Sn_{10}$ samples, as well as the densities of states (local, extended, and Fermi levels). This paper will be finished to exploit amorphous chalcogenides in electrical device applications.

2. Experimental Part

Four samples of $Se_{55}S_{20}Sb_{15}Sn_{10}$ alloy (A, B, C and D) were prepared by melt-cooling technique. The raw material powders of high purity Se, S, Sb, and Sn (99.99%) were weighed according to the atomic weight ratios. The mixture was mixed using an electric mill to obtain a homogeneous powder. After the mixture was put into a quartz glass tube and evacuated to 10^{-4} Torr, the tube was securely sealed. This was done to remove any impurities from the capsule and ensure that it could resist the pressure created by the alloy's constituent chemical elements interacting with one another without blowing apart within the furnace due to the high temperature. Seal the ampoule hermetically. To prevent selenium from precipitating on the inner wall of the quartz tube and from evaporating suddenly, the ampoule was then heated in two phases. Three hours were spent gradually heating and holding the ampoule at 500 °C. For seven hours, the furnace's temperature was increased to 960°C at a rate of 6°C per minute. To get the glassy state, the ampoule was quickly chilled with ice-cooled water. The sample powder was then extracted by grinding the resulting ingot using a pestle and mortar. The powder was divided into four parts, and the powder was pressed for each of these parts using a hydraulic press with a pressure of 5 tons per square cm to obtain the tablets (A, B, C and D) with a diameter of one and a half centimeters and a thickness of 5mm. Continuous electrical conductivity was measured as a function of temperature within the room temperature range up to 227°C for sample A, and samples B, C and D were subjected to a thermal neutron beam with different doses (6.04×10^{10}, 12.08×10^{10}, 18.12×10^{10} n.cm^{-2}s^{-1}). For the irradiation samples (B, C, and D), the continuous electrical conductivity was evaluated as a function of temperature within the room temperature range up to 227°C, and then theoretical calculations were made on the results of electrical conductivity before and after irradiation using computer software.

3. Results and Discussion

The electrical (I-V) measurements were carried out at different temperatures (from 22 to 207 °C) to observe how the direct current electrical conductivity of $Se_{55}S_{20}Sb_{15}Sn_{10}$ alloy's glass. The electrical resistivity and then the electrical conductivity were calculated for all samples. All values of electrical conductivity of the samples were calculated about temperature. Based on testing the $Se_{55}S_{20}Sb_{15}Sn_{10}$ alloy's electrical resistance before and after exposure to thermal neutron beam radiation.

To demonstrate the relationship between continuous electrical conductivity and temperature changes, figure (1) shows the relationship between electrical conductivity ln(σ) and temperature. It is noted from this figure that all samples of the alloy $Se_{55}S_{20}Sb_{15}Sn_{10}$ before and after exposure to irradiation behave like semiconductors (that is, they have an electrical conductivity that increases with temperature in an exponential relationship) [18,19].

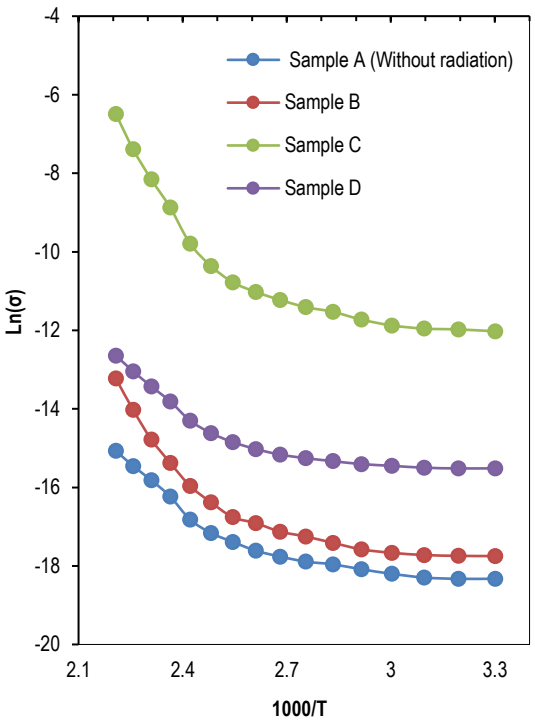

Fig. (1) Electrical conductivity plot (Ln σ) for $Se_{55}S_{20}Sb_{15}Sn_{10}$ samples as a function of temperature sample A without irradiation. Samples B, C and D were irradiated with doses of 6.04×10^{10}, 12.08×10^{10}, 18.12×10^{10} n.cm^{-2}, respectively

Additionally, it is shown that, in general, continuous electrical conductivity rises whenever subjected to a thermal neutron beam; however, sample C (dose 12.08×10^{10} n.cm^{-2}) has been significantly impacted in comparison to samples B and D (dose 6.04×10^{10} and 18.12×10^{10} n.cm^{-2}s^{-1}). This behavior in electrical conductivity explains that the alloys were affected when they collided with thermal neutrons, which led to their acquisition of additional energy by rearranging the atoms. The alloy had the best energy absorbed by the sample, while less or more than this dose, the conductivity increased slightly [16].

Figure (1) depicts the relationship between temperature and dc electrical conductivity for all glass samples $Se_{55}S_{20}Sb_{15}Sn_{10}$ both before and after irradiation. Additionally, each sample's curve reveals three distinct conduction regions at low, medium, and high temperatures, indicating the existence of three distinct electrical conduction mechanisms [10,11]. It was found that the conductivity increases slowly from 22 to 72 °C and increases remarkably quickly beyond

72 to 122 °C, and then the conductivity increases rapidly when the temperature is increased from 122 to 207 °C. The charge carriers gain energy when the temperature rises from 22 to 72 °C, and conduction happens as a result of the carriers in the local states jumping in the ranges near the Fermi level. The low temperature also results in low obtained conduction energy [14,20]. The conductivity is shown to rise as a result gradually. However, the charge carriers become more mobile above 22 K, and conduction happens as a result of the charge carriers leaping in the band tails. As a result, conduction is anticipated to occur by variable mobility (VRH) in the lower temperature range (122 to 207 °C). In contrast, in the higher temperature range (72 to 122 °C), as demonstrated in Fig. (1), conductivity increases, and conduction occurs via the thermally assisted process by the transfer of conduction electrons between the stretched states (between the conduction and valence bands this behavior fits Eq. (1) [15,21].

$$\sigma = \sigma_{01} e^{(-\frac{E_1}{KT})} + \sigma_{02} e^{(-\frac{E_2}{KT})} + \sigma_{03} e^{(-\frac{E_3}{KT})} \qquad (1)$$

where ΔE_1, ΔE_2, and ΔE_3 are the activation energies of each term, T is the absolute temperature, and σ_{01}, σ_{02}, σ_{03} are the pre-exponential factor parameters

The slope and intercept of the plot were used in the temperature range of low (22-72°C), middle (72-122°C) and high (122-207°C) to determine the activation energy (E_1, E_2, E_3) and the factor (σ_{01}, σ_{02}, σ_{03}) of $Se_{55}S_{20}Sb_{15}Sn_{10}$ glass, respectively. In table (1), the pre-exponential factor (σ_0) provides important information regarding the conduction process in chalcogenide glass.

The curves demonstrate that there are three separate paths leading to three different slopes produced by three activation energies in thermal activation conduction. According to equation 1, the slope of the plot of ln(σ) against 1000/T can be used to determine the activation energy (E_1, E_2, E_3).

Equation (1) may be used to calculate the pre-exponential factors σ_{01}, σ_{02} and σ_{03} for all samples in the three areas based on the span of the curves and their intersection with the y-axis when the x-axis equals zero. Table (1) shows the values for the pre-exponential factor 0, which were calculated [22]. This figure also, shows that the relationship between lnσ and 1000/T is nonlinear and that the many defects in the grain boundaries that result from insufficient atomic bonding are what cause the changes in electric conduction by enclosing charge carriers in the low-temperature zone and also densities of the state also promote the mobility of the carriers in the high-temperature area because they lower the trapping state and potential barrier [23,24]. There is no doubt that the electrical conductivity after the neutron radiation improved more quickly than the compound without neutron radiation. The density of states near the Fermi level, therefore, starts to change. We will use the activation energies (E_1, E_2, E_3), the exponential factor parameters (σ_{01}, σ_{02}, σ_{03}) and the width of the tails that were calculated from the relation ($\Delta E=E_2-E_1$) of each part of the curves shown in Eq. (1) and written in tables (1) and (2) to determine the densities of local and extended states for each sample before and after irradiation.

Figure (2) depicts the correlation between the energy tail width values ($\Delta E=E_1-E_2$) and the thermal neutron radiation dosage. This graph illustrates the variation in the amplitude of the energy tail values between samples that were exposed to thermal neutron radiation doses of 6.04×10^{10}, 12.08×10^{10}, and 18.12×10^{10} n.cm^{-2}s^{-1} and without irradiation sample. This suggests that the radiation had an impact on the density of the energy levels inside the samples' mobility gaps, this modification results from the samples' crystal recombination as a result of their absorption of radiation energy [16,17].

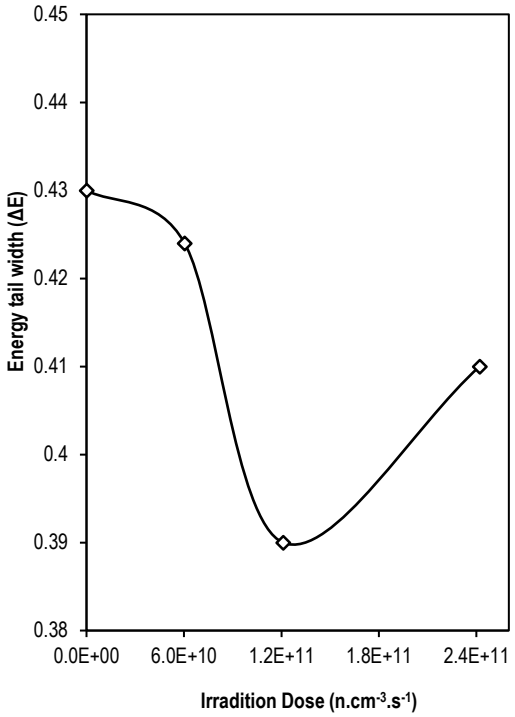

Fig. (2) Energy tail width ΔE values plot for $Se_{55}S_{20}Sb_{15}Sn_{10}$ as a function of thermal neutron irradiation dose

To calculate the energy state densities in three different regions – localized $N(E_{loc})$, extended $N(E_{ext})$, and Fermi level $N(E_F)$ after and before irradiation. After substituting the values of the constants (electron charge e, the electron mass and the values σ_{01}, σ_{02}, σ_{03} into the equations in references [13,14] mentioned below the energy state density was calculated in three different regions—local, extended, and Fermi level. The results are recorded in table (2).

$$N(E_{ext}) = [\frac{6m}{e^2\hbar}]\sigma_{0ext} \qquad (2)$$

where ħ = 1.0545×10^{-34} J.s

$$N(E_{loc}) = [\frac{6}{e^2 V_{ph} \hbar R^2}]\sigma_{0loc} \quad (3)$$

where V_{ph} is the phonon frequency, which is of order 10^{13} $s^{-1}$and R is the hopping distance and is given by

$$R = 0.7736[\frac{\Delta E a^{-1}}{N(E_C)(KT)^2}]^{0.25}$$

and

$$\gamma^{-1} = 10 \text{ A}$$

$$N(E_F) = [\frac{6}{e^2 V_{ph} \hbar R^2}]\sigma_{03} \quad (4)$$

It is noted from table (2) and Fig. (3) the intensity of the values of the stretched state ($N_{(Eext)}$), the density of the stretched state increases from the value 1.5×10^{18} $eV^{-1}cm^{-3}$ for the non-irradiated sample to 3.94×10^{19}, 5.78×10^{20} and 3.62×10^{19} $eV^{-1}cm^{-3}$ at a radiation dose with thermal neutrons of 6.04×10^{10}, 12.08×10^{10}, 18.12×10^{10} $n.cm^{-2}s^{-1}$, respectively. It can be seen from Fig. (3) that the density of extended states ($N_{(Eext)}$) increases with increasing radiation dose and the greatest value is at sample C. This is due to an increase in radiation energy, which may occur for several reasons, such as change in the value of the mobility gap, width of the E tails, concentration of conductors, or a shift in the conductor [12,18,19].

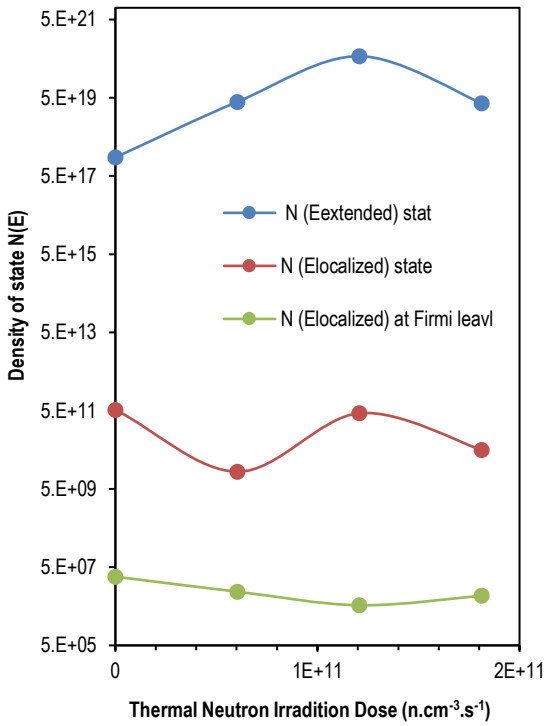

Fig. (3) Densities of energy states in localized, extended and Fermi level regions plot for $Se_{55}S_{20}Sb_{15}Sn_{10}$ as a function of thermal neutron irradiation dose

The local state density determined by Eq. (3) can also be calculated as table (2) and figure (3) note how the thermal neutron radiation dose affects it [18]. As for the local state density, it was before irradiation 5.28×10^{11} $eV^{-1}cm^{-3}$ for sample A, and it decreased after irradiation, and it was 1.38×10^{10}, 4.32×10^{11}, and 4.94×10^{10} $eV^{-1}cm^{-3}$ for samples B, C and D at a radiation dose of 6.04×10^{10}, 12.08×10^{10}, 18.12×10^{10} $n.cm^{-2}s^{-1}$, respectively, as shown in Fig. (3) and table (2). The transition of the alloy's crystalline structure from an amorphous to a crystal state is largely influenced by the rise in the stretched state's density and the fall in the state's density. Polycrystalline means that this behavior has reduced the randomness of the crystal structure of the samples irradiated with thermal neutrons [16].

To determine the localized state density around the Fermi level $N(E_F)$ for all samples before and after radiation, we substitute the parameter values of the pre-exponential factor σ_{03} and the jump distance R in the low-temperature region into Eq. (4) and write the results in table (2).

From Fig. (3) and table (2), it can be seen that the densities of local states close to the Fermi level decrease with the increase in the dose of thermal neutrons, where the value was recorded as 2.85×10^{7} $eV^{-1}cm^{-3}$ before radiation and became 1.18×10^{7}, 5.3×10^{6} and 9.32×10^{6} $eV^{-1}cm^{-3}$ after radiation for samples B, C and D respectively.

4. Conclusions

The effects of thermal neutron radiation exposure on the density of localized, extended, and localized Fermi level states in melting-quenched $Se_{55}S_{20}Sb_{15}Sn_{10}$ alloy were studied. When determining electrical conductivity, three conduction pathways are discovered, indicating the existence of extended, local, and Fermi-level states at low, medium, and high temperatures, where it was found that all of these densities of states are unmistakably affected by variations in the dose of thermal neutron radiation. The width of the energy tails, the hopping distance of the electrons, as well as the activation energy all vary with the radiation dose.

References

[1] N. Tohge, H. Matsuo and T. Minami, "Electrical properties of n-type semiconducting chalcogenide glasses in the system Pb-Ge-Se", *J. Non-Cryst. Solids*, 95 (1987) 809-816.

[2] N. Tohge, K. Kanda and T. Minami, "Formation of chalcogenide glass p-n junctions", *Appl. Phys. Lett.*, 48(25) (1986) 1739-1741.

[3] R.A Street and N.F. Mott, "States in the gap in glassy semiconductors", *Phys. Rev. Lett.*, 35(19) (1975) 1293.

[4] N.F. Mott, "Introductory talk; Conduction in non-crystalline materials", *J. Non-Cryst. Solids*, 8 (1972) 1-18.

[5] K.A. Shore, "Electronic processes in non-crystalline materials", 2nd ed., N.F. Mott and E.A. Davis, *Contemp. Phys.*, 55(4) (2014) 337.

[6] S.P. Vikhrov, P. Nagels and P.K. Bhat, "n-Type Conduction in Chalcogenide Glasses of the Ge-Se-Bi System", *Recent Develop. Cond. Matter*

Phys.: vol. 2, Metals, Disordered Systems, Surfaces, and Interfaces, Springer (NY, 1981), 333-340.

[7] N. Tohge, T. Minami and M. Tanaka, "Photoconductivity of vitreous chalcogenides chemically modified by bismuth", *J. Non-Cryst. Solids*, 59 (1983) 999-1002.

[8] J.S. Mohammed et al., "Investigating the optical and electrical characteristics of $As_{60}Cu_{40-x}Se_x$ thin films prepared using pulsed laser deposition method", *Chalcogen. Lett.*, 20(7) (2023) 449-458.

[9] K.A. Jasim, S.A. Makki and A.A. Almohsin, "Comparison Study of Transition Temperature between the Superconducting Compounds $Tl_{0.9}Pb_{0.1}Ba_2Ca_2Cu_3O_{9-\delta}$, $Tl_{0.9}Sb_{0.1}Ba_2Ca_2Cu_3O_{9-\delta}$ and $Tl_{0.9}Cr_{0.1}Ba_2Ca_2Cu_3O_{9-\delta}$", *Phys. Procedia*, 55 (2014) 336-341.

[10] B.A. Ahmed et al., "The dependence of the energy density states on the substitution of chemical elements in the $Se_6Te_{4-x}Sb_x$ thin film", *Chalcogen. Lett.*, 19(4) (2022) 301-308.

[11] N.H. Khudhair and K.A. Jasim, "Study the effect of tin on the energy density of states of $Se_{60}Te_{40-x}Sn_x$ chalcogenide glass", *AIP Conf. Proc.*, 2769(1) (2023) 020062.

[12] N.H. Khudhair and K.A. Jasim, "Preparation and study the effective of Sb on the energy density of states of $Se_{60}Te_{40}$", *AIP Conf. Proc.*, 2769(1) (2023) 020056.

[13] N.H. Khudhair and K.A. Jasim, "A Study of the Effectiveness of Tin on the Thermal Conductivity Coefficient and Electrical Resistance of $Se_{60}Te_{40-x}Sn_x$ Chalcogenide Glass", *Ibn Al-Haitham J. Pure Appl. Sci.*, 36(1) (2023) 149-157.

[14] A.N. Abdulateef et al., "Calculating the Mechanisms of Electrical Conductivity and Energy Density of States for $Se_{85}Te_{10}Sn_{5-x}In_x$ Glasses Materials", *J. Green Eng.*, 10 (2020) 5487-5503.

[15] R.K. Chillab et al., "Fabrication of $Ge_{30}Te_{70-x}Sb_x$ Glasses Alloys and Studying the Effect of Partial Substitution on D.C Electrical Energy Parameters", *Key Eng. Mater.*, 900 (2021) 163-171.

[16] K.A. Jasim et al., "The effect of neutron irradiation on the properties of $Tl_{0.6}Pb_{0.3}Cd_{0.1}Ba_2Ca_2Cu_3O_{9-\delta}$ superconductors", *Turkish J. Phys.*, 37(2) (2013) 237-241.

[17] Z.J. Neamah et al., "The effect of gamma radiation on the manufactured $HgBa_2Ca_2Cu_{2.4}Ag_{0.6}O_{8+\delta}$ compound", *Mater. Sci. Forum*, 1050 (2022) 41-47.

[18] D. Adler, (1975). **"Disordered materials: Amorphous and liquid Semiconductors"**. J. Tauc (ed.), Plenum Press (NY, 1974), p. 442.

[19] J.K. Lee et al., "Control of thermoelectric properties through the addition of Ag in the $Bi_{0.5}Sb_{1.5}Te_3$ alloy", *Electron. Mater. Lett.*, 6 (2010) 201-207.

[20] M. Mobarak, H.T. Shaban and A.F. Elhady, "Electrical and thermoelectric properties of $CuInS_2$ single crystals", *Mater. Chem. Phys.*, 109(2-3) (2008) 287-290.

[21] H.A. Mahdi, K.A. Jasim and A.H. Shaban, "Manufacturing and improving the characteristics of the isolation of concrete composites by additive Styrofoam particulate", *Energy Procedia*, 157 (2019) 158-163.

[22] D.K. Paul and S.S. Mitra, "Evaluation of Mott's parameters for hopping conduction in amorphous Ge, Si, and Se-Si", *Phys. Rev. Lett.*, 31(16) (1973) 1000.

[23] K.A. Jassim, W.H. Jassim and S.H. Mahdi, "The effect of sunlight on medium density polyethylene Water pipes", *Energy Procedia*, 119 (2017) 650-655.

[24] D.J. Thouless, "Disordered materials: Electronic processes in non-crystalline Materials", N.F. Mott and E.A. Davis (ed.), 2nd ed., Clarendon (Oxford University Press), (NY, 1979), p. 590.

Table (1) Activation energies (ΔE_1, ΔE_2, ΔE_3) and values of (σ_{01}, σ_{02} and σ_{03}) are dependence on Neutron radiation of $Se_{55}S_{20}Sb_{15}Sn_{10}$ sample after and radiation

Neutron Dose ($n.cm^{-2}.s^{-1}$)	ΔE_1	σ_{oext}	ΔE_2	σ_{oLoc}	ΔE_3	σ_{ofermi}
0	0.43	4.66×10^{-4}	0.142	2.27×10^{-2}	0.0879	1.52×10^{-8}
6.04×10^{10}	0. 424	1.22×10^{-3}	0.242	9.22×10^{-2}	0.0168	9.25×10^{-6}
12.08×10^{10}	0. 39	1.79×10^{-3}	0.231	7.078×10^{-1}	0.0547	1.68×10^{-6}
18.12×10^{10}	0.41	$1.1\,2\times 10^{-3}$	0.217	3.54×10^{-1}	0.063	1.85×10^{-7}

Table (2) Tail width ΔE, a, R, N (E_{ext}), N (E_{loc}) and N(E_F) of $Se_{55}S_{20}Sb_{15}Sn_{10}$ alloy dependent on the of thermal neutron Irradiation Dose

Neutron Dose ($n.cm^{-2}.s^{-1}$)	ΔE (eV)	R A^0	a A^0	$N_{(Ext)}$ ($eV^{-1}cm^{-3}$)	$N_{(Eloc)}$ ($eV^{-1}cm^{-3}$)	$N_{(EF)}$ ($eV^{-1}cm^{-3}$)
0	0.288	2.7	1.45	1.5×10^{18}	5.28×10^{11}	2.85×10^{7}
6.04×10^{10}	0.182	2.8	1.16	3.94×10^{19}	1.38×10^{10}	1.18×10^{7}
12.08×10^{10}	0.159	1.08	1.09	5.78×10^{20}	4.32×10^{11}	5.3×10^{6}
18.12×10^{10}	0.193	3.30	1.215	3.62×10^{19}	4.94×10^{10}	9.32×10^{6}

Hind I. Fadhel

Department of Physics, College of Science, University of Baghdad, Baghdad, IRAQ

Synthesis and Characterization of Ag@Cu Core/Shell Nanoparticles via Pulsed Laser Ablation

This study explores the synthesis and characterization of Ag@Cu core/shell NPs through laser ablation in dimethyl sulfoxide (DMSO) and dimethylformamide (DMF) liquids. Employing a Q-switched Nd-YAG laser, we achieved controlled synthesis by directing the laser beam onto pure silver (Ag) and copper (Cu) metal targets immersed in DMSO and DMF, respectively. The two-step ablation method, using Ag nanoparticles as seeds, facilitated the creation of the core/shell structure with varying shell thickness. Detailed characterization was carried out and they provided insights into the optical properties, absorption peaks appear at the wavelength of 350 and 570nm, while the high absorption peak is at the wavelength of 410nm. The crystalline nature and phase composition of Ag was confirmed. The average size is around 30-50nm for Ag in DMF, 55-59nm for Ag@Cu in DMF, 23-70nm for Ag in DMSO and 22-60nm) for Ag@Cu in DMSO.

Keywords: Nanoparticles, Ag@Cu core/shell, Pulsed laser ablation, Nd:YAG laser
Received: 20 January 2024; **Revised:** 02 March 2024; **Accepted:** 09 March 2024

1. Introduction

Nanoparticles (NPs) have become pivotal players in contemporary materials science, exhibiting unique properties and promising applications across diverse fields [1]. Among the myriad of NP architectures, core/shell nanoparticles have garnered substantial attention due to their tunable properties and multifaceted functionalities [2]. The addition of metal ions, such as silver (Ag) and copper (Cu), to glass compositions can modify their physical and chemical properties and provide unique functionality for clinical applications. These metal ions are known to possess antimicrobial properties that can be useful in preventing or controlling infections [3,4]. For instance, silver ions are highly effective against a broad range of microorganisms, including bacteria, viruses, and fungi, by disrupting their cellular processes [5]. There is a high need for antibacterial formulations employed in tissue regeneration therapies [6]. Antibacterial metal ions have been around for a long time [7], and Ag has been shown to have good broad-spectrum bactericidal activity [8].

The utilization of laser ablation as a synthesis technique provides an innovative avenue for the controlled fabrication of nanoparticles. This method offers advantages such as precision, purity, and the ability to tailor the size and morphology of the resulting nanostructures [10]. Investigations focused on the impact of DMSO and DMF, both known for their solvating capabilities [11], in the synthesis of Ag@Cu core/shell NPs. The choice of these liquid media introduces an additional dimension to the synthesis process, allowing us to explore their role in shaping the core/shell architecture.

Figure (1) shows the Ag@Cu core/shell configuration chosen for its inherent synergies between silver (Ag) and copper (Cu). This combination not only enhances the stability of the nanoparticles but also imparts unique properties [12], opening avenues for applications in catalysis, sensing, and beyond. The investigation is centered on the exploration of surface plasmon resonance (SPR) in Ag@Cu core/shell nanoparticles. The collective oscillation of conduction electrons, as exhibited by SPR, governs the optical and electronic characteristics of nanoparticles and is a key determinant in their applications [13].

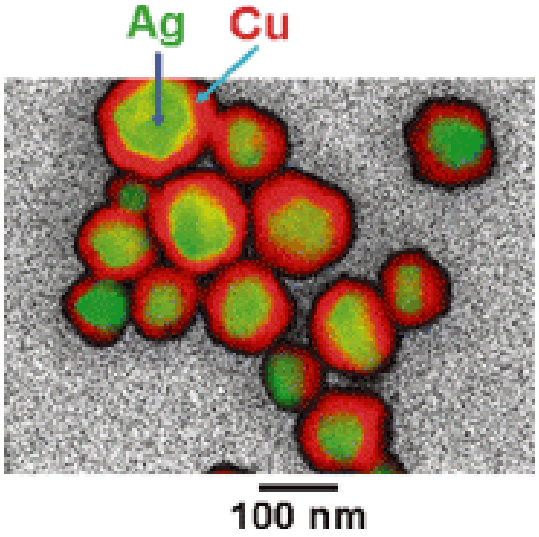

Fig. (1) Ag core-Cu shell nanoparticles [9]

To comprehensively characterize the Ag@Cu core/shell nanoparticles, a series of tests on each sample. UV-visible spectrophotometry analysis was employed to gain insights into the electronic transitions occurring within the nanoparticles, shedding light on their optical properties [14]. The x-ray diffraction (XRD) provided valuable information about the crystal structure and composition, elucidating the structural integrity of the synthesized nanoparticles [15]. Additionally, field-emission scanning electron microscopy (FE-SEM) allowed to introduce the morphology and surface features at the

nanoscale [16], contributing to a holistic understanding of the synthesized Ag@Cu core/shell nanoparticles.

In this study, we delve into the intricacies of synthesizing Ag@Cu core/shell nanoparticles, employing a laser ablation method and using dimethyl sulfoxide (DMSO) and dimethylformamide (DMF) as liquid media. Our exploration of surface plasmon resonance and comprehensive characterization throughout UV-visible spectra, XRD and FE-SEM analyses not only contributes to the fundamental understanding of core/shell nanostructures but also paves the way for their practical applications. By leveraging recent research and insights from the literature.

2. Experimental Part

Monometallic nanoparticles were synthesized utilizing a Q-switched Nd:YAG laser operating at a wavelength of 1064 nm, with a pulse width of 5 ns, and a repetition rate of 6 Hz. The laser beam was directed onto pure (99.9%) metal targets of silver (Ag) and copper (Cu) immersed in two distinct solvents, namely dimethylformamide (DMF) and dimethyl sulfoxide (DMSO). The metal targets were placed within a glass vessel with a total volume of 5 ml. To achieve nanoparticles of varied sizes, the laser energy was set at 1000 mJ using 400 pulses.

A sequential two-step ablation method, schematically depicted in Fig. (2), was employed for the synthesis of bimetallic Ag@Cu core-shell nanoparticles in DMSO and Ag-Cu core-shell nanoparticles in DMF. Initially, a colloidal solution of Ag nanoparticles was prepared by ablating an Ag target in both DMSO and DMF fluids. Subsequently, the Ag target was subjected to laser ablation in the freshly prepared Ag nanoparticle colloidal solution. The Ag nanoparticles served as seeds, forming the core for the ablated Cu species. The ablation process comprised 400 pulses for both Ag and Cu targets to achieve a core-shell morphology.

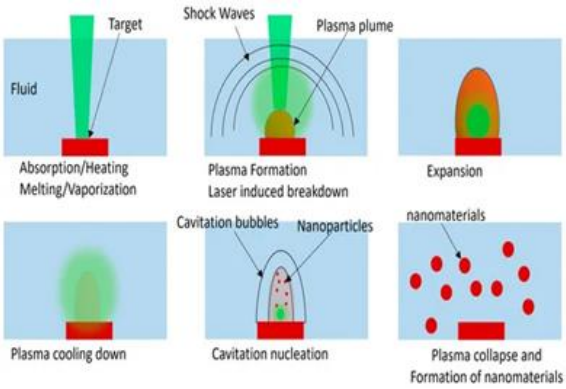

Fig. (2) Schematic illustration of the laser ablation during the laser−target-liquid system for each laser pulse [7]

Optical absorption spectra of the freshly prepared nanoparticles were recorded using a Shimadzu 1800 UV–visible spectrophotometer providing insights into their electronic transitions and optical properties. An AERIS Malvern Panalytical x-ray diffraction (XRD) instrument and Inspect^{tm} F50 FEI field-emission scanning electron microscope (FE-SEM) were used to introduce the structural characteristics of the prepared nanoparticles. The collected nanoparticles were then dried drop by drop onto p-type (100) silicon substrates, preparing them for subsequent XRD and SEM analyses.

This comprehensive experimental approach allowed us to control the size and composition of the monometallic nanoparticles and engineer the morphology of the bimetallic Ag-Cu core-shell nanoparticles. The spectroscopic and structural characterizations undertaken throughout UV–visible, XRD and FE-SEM analyses will provide essential insights into the properties and potential applications of the synthesized nanoparticles. The use of different solvents and the two-step ablation process contribute to the versatility of the proposed synthesis method, offering a platform for tailoring nanoparticle characteristics for specific applications.

3. Results and Discussion

The UV-visible spectra of the synthesized Ag@Cu core/shell nanoparticles revealed distinctive absorption peaks, indicative of the plasmon resonance associated with the nanoparticles.

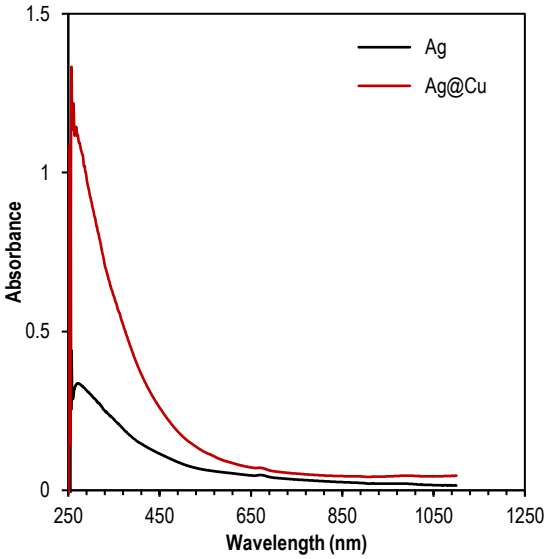

(a) Ag and Ag@Cu in DMF

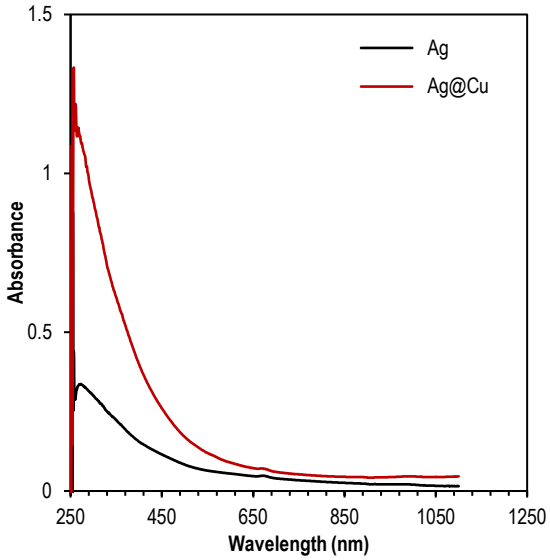

(b) Ag and Ag@Cu in DMSO

Fig. (3) UV-visible spectra for (a) Ag and Ag@Cu in DMF and (b) DMSO

In Fig. (3a), weak absorption peaks appear at the wavelength of 350 and 570nm, while the curve in the same figure shows a relatively high absorption peak at the wavelength of 410nm. This curve is very similar to the curve for silver (Ag). In Fig. (3b), curve no. 1 shows high absorbance in the UV wavelength region, gradually decreasing with increasing wavelength, reaching its lowest value at infrared wavelengths. As for curve no. 2, it shows behavior similar to curve no. 1. With a lower intensity, two absorption peaks appear in this spectrum: the first is high, at a wavelength of approximately 260 nm, while the second peak is centered at a wavelength of approximately 685 nm.

The presence of sulfur (S) within the chemical structure of DMSO solvent led to the formation of the S=O bond [17] and thus increased the polarity of the mixture due to the higher polarity of DMSO solvent compared to DMF solvent (7.2 for DMSO solvent and 6.4 for DMF solvent) as well as the larger value of the dielectric constant (49 for DMSO solvent and 37 for DMF solvent DMF), which caused an increase in the absorption of the mixture in the ultraviolet region (200-400nm), as the dominant spectral activity in this region of the electromagnetic spectrum is due to the $\pi \rightarrow \pi^*$ transitions, which are greatly affected by the polarity of the materials composing the mixture. It is noted that the distinct absorption peak at length The wavelength of 410nm almost disappeared in the case of the mixture in DMF solvent, as the hydrocarbon bonds that make up this solvent are generally characterized by high absorbance in the ultraviolet region of the electromagnetic spectrum.

FE-SEM was employed to unravel the morphological intricacies of the synthesized Ag@Cu core/shell nanoparticles. The obtained images shed light on the structural features, offering valuable insights into the size, shape, and surface characteristics of the nanoparticles.

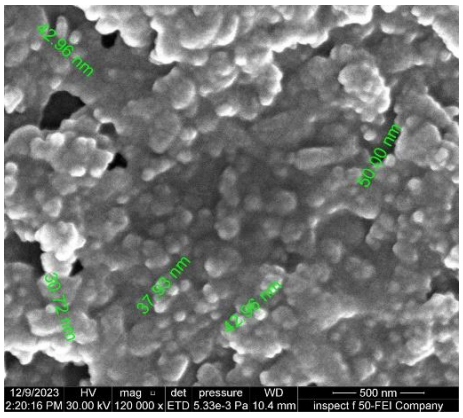

(a) Ag DMF

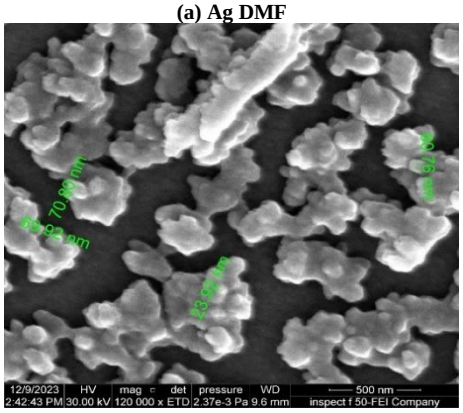

(b) Ag DMSO

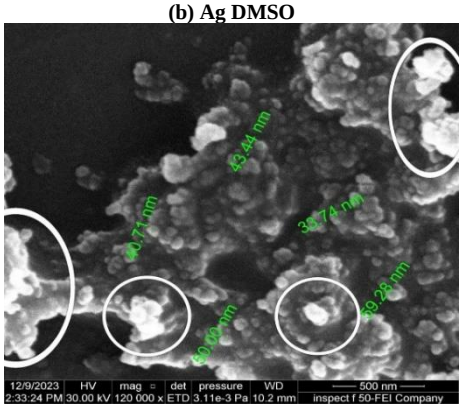

(c) Ag@Cu DMF

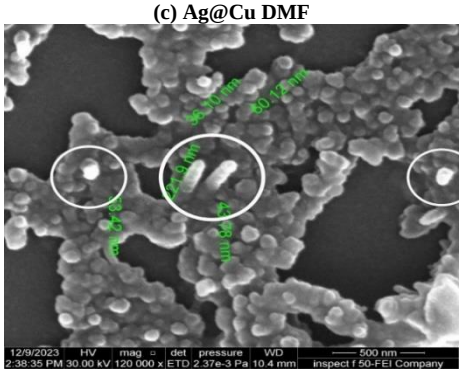

(d) Ag@Cu DMSO

Fig. (4) FE-SEM microimages for (a) Ag in DMF, (b) Ag in DMSO, (c) Ag@Cu in DMF and (d) Ag@Cu in DMSO

In both DMF and DMSO solutions, figure (4) shows that the FE-SEM images revealed well-defined

spherical nanoparticles with a discernible core/shell architecture. The average particle size is around 30-50nm for Ag in DMF and it is more compacted, 23-70nm for Ag in DMSO, and has more aggregation, which means that the same particle size with different solutions, 55-59nm for Ag@Cu in DMF, and 22-60nm for Ag@Cu in DMSO. The colloidal of Ag@Cu core/shell in DMSO is the most homogeneous than the Ag@Cu core/shell in DMF and also has the same particle size with different solutions, and notice that brightness reign shows crystal building, as in figures (4c) and (4d), underscores the precision of the laser ablation technique in controlling particle dimensions [18].

The uniform and spherical morphology observed in the FE-SEM images aligns with the successful formation of Ag@Cu core/shell nanoparticles. This structural integrity is crucial for potential applications in catalysis, sensing, and other nanotechnology domains where specific morphologies are often essential [19]. The distinct core and shell regions observed in the images indicate the effectiveness of the laser ablation process in achieving controlled synthesis [20].

The observed variations in particle size and morphology between DMF and DMSO solutions could be attributed to the solvent influence on nucleation and growth processes during synthesis [21]. DMF, being a polar aprotic solvent, may contribute to different nucleation kinetics compared to DMSO, a highly polar solvent. Such solvent-dependent variations have been noted in recent studies [22].

Additionally, the high-resolution FE-SEM images provide valuable insights into the surface roughness and porosity of the nanoparticles, factors that can influence their catalytic activity [23]. This detailed morphological understanding enhances our comprehension of the structure-property relationships critical for optimizing the performance of Ag@Cu core/shell nanoparticles in diverse applications.

The XRD patterns of Ag@Cu core/shell nanoparticles in DMSO and DMF are characterized by distinct peaks, each corresponding to specific crystallographic planes denoted by the (*hkl*) indices. The (*hkl*) values represent the Miller indices that uniquely identify the crystal planes contributing to the diffraction peaks.

Table (1) XRD peak results for Ag and Ag@Cu in both DMF and DMSO

Ag NPs in DMSO and DMF		Cu NPs in DMSO and DMF	
hkl	2θ	hkl	2θ
(111)	38.10°	(111)	43.47°
(200)	44.37°	(200)	50.37°
(220)	64.17°	(220)	73.99°

The XRD patterns exhibit sharp diffraction peaks, indicative of the crystalline nature of the synthesized nanoparticles. Table (1) illustrates that the corresponding (*hkl*) indices for these peaks can be assigned based on their positions in the XRD spectrum. For Ag, the (111), (200), and (220) peaks agree with the JCPDS card no. (00-001-1167), and for Cu the (111), (200), and (220) peaks in agreement with the JCPDS card no. (00-002-1225). These results signify the predominant crystallographic orientations within the Ag@Cu core/shell nanoparticles.

It can be seen that figure (5a) contains two curves. Seriously, when the XRD analysis subject to the Ag in DMF and Ag in DMSO solutions, at the first moment it has been observed a single crystal with very high-intensity 2θ = 68.80°. When this result was compared with another work, it didn't find the same single crystal, which means that this experiment revealed a novel result that the special peak has 2θ = 68.80° but, to match our results with other works, the XRD pattern has been split into two curves. The top contains concentrated crystalline particles with a high intensity greater than 6400 counts while the bottom has several peaks related to Ag metal obtained using a pulsed laser with low intensity of fewer than 100 accounts have miller indicates by (111), (200), and (220). Figure (5b) shows the result for Ag-DMSO revealed lower intensity (400 counts) compared to the Ag-DMF solution which means that the DMF solution leads to the arrangement of Ag crystals in specific 2θ = 68.80°.

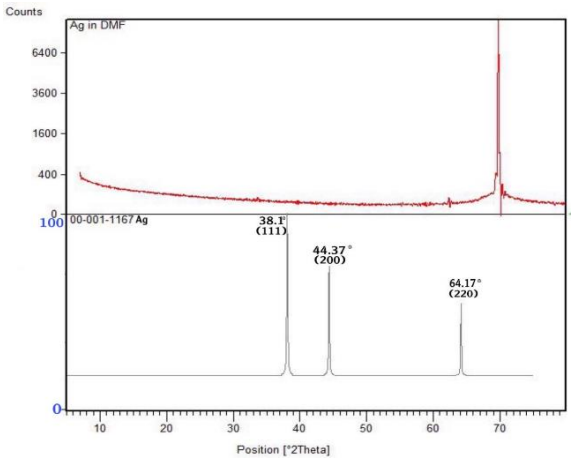

(a) Ag in DMF

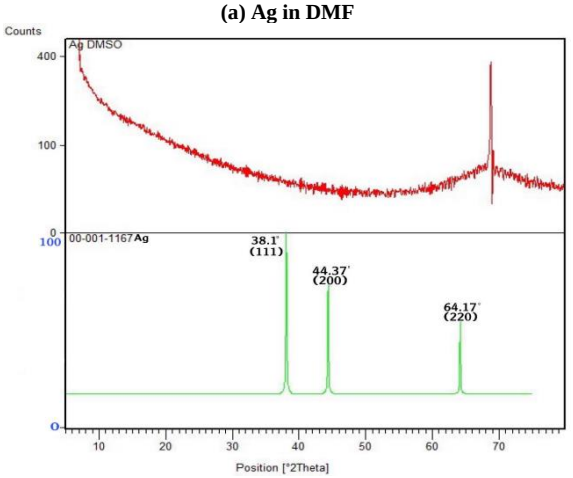

(b) Ag in DMSO

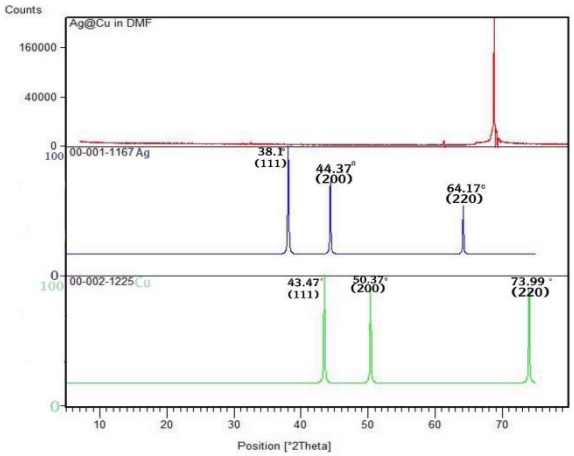

(c) Ag@Cu in DMF

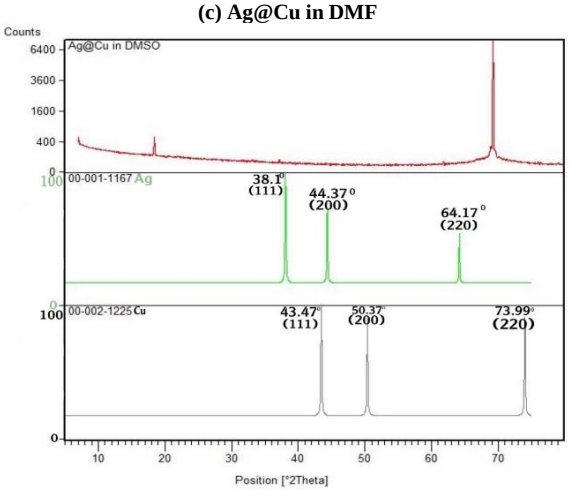

(d) Ag@Cu in DMSO

Fig. (5) XRD results for (a) Ag in DMF, (b) Ag in DMSO, (c) Ag@Cu in DMF and (d) Ag@Cu in DMSO

Figure (5c) demonstrates the incredible outcome analysis of Ag-Cu core/shell in DMF solution produced a very sharp, remarkable, and highest intensity crystal orientation which emphasizes the effect of DMF to conform the order configuration of core/shell, Ag-Cu ordering pattern with the presence of Ag and Cu basis peaks. Figure (5d) illustrates the addition of Cu target in Ag-DMSO solution and application of pulsed laser ablation in the same environment leads to enforcement to produce high intensity (6400 counts) crystal orientation in the same $2\theta = 68.80°$ when comparing with Fig. (5b).

4. Conclusion

The results obtained from this work proved the nanosized core-shell metal NPs with spherical shape. Results also showed that the colloidal of Ag NPs in DMSO is the most aggregation than Ag NPs in DMF, the colloidal of Ag@Cu core/shell in DMSO is the most homogeneous as Ag@Cu core/shell in DMF and has the same particle size with a different solution. The results unveil disparities in the crystalline nature and phase composition of Ag@Cu core/shell NPs. The diffraction patterns exhibit unique peaks (single crystalline) at 2θ=68.80° emphasizing the solvent-driven influence on the formation of the core/shell structure.

References

[1] M. Sajid and J. Płotka-Wasylka, "Nanoparticles: Synthesis, characteristics, and applications in analytical and other sciences", *Microchem. J.*, 154 (2020) 104623.

[2] S. Dhiman et al., "Application of core/shell nanoparticles in smart farming: A paradigm shift for making the agriculture sector more sustainable", *J. Agricul. Food Chem.*, 69(11) (2021) 3267-3283.

[3] A. Mishra, J. Rocherullé and J. Massera, "Ag-doped phosphate bioactive glasses: Thermal, structural and in-vitro dissolution properties," *Biomed. Glass.*, 2(1) (2016) 38-48.

[4] N. Alasvand et al., "Copper/cobalt doped strontium-bioactive glasses for bone tissue engineering applications", *Open Ceram.*, 14 (2023) 100358.

[5] R.H. Hussian and D.K. Mahdi, "Investigation of the Structural Influences of Silver Oxide Addition in the Bioactive Phosphate Glasses", *East Euro. J. Phys.*, (3) (2023) 321-328.

[6] T.A. Kareem and D.K. Mahdi, "Synthesis and characterization of silver nanoparticles-doped mesoporous bioactive glass prepared by spray pyrolysis", *Eurasian Chem. Commun.*, 4 (2022) 330-337.

[7] F.E. Ciraldo et al., "Tackling bioactive glass excessive *in vitro* bioreactivity: Preconditioning approaches for cell culture tests", *Acta Biomater.*, 75 (2018) 3-10.

[8] S. Chernousova and M. Epple, "Silver as Antibacterial Agent: Ion, Nanoparticle, and Metal", *Angewendte Chemie Int. Ed.*, 52(6) (2013) 1636-1653.

[9] M. Tsuji et al., "Synthesis of Ag@ Cu core–shell nanoparticles in high yield using a polyol method", *Chem. Lett.*, 39(4) (2010) 334-336.

[10] M. Alheshibri, "Fabrication of Au–Ag Bimetallic Nanoparticles Using Pulsed Laser Ablation for Medical Applications: A Review", *Nanomater.*, 13(22) (2023) 2940.

[11] V. Vasudevan and S.H. Mushrif, "Insights into the solvation of glucose in water, dimethyl sulfoxide (DMSO), tetrahydrofuran (THF), and N,N-dimethylformamide (DMF) and its possible implications on the conversion of glucose to platform chemicals", *RSC Adv.*, 5(27) (2015) 20756-20763.

[12] K.S. Tan and K.Y. Cheong, "Advances of Ag, Cu, and Ag–Cu alloy nanoparticles synthesized via chemical reduction route", *J. Nanoparticle Res.*, 15 (2013) 1-29.

[13] A. Piatek, "Laser generated magneto-plasmonic Fe-Au Nanoparticles: Formation, Real Structure and Properties", PhD dissertation, Universität Duisburg-Essen (2020).

[14] J. Pansieri et al., "Ultraviolet–visible–near-infrared optical properties of amyloid fibrils shed

light on amyloidogenesis", *Nature Photon.*, 13(7) (2019) 473-479.
[15] R. Schloegl, "X-ray Diffraction: A Basic Tool for Characterization of Solid Catalysts in the Working State", *Adv. Catal.*, 52 (2009) 273-338.
[16] M.A. Majeed Khan et al., "Structural and thermal studies of silver nanoparticles and electrical transport study of their thin films", *Nanoscale Res. Lett.*, 6 (2011) 1-8.
[17] M. Calligaris, "Structure and bonding in metal sulfoxide complexes: an update", *Coordin. Chem. Rev.*, 248(3-4) (2004) 351-375.
[18] T.A. Schmitz et al., "Towards nanoscale molecular analysis at atmospheric pressure by a near-field laser ablation ion trap/time-of-flight mass spectrometer", *Anal. Chem.*, 80(17) (2008) 6537-6544.
[19] F.C. Adams and C. Barbante, "Nanoscience, nanotechnology, and spectrometry", *Spectrochim. Acta B: Atom. Spectro.*, 86 (2013) 3-13.
[20] S. Petrović et al., "Agglomeration in the core-shell structure of CuAg nanoparticles synthesized by the laser ablation of Cu target in aqueous solutions", *J. Opt.*, 17(2) (2015) 025402.
[21] V.A. Ermakov et al., "Size control of silver-core/silica-shell nanoparticles fabricated by laser-ablation-assisted chemical reduction", *Langmuir*, 33(9) (2017) 2257-2262.
[22] D.G. Kwabi et al., "Controlling solution-mediated reaction mechanisms of oxygen reduction using potential and solvent for aprotic lithium–oxygen batteries", *J. Phys. Chem. Lett.*, 7(7) (2016) 1204-1212.
[23] J. Ustarroz et al., "Electrodeposition of highly porous Pt nanoparticles studied by quantitative 3D electron tomography: influence of growth mechanisms and potential cycling on the active surface area", *ACS Appl. Mater. Interfac.*, 9(19) (2017) 16168-16177.

Thikra K. Al-Khafaji

Open Educational College, Ministry of Education, Baghdad, IRAQ

Effects of Variable Applied Voltage on Dielectric Barrier Discharge Plasma Parameters: Comparative Study

The purpose of the COMSOL Multiphysics program is to create a simulation that is similar to an experimental device. In this paper, a one-dimensional simulation for discus plate DBD is done in COMSOL Multiphysics software. DBD system, which used argon as the working gas and an ac power supply running at a frequency of 9.1 kHz, is reported in this study. Investigating the effects of voltage on temperature and electron density in our device, it is shown that an increase in voltage from 2 to 12 kV results in an increase in electron density from 5.405×10^{17} to 7.432×10^{17} cm^{-3} and also increasing the electron temperature. By utilizing COMSOL, results showed an excellent agreement between experiment and COMSOL simulations results. According to the study, electron density could reach orders of 1017 cm-3 by optimizing which control of applying Voltage. The results of this study provide important insights into the field of plasma technology and its applications, where they may serve as a basis for future extensive research.

Keywords: Plasma; Electron density; Electron temperature; DBD; COMSOL
Received: 04 November; **Revised:** 05 December; **Accepted:** 12 December 2023

1. Introduction

Many research studies have explored non-thermal plasma, like dielectric barrier discharge plasma (DBD), for various applications due to its significant potential in technology. Non-thermal plasma, which can produce high-density plasma at room temperature, is widely favored for its eco-friendliness, cost-effectiveness, and independence from expensive specialized labs [1,2]. A dielectric barrier discharge, often known as a silent discharge or barrier discharge, involves using at least one electrode covered with a dielectric material. The dielectric layer serves as a safety measure, limiting electric current and preventing the occurrence of sparks or arc discharges [3]. Common materials used for this purpose are glass, ceramics, quartz, enamels, and epoxy. Among others [4,5], a dielectric barrier discharges (DBDs) exhibit a unique behavior, combining non-equilibrium and near-continuous properties. They are known for having high-energy electrons while keeping other heavy particles (neutrals and ions) at lower temperatures. DBDs generate various chemically active components, including electrons, free radicals, and ions, without significantly heating the surrounding gas. Because of these characteristics, DBDs find extensive use in applications such as gas purification (removing sulfur oxides, nitrogen oxides,, and volatile organic compounds), notably in the generation of ozone, the alteration of polymer surfaces, plasma-based vapor deposition, and pollution control, sterilization in medical applications water treatment, agriculture and numerous other technologies [6,7] micro discharge plasma parameters, especially electron density and temperature that affect the properties of plasma, additionally other number of factors, including flow rate, gas composition, applied voltage, frequency, electrode design, and dielectric type [1,8]. There must be coherence between theory and experiment in science. This implies that there is essentially a theoretical foundation for what is done empirically. We use the simulation technique to avoid the high cost on setup design and to prevent wasting time with the goal of applying the optimal conditions to real-world trials, and forecast plasma behavior under various circumstances especially if the input data that the program requires are accurate. It will give us results that are very close to the experimental results [9]. In this study, we use the COMSOL Multiphysics program to simulate the phenomenon and investigate the degree to which experimental data match the simulation [10].

There are two goals of this work, the first goal is to thoroughly examine how the dielectric barrier discharge (DBD) plasma behaves when the voltage in the system is changed, and the second is to investigate if the simulation of the experiment using COMSOL program gives a good match with the experimental work result. Electron temperature, electron density, plasma frequency, and Debye length – all of which are impacted by voltage variations – were measured using spectroscopy techniques, and the outcomes of the simulation and the experiment were compared.

2. Experimental Part and Plasma diagnostics

The plasma generation chamber is made up of two solid brass cylinders, each measuring 40 mm in height and 25 mm in diameter. They are positioned about 5 mm apart. A thin layer of insulating glass, just 1 mm thick, is sandwiched between these two cylinders. The chamber itself is cylindrical and constructed from Teflon material. It has a 50 mm diameter and includes two openings: one for introducing argon gas and the other for letting it escape. To ignite the plasma, we

use an alternating electric current source that can vary in frequency. This source provides a high voltage in the range of 0 to 20 kilovolts, as well as the argon gas flow rate was kept constant at 2 L/min. In this setup, the electric field created by the voltage difference between the electrodes is uniform. This ensures that the resulting plasma occupies the entire space from just beneath the anode to the surface of the dielectric covering the lower electrode (cathode) [11]. As depicted in Fig. (1), the AC dielectric barrier discharge (DBD) system that was used in this work, (a) for experimental setup, and (b) simulation setup in the COMSOL software.

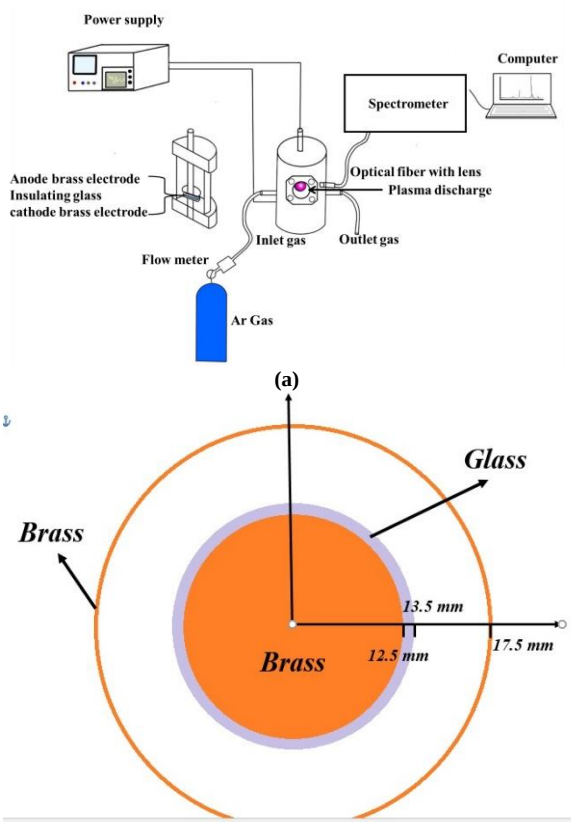

Fig. (1) (a) The experimental setup design for the Dielectric Barrier Discharge, and (b) Schematic design of the simulation setup

A discharge begins when the breakdown voltage is attained. Ionization takes place during discharges in gases at atmospheric pressure, and a large number of random arcs emerge in the operating gap between the two electrodes. [12]. The layer is charged by the accumulation of the charge incoming ions or electrons, where they discharge in microseconds, reforming elsewhere on the surface. Moreover, the surface charge restricts the amount of charge that can be transported to the electrodes by lowering the electric field in order to prevent the glow discharge from turning into an arc [13]. This charge accumulation process is transient; as long as a sinusoidal voltage is applied, the process will repeat itself and reverse in the other way when the electric field potential is reversed. This so-called dielectric barrier is what causes the plasma to self-pulse, which in turn causes a nonthermal plasma to form at room pressure. [14]. The large electrodes and short spacing between them result in a large surface-to-volume ratio for the DBD. In addition to maintaining a low gas temperature, this encourages heat diffusion losses. [15]. Optical emission spectroscopy (OES) is one technique for diagnosing plasma. In fact, it's possible to say that the emission lines serve as the excited species' fingerprints, to determine the plasma's parameters such as plasma frequency, electron density, and Debye length. The plasma electron temperature was counted using Boltzmann plot method [16]

$$ln\left[\frac{\lambda_{ji} I_{ji}}{hcA_{ji} g_j}\right] = -\frac{1}{k_B T}(E_j) + ln\left|\frac{N}{U(T)}\right| \quad (1)$$

where g_i is statistical weight, while I_{ji} is the relative emission line density between energy levels i and j, λ_{ij} is the wavelength (in nm), k_B is the Boltzmann constant, A_{ji} is the potential for radiation to be automatically transmitted from level i to the lower level j, E_j is the excitation energy for level i, N refers to the densities of the population of the state, $U(T)$ is the partition function, h is the Planck's constant, and c is the speed of light. Debye's length (λ_D) is calculated using the formula shown below [17]

$$\lambda_D = \left(\frac{\varepsilon_0 k_B T_e}{n_e e^2}\right)^{1/2} \quad (2)$$

where n_e is the density of the electrons, Free space permittivity is denoted by ε_0, e is the electron charge, and T_e is the electron temperature. Plasma frequency (ω_p) can be given as [18,19]:

$$\omega_p = \left(\frac{n_e e^2}{\varepsilon_0 m_e}\right)^{1/2} \quad (3)$$

where m_e is the mass of the electron, and the rest of the parameters are known above

2.1 Governing Equations to DBD simulations

We use COMSOL Multiphysics program (version 6.1) to simulate the phenomenon. COMSOL software calculates the average electron density and electron energy that solved by COMSOL are respectively [20,21]:

$$\frac{\partial y}{\partial t}(n_e) + \nabla \cdot [-n_e(\mu_e \cdot E) - D_e \cdot \nabla n_e] = R_e \quad (4a)$$

$$\frac{\partial y}{\partial t}(n_\varepsilon) + \nabla \cdot [-n_\varepsilon(\mu_e \cdot E) - D_\varepsilon \cdot \nabla n_\varepsilon] + E \cdot \Gamma_e = R_e \quad (4b)$$

where n_e is the electron density, D_e is the electron diffusion coefficient, and Γ_e is the electron flux, R_e the rate of electron production, μ_e the electron mobility, n_ε is the electron energy density and E is the electric field

3. Results and Discussion

3.1 Optical Emission Spectroscopy (OES)

In order to investigate the effect of voltages applied on the spectra generated, figure (2) displays the emissions spectra of the generated plasma using various voltage values. According to NIST data [22],

this figure exhibits a variety of peaks, the majority of which are associated with ArI. The results for the locations of the most important peaks in the spectrum at 696.54, 763.51, 772.38, 801.47, 811.53, 826.45, 842.46, and 912.30 nm, as well as found that the maximum intensity was at 763.6 nm at 12 kV.

According to the figure, as the applied voltage is raised, the peak intensity rises. Due to an increase in the potential difference between the electrodes, which gives the electrons sufficient excitation energy, the acceleration of the electrons increases with the potential difference. This causes more ionization collisions, which in turn increases the intensity of the plasma emission. This result which agrees with [16,23].

The relation between between (Ln[$\varepsilon_{ji}\lambda_{ij}/A_{ji}g_j$]) versus upper energy level (Ej) for the dielectric barrier discharge (DBD) system for each voltage was utilized to compute the T_e values using Eq. (1). The results are displayed in Fig. (3). Additionally, the fitting equation for each voltage as well as the statistical coefficient (R^2) are included in this figure.

The figure's results show that the range of 0.9292-1 eV is where the fluctuation in the (0,1) values occurs proving the accuracy of the linear fit. Electron density ne can be calculated by Eq. (2) of a different voltage the outcomes are shown in Fig. (4). We notice an increase in the electron density in the range of 5.405-7.432x10^{17} cm^{-3} with different applied voltages, while the electron temperature (T_e) in the range of 1.236-2.551. This value clearly resulted that density and temperature of electron depends on the applied voltage and we notice of the figure that the electron temperature increasing from 1.236 to 2.648 eV, with increasing applied voltage from 2 to 10 kV, respectively, while decreasing slightly to 2.551 eV with 12 kV. Table (1) displays the plasma properties. Such as plasma frequency, electron density, electron temperature, and Debye length. For DBD plasma, at various voltages of an atmospheric pressure.

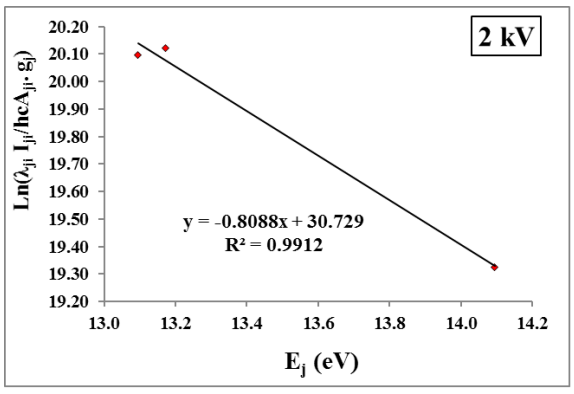

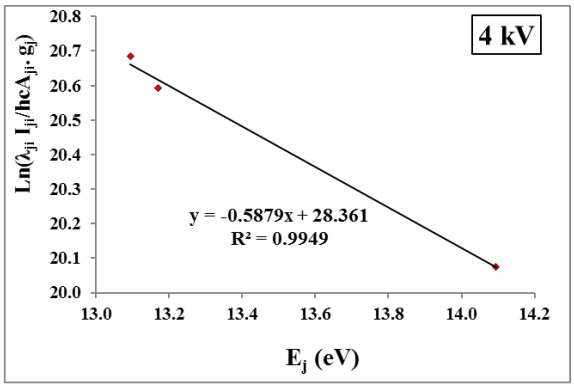

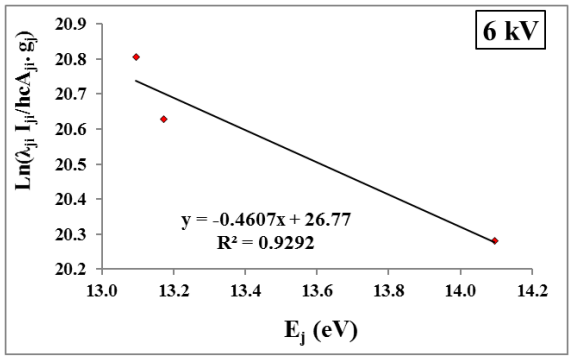

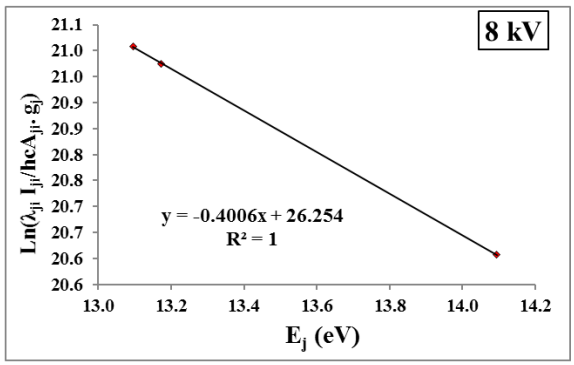

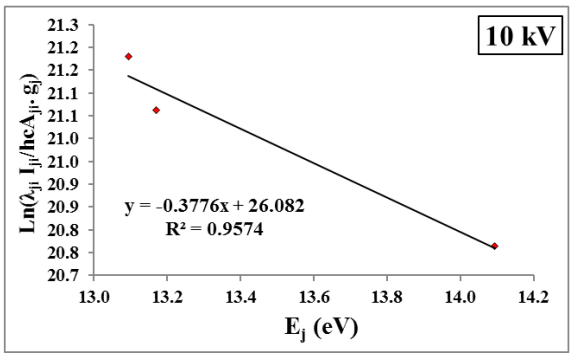

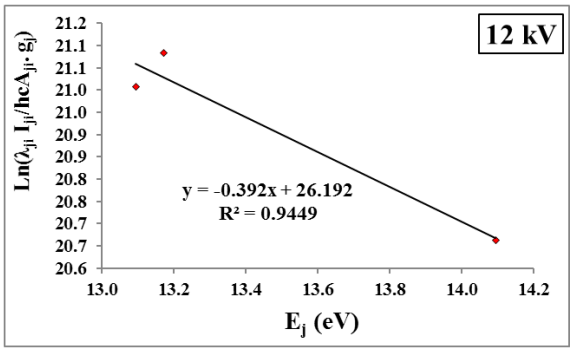

Fig. (3) Boltzmann plot for ArI peaks using the DBD system at various voltages

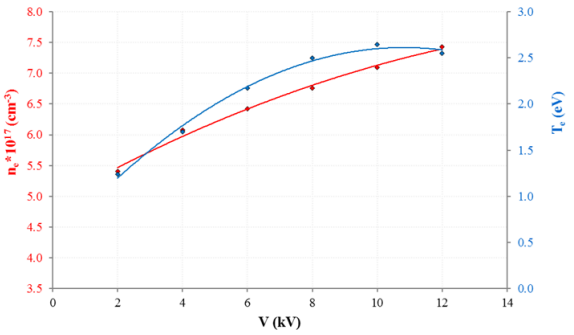

Fig. (4) The relationship between electron temperature (Te), electron density (ne) with Ar gas flow rates

According to that Figure and data listed in table (1), as the applied voltage between the two electrodes, is raised, electric field intensity in the electrodes gap increases, this is due to the fact that when the electrons are exposed to a high potential difference, they accelerate more and their kinetic energy increases, and thus their electron temperature increases. Although increasing the kinetic energy of the electrons causes an increase to more ionization collisions and thus an increase in the speed of the electrons.

The energy that the electrons gain as a result of acceleration is much greater than the energy that they lose as a result of the collisions. Therefore, we note that increasing the potential difference between the two electrodes causes an increase in the temperature of the electrons. However, this process is not achieved in absolute terms. Increasing the applied voltage also results in an increase in the density of particles, leading to heightened collisions. This, in turn, causes a reduction in the kinetic energy of the electrons and a subsequent decrease in electron temperature. Thus, it can be said that two factors are at play, competing for predominance whichever is predominant becomes the prevailing. And this maybe to explains the vacillated between the increase and decrease of electron temperature in different applied voltage. On the other hand, the electron density increases and thus an increase in the plasma emission intensity [24]. This result agrees with [23,25].

3.2 Simulation results

The simulation was carried out under constant conditions such as frequency of 9.1 Hz, a gas flow rate of 2 L/min, and fixed dimensions of setup, while voltage parameters that were changed in the range of 2 to 12 kV. Consequently, calculations were made for the electron temperature and electron density, and the results were compared with experimental data. A close examination of the COMSOL-provided diagrams for Fig. (5a) illustrate the electron temperature as a function of applied voltage; each point in the figure corresponds to a new run in the COSMOL with the specified working conditions.

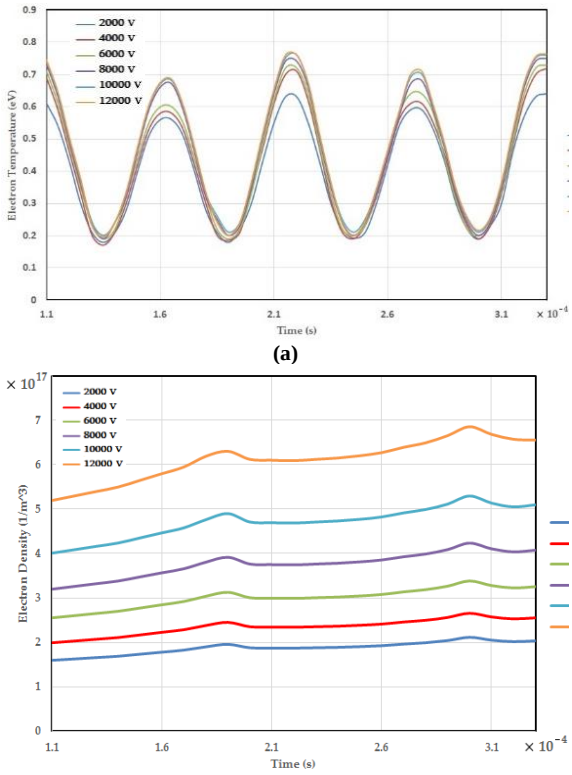

Fig. (5) Simulation results from COMSOL of (a) electron temperature, and (b) electron density, of versus applied potential at atmospheric air pressure

Table (1) Plasma parameters at various voltages

V (kV)	T_e (eV)	FWHM (nm)	n_e x10^{17} (cm^{-3})	f_p x10^{12} (Hz)	λ_D x10^{-6} (cm)
2	1.236	0.800	5.405	6.602	1.124
4	1.701	0.900	6.081	7.003	1.243
6	2.171	0.950	6.419	7.195	1.366
8	2.496	1.000	6.757	7.382	1.428
10	2.648	1.050	7.095	7.564	1.436
12	2.551	1.100	7.432	7.742	1.377

We notice the electron temperature curves increase against applied voltage increases. In Fig. (5b), we see the electron density at the mentioned voltages, also increased when the potential difference between the two electrodes increased. Based on the data obtained in this simulation, and according to Fig. (5a,b), we find that there is a good match with experimental data for the electron temperature and

electron density. Taking into account the small difference in the accuracy of the values between simulation and practical values.

4. Conclusion

In this work, the effects of applied voltage on DBD plasma characteristics are investigated experimentally and compared with the outcomes of a COMSOL Multiphysics simulation. The study examined how different voltages affected the parameters for plasma electron temperature and density. It has been demonstrated that the simulation results are consistent with the experimental data, suggesting that this approach is a successful substitute for practical experiments, the results showed that the behavior of the electron temperature and density changed with applied voltage, indicating that increasing the voltage caused the electron density to increase. Still, the temperature of the electrons increases.

References

[1] L. Dong et al., "Electron density of an individual microdischarge channel in patterns in a dielectric barrier discharge at atmospheric pressure", *Plasma Sources Sci. Technol.*, 17(1) (2008) 015015-1- 015015-5.

[2] S.M. Al Qaseer, M.K. Khalaf and S.I. Salih, "Optimal Power of Atmospheric Pressure Plasma Jet with a Simple DBD Configuration for Biological Application", *J. Phys.: Conf. Ser.*, 1999(1) (2021) 1-15.

[3] Y. Li et al., "The Effect of Voltage Pulse Shape on the Discharge Characteristics in the Packed Bed Reactor under Air and Nitrogen", *Appl. Sci.*, 12(4) (2022) 2215-1-2215-14.

[4] M.Y. Naz et al., "A low-frequency dielectric barrier discharge system design for textile treatment", *Synth. React. in Inorg. Metal-Org. Nano-Metal Chem.*, 46(1) (2016) 104-109.

[5] T.K. Al-Khafaji, "Treatment with Dielectric Barrier Discharge (DBD) plasma restricts Aspergillus niger growth isolated from wheat grain", *Baghdad Sci. J.*, 20(4(SI)) (2023) 1480-1488.

[6] R. Abidat, S. Rebiai and L. Benterrouche, "Numerical simulation of atmospheric dielectric barrier discharge in helium gas using COMSOL Multiphysics", in *3rd Int. Conf. Sys. Control*, IEEE (2013) 134-139.

[7] A. Bose et al., "Modelling and simulation of microplasma discharge device for sterilization applications", *MDPI Proc.*, 2(1) (2018) 1-6.

[8] O. Goossens et al., "Physical and chemical properties of atmospheric pressure plasma polymer films", *Gas*, 1(10) (2002) 00.

[9] S. Gadkari and S. Gu, "Numerical investigation of co-axial DBD: Influence of relative permittivity of the dielectric barrier, applied voltage amplitude, and frequency", *Phys. Plasmas*, 24(5) (2017) 053517-1-053517-12.

[10] M.K. Jassim, "Investigation in the Effect of Applied Voltage and Working Pressure on Some Plasma Parameters in the Positive Column of Dc Glow Discharge", *Ibn Al-Haitham J. Pure Appl. Sci.*, 32(2) (2019) 9-20.

[11] I.A.D. Souza et al., "Study of the influence of variation in distances between electrodes in spectral DBD plasma excitation", *Mater. Res.*, 19 (2016) 202-206.

[12] U.N. Pal et al., "Discharge characteristics of dielectric barrier discharge (DBD) based VUV/UV sources", *J. Phys.: Conf. Ser.*, 114(1) (2008) 012065 1-7.

[13] H. Ayan, "Uniform Dielectric Barrier Discharge with Nanosecond Pulse Excitation for Biomedical Applications", Ph.D. thesis, Drexel University (2009).

[14] E.O.M. Ruiz, "Partial oxidation of methane in a dielectric barrier discharge plasma milli-reactor", Ph.D. thesis, Université Pierre et Marie Curie-Paris VI (2017).

[15] R.E.J. Sladek, "Plasma needle non-thermal atmospheric plasmas in dentistry", Ph.D. thesis, Technische Universiteit Eindhoven, Netherlands Organization for Scientific Research (NWO) (2006).

[16] T.K. Al-Khafaji, "Design and Development of Atmospheric Pressure DBD Ar Plasma Jet for Investigating Cotton Fabric Hydrophilicity", *Iraqi J. Appl. Phys.*, 19(4C) (2023) 205-210.

[17] P.M. Bellan, **"Fundamentals of Plasma Physics"**, Cambridge University Press (2006).

[18] F.F. Chen, **"Introduction to Plasma Physics and Controlled Fusion"**, Cham: Springer International Publishing (2016), pp. 183-202.

[19] T.A. Hameed and S.J. Kadhem, "Plasma diagnostic of gliding arc discharge at atmospheric pressure", *Iraqi J. Sci.*, 60(12) (2019) 2649-2655.

[20] A. Mazandarani et al., "Calculation of temperature and density for dielectric-barrier discharge (DBD) plasma using COMSOL", *J. Nucl. Sci. Technol.*, 40(4) (2020) 99-108.

[21] M.H.A. Lahouel, D. Benyoucef and A. Gadoum, "One Dimensional Modeling Of Dielectric Barrier Discharge in Pure Oxygen at Atmospheric Pressure Using COMSOL Multiphysics", *arXiv preprint*, 20-21 January (2023), 2302-13813.

[22] J.E. Sansonetti and W.C. Martin, "Handbook of Basic Atomic Spectroscopic Data", *J. Phys. Chem. Ref. Data*, 34(4) (2005) 1559-2259.

[23] M.M. Kadhim, Q.A. Abbas and M.R. Abdulameer, "Study of some plasma characteristics in dielectric barrier discharge (DBD) system", *Iraqi J. Sci.*, 63(5) (2022) 2048-2056.

[24] N.C. Roy and M.R. Talukder, "Electrical and spectroscopic diagnostics of atmospheric pressure DBD plasma jet", *J. Bangladesh Acad. Sci.*, 40(1) (2016) 23-36.

[25] G. Rainer et al., "Development of atmospheric plasma sprayed dielectric ceramic coatings for high efficiency tubular ozone generators", *J. Water Resour. Protect.*, 2 (2010) 799-808.

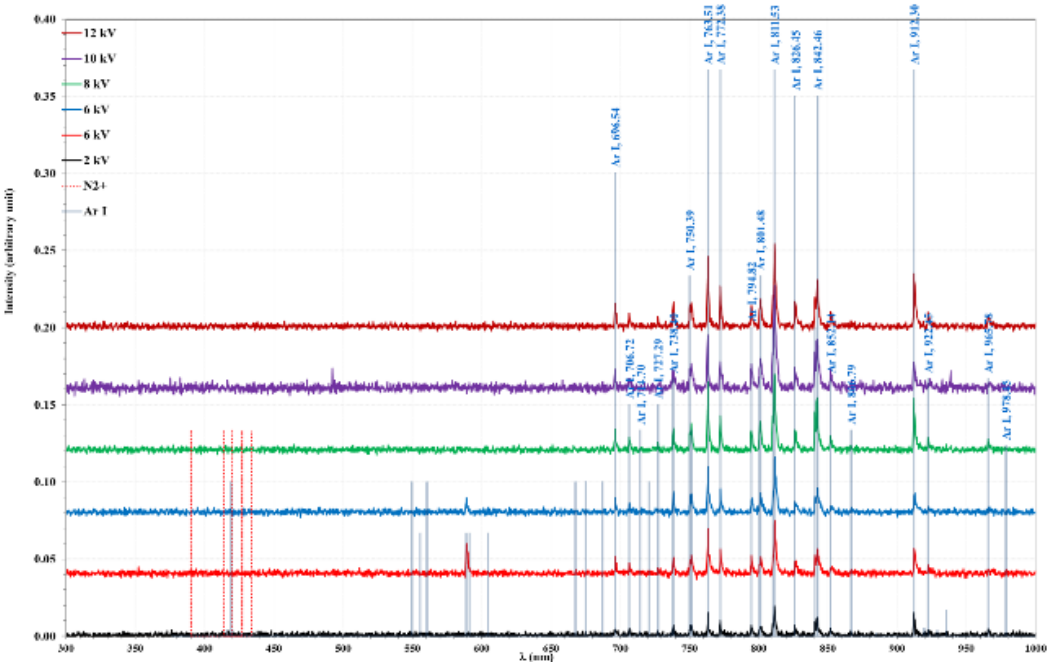

Fig. (2) The optical emission spectra of DBD plasma produced at various voltages of 2, 4, 6, 8, 10, and 12 kV

Emad Abdulmajeed [1]
Mohammed A. Hussein [2]

[1] *Department of Physics, College of Science, University of Kirkuk, Kirkuk, IRAQ*
[2] Department of Mechanization and Agricultural Equipment, College of Agriculture /Hawija, University of Kirkuk, Kirkuk, IRAQ

Effect of Changing Distance between Poles on Optical Properties of Gemini Lens

Modern and advanced software was used to reach quick results of the optical properties of the proposed models of Gemini lenses. Four basic designs of the objective magnetic lens were employed in scanning electron microscope, according to the design site and the required analysis ability, the four models were designed equal in geometric dimensions and file size, and the results showed that the Gemini objective lens (S3) achieved the best results because it obtained the lowest values for the final effective probe diameter and the focal length (f=4.76 mm) that corresponds to the highest value for analysis. At a constant value of the excitation (NI = 1000 A-t), it also had the lowest coefficients of spherical and chromatic aberration (Cs=4.14 mm) and (Cc=3.63 mm).

Keywords: Gemini lenses; Optical properties; Spherical and chromatic aberrations
Received: 04 November; **Revised:** 05 December; **Accepted:** 12 December 2023

1. Introduction

Revolution in the field of electronic optics led to the invention of the electron microscope in 1931 by Ruska and Knoll with an acceleration voltage of 50 kV and a magnification of 16 times, while Knoll evaluated the flaws that exist on object surfaces in them by designing a new electronic microscope called the scanning electron microscope (SEM) in 1935 [1]. In 1942, Zworykin developed the first scanning electron microscope by testing secondary electrons which give us images of features and properties of surface with an analysis capacity 25-50 nm [2]. The magnetic lens is one of the most important types of electronic lenses. Therefore, it is included in the manufacture of scanning electron microscopes, as it is characterized by the fact that unlike the electrostatic lens, it doesn't operate at high voltages, with its high analytical capacity and the advantage of being easy to manufacture. The accuracy of the work and the lack of costs, since the electromagnetic component of the lens performs the majority of its functions, it is more appropriate than a permanent magnet because it allows one to alter the magnetic field's strength by varying the current flowing through the coil or the number of turns it has [3]. The three basic categories of electromagnetic lenses are the iron-free lens, the monopolar lens, and the bipolar lens. Additionally, there exist three-pole lenses, which have more than two poles. The iron-free lens consist of ring coil in form of tape or wire, and the primary dependence of magnetic field in this type is the geometric shape of the coil [4]. The protrusion of the outer pole of this type of lens is one of its most important features, which leads to the magnetic flux density creeping away from the lens mount, which gives freedom of movement to the sample This type was used when there was a hole in its pole as an objective lens in the transmission electron microscope (TEM) and the scanning electron microscope (SEM) [5]. Bipolar lens is more widely used than others. This lens is designed from a coil, two iron poles, and an iron circle surrounding the two, and its working principle depends on the passage of a continuous electric current in the circular file, which generates an axially symmetrical magnetic field. It deflects the charged particles passing through it towards the axis of the coil, and for the purpose of increasing the magnetic flux density's maximum value and achieving a strong field confined to a small area, The gap is the area where the magnetic field is concentrated, and it is encircled by a cover made of (ferromagnetic) material with high magnetic permeability, such as wrought iron. The antenna, via which the electronic beam enters and leaves, is situated between two pieces of iron that symbolize two magnetic poles [6].

The aim of this work is to evaluate and investigate optical properties of four types of objective Gemini lenses and decided which one is the best by using computer programs.

2. Designed electronic lenses and used software

In this study, four models of Gemini objective lenses (S1, S2, S3, and S4) were used, and the distance between the pole pieces of these lenses is respectively S1=10 mm, S2=7 mm, S3= 4mm, S=1 mm, and the excitation factor is NI = 1000 A-t, and low voltage (V_r= 8kV).

2.1 Finite Element Method (FEM)

It is a numerical technique for solving a set of ordinary differential equations and solving the problem of voltage limits instead of approximating it. It was presented by Munro [13] and developed by Lencová [8] within the AMAG program as a basic basis for calculating the magnetic field. The total area, including the empty space around the poles, is divided into finite elements, forming "rough gratings" as a result of the overlapping of axial lines with radial lines, and the rough gratings are divided into smooth gratings, and these lines are processed by the program automatically [7]. The asymmetric pole is taken by taking the upper half of the lens and selecting the borders around the lens in which the voltage distribution is zero [8] to maintain the most dense distribution of the grid lines at the air gap of the lens and near the poles [9]. Gradually towards the outer limits, and the method of finite elements became one of the main methods used in the design of electronic devices and advanced micro devices [14].

2.2 AMAG Program

This program is distinguished by its high accuracy due to using many gridlines more than those used in the program [13]. This program can compute the magnetic flux density distribution of the electromagnetic lens that is rotationally symmetrical [8,13].

2.3 Flux M31 software

Munro created this program in 1975 [13] to depict the magnetic flux lines of electromagnetic lenses. This program is fed with the magnetic flux values obtained from the AMAG program, and then the magnetic flux values are calculated at each point of the finite element grids, and then these values are stored in A special file (File) to be inserted into the (Flux) program modified by Murad in 1998 [11], who made some software modifications to the M31 program, which was developed by Munro to be run on a compatible microcomputer (IBM) and called it "Flux". Magnetic flux lines are drawn by connecting the magnetic flux points at each point of the clamp, which have the same voltage value, where these lines take circular shapes concentrated around the iron poles, and these lines are convergent in areas of high density in the flux and divergent in areas of low density [10].

3. Results and Discussion

3.1 Axial Magnetic Flux Density Distribution:

Different values have been used for the distance between the lens's pole, which is S=10, 7, 4, 1 mm, in order to study the impact of the diameter on the axial magnetic field (B_z) and the path of the electronic beam [11], and consequently on the objective optics of the electromagnetic lens, where the figure (1) shows the axial magnetic flux density (B_z) distributions for symmetrical bipolar electromagnetic lenses along optical axis (z) and for different values of distance between the poles of the Gemini lenses (S=10, 7, 4, 1 mm). Figure (1) shows that decreasing the diameter of the axial aperture results in an increase. This feature is helpful for focusing the electron beam that passes through the optical axis of the lens (B_z) at the highest value of the magnetic flux density. Because it is generally known that peaks higher than (B_z) can be achieved by increasing the area CT of the excitation coil and reducing the distance between the coil and the sample, it can be claimed that this result is preliminary but it is not definitive [12].

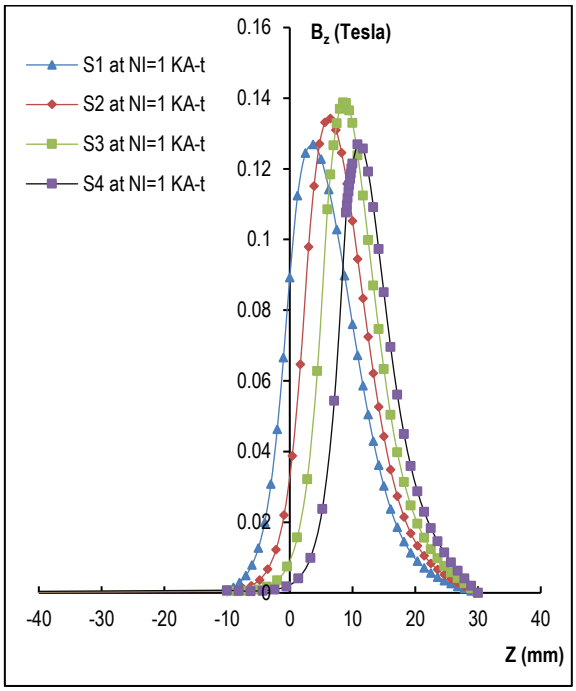

Fig. (1) The distribution curves of the axial magnetic flux density (B_z) at variable values of the axial aperture (z)

Table (1) Distribution curves of the axial magnetic flux density 4. Magnetic flux lines for electronic lenses designed

Lens icon	Z (mm)	B_{max} (T)
S1	3.75	0.125
S2	6.5	0.134
S3	8.5	0.139
S4	10.8	0.126

3.2 Magnetic flux lines for designed electronic lenses

The flux density and distribution across the magnetic circuits of unsaturated magnetic lenses were calculated for the flow assay using the M31 software [13] at NI = 1000 A-t. The designed lenses' flow path lines are shown in Fig. (2). By virtue of the uniform and minimal leaking of its flow lines, it is obvious that the S3 lens has the best appearance. Additionally, because they are required to have the intended impact on the charged particles passing through the lens, their flux lines propagate along the preferred direction and in the recommended manner. This outcome

provides a clear indicator of the desired lens. However, this requires more research.

3.3 Calculation of path of electronic beam inside objective lenses

The path of the electronic beam inside the magnetic lenses was calculated by entering the engineering data into the M21 program prepared by Munro in 1975 [13], and this is done using the fourth-order Runge-Kutta method by solving the axial beam equation. Figure (3) shows the path of the electronic beam with an accelerated voltage (V_r=8kV) and at excitation (NI=1000 A-t). It is clear from the shapes of the beam paths that the S2 lens has the lowest focal length compared to the rest of the lenses, and this in turn will give the lens the possibility of stronger focalization and thus less aberration compared to its counterparts [14]

Table (2) The change in chromatic and spherical aberration and focal length when the excitation coefficient is fixed (NI = 1000 A-t) and a variable voltage (V_r=8kV)

Lens icon	Cs	Cc	F_0 (mm)
S1	6.25	3.91	5.63
S2	5.07	3.71	4.91
S3	4.14	3.63	4.76
S4	5.71	4.17	5.34

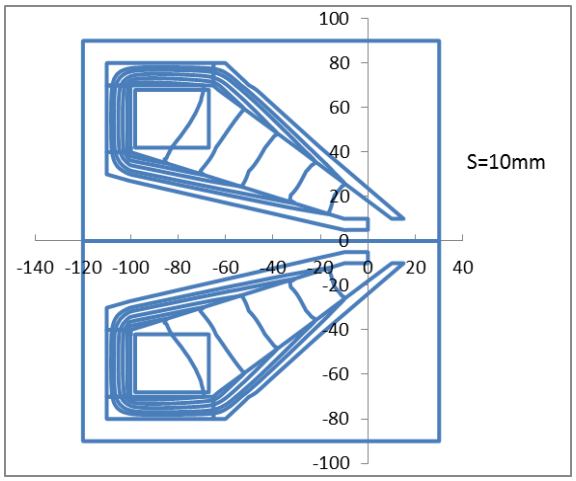

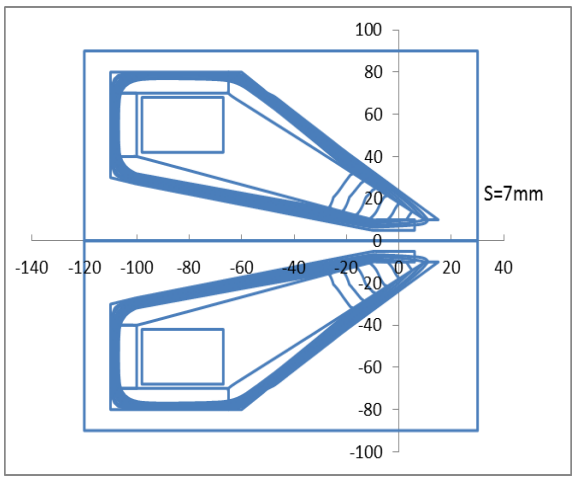

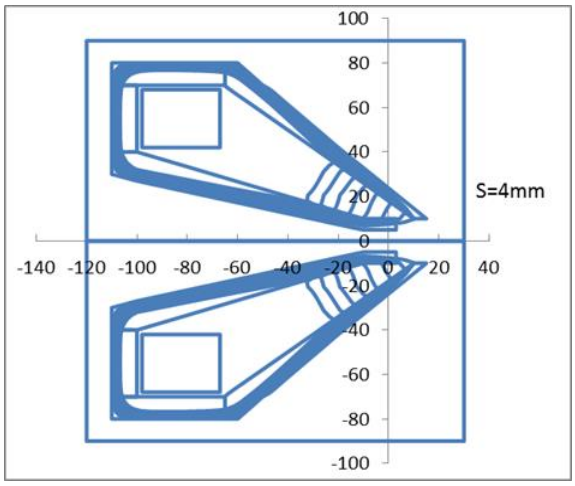

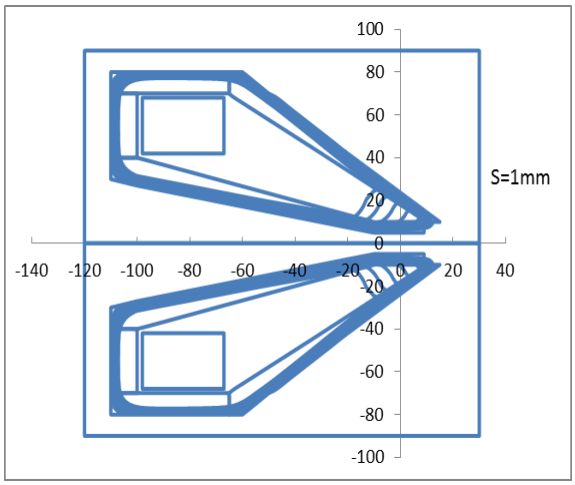

Fig. (2) Magnetic flux lines for Gemini lenses (S1, S2, S3, S4)

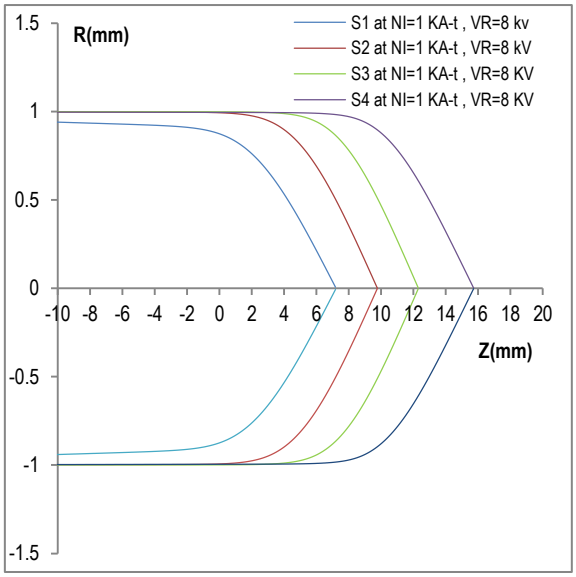

Fig. (3) The trajectory of the electronic beam at an accelerated voltage of V_r=8kV and excitation of NI=1000 A-t

3.4 Calculation of focal optical properties of objective lenses

The efficiency of magnetic-optical lenses can be determined by their similar properties such as the coefficient of chromatic aberration (C_C), This depicts the lens's capacity to focus the beam at a consistent wavelength, and The capacity of the lens to create an electronic beam that is configured in a dotted fashion with the least chance of distortion is known as the spherical aberration (C_S) or electronic spherical. And the focal length (f_0) defined as lens ability to focus the electron beam, the optical properties are estimated as a function of the excitation factor (NI) and as a function of the acceleration voltage (V_r) for the four designs to determine how well the lens can concentrate the electronic beam.

From the figures (4) and (5), we see that with increasing voltage (V_r) and constant excitation function (NI), the coefficient of spherical aberration (C_S) and chromatic aberration (C_C) both rise. Additionally, we observe that lens S3 has the lowest combined value for the coefficients of spherical and chromatic aberration. Comparing the voltage to the other lenses (S1, S2, S4). As seen in Fig. (6), the increase in voltage is to push the electrons to a far point, which leads to the formation of a focal length at the farthest point.

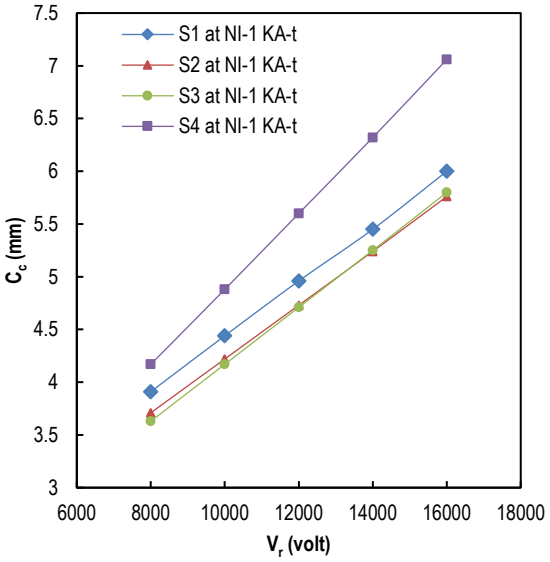

Fig. (4) Change of chromatic aberration with constant excitation function NI to the change of accelerating voltage V_r

3.5 Calculation of probe diameter formed in objective lenses

When determining the electronic beam's effective total diameter (d_p) as it strikes the model's surface, and the accompanying exposure due to the contributions of spherical or chromatic aberration and diffraction experienced by models the four models' objective lens as a function of aperture angle α_p [15], As shown in Fig. (7), where this figure shows the relationship between the diameter of the final effective probe (d_p) according to the aperture angle (α_p) for the four designs at fixed values for each of the excitation factor (NI=1000 A-t) and the voltage of acceleration (V_r=8kV), as a result (S3) lens has a lowest value of final effective electron probe diameter which corresponds to a aperture angle value as shown in table (3)

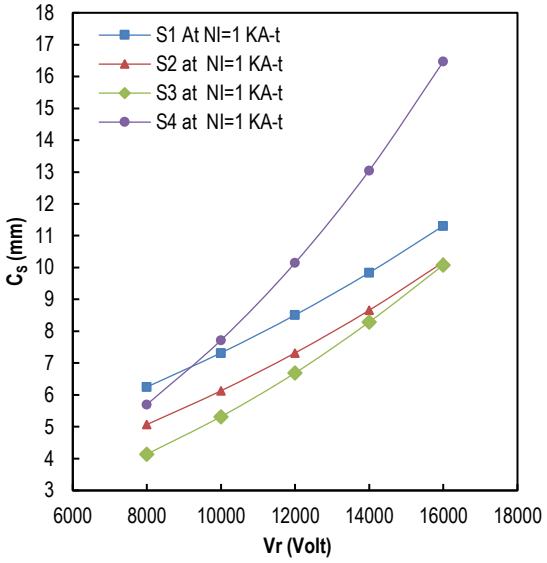

Fig. (5) Change of spherical aberration with constant excitation function NI to the change of accelerating voltage V_r

Table (3) Final effective electron probe diameter to the aperture angle

Lens icon	α_{opt} (mrad)	d_{pmin} (mm)
S1	5.5	5.7
S2	5.5	5.5
S3	5.5	5.4
S4	5.5	5.9

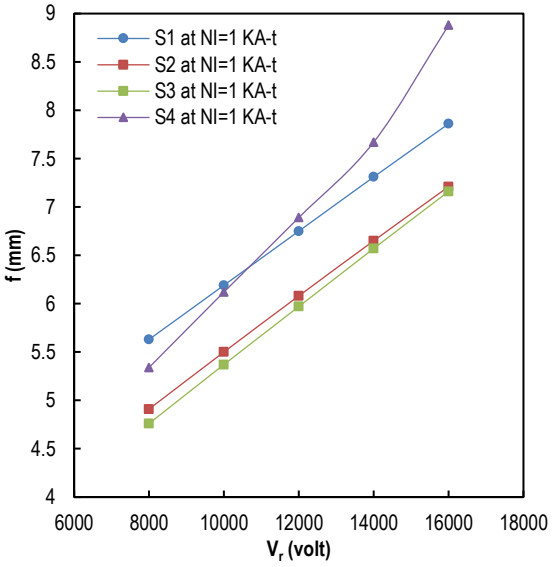

Fig. (6) The focal length change with the constant excitation function NI to the change in accelerating voltage V_r

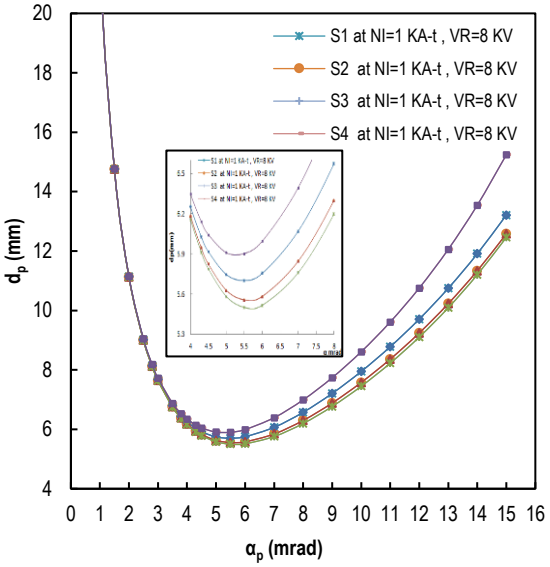

Fig. (7) The relationship between the diameter of the final acting probe d_p as a function of the aperture angle α_p for the four designs at fixed values for the excitation factor NI=1000(A-t) and the acceleration voltage V_r=8kV

4. Conclusions

It was noted that the Gemini objective lens with (S3=4mm) distance between the two pole pieces achieved good results compared to the other designs, studying the optical properties at a constant value of the excitation factor (NI = 1000 A-t) for all designs and changing the distance between the poles of the objective magnetic lens has a significant impact on the spherical and chromatic aberration coefficients and the focal length and increases with the increase in the distance between the poles and lens (S3) achieved the best results at the acceleration voltage (V_r=8kV), this lens has the lowest values for the focal length (f_0=4.76mm), as well as having the lowest value for the coefficients of spherical aberration (Cs=4.14mm) and chromatic aberration (Cc=3.63mm) at (NI=1000A-t) and final effective electron probe diameter (5.4mm) as a result we get an objective lens with better optical properties.

References

[1] D. McMullan, **"Scanning Electron Microscopy 1928 -1965"**, Scanning, 17 (1995) 175-185.

[2] S.A. Rishton, "Resolution limits in electron beam Lithography", Ph.D. thesis, University of Glasgow (1984).

[3] S.M.A. Al-Hali, "Electronic Microscope", Ministry of Higher Education and Scientific Research, University of Baghdad (1990). T.M.A Al-Shafi'i, "Magnetic Leakage through Magnetic Lens Electrode Slots", MSc thesis, University of Babylon (2001).

[4] A.S.A. Alamir, "Magnetic electron lenses performance", *Optik*, 112(11) (2001) 507-510.

[5] E. Plies, "Modren Electron Optics in SEM and Inspection", *Proc. 12th Euro. Cong. Electron Microscopy*, vol. 3 (2000).

[6] K. Tsuno, "Resolution limit of a transmission electron microscope with an uncorrected conventional magnetic objective lens", *Ultramicroscopy*, 50(3) (1993) 245-253.

[7] M.A.K. Al-Khashab, "The electron optical limits of performance of single-polepiece magnetic electron lenses", PhD dissertation, Aston University (1983).

[8] B. Lencová, "Computation of Electron-Optical Components", *IOP Conf. Ser.*, no. 93 (1988).

[9] B. Lencová and G. Wisselink, "Program package for the computation of lenses and deflectors", *Nucl. Instrum. Meth. Phys. Res. A: Acceler. Spectrom. Detect. Assoc. Equip.*, 298(1-3) (1990) 56-66.

[10] B. Lencová, **"Electrostatic Lenses"**, in Handbook of Charged Particle Optics, ed. J. Orloff, 2nd ed., CRC Press, Taylor & Francis (NW, 2009) Ch. 5, pp. 161-208

[11] W.M. Murad, "Design of iron-free magnetic electron lenses", M.Sc. thesis, University of Mosul (1998).

[12] M.A. Hussein, "Numerical analysis to verifying the performance of condenser magnetic lens in the scanning electron microscope", *Adv. Phys. Theor. Appl.*, 58 (2016) 44-49.

[13] E. Munro, "A set of computer programs for calculating the properties of electron lenses", *Cambridge University, Engineering Dept. Report* (1975).

[14] J. Podbrdsky, "High current density magnetic electron lenses in modern electron microscopes", *J. Scan. Electron Microscopy*, 3 (1986) 887-896.

[15] M.A. Hussein and M.Q. Kareem, "Estimating electron probe diameter in the scanning electron microscope", *J. Nat. Sci. Res.*, 6(18) (2016) 68-73.

Nada F. Mahdi
Mithaq M.M. Al-Sultani

Department of Physics,
College of Education for Girls,
University of Kufa,
Najaf, IRAQ

Thermal Properties of Fragmented Human Kidney Stones by Ho:YAG Laser

This study aims at investigating the thermal properties of various kidney stone types that fragmented by laser. It attempts to understand their behavior during Ho:YAG laser with maximum power of 30 W. The pulse duration is 600 μs, wavelengths is 2100 nm, and the maximum energy level is 5J with maximum frequency level 30Hz. This is used for lithotripsy in Al-Sadr Medical City in Najaf for 40 samples divided to 27 calcium oxalate, 11 uric acid, 1 cystine, and 1 protein. Optical penetration depth, thermal diffusion time, temperature rise, and thermal relaxation time have been calculated using established equations. The Optical penetration depth is varied between 0.165-0.327 mm, the highest value has been recorded in sample p12. The highest temperature levels are observed in calcium oxalate sample P5 and uric acid sample P14. Temperature rise increases with increasing pulse energy in both calcium oxalate and uric acid stones.

Keywords: Ho:YAG laser; Calcium oxalate; Uric acid; Kidney stones
Received: 13 January 2024; **Revised:** 15 February 2024; **Accepted:** 22 February 2024

1. Introduction

Urinary stone disease is still a major problem throughout the world, and kidney stones are one of the most common and painful ailments of the urinary system [1]. Known also as uroliths or the kidney/ureter/bladder/urethra calculus, urinary calculi are crystalline deposits that develop in the urinary system [2]. Kidney stone disease affects 50 million persons worldwide and 10% of Americans [3]. It is noted that the ailment is becoming more common; during the course of their lives, 7% of women and 12% of men will be affected [4]. Urinary tract stones are classified into various categories based on the materials or crystals that make them up [1]. Calcium stones are the most prevalent kind of renal stones, accounting for around 80% of all urinary calculi [5]. Most kidney stones are composed totally or partially of CaOx, which can occur as a monohydrate (COM) or dihydrate (COD) [6-8]. Eight to ten percent of kidney stones worldwide are uric acid stones, which are disproportionately common in obese and insulin-resistant stone formers—two major markers of metabolic syndrome. Unlike calcium stone types, urine with a pH of less than 5.5 is the primary source of uric acid nephrolithiasis. [5,7]. While other forms of kidney stones do exist, they are less common than uric acid and calcium stones [9,10]. Over the past ten years, advancements in the three primary components of laser lithotripsy—optical fiber, ureteroscope, and laser—have made the operation more widely used in clinical settings. For nearly two decades, the gold standard for lithotripsy has been the Holmium:YAG infrared laser, which is powered by a flashlamp and has a long pulse duration [11-13]. The Ho:YAG laser's architecture shifts depending on the power supply used to pump the crystal. Flashlamp light (usually Xenon or Krypton) is used to create laser pulses, and when it interacts with the Holmium ions, it causes them to generate new photons at a wavelength of 2120 nm [14,15]. The delivery of holmium laser energy occurs via a compact optical fiber, resulting in the fragmentation of the stone into numerous smaller pieces [4,16]. These fragments can then be extracted individually using a stone basket. Alternatively, if the stone size is reduced to 2 mm or smaller, it can traverse the urinary tract without obstruction and be naturally expelled by the patient [17]. The tiny, malleable optical fibers with diameters between 200 and 1000 μm are used [18]. Because of its adaptability, lithotripsy may be performed anywhere in the upper urinary system, including during flexible ureteroscopy (FURS) and flexible nephroscopy [12,19,20]. The photothermal effect is the first stage of interaction the laser light with tissue. Tissue can be rapidly heated with a laser by absorb some of the light, and then their vibrations and collisions transform some of that energy into heat. The laser's adjustable settings allow for a range of thermal effects on tissue. These include coagulation, evaporation, and selective thermolysis (heat-induced chemical/cell disintegration) [21,22].

2. Materials and Methods

Forty samples that have been collected from Al-Sader Medical City in the city of Najaf as shown in Fig. (1), were fragmented by Ho:YAG laser with a maximum power of 30 W, pulse duration of 600 μs, wavelengths 2100 nm, the maximum energy level 5J with maximum frequency level 30Hz. This laser from Litho company and brand Quanta System Italy with optical fiber from the REOSABLE company have been used with a diameter of 550 µm to insert the laser beams into the ureter and shine the rays on the stones. The patient is positioned on an exam table and the urethra is numbed with a local anesthetic. The laser is passed by the optical fiber through a thin tube (catheter) that is inserted into the ureter through the urethra. The laser fragments the stone into small pieces less than 4 mm that can be passed out of the body in the urine. A stone sample was taken from

each patient, its chemical and optical properties were studied by FTIR-ATR analyzer, and the value of the optical absorption coefficient was calculated.

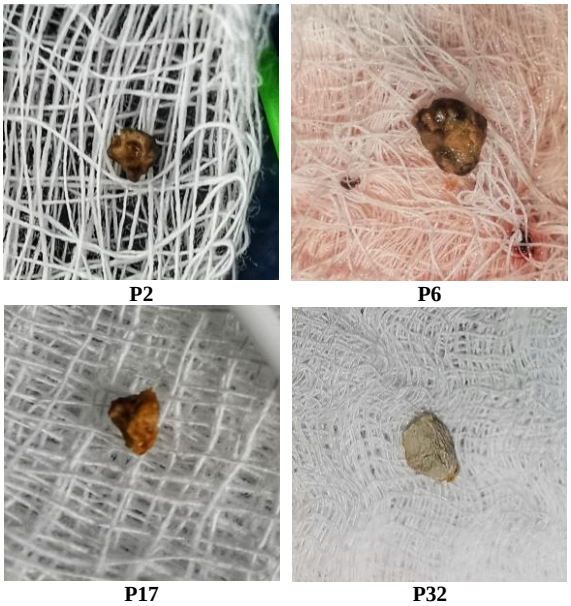

Fig. (1) Pictures of different samples

3. Results and Discussion

The results of the FTIR-ATR analyzer show that the majority of the stone samples have been of the calcium oxalate type, labeled 27, 11 of the acid type stones, one sample of cystine, and one sample of protein. Each stone sample is not completely pure, but contains different proportions of other types of other substances, such as uric acid, ammonium urate, sodium urate, and carbonate apatite. But they can be considered one species according to the proportion of its predominant substance. The optical penetration depth δ for the highest absorption coefficient ($\mu_a(\lambda)$) for every stone is calculated by using [23]:

$$\delta = \frac{1}{\mu_a(\lambda)} \quad (1)$$

As noticed in table (1), although it is the same type as in samples P1, P6, P7, P12, and P21, the absorption coefficient differs from one stone to another. This is due to the difference in absorbance and may be due to the presence of other percentages of different types of substances in the stones. What confirms this result is that the ratios in the P6 and P7 samples are the same. So, it can be found that the absorbance is the same and the results are all the same. This applies to all other samples. It is, also, noted in table (1) that the highest value of penetration depth is in sample P12 due to its low absorbance, as the penetration depth ranges between 0.165- 0.327 mm. These results agree with the results of researches [24-26].

The thermal diffusion time (τ_{TH}), the temperature rise ($\Delta T(\chi)$) and thermal relaxation time (t_{st}) are calculated by equations (2), (3) and (4), respectively.

$$\tau_{TH} = \frac{\delta^2}{4\alpha} \quad (2)$$

where α represent the thermal diffusivity (i.e., α = 0.15 mm^2/sec for water at 37°C) [23].

$$\Delta T(\chi) = \frac{\mu_a(\lambda) H_o}{\rho c_p} e^{-\mu_a(\lambda)\chi} \quad (3)$$

where ΔT represents differential temperature increase, ρ represents the material density, the densities of COM and COD are 2.17 and 1.96 g/cm^3, respectively [27]. c_p represents the material specific heat at constant pressure for calculus is about 1524 J/kg.°C [28], H_o represents the surface fluence, and χ is depth [23].

$$t_{st} = \frac{\delta}{c} \quad (4)$$

Here c is the speed of sound [29].

Figure (2) shows the highest temperature rise in P5 sample for calcium oxalate stones, while in Fig. (3), sample P14 has the highest temperature rise for uric acid stones due to high energy pulse used in fragmentation and high $\mu_a(\lambda)$ of the sample compared to other samples.

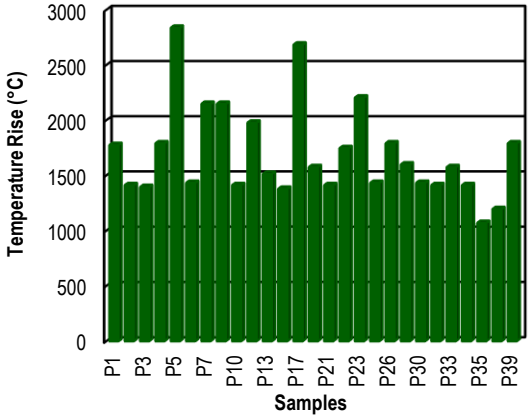

Fig. (2) The temperature rise for calcium oxalate stones

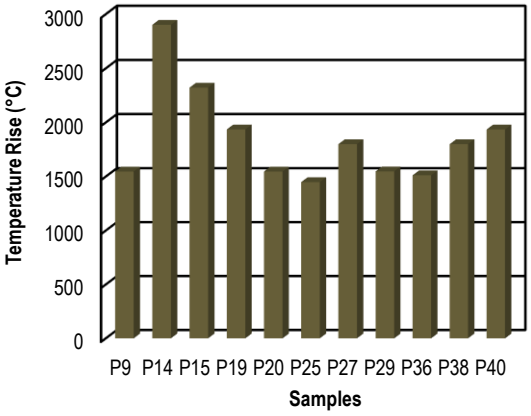

Fig. (3) The temperature rise for uric acid stones

Moreover, it is noticed that the temperature rise increases with increasing the energy of the pulse in both types of kidney stones, calcium oxalate and uric acid, as in figures (4) and (5). Where the high temperature values in the results are normal in the Ho:YAG laser, as this has been shown in different studies "Schafer and coworkers investigators reported a blackbody temperature of 5000°K from the irradiated calculus" [23,24]. It can be noticed that the

relaxation time is much less than the pulse duration, this indicates that the stones absorb the pulse energy during the pulse duration only and the heat dissipates quickly.

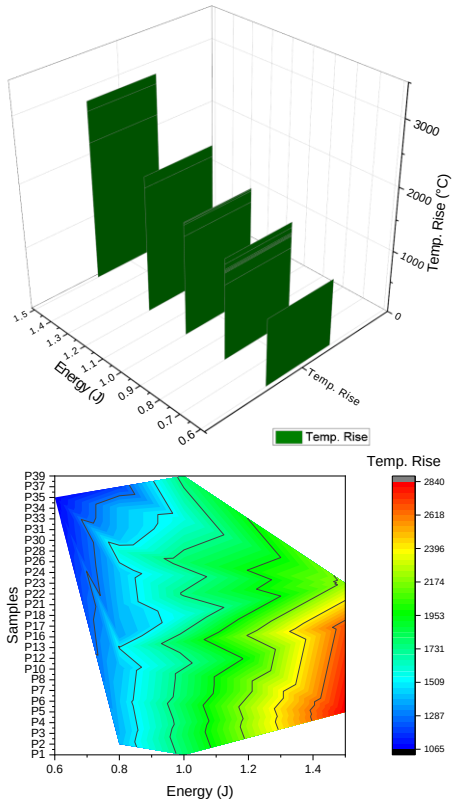

Fig. (4) The temperature rise for calcium oxalate stones with its energy pulse

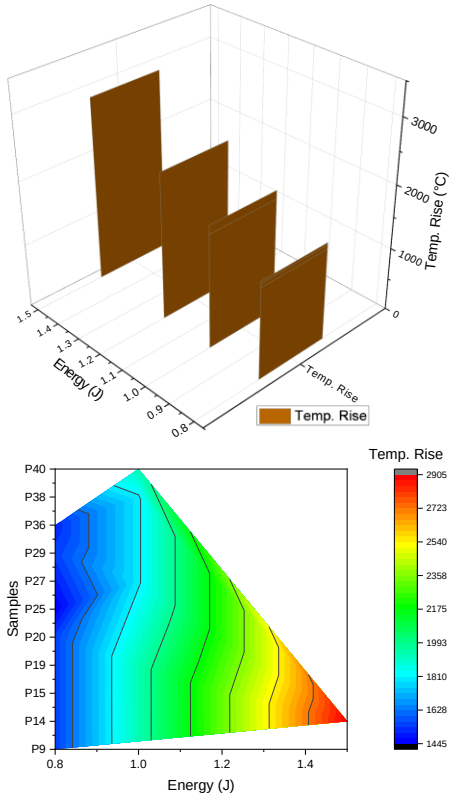

Fig. (5) The temperature rise for uric acid stones with its energy pulse

4. Conclusions

The key conclusion of the study is that kidney stone composition and optical properties have a significant impact on laser lithotripsy outcomes. The study identifies calcium oxalate as the predominant stone type (67.5%), followed by uric acid (27.5%), with rare occurrences of cystine and protein stones. The variation in absorption coefficient influence laser interaction even within the same stone type (e.g., P1-7, P12, P21). While penetration depth varies (0.165-0.327mm), temperature rise increases with pulse energy for both calcium oxalate and uric acid stones. Sample-specific properties like high absorption in P14 (uric acid) lead to the highest temperature increases about 2902.03°C. These findings underscore the importance of pre-operative stone characterization to determine composition and optical properties. By understanding the interplay between stone type, absorption coefficient, and penetration depth, laser settings can be customized to achieve optimal fragmentation with minimal collateral damage.

Acknowledgment

The authors offer their thanks and gratitude to Najaf health department for facilitating entry to the operating room of Al-Sadr Hospital in Najaf city to collect data. We also thank all the medical staff for their support and dedication to completing this study. We are very grateful for the Department of Physics, College of Education for Girls, University of Kufa, Iraq for allowing us to do this work. Also, we hope this research will be a reason to accomplish more future development.

References

[1] L.G. Awazli and A.S. Mahmood, "Urinary Tract Stones Fragmentation using 2100nm Ho:YAG Laser: *in vitro* Analysis", *Iraqi J. Laser*, 12 (2013) 1-12.

[2] J.J. Zhang et al., "Numerical Response Surfaces of Volume of Ablation and Retropulsion Amplitude by Settings of Ho:YAG Laser Lithotripter", *J. Healthcare Eng.*, 2018 (2018) 1-11.

[3] L.A. Hardy et al., "Fragmentation and Dusting of Large Kidney Stones using Compact, Air-cooled, High Peak Power, 1940-nm, Thulium Fiber Laser", *Therapeut. Diagnost. Urology*, 10468 (2018).

[4] D.S. Frank et al., "Polymer − Mineral Composites Mimic Human Kidney Stones in Laser Lithotripsy Experiments", *ACS Biomater Sci. Eng.*, 5(10) (2019) 4970-4975.

[5] T. Alelign and B. Petros, "Kidney Stone Disease : An Update on Current Concepts", *Adv. Urol.*, (2018) 1-12.

[6] S.R. Khan et al., "Kidney stones", *Nat. Rev. Dis. Primers*, 2(1) (2016) 1–23.

[7] O.W. Moe, "Kidney stones: pathophysiology and medical management", *The Lancet*, 367(9507) (2006) 333–344.

[8] F.L. Coe, A. Evan and E. Worcester, "Kidney stone disease", *J. Clin. Invest.*, 115(10) (2005) 2598–2608.
[9] M.E. Mayo, "Interaction of Laser Radiation with Urinary Calculi", Ph.D. thesis, Cranfield University (2009).
[10] E. Meimaridou, "Calcium Oxalate Modulation of Tubular Epithelial Cell Mitochondria: Oxidative Vulnerability Due to Restricted Glutathione Homeostasis", Ph.D. thesis, University College London (2007).
[11] D.E. Johnson, D.M. Cromeens and R.E. Price, "Use of the holmium: YAG laser in urology", *Lasers Surg. Med.*, 12(4) (1992) 353–363.
[12] E. Emiliani, "Evaluation of Ho:YAG Laser settings for the Non-Contact Stone Fragmentation Technique and the Curved Laser Fiber", Ph.D. thesis, (2019).
[13] A.D. Mahajan and S.A. Mahajan, "Thulium fiber laser versus Ho:YAG laser for stone lithotripsy during mini-percutaneous nephrolithotomy: A prospective randomized trial", *Indian J. Urol.*, 38(1) (2022) 1-42.
[14] P.T. Cleve, "Sur deux nouveaux éléments dans l'erbine", *CR. Acad. Sci.*, 89(9) (1879) 478–480.
[15] O. Traxer and E. X. Keller, "Thulium fiber laser: the new player for kidney stone treatment? A comparison with Ho:YAG laser", *World J. Urol.*, 38(8) (2020) 1883-1894.
[16] O. Schatloff et al., "Randomized Trial of Stone Fragment Active Retrieval versus Spontaneous Passage During Holmium Laser Lithotripsy for Ureteral Stones", *J. Urol.*, 183(3) (2010) 1031-1036.
[17] N.M. Fried, "Recent advances in infrared laser lithotripsy", *Biomed Opt. Exp.*, 9(9) (2018) 4552-4568.
[18] P. Kronenberg and O. Traxer, "The truth about laser fiber diameters", *Urology*, 84(6) (2014) 1301–1307.
[19] B.K. Somani et al., "Outcomes of Flexible Ureterorenoscopy and Laser Fragmentation for Renal Stones: Comparison between Digital and Conventional Ureteroscope", *Urology*, 82(5) (2013) 1017–1019.
[20] O.A. Nazif et al., "Review of Laser Fibers: A Practical Guide for Urologists", *J. Endourol.*, 18(9) (2004) 818–829.
[21] S. Thomse, "Pathologic Analysis of Photothermal and Photomechanical Effects of Laser-Tissue Interactions", *Photochem. Photobiol.*, 53(6) (1991) 825–835.
[22] M.H. Niemz, **"Laser-Tissue Interactions"**, Springer-Verlag Berlin Heidelberg (2007) p. 322.
[23] K.F. Chan et al., "A Perspective on Laser Lithotripsy: The Fragmentation Processes", *J. Endourol.*, 15(3) (2001).
[24] S.L. Jacques, "Laser-Tissue interactions: Photochemical, photothermal, and photomechanical", *Surg. Clin. North America*, 72(3) (1992) 531–558.
[25] R.S. Terry, P.S. Whelan and M.E. Lipkin, "New devices for kidney stone management", *Curr. Opin. Urol.*, 30(2) (2019) 144–148.
[26] G.M. Hale and M.R. Querry, "Optical Constants of Water in the 200-nm to 200-Mm Wavelength Region", *Appl. Opt.*, 12(3) (1973) 555–563.
[27] R.C. Walton, J.P. Kavanagh and B.R. Heywood, "The density and protein content of calcium oxalate crystals precipitated from human urine: a tool to investigate ultrastructure and the fractional volume occupied by organic matrix", *J. Struct. Biol.*, 143 (2003) 14–23.
[28] M. Moghimnezhad, A. Shahidian and M. Andayesh, "Multiphysics Analysis of Ultrasonic Shock Wave Lithotripsy and Side Effects on Surrounding Tissues", *J. Biomed. Phys. Eng.*, 11(6) (2021) 701–712.
[29] M. Mohammadzadeh, J.M. Mercado and C.-D. Ohl, "Bubble Dynamics in Laser Lithotripsy", *J. Phys.*, 656 (2015) 012004.

Table (1) Thermal coefficients for stones treated by Ho:YAG laser

Samples	Stone Type	Wavelength (mm)	$\mu_a(\lambda)$ (mm^{-1})	δ (mm)	τ_{TH} (sec)	$\Delta T(\tau)$ (°C)	t_{st} *10^{-6} (sec)
P1	calcium oxalate	0.3220	3.9658	0.2522	0.0318	1774.94	0.0556
P2	calcium oxalate	0.3194	4.4085	0.2268	0.0257	1411.32	0.0500
P3	calcium oxalate	0.3185	5.0007	0.2000	0.0200	1394.45	0.0441
P4	calcium oxalate	0.3199	4.4377	0.2253	0.0254	1789.83	0.0497
P5	calcium oxalate	0.3182	3.6867	0.2712	0.0368	2837.47	0.0598
P6	calcium oxalate	0.3201	4.8895	0.2045	0.0209	1431.97	0.0451
P7	calcium oxalate	0.3201	4.8895	0.2045	0.0209	2147.96	0.0451
P8	calcium oxalate	0.3201	4.8895	0.2045	0.0209	2147.96	0.0451
P9	uric acid	0.3342	4.9529	0.2019	0.0204	1546.87	0.0582
P10	calcium oxalate	0.3194	4.4085	0.2268	0.0257	1411.32	0.0500
P11	protein	0.3271	3.4492	0.2899	0.0420	1205.45	-
P12	calcium oxalate	0.3208	3.0498	0.3279	0.0538	1977.02	0.0723
P13	calcium oxalate	0.3209	3.0829	0.3244	0.0526	1512.86	0.0715
P14	uric acid	0.3278	4.8432	0.2065	0.0213	2902.03	0.0595
P15	uric acid	0.3278	4.8432	0.2065	0.0213	2321.62	0.0595
P16	calcium oxalate	0.3187	4.1508	0.2409	0.0290	1378.14	0.0531

P17	calcium oxalate	0.3201	4.8895	0.2045	0.0209	2684.94	0.0451
P18	calcium oxalate	0.3308	5.0289	0.1989	0.0198	1574.74	0.0438
P19	uric acid	0.3278	4.8432	0.2065	0.0213	1934.68	0.0595
P20	uric acid	0.3342	4.9529	0.2019	0.0204	1546.87	0.0582
P21	calcium oxalate	0.3194	4.4085	0.2268	0.0257	1411.32	0.0500
P22	calcium oxalate	0.3223	4.9803	0.2008	0.0202	1746.62	0.0443
P23	calcium oxalate	0.3286	5.1006	0.1961	0.0192	2204.47	0.0432
P24	calcium oxalate	0.3201	4.8895	0.2045	0.0209	1431.97	0.0451
P25	uric acid	0.3308	5.8319	0.1715	0.0147	1448.98	0.0494
P26	calcium oxalate	0.3201	4.8895	0.2045	0.0209	1789.96	0.0451
P27	uric acid	0.3333	5.8831	0.1700	0.0144	1799.26	0.0490
P28	calcium oxalate	0.3212	3.7259	0.2684	0.0360	1598.11	0.0592
P29	uric acid	0.3278	4.8432	0.2065	0.0213	1547.75	0.0595
P30	calcium oxalate	0.3201	4.8895	0.2045	0.0209	1431.97	0.0451
P31	calcium oxalate	0.3194	4.4085	0.2268	0.0257	1411.32	0.0500
P32	cystine	0.2752	5.7747	0.1732	0.0150	1736.87	0.0372
P33	calcium oxalate	0.3308	5.0289	0.1989	0.0198	1574.74	0.0438
P34	calcium oxalate	0.3194	4.4085	0.2268	0.0257	1411.32	0.0500
P35	calcium oxalate	0.3201	4.6222	0.2163	0.0234	1069.73	0.0477
P36	uric acid	0.3315	5.4861	0.1823	0.0166	1512.05	0.0525
P37	calcium oxalate	0.3330	6.0347	0.1657	0.0137	1195.11	0.0365
P38	uric acid	0.3333	5.8831	0.1700	0.0144	1799.26	0.0490
P39	calcium oxalate	0.3201	4.8895	0.2045	0.0209	1789.96	0.0451
P40	uric acid	0.3278	4.8432	0.2065	0.0213	1934.68	0.0595

IRAQI JOURNAL OF MATERIALS

About IJM

Iraqi Journal of Materials (IJM) aims to provide a leading international forum for material researchers across the disciplines of theory, experiment, and device applications. It publishes original studies and reviews related to the calculation, synthesis, processing, characterization, and understanding of advanced quantum materials such as low-dimensional materials, topological materials, meta-materials, correlated electronic materials, and novel magnetic materials, as well as how these materials can be utilized in the construction of novel devices like quantum computers, quantum sensors, spintronics and optoelectronics devices. Studies including demonstrations of these devices are also welcome.

To be published in Iraqi Journal of Materials (IJM), papers must meet high scientific standards, contain original science, and make significant advances within the field. An editor will first assess submissions before being sent to independent referees to ensure they meet the scope and standards of Iraqi Journal of Materials (IJM).

Editorial Office:

P. O. Box 88052,
Baghdad 12631,
IRAQ
Website: www.ijmaterials.com
Emails: info@ijmaterials.com

Akeel M. Kadim
Ali K. Attia

Department of Medical Physics, College of Science, Al Karkh University of Science, Baghdad, IRAQ

Colloidal Synthesis of CdTe Nanocrystals by Laser Ablation and Fabrication of Hybrid Light Emitting Device

Cadmium telluride (CdTe) nanocrystals (NCs) have gained the interest of researchers as an electrode material in hybrid light emitting devices (HLEDs) due to their potential high ability. In this study, CdTe nanocrystals were synthesized applying a 600 mJ Nd: YAG laser with 150 pulses to create a light emitting device consisting of ITO/CdTe/TPD/Ni. The spectra of CdTe NCs have been measured using UV-VIS and photoluminescence. The energy gap (Eg) within cadmium telluride (CdTe) NCs described as the (PL) spectrum has been determined to be around 3.6 eV. Cadmium telluride (CdTe) NCs developed via laser ablation improve the performance of the HLEDs by enhancing the carrier's charge mobility and, as an additional reward, by increasing recombination reactions inside cadmium telluride (CdTe) NCs with TPD organic polymer. In addition to illumination at 3V, current-voltage (I-V) requirements determine the appropriate environment and formation.

Keywords: Cadmium telluride; Laser ablation; Nanocrystals; Electrode materials
Received: 24 January 2024; **Revised:** 19 February 2024; **Accepted:** 26 February 2024

1. Introduction

The generation of electrical power from photovoltaic light conversion is gradually increasing. This may be ascribed to the development of novel renewable energy materials and low-cost production systems, which has resulted in a decrease in the cost of a watt-hour generated by photovoltaic means. Using polycrystalline semiconductor thin films is an intriguing approach to lower the cost of photovoltaic cells [1]. The covers of batteries are made up of several semiconductor and conductive organic polymer layers, including the absorber or active material. Cadmium tellurium (CdTe), silicon (Si), gallium arsenide (GaAs), N, N′-Bis(3-methylphenyl)-N,N′-diphenylbenzidine (TPD), and poly(3,4-ethylenedioxythiophene) polystyrene sulfonate (PEDOT:PSS) [1,2] are now used in the industrial fabrication of high-efficiency light emitting devices [2].

For many years, researchers have been interested in the cadmium telluride (CdTe) semiconductor, which belongs to the II-VI family owing to their suitable band gaps and high absorption coefficients. Cadmium telluride (CdTe) has mostly been investigated in the last ten years as a polycrystalline thin film and as a nanocrystal [3], and a cadmium telluride (CdTe) has been identified as an interesting thin-film HLEDs material. It has been created as a thin film using laser ablation, electrodeposition, and spray pyrolysis, and it has mostly been employed as the absorber material of thin-film photovoltaic [3,4]. Recent cadmium telluride (CdTe) deposition techniques are based on dispersing cadmium telluride (CdTe) nanocrystals in water or organic solvents [4-6] and transforming them into cadmium telluride (CdTe) thin films utilizing simple and inexpensive deposition processes such as dip-coating or spin-coating and an annealing procedure. Many approaches have lately been studied in order to overcome the limitations of cadmium telluride (CdTe) nanocrystals-based cathode [5,6]. Furthermore, when already realized on a combination (CdTe nanocrystals and TPD organic polymer), all of these components should be as large as possible in order to set up a technique. A standard approach to generate transparent devices, as proved in nanocrystals and organic semiconductors, is working to components with low contrast sensitivity and high absorbance [6,7]. However, nanostructured cadmium telluride (CdTe) with a high surface area promotes electrolyte side reactions, resulting in irreversible capacity loss during the first cycle. Furthermore, this method is insufficient to increase cadmium telluride (CdTe) high electric conductivity altogether. To further overcome the constraints of the cadmium telluride (CdTe) cathode, nanostructured materials might be blended with a highly conductive and elastic matrix to form a nanocomposite structure [8,9]. One of the most important problems in this work is controlling the thickness of the layers while depositing them on the indium tin oxide (ITO) glass substrate. As the thickness of the layer's increases, it causes a disconnection in the electrical current passing through the device. Therefore, the deposition of the layers must be controlled, and the best solution for this is to deposit the layers separately from the others in a way chemical spraying and drying in oven. Laser ablation synthesis (LAS) in solution is a physical approach that may be used instead of chemicals. Typically, the methods most often

employed for the creation of nanoparticles involve the use of toxic substances as indicators as well as reducing or stability agents [9]. In addition, LAS has a low environmental effect since it does not require any preparations or reducing chemicals and may produce high purity colloids while producing no toxic waste [10]. Laser-ablation synthesis techniques have emerged as an effective and adjustable technique for nanomaterials synthesis [8-10], demonstrating the ability to be used for the synthesis of nanostructures using several starting materials in a variety of liquid environment.

In the current assignment, a simple sustainable synthesis method for reconstructing colloidal cadmium telluride (CdTe) nanocrystals are used by laser ablation deposition with a TPD layer on the ITO surface to fabricate cadmium telluride (CdTe) hybrid light-emitting devices (CdTe-HLEDs), as well as to study the effectiveness of the resulting CdTe-HLEDs. The electrolayer that adds cadmium telluride (CdTe) nanocrystals to the surface of the TPD substrate allows more surface area to increase, demonstrates high specific capacity, great cycle stability, and distinguished rate performance. These features make cadmium telluride (CdTe) nanocrystals a remarkable fitting as emissive material in CdTe-HLEDs. Also makes the HLEDs environment friendly for the better reversible performance of the light emitting device environment.

2. Experimental Part

All of the main compounds were purchased from Fluka Company, which were employed without further purification. In the beginning 0.8 g of cadmium chloride ($CdCl_2$) and 0.3 g of sodium telluride (Na_2Te) were dissolved in 40 ml of deionized water. The Nd: YAG laser operating at (1064 nm) with energy up to 600 mJ/pulse was used to synthesis cadmium telluride (CdTe) nanocrystals (see Fig. 1).

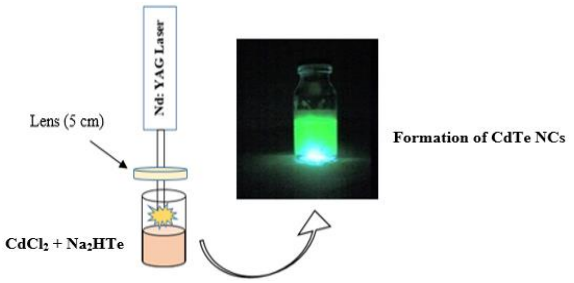

Fig. (1) Laser ablation technique used for prepare of cadmium telluride (CdTe) nanocrystals colloidal

The laser beams of a focal length of 20 cm focused on the mixed solution from a lens distance of 5 cm. A container was formed for generating homogenous nanocrystals and stirred for 2 hours before passing the nanocrystals solution with an increased pulse number of 150 pulses, allowing the color of the cadmium telluride (CdTe) nanocrystals solution change to light green. The cadmium telluride (CdTe) nanocrystals were then cleaned five times with deionized water before being completely vacuum packed.

The hybrid light emitting device was developed applying two layers of cadmium telluride (CdTe) nanocrystals and TPD. organic polymer provided by Sigma-Aldrich Chemie GmbH. Organic polymer coating dissolving 40 mg/ml in ethanol and injection by syringe on ITO glass substrate using covered spinning at 2000 r.p.m. in around 10 second for separate covered polymers. To avoid crashes, the first layer was 0.2 wt% cadmium telluride (CdTe) nanocrystals in the cover, the second layer was always layer TPD conductive polymer. Immediately after coating in a 40 °C oven for 10 minutes, the coating on each cover dries away. The thicknesses of the films have been measured by interference method (Tolansky method of thin film thickness measurement) while the thickness of TPD layer appear to be 30 nm, while a cadmium telluride (CdTe) nanocrystals cover appears to be 10 nm thick. Next that, a nickel (Ni) cathode is coated in system layer. Hybrid light emitting devices that process cadmium telluride (CdTe) nanocrystals covering TPD may increase the transport rates of cadmium telluride (CdTe) and TPD ions in HLEDs in response to light emitting device operations.

3. Results and discussion

Figures (2) and (3) illustrate the absorption and photoluminescence spectra of cadmium telluride (CdTe) nanocrystals at room temperature. The absorption spectrum in the UV-visible region of high-level cadmium telluride (CdTe) nanocrystals is shown. These findings have been obtained in an adequate setting when compared to the absorption spectra of previous studies [11-13].

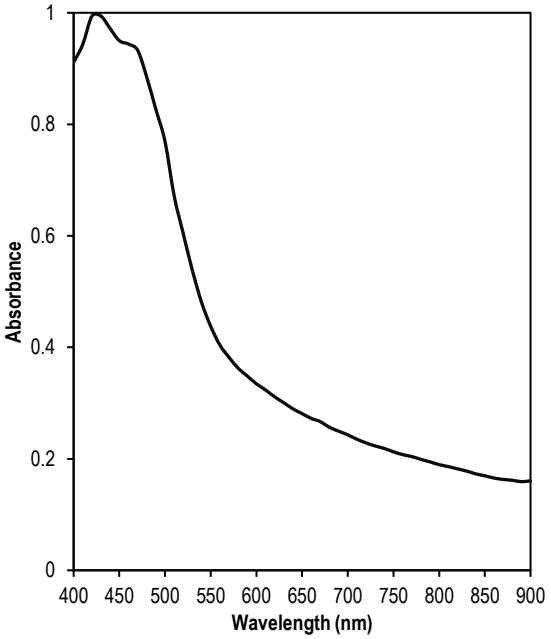

Fig. (2) Absorption spectrum of cadmium telluride (CdTe) nanocrystals

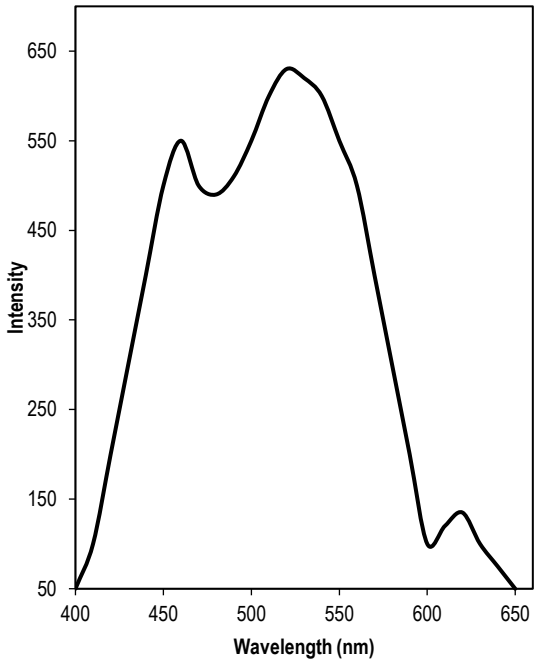

Fig. (3) Photoluminescence spectrum of cadmium telluride (CdTe) nanocrystals

Figure (3) exhibits the photoluminescence of cadmium telluride (CdTe) nanocrystals, which suggests that a specific energy band conduction occurs at 530 nm. Excessive fluorescence occurs as a result of the emission of the near-band edge of cadmium telluride (CdTe) nanocrystals, with additional highlights at 460 and 620 nm caused by free excitons recombination. These broad emissions are linked to deep-level leaks, which can be caused by defects in structure [12]. According to that circumstance, the presence of the relevant defect identified as a beyond observer, an emission associated with nanocrystalline defects cadmium telluride (CdTe) nanocrystals might be due to Cd or Te vacant seats [14-18]. The energy-gap in cadmium telluride (CdTe) nanocrystals must have been established formulated at essentially 3.6 eV.

As shown in Fig. (4), the surface morphology of the grown cadmium telluride (CdTe) nanocrystals has been imaged using SEM at 50 KX magnification. The nanocrystals covering's SEM properties serve as an acceptable notice for the formation of cadmium telluride (CdTe) nanocrystals. The average grain size was found to be around 10 nm Figure 4 depicts spherical morphology with low aggregation of nanocrystals generated at 100 nm scale.

The electrically charged cadmium telluride (CdTe) nanocrystals that perform in Hall Effect assignments of magnitude are described. Developed and introduced a semiconductor electrical characterization technique called differential Hall effect metrology (DHEM). HEM provides depth profiles of critical electrical properties through semiconductor layers at nanometer-level depth resolution. HEM is based on the differential Hall effect (DHE) method, which makes successive sheet resistance and mobility measurements on a layer using Hall effect and Van der Pauw techniques as the thickness of the layer is reduced through successive processing steps, typically involving chemical or electrochemical etching or oxidation. The data obtained as a function of thickness removed can then be used to determine the depth profiles of carrier concentration, resistivity and mobility. Thin films with thicknesses of 10, 20, and 30nm exhibit semiconductor activity and n-type conductivity. Table (1) summarizes the Hall Effect.

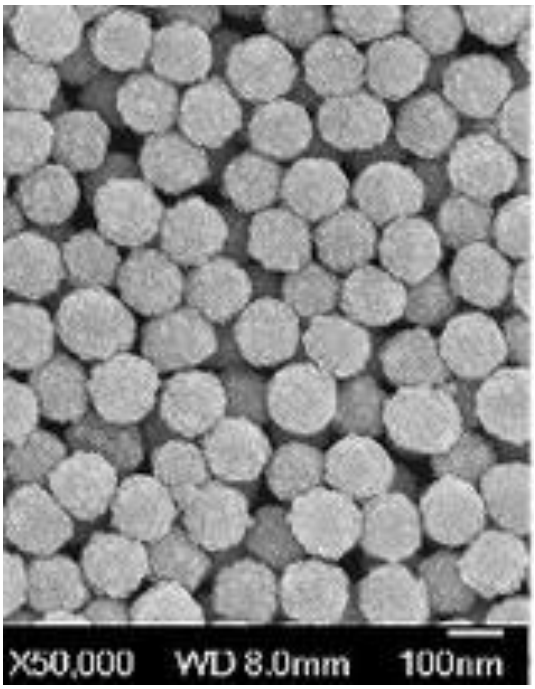

Fig. (4) Scanning electron microscope (SEM) image of the cadmium telluride (CdTe) nanocrystals prepared in this work

Table (1) Overview of cadmium telluride (CdTe) nanocrystals Hall Effect measurements with varying thickness

Sample	Thickness (nm)	Conductivity $(\Omega.cm)^{-1}$	Mobility (cm^2/Vs)	Hall Coefficient (cm^2/C)
CdTe	10	2.56	48.5	-1.23×10^{8}
	20	1.48	16	-1.27×10^{8}
	30	1.34	13.5	-1.31×10^{8}

When compared to other cadmium telluride (CdTe) nanocrystals thicknesses, it was suggested that cadmium telluride (CdTe) nanocrystals had strong conductivity at 10 nm thickness. In addition, the mobility of cadmium telluride (CdTe) nanocrystals at 10 nm thickness is greater than that of cadmium telluride (CdTe) nanocrystals at 20 and 30 nm thicknesses, implying that the cadmium telluride (CdTe) are impacted by a decrease in the resistance of the cadmium telluride (CdTe) nanocrystals, which suggests that, amid substantial increases in the nanocrystals, the growth of recombination extremely emerged a cadmium telluride (CdTe) battery device

and induced charges, which governed. In the light of the improved electron confinement in cadmium telluride (CdTe) nanocrystals, mobility in a carrier increases as dimensions' decrease.

This feature separates batteries from commercial batteries, which operate at higher voltages and have lower efficiency [19,20]. Figure (5) explains the I-V combinations of the CdTe-HLEDs achieved with the ITO/CdTe/TPD/Ni performance. The figure shows the capacity to rearrange with a general conversion voltage of 3 voltage bias and a current of just under 0.01-0.44 mA.

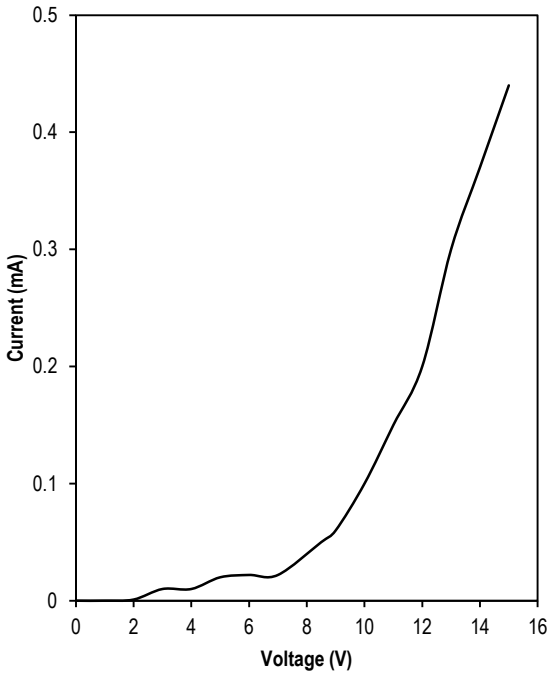

Fig. (5) I-V characters of the ITO/CdTe/TPD/Ni HLEDs

A hybrid light emitting device product performed current-voltage reveals an overall increase concerning current induced beside a decrease during the depletion-edge layer's size. The propagation band barrier will decrease in the forward bias owing to dramatic increase dispersion of ions (CdTe and TPD) inside the valence and conduction band [20]. Because allowed towards charge besides discharging processes shifted significantly across one cycle to another remained when the stream is steady for the duration of the cycle [21,22]. The number of charging and discharging cycles that a CdTe-HLEDs may go through before it stops operating is referred to as its life-cycle. The discharge depth has a significant impact on the life of CdTe-HLEDs. The depths of discharge describe how much of a battery's storage is consumed. As a result of the rechargeable batteries provide ions (TPD) to (cadmium telluride (CdTe) nanocrystals) owing to system discharges, recombination would increase the forward bias's current flow [23]. At this point, these processes emerge as a result of multiple techniques that influence the production of batteries.

One particular technique stands out, as it does not seem to be directly controlled by another synthesis. Insufficient results have an influence on success, as is shown in a band gap the semi-conductors that is operating even more devices for generating current [22-24]. These devices in the gap charge domain can be classified as surface imperfections, barrier annealing, output recombination, and boundary configurations [24]. Figure (6) illustrates a view of an ITO/CdTe/TPD/Ni displays the light emitted by this component.

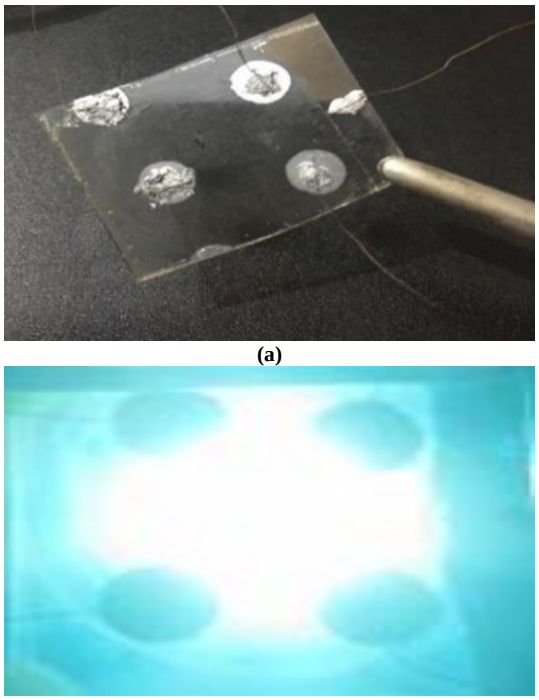

(a)

(b)

Fig. (6) (a) A picture of the ITO/CdTe/TPD/Ni HLEDs (b) Light illumination produced by ITO/CdTe/TPD/Ni HLEDs

4. Conclusion

In summary, composition analysis confirms of the controlled size of cadmium telluride (CdTe) nanocrystals using laser ablation technique, which has been highly useful because the size reduced as the number of laser pulses increased. Cadmium telluride (CdTe) nanocrystals raised more the ability of the HLEDs by improving the carrier's charge mobility as well as the interactions between cadmium telluride (CdTe) nanocrystals and TPD organic conductive polymer. The (I-V) characteristics are completely matched with the needed voltage, which produces critical features for the functioning of the light emitting system. A progressive interaction development in the HLEDs including cadmium telluride (CdTe) nanocrystals and TPD organic polymer ions may give forward current flow bias in order to use a few volts and create positive effects for light output.

References

[1] A. Tze-Zhang et al., "A Comprehensive Study of Renewable Energy Sources: Classifications, Challenges and Suggestions", *Ener. Strat. Rev.*, 43(2022) 1-27.

[2] M.K. Akeel, "Fabrication of nano battery from CdS quantum dots and organic polymer", *Kuwait J. Sci*., 49(1) (2022) 1-9.

[3] M.K. Akeel and M.S. Amjed, "Enhanced White Light Emitting Device Based on ZnTe Nanocrystals and Conductive Organic Polymer by Surface Excitons", *Chalcog. Lett.*, 18(6) (2021) 289-295.

[4] A.P. Antonio et al., "Study and Application of Colloidal Systems for Obtaining CdTe+Te Thin Films by Spray Pyrolysis", *J. Anal. Appl. Pyrol.*, 124 (2017) 285-289.

[5] S. Sudeshna et al., "A new Route for Preparing CdTe Thin Films by Chemical Bath Deposition", *Mater. Today: Proc.*, 44(1) (2021)1463-1467.

[6] M. Tetiana, M. Myroslav and H. Marian, "Surface-Barrier CdTe Diodes for Photovoltaics", *J. Nano- Electron. Phys.*, 15(2) (2023)1-5.

[7] I.G. Orletskyi et al., "Electrical Properties of the n-NiS2/n-CdTe Isotype Heterojunction Fabricated by Spray Pyrolysis", *Proc. 50th Int. School Conf. Phys. Semicond.*, Szczyrk, Poland (2022).

[8] M.K. Akeel, "Zinc Selenide Quantum Dots Light Emitting Devices (ZnSe QDs-LEDs) with Different Organic Polymers", *Nano Hybr. Compos.*, 18 (2017) 11-19.

[9] Z. Ghassan et al., "Concept Development and Techno-Economic Assessment for A Solar Home System Using Lithium-Ion Battery for Developing Regions to Provide Electricity for Lighting and Electronic Devices", *Ener. Conver. Manag.*, 122 (2016) 439-448.

[10] E. Al-Bermany et al., "Effect of Green Synthesis Bimetallic Ag@SiO_2 Core–Shell Nanoparticles on Absorption Behavior and Electrical Properties of PVA-PEO Nanocomposites for Optoelectronic Applications", *Silicon*, 15 (2023) 4095-4107.

[11] B. Anugop et al., "Nanoparticle Production via Laser Ablation Synthesis in Solution Method and Printed Electronic Application - A Brief Review", *Resul in Eng.*, 16 (2022) 1-14.

[12] R. Grover, R. Srivastava and K. Saxena, "Luminescence studies in cadmium telluride nanocrystals grown on glass substrates", *RSC Adv.*, 12 (2022) 26596-26602.

[13] M.K. Akeel "Fabrication of Quantum Dots Light Emitting Device by Using CdTe Quantum Dots and Organic Polymer", *J. Nano Res.*, 50 (2017) 48-56.

[14] M.K. Akeel, "Hybrid White Light Emitting Devices (HWLEDs) From Organic Polymer and PbS Nanocrystals by Multiple Excitons", *Mater. Sci. Poland*, (2020)1-6.

[15] L. Guangmin et al., "Fluorescence and Optical Activity of Chiral CdTe Quantum Dots in their Interaction with Amino Acids", *ACS Nano*, 14(4) (2020) 4196-4205.

[16] Q. Guillermo, S. Hugo and R. Jesus, "Characterization of CdTe Thin Films Using Orthogonal Double-Pulse Laser-Induced Breakdown Spectroscopy", *Chemosensors*, 11(1) (2023).

[17] A.I. Omar, M.K. Akeel and R.S. Wasan "White Light Generation from Electroluminescence Devices Using TPD:PMMA/QDs/Alq_3", *Nano Hybr. Compos.*, 15 (2017) 10-20.

[18] M.K. Akeel, A.I. Omar and R.S. Wasan, "Electroluminescence Devices from Quantum Dots with TPD Polymer White Light Generation", *J. Nano Res.*, 48 (2017)104-113.

[19] S. Meng-Yao, L. Xin-Yuan and Z. Jia-Tao, "Telluride Semiconductor Nanocrystals: Progress on their Liquid-Phase Synthesis and Applications", *Rare Met.*, 41 (2022), 2527-2551.

[20] G.U. Fehmi and A. Adisa "Environmental Impacts of Small-Scale Hybrid Energy Systems: Coupling Solar Photovoltaics and Lithium-Ion Batteries", *Sci. Total Enviro.*, 643 (2018) 1579-1589.

[21] M.J. Simon and A.M. Brian, "Battery and Energy Metals: Future Drivers of the Minerals Industry", *SEG Discovery*, 127 (2021)11-18.

[22] Y. Xiutao et al., "Investigation of the Surface and Interfacial Properties of Polycrystalline CdTe/Monocrystalline Si Structure", *J. Electron. Mater.*, 51 (2022) 4378-4387.

[23] X. Yiqiu et al., "Advances in the Applications of Graphene-Based Nanocomposites in Clean Energy Materials", *Crystals*, 11(47) (2021)1-26.

[24] Z. Yue et al., "A Durable Lithium–Tellurium Battery: Effects of Carbon Pore Structure and Tellurium Content", *Carbon*, 173 (2021)11-21.

IRAQI JOURNAL OF SCIENTIFIC AND INDUSTRIAL RESEARCH

About IJSIR

The Iraqi Journal of Scientific and Industrial Research (IJSIR) is a peer reviewed journal of high quality devoted to the publication of original research papers from applied sciences and their broad range of applications. IJSIR publishes quality original research papers, comprehensive review articles, survey articles, letters and short communications in pure and applied sciences and their applications in the broadest sense. It is intended that the journal may act as an interdisciplinary forum for scientists, researchers and manufactures. Innovative applications and material that brings together diverse areas of pure and applied sciences are particularly welcome. Review articles in selected areas are published from time to time. It aims to disseminate knowledge; provide a learned reference in the field; and establish channels of communication between academic and research experts, policy makers and executives in industry, commerce and investment institutions. IJSIR is a quarterly specialized periodical dedicated to publishing original papers, letters and reviews in: Agricultural Sciences, Alternative & Renewable Energy, Biochemistry & Biotechnology, Biological Sciences, Biomedical Engineering, Chemistry, Drugs & Pharmaceuticals, Environment & Pollution, Geology, Industrial Chemistry, Materials Science & Technology, Mathematics & Numerical Analysis, Microbiology & Immunity, Modeling & Simulation, Nanostructures & Nanotechnology, Nondestructive Tests & Inspections, Radiology & Radiation Physics, Semiconductors & Applications, Sensorics & Sensor Applications, Signal & Data Processing, Statistics & Optimization, Structure & Properties of Matter, Superconductivity & Applications, and Vacuum Science & Technology.

Editorial Office:

P. O. Box 6065, Baghdad 12631, IRAQ
Website: www.ijsir.com
Emails: info@ijsir.com

Aseel M. Al-Khafaji [1]
Wasmaa S. Mahmood [1]
Ihab Nabeel Safi [1]
Ahmed A. Ali [2]

[1] *Department of Prosthodontics, College of Dentistry, University of Baghdad, Baghdad, IRAQ*
[2] *Applied Laser and Research Unit, Dijlah University College, Baghdad, IRAQ*

Surface Characteristics and Corrosion Behavior Assessment of RF-Sputtered PEKK on Titanium

In this study, radiofrequency magnetron sputtering technique (RFMS) was used to coat the titanium with polymer Polyetherketoneketone (PEKK). The corrosion behavior was tested by the electrochemical test in Hank's solution, the corrosion rate was studied by the polarization test. Furthermore, to investigate the phases of the tested samples XRD technique was performed. The titanium samples coated with polymer were compared to untreated titanium and titanium treated by fiber laser followed by PEKK coated samples.

Keywords: Titanium; Corrosion: RF magnetron sputtering; Polyetherketoneketone
Received: 25 January 2024; **Revised:** 19 February; **Accepted:** 26 February 2024

1. Introduction

Dental implants remain one of the most demanding options for tooth replacement in the last few decades. Thus, attention should be drawn toward maintaining the restoration in optimal shape and quality to minimize the risk of implant failure such as mobility, and inflammation [1]. Since, the oral environment and body fluids contain complex materials such as organic material, protein, amino acids, chlorine, and so on. Thus, corrosion and ion release are possible complications of implanting titanium into the human body. This could lead to biological complications such as inflammation, toxicity, and hypersensitivity [2-4].

Accelerating the rate of bone formation, and shortening the healing time, are significant factors for the success of dental implants. Thus, various attempts have been made to change the properties of implant surface morphology and composition [5-8]. In particular, the topography of the implant surface gained wide attention, as it plays a major role in implant success [9].

Coating with thin film is considered an effective method for metal protection. Various methods of film deposition were developed despite several restrictions that may accompany the process. Physical vapor deposition (PVD) is a widely used technique such as magnetron sputtering deposition with film deposition ranging from a few millimeters to several micrometers [10]. Introducing the magnetic field becomes an extensive method since it can be used with a vast range of substrates of different sizes. Ceramics, polymers, ionic and metallic materials can be deposited using the RFMS method [11,12]. RF sputtering is known as 'green technology' because of the absence of (gas and liquid precursors) compared with plasma chemical vapor deposition (CVD). It permits a uniform distribution and directional deposition of the nanoparticles (NPs,) in addition, pattern surface structure can be obtained, and the deposition of nanoparticles on any substrate is possible in conditions that it tolerate high vacuum conditions [13].

Polyetherketoneketone (PEKK) is a new polymer material with superior physical and mechanical properties. It has gained good attention in the biomedical field because of its' valuable features such as being highly resistant to thermo-oxidative degradation, light weight, anti-bacterial properties, resisting hydrolysis, highly biocompatible, and high mechanical strength [14]. The presence of an extra ketone ring gives better properties compared to the other polyaryletherketone polymers group [15]. Earlier research used different polymers for metal coating [16,17] but, the authors found no previous work on the use of PEKK as a polymeric coating material on titanium using RFMS technique.

Due to the unique features of laser, such as specific patterns that can be obtained even with sophisticated parts due to the directional pattern of the laser beam that can be highly controlled. It became an effective method to improve the properties of titanium [18].

This study aimed to assess the efficacy of RFMS in polymer coating (with or without laser surface treatment) to minimize the corrosion rate of titanium when immersed in Hank's solution.

2. Experimental Part

Disc shape samples were fabricated by cutting the titanium rod with a wire cut (Lathe machine) according to the manufacturer's instructions, measured 7 mm in diameter and a thickness of 2 mm.

A- For untreated substrates: titanium samples were polished with silicon carbide paper starting from 500 to 2400 grit to grind and bring the disks to a

uniform smooth mirror surface using a rotated grinding and polishing machine.

B- For laser-treated substrates: roughening of titanium surface will be built up by CNC fiber laser machine (Jinan JinQiang 20W laser, China) by prompting dot structure. Dot laser structure design with 25 laser scan (D-L 25) [19]

Then, the substrate was cleaned using an ultrasonic bath immersed in absolute ethanol for 30 min and then dried in air. A custom stainless steel plate holder is designed to hold the circular substrates in the vacuum chamber during sputtering to ensure uniformity of the coating,

The target was made by mixing 16 g of PEEK powder with a few drops of polyvinyl alcohol (PVA) as a binder. Then the mixture was loaded and pressed in a cylindrical stainless-steel mold with the dimension of 50 mm in diameter and 3 mm in height, the pressing was done under 8 tons pressure for 2 min. The electrical press was used, to obtain a uniform target and to avoid target fracture. A copper cover to protect the target from cracks was used.

Several sputtering trials were conducted in a pilot study to determine the suitable sputtering parameters for optimal coating deposition. A magnetron sputtering device (Torr International Inc., USA) was used with different variables, for the magnetron power, working pressure, substrate temperature, and the time of the sputtering. Whereas only target-to-substrate distance was fixed, three sputtering intervals (runs) were performed. The working conditions are summarized in table (1).

Table (1) Different parameters for coating metal by radiofrequency magnetron sputtering technique

Sample	Power (W)	Pressure (Torr)	Substrate Temperature (°C)	Time of Deposition (min)
A	50	$3x10^{-2}$	60	180
	50	$3x10^{-2}$	60	120
C	50	$3x10^{-2}$	60	60

The results of the pilot showed that A and B samples the PEKK target became black after the RF sputtering which indicated the damage of polymer during the sputtering process while no damage was seen in group C. Thus, one hour exposure was considered as a suitable time for confirming the sputtering process. A thin film of PEKK was obtained after fixing the substrate temperature at 60°C and the working PF with 50W power for one hour.

The sputtering target of the PEKK disk was 50mm in diameter and 4mm in thickness and was attached to the anode (positive charge) of the system. The substrate (titanium) was attached to the cathode (negative charge) with a rotating disk, and a magnetron power of 50W was applied to the target. The substrates were heated gradually; the temperature was fixed at 60°C for one hour according to the pilot study. During the sputtering process, water passes through the system, and the procedure was performed under a vacuum of 3×10^{-2} torr. To achieve this vacuum pressure first, the mechanical pressure worked until the pressure reached the operating pressure (rotary pressure) of the turbomolecular pump (5×10^{-1} torr) the chamber was then evacuated to a high vacuum at $\sim10^{-4}$ torr. Then the substrates were moved in a rotary direction at 2 rpm during the deposition; with a steady rotary speed. The operation frequency of the RF-generator and the distance between the substrate and magnetron target were fixed to 10cm. The sputtering chamber was evacuated and the argon was introduced as a sputter gas.

The specimens were grouped according to the type of surface treatment.

1. CG represents the Control group.
2. L-ArG represents laser-treated group coated with PEKK using Argon gas by RFMS technique.
3. ArG represents a group coated with PEKK using Argon gas by RFMS technique without laser treatment.

Then all the groups were measured using XRD and Electrochemical test.

An automated x-ray diffractometer was employed for phase characterization using Cu-Kα radiation (λ=1.5406Å). The operation was done at 40 mA and 40 kV. Ambient laboratory temperature using 10s/angular step (1 angular step = 0.02°) was used for taking diffraction patterns.

Metal corrosion resistance is usually characterized by the corrosion rate that can be achieved using the polarization technique. Polarization test is one of the measurements of corrosion rate. The polarization means no (equilibrium potential) is obtained but can be obtained through open circuit potential (OCP). Three electrodes were connected to the corrosion cell which are (reference electrode, auxiliary electrode, and working electrode). The difference potential between (working and reference) electrodes represents the corrosion behavior of titanium. A freshly prepared Hank's solution at 37±2°C was prepared for each measurement to simulate normal biological conditions.

3. Results and Discussion

The high demand for dental implants brings challenges to researchers to provide restorations with optimum outcomes by minimizing the rate of failure. To achieve this, modification and coating the metal surfaces is an interesting choice for improving the properties of the materials such as corrosion resistance, biocompatibility, and scratch resistance [20-23].

Various polymers were introduced as effective coating materials, but the selection of PEKK as a protective barrier depends on its wide satisfying features which render it a good candidate for the present work. The coating technique is another challenge because of the wide range of methods available, but RFMS being a 'green technology' in

addition to the ability to deposit a wide range of materials with various particle sizes [24] proved to be an effective method of coating.

The XRD patterns for all measured groups are seen in Fig. (1). The peak indexing of the titanium was carried out based on the Joint Committee on Powder Diffraction Standards (JCPDS) (JCPDS-ICDD file 55-0898) [25].

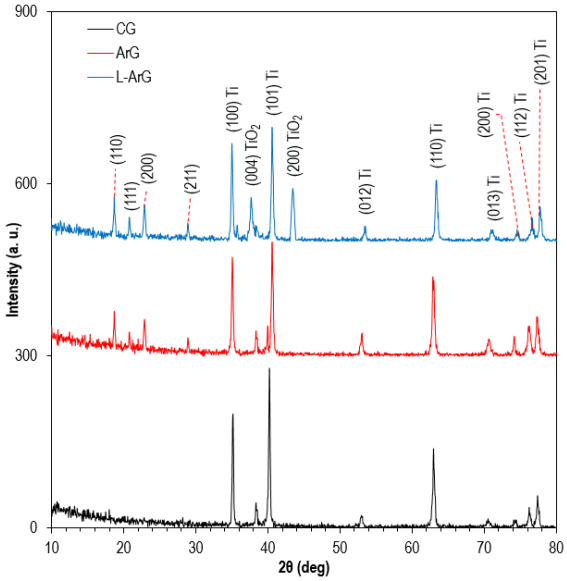

Fig. (1) XRD analysis for the experimental groups

The XRD result showed that the titanium phase remained constant after surface laser treatment. Signifying no change in the titanium phase was observed, which is important when dealing with the titanium. The new peaks of TiO_2 observed beside the Ti after laser structuring are due to the titanium air interaction during the surface structuring. Whereas the XRD pattern of the control group showed only titanium peaks as no other peaks were observed. New titanium oxide peaks were seen at 37.65° and 43.45° according to the diffraction plane of (002) and (200) which revealed an increase in oxygen percentage in L-ArG.

The new coat of PEKK on L-ArG and ArG showed diffraction peaks at 18.70°, 20.80°, 22.90° and 28.90°, which correspond to the diffraction planes of (110), (111), (200) and (211) based on Leiner [26].

The process of corrosion is known as an electrochemical behavior of metals, so the electrical method is an acceptable tool of measurement. The titanium behavior of the experimental groups is seen in the open circuit potential (OCP) curve (Fig. 2), where the PEKK-coated groups showed a shift toward positive values with time, whereas CG moved toward negative values. Table (2) presents the (I_{corr}, E_{corr}, and corrosion rate), where a slight decrease in (I_{corr}) value in ArG group followed by a gradual decrease in L-ArG. The improvement of corrosion resistance in L-ArG can be ascribed to the strong boundaries among the metal grains and the increase in the homogeneity which is due to the refinement of the grain size that improved the titanium oxide layer formation [27]. A study conducted by Tian et al explained the increase in corrosion resistance after laser treatment due to the formation of a new titanium oxide layer [28].

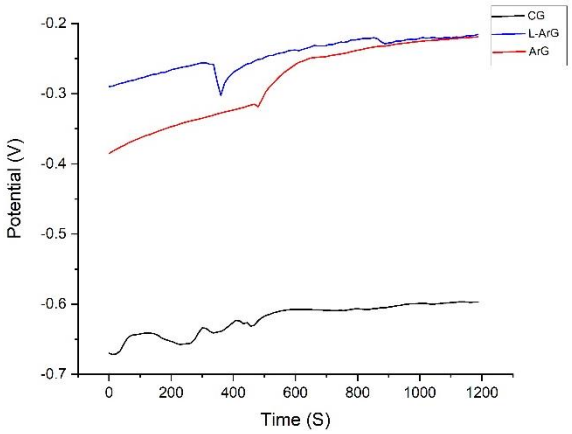

Fig. (2) Open-circuit potential for the experimental groups

Table (2) Different parameters of corrosion behavior for all the experimental groups

Group	$E_{(i=0)}$ (V)	$I_{corrosion}$ (A/cm²)	Corr. Rate (mm/y)
CG	-0.485	$2.032x10^{-6}$	0.1651
ArG	-0.332	$3.677x10^{-6}$	0.1480
L-ArG	-0.305	$9.424x10^{-7}$	0.0398

From our previous work, an increase in surface roughness after the modification of the titanium surface by laser was found [19]. At the same time, other studies related the decrease in corrosion rate after laser treatment was due to the increase in surface roughness and the formation of titanium oxide layer [25,27,29]. Conradi explained the decrease in corrosion after laser treatment was ascribed to the increase in surface roughness which slightly turned the surface properties from hydrophilic to a more hydrophobic nature. This feature will repel liquids from adhering to metal and improve the titanium's properties [30].

The presence of a PEKK layer on the titanium surface clearly showed the shifting of anodic and cathodic curves to more positive E_{corr} values as presented in Fig. (3) of the Tafel plot. This behavior explains the decrease in corrosion rate, because the PEKK coat may retard the process of anodic dissolution. The presence of a PEKK coat acts as a barrier permitting minimum electrolyte to pass through and inhibits the ionic conduct which will impede the passage of solutions that inhibit corrosion [31].

The decrease of I_{corr} value for ArG and L-ArG explains the efficiency of the PEKK coat by RFMS method since this technique permits a longer distance for the generated electrons to move for every half cycle. This will generate plasma of high density which enhances the sputtering process efficiency

[24]. In other words, permitting an even dense coat formation that resists cracks which prohibits seepage of fluids thus increasing corrosion resistance.

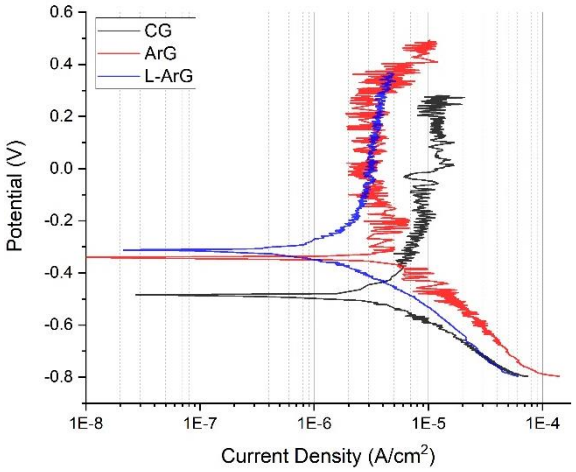

Fig. (3) Tafel plot for the experimental groups

Several authors demonstrated the importance of surface treatment before bonding to create a good mechanical interlock [32]. Good adhesion promotes corrosion resistance by enhancing the coat integrity. Thus, the formation of small metal projections after laser treatment will provide a better bond between the metal and polymer, consequently minimizing the risk of external forces and corrosion attacks [33]. This explains the lowest value of corrosion rate in L-ArG compared to the other experimental groups. The result agrees with an earlier study that found an improvement in the metal/polymer interface after surface laser treatment, increasing resistance against degradation and humidity [34].

4. Conclusion

RF magnetron sputtering proved to be an effective method to coat the titanium with polymer (PEKK), a decrease in corrosion rate showed the efficacy of the polymer coat. XRD analysis verifies the results by the formation of new peaks of PEKK. The laser surface treatment of the titanium before PEKK coating enhances the polymer adhesion to the metal, therefore it prevents the electrolytes from reaching the metal.

References

[1] X. Shen et al., "Mesenchymal stem cell growth behavior on micro/nano hierarchical surfaces of titanium substrates", *Colloids Surf. B: Biointerfac.*, 172 (2015) 221-232.

[2] D.F. Williams, "Tissue-biomaterial interactions", *J. Mater. Sci*., 22 (1987) 3421-3445.

[3] M. Idrees and A.Z. Jebakumar, "A review on corrosion scenario of bio implants in human body", *Am. j. Biol. Chem. Pharm. Sci.*, 1 (2014) 100-104.

[4] N.S. Manam et al., "Study of corrosion in biocompatible metals for implants: A review", *J. Alloys Comp*., 701 (2017) 698-715.

[5] H. Kim et al., "The biocompatibility of SLA-treated titanium implants", *Biomed. Mater.*, 3 (2008) 025011.

[6] G. Wang et al., "Magnesium ion implantation on a micro/nanostructured titanium surface promotes its bioactivity and osteogenic differentiation function", *Int. J. Nanomed.*, 9 (2014) 2387-2398.

[7] A. Fukuda et al., "Bone bonding bioactivity of Ti metal and Ti-Zr-Nb-Ta alloys with Ca ions incorporated on their surfaces by simple chemical and heat treatments", *Acta Biomater*., 7 (2011) 1379-1386.

[8] J. Park et al., "Nanosize and vitality: TiO_2 nanotube diameter directs cell fate", *Nano Lett*., 7 (2007) 1686-1691.

[9] R.G. Flemming et al., "Effects of synthetic micro-and nano-structured surfaces on cell behavior", *Biomater*., 20 (1999) 573-588.

[10] A. Fragiel et al., "Influence of the N2 partial pressure on the mechanical properties and tribological behavior of zirconium nitride deposited by reactive magnetron sputtering", *Surf. Coat. Technol.*, 202 (2008) 3653–3660.

[11] J.W. Lee et al., "The mechanical properties evaluation of the CrN coatings deposited by the pulsed DC reactive magnetron sputtering", *Surf. Coat. Technol.*, 200 (2006) 3330–3335.

[12] T. Elangovan et al., "Nanostructured CrN thin films prepared by reactive pulsed DC magnetron sputtering", *Mater. Sci. Eng. B*, 167 (2010) 17–25.

[13] S. Swann, "Magnetron sputtering", *Phys. Technol.*, 19(2) (1988) 67.

[14] S. Najeeb et al., "Applications of polyetheretherketone (PEEK) in oral implantology and prosthodontics", *J Prosthodontic Res.*, 60 (2016) 12–19.

[15] Z. Horák et al., "Polyetheretherketone (PEEK). Part I: prospects for use in orthopaedics and traumatology", *Acta Chir. Orthop. Traumatol. Cech.*, 77 (2010) 463-469.

[16] N.N. Kumar et al., "Effect of Argon Plasma Treatment on Tribological Properties of UHMWPE/MWCNT Nanocomposites", *Polym.*, 8 (2016) 295.

[17] T. Moskalewicz et al., "The Effect of the Polymer Structure in Composite Alumina/Polyetheretherketone Coatings on Corrosion Resistance, Micro-mechanical and Tribological Properties of the Ti-6Al-4V Alloy" *J. Mater. Eng. Perform.*, 29 (2020) 1426-1438.

[18] Y.S. Tian et al., "Laser surface modification of titanium alloys - a review", *Surf. Rev. Lett.*, 12 (2005) 123–130.

[19] A.M. Al-Khafaji and T.I. Hamad, "Assessment of Surface Roughness and Surface Wettability of

Laser Structuring Commercial Pure Titanium", *J. Res. Med. Dent. Sci.*, 8 (2020) 81-85.
[20] F. Galliano and D. Landolt, "Evaluation of corrosion protection properties of additives for waterborne epoxy coatings on steel", *Prog. Org. Coat.*, 44 (2002) 217–225.
[21] A. Talo, O. Forsén and S. Yläsaari, "Corrosion protective polyaniline epoxy blend coatings on mild steel", *Synth. Met.*, 102 (1999) 1394–1395.
[22] H. Ali, S. Saleem and T.L. Al-Zubaydi, "Evaluation of corrosion behavior of bioceramics coated commercially pure titanium and Ti-6Al-4V alloy", *J. Baghdad College Dent.*, 26 (2014) 41- 48.
[23] M. Nasir and H,A. Rahman, "Mechanical Evaluation of Pure Titanium Dental Implants Coated with a Mixture of Nano Titanium Oxide and Nano Hydroxyapatite", *J Baghdad College Dent.*, 28 (2016) 38-43.
[24] L. Aissani et al., "Magnetron Sputtering of Transition Metal Nitride Thin Films for Environmental Remediation", *Coatings*, 12 (2022) 1746.
[25] I.N. Safi et al., "Implementation and characterization of coating pure titanium dental implant with sintered b-TCP by using Nd:YAG laser", *Saudi Dent. J.*, 31 (2019) 242–250.
[26] G.M. Leiner, D.P. Dennies and A. Yardimci, "High Performance Polymers in Additive Manufacturing Processes: Understanding Process, Structure and Property", *Microscop. Microanal.*, 21 (2015) 127-128.
[27] R. Kumari et al., "Laser surface textured titanium alloy (Ti-6Al-4V) Part II: Studies on bio-compatibility", *Appl. Surf. Sci.*, 357 (2015) 750–758.
[28] Y. Tian et al., "Research progress on laser surface modification of titanium alloys", *Appl. Surf. Sci.*, 242 (2005) 177–184.
[29] Y. Xu et al., "Electrochemical corrosion and anisotropic tribological properties of bioinspired hierarchical morphologies on Ti-6Al-4V fabricated by laser texturing", *Tribol. Int.*, 134 (2019) 352–364.
[30] M. Conardi et al., "Influence of Laser Texturing on Microstructure, Surface and Corrosion Properties of Ti-6Al-4V", *Metals*, 10(11) (2020) 1504.
[31] N. Madaoui et al., "Effect of Argon-Oxygen Mixing Gas during Magnetron Sputtering on TiO_2 Coatings", *Adv. Mater. Sci. Eng.*, 1 (2017) 1-6.
[32] V.M. Marinosci et al., "Effect of grit-blasting on the fracture toughness of hybrid titanium-thermoplastic composite joints", *Int. J. Adhes. Adhes.*, 109 (2021) 102893.
[33] S.G. Croll, "Surface roughness profile and its effect on coating adhesion and corrosion protection: A review", *Prog. Org. Coat.*, 148 (2020) 105847.
[34] J. Haubrich, K. Schulze and J. Hausmann, "Laser treatment of titanium surfaces in different atmospheres for improved adhesion properties", *Euro Hybr. Mater. Struct.*, (2014) 10-11.

IRAQI JOURNAL OF APPLIED PHYSICS LETTERS

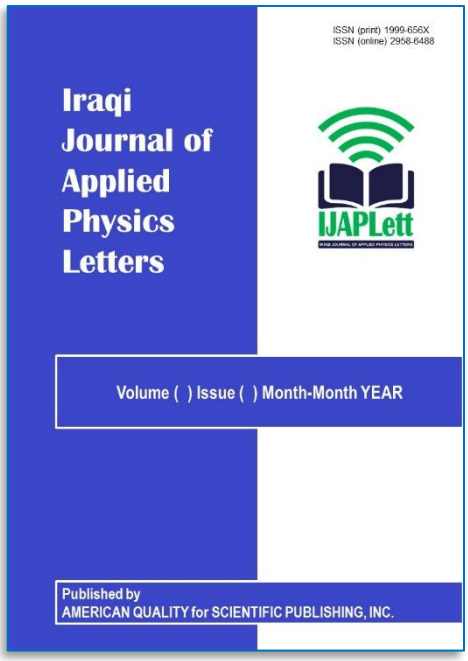

About IJAPLett

The Iraqi Journal of Applied Physics Letters (IJAPLett) is a peer-reviewed journal of high quality devoted to the publication of original research letters from applied physics and their broad range of applications. IJAPLett publishes quality original research letters in physics and its applications in the broadest sense. It is intended that the journal may act as an interdisciplinary forum for physics and its applications. Innovative applications and materials that bring together diverse areas of physics are particularly welcome. IJAPLett aims to disseminate knowledge; provide a learned reference in the field; and establish channels of communication between academic and research experts, policy makers, and executives in industry, commerce, and investment institutions.

IJAPLett is a quarterly specialized periodical dedicated to publishing original letters in:

- Alternative & Renewable Energy
- Applied Mechanics & Thermodynamics
- Applied Optics & Optical Design
- Biophysics & Bioengineering
- Cryptography & Applications
- Electromagnetic Fields
- Electronic Materials & Devices
- Energy Generation & Conversion
- Fluids Physics & Mechanics
- Imaging, Microscopy & Spectroscopy
- Laser Physics & Applications
- Magnetism & Applications
- Instrumentation, Measurements & Metrology
- Nanostructures & Applications
- Nonlinear & Ultrafast Optics
- Nuclear Physics & Engineering
- Optical Communications & Systems
- Optoelectronics Devices & Applications
- Organic Materials, Devices & Applications
- Physical Chemistry & Biochemistry
- Plasma, Discharge Physics & Applications
- Quantum Physics & Spectroscopy
- RF & Digital Communications
- Semiconductors & Devices
- Simulation & Modeling Research
- Solar Energy & Devices
- Solid State Physics & Applications
- Structure & Properties of Matter
- Superconductivity & Related Devices
- Surfaces, Interfaces & Films
- Thin Films & Applications
- Vacuum Science & Technology.

EDITORIAL BOARD

Ahmad K. Ahmad [1]
Firas A. Abdularhman [2]
Roaa Ayad Aldoori [3]

[1] *College of Engineering, Al-Nahrain University, Baghdad, IRAQ*
[2] *Mobile communication and computing engineering department, College of Engineering, University of Information and Communication Technology, Baghdad, IRAQ*
[3] *College of Engineering, Al-Iraqia University, Baghdad, IRAQ*

Design of Einzel Electrostatic Lenses Using Inverse Schiske's Model

This paper examines the computational design of an electrostatic Einzel lens utilizing the inverse Schiske's model with certain magnification conditions. The electrostatic lens potential distribution has been characterized by an analytical function referred to as the inverse Schiske model. By solving the paraxial ray equation with the Runge-Kutta technique of fourth order, the charged particle beam trajectory and its derivatives via the lens have been determined. One can determine the proposed electrostatic lens optical properties, for instance, magnification, focal properties, and aberrations (spherical and chromatic), from knowing the axial potential distributions of the Einzel lens' and its first and second derivatives, as well as the beam trajectory and its derivatives. Based on our findings, we can infer that the constant k substantially affects the aberration values, with the best results happening at k = 0.1 for constants (V_o = 1V and a = 0.025) with a 10mm lens length. Also, the form of the suggested lens' electrodes is calculated.

Keywords: Electrostatic lens; Spherical aberration; Paraxial ray equation
Received: 25 February 2024; **Revised:** 24 March 2024; **Accepted:** 31 March 2024

1. Introduction

Einzel lenses are distinguished by having constant potential U1=U3 on both the object and image sides, whereas the center electrode has a separate potential U2. Consequently, they are utilized when simply focusing is necessary. Nevertheless, the energy of the beam needs to be conserved. Einzel lenses are symmetrical cylinder electrodes, where the lens's center for both foci. Consequently, they are commonly known as symmetrical round lenses [1]. Due to their adaptability and the fast development of contemporary instrumentation, Einzel lenses are finding growing usage in various scientific and technological fields [2-7].

The current work aims to discover a more straightforward expression to represent the potential axial distribution of the Einzel lens with bearable aberrations. The inverse Schiske's recommended model [8] has been used to illustrate the Einzel lens's potential field distribution as follows:

$$U(z) = \frac{1}{V_0\left(1-\frac{k^2}{1+\left(\frac{z}{a}\right)^2}\right)} \quad (1)$$

Equation (1) may reflect the accelerator mode potential distribution along an Einzel lens' optical axis, where z is the lens optical axis, and (a, k, and V_0) are parameters by which the shape and symmetry of the lens and the value of the voltage inside the lens can be controlled. A non-relativistic electron beam traveling close to the axis in a symmetrical cylindrical electrostatic field of a lens system can controlled by the equations of motion called the paraxial ray equation [1,9].

$$r'' + r'\frac{U'}{2U} + r\frac{U''}{4U} = 0 \quad (2)$$

where U' and U'' are the axial potential's first and second derivatives, respectively. The primes signify a derivative for z, and r denotes beam radial displacement from the optical axis z

Equation (2) is a linear and homogeneous second-order differential equation. Knowing the potential distribution along the z-axis $U_{(z)}$, you also know the factors in front of r'', r', and r [10]. To calculate the aberration coefficients, spherical and chromatic, the following equations are used [11,12].

The electrode shapes are found by using a synthesis approach where the profiles of the electrodes correspond to the axial field distribution found with the aid of the following equation [12,13]:

$$R = 2\left(U(z) - \frac{U(r,z)}{U''(z)}\right)^{0.5} \quad (5)$$

The Wolfram Mathematica program is used in the design of the electrostatic einzel lens which is described in previous research [14].

2. Results and Discussion

An Einzel lens with a center electrode at a higher voltage than the two outer electrodes is seen in Fig. (1a) called the axial potential distribution. Away from the lens terminals, there is a field-free region, i.e. there is no force acting on the trajectory of the charged particle beam, that is, a straight line. This indicates that there is no electric field outside the lens because the potential distribution $U(z)$ is constant at the boundaries, and therefore its first derivative $U'(z)$

is zero. The lens contains three electrodes since the potential second derivative $U''(z)$ has two inflection points [12]. The axial potential distribution $U(z)$ for the inverse Schiske's electrostatic einzel lens is shown in Fig. (2a) for different values of V_0 at constant (a=0.025, k=0.7), (2b) different values of a, at constant (V_0=1, k=0.3), and (2c) different values of k at constant (V_0=1, a=0.025).

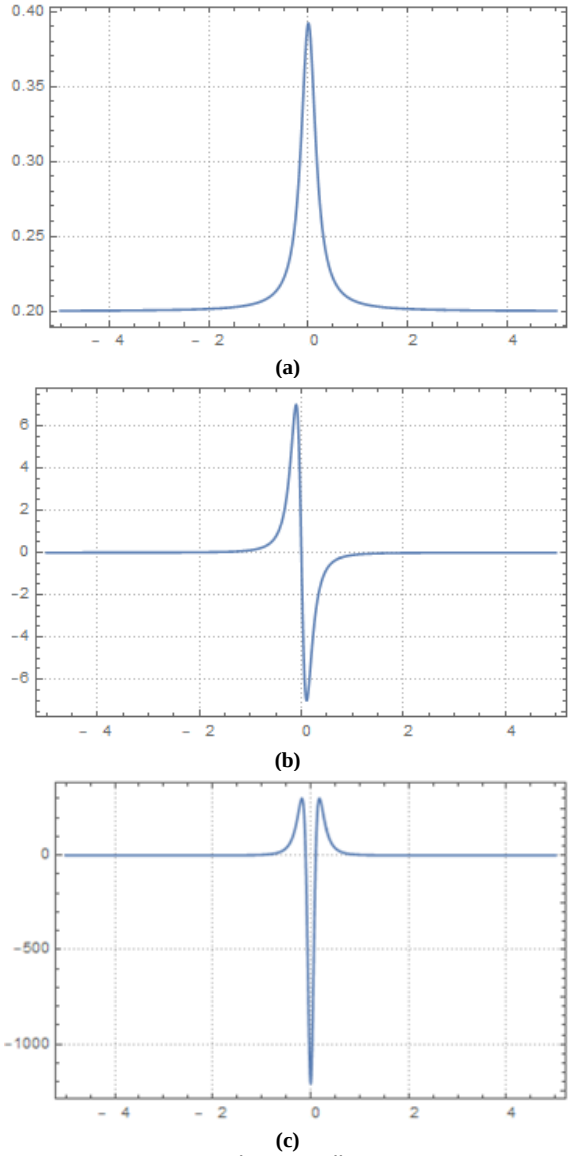

Fig. (1) (a) $U_{(z)}$, (b) $U'_{(z)}$, (c) $U''_{(z)}$. The axial potential distribution and its first and second derivatives respectively, for inverse Schiske's model electrostatic Einzel lens for (V_o=5V, a=0.025, k=0.7 and L=10mm)

From Fig. (2), one can notice that the values of the maximum potential decrease as V_0 increases when a and k are constant as shown in Fig. (2a). When changing values of a when keeping V_0 and k are constants, we notice that the full-width at half maximum (FWHM) increases with increasing values of a as shown in Fig. (2b). Also, when increasing values of k, with constants a and V_0, the values of the maximum potential decrease as shown in Fig. (2c).

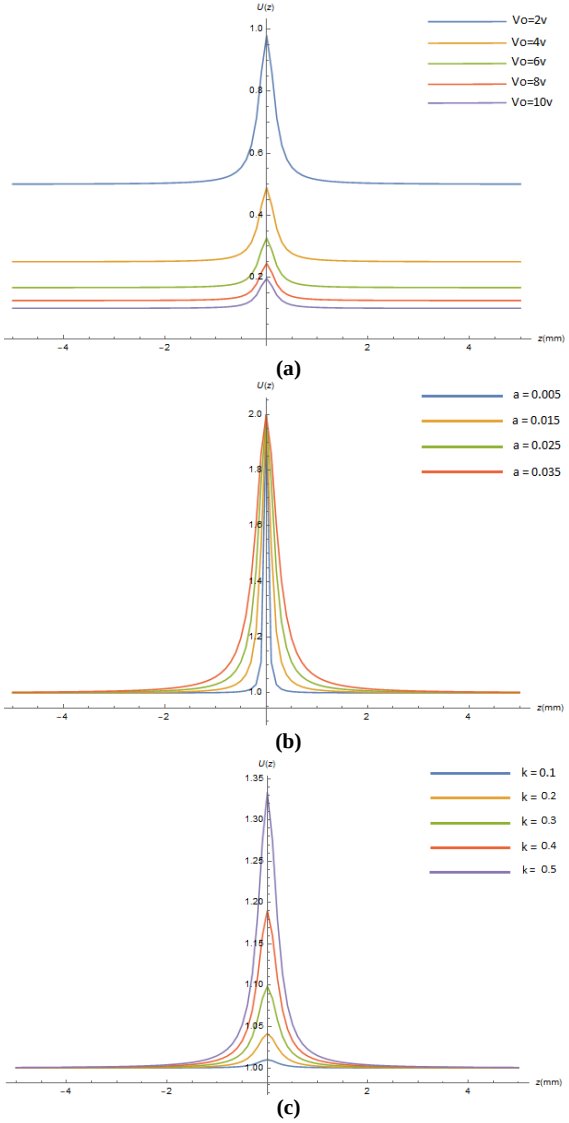

Fig. (2) The potential field $U(z)$ axial distribution for inverse Schiske's electrostatic Einzel lens for (a) different value of V_0 at constant (a=0.025, k=0.7) (b) different values of a, at constant (V_0=1, k=0.3) and (c) different values of k, at constant (V_0=1, a=0.025)

Figures (3a) and (4a) show the electron beam's course in the electrostatic einzel lens field at zero and infinite magnification, respectively, at various values of V_0. Considering that (a and k) are constants. The trajectory of the electron beams gradient increases as V_0 value increases. At a=0.025 and k=0.2, whereas the other electron beam paths (various values of V_0) shifted downward, the electron beams intersect the lens optical axis.

Figures (3b) and (4b) show the electron beam trajectory for various values of a; it is seen that the trajectory beam tends to be straight with the increasing value of a. As increasing of the constant a, the trajectory converges until they become constants for large values of a. Figures (3c) and (4c) show the electron beam trajectory for constant values (V_0=1V, a=0.025) and various values of k. It is observed that

with increasing the values of *k*, the trajectory shifted down and got closer to the optical axis *z*.

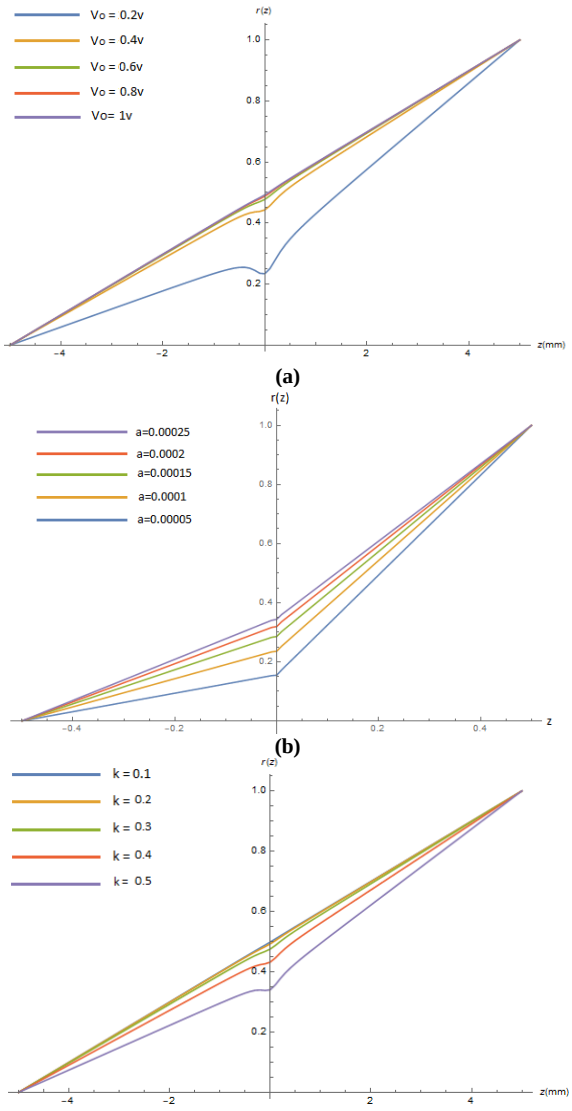

Fig. (3) The trajectories of electron beam for the einzel electrostatic lens under infinite magnification conditions at diverse values of (a) V_0 , (b) *a*, and (c) *k*

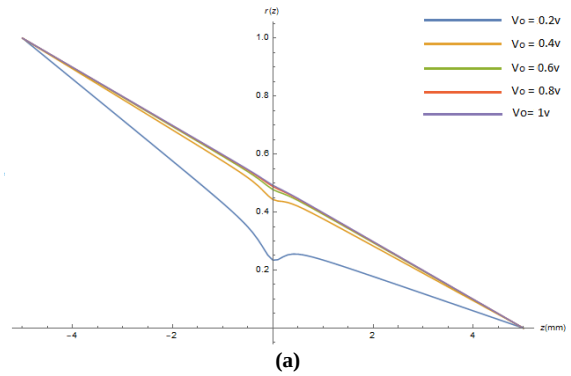

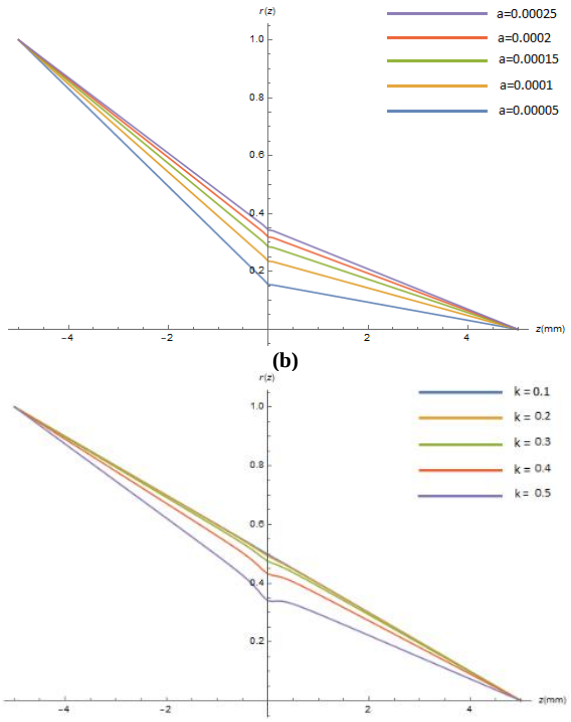

Fig. (4) The trajectories of electron beam for the Einzel electrostatic lens under zero magnification conditions at diverse values of (a) V_0, (b) *a*, and (c) *k*

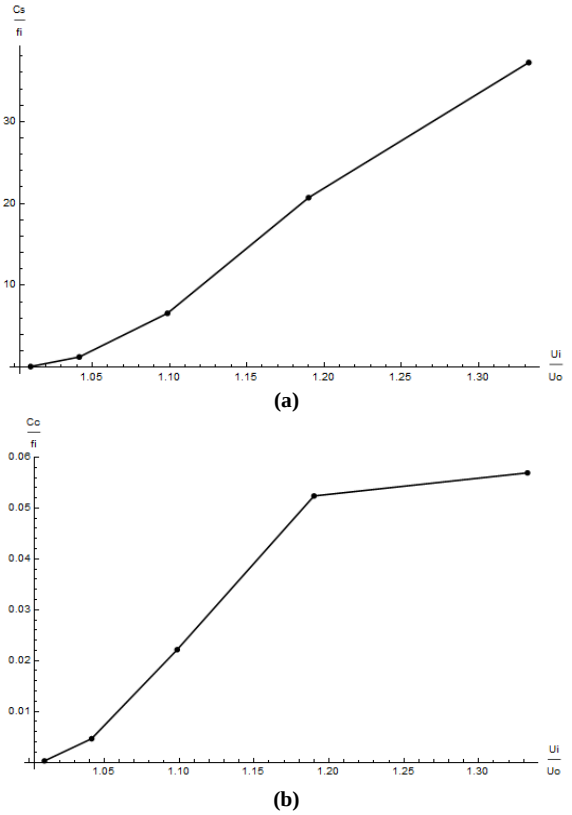

Fig. 5 (a) Spherical and (b) Chromatic relative aberrations coefficients respectively, versus Ui/U_o for zero magnification conditions at *a*=0.025 and V_0 =1V

Figure (5) displays the U_i/U_0 voltage ratio-dependent image-side relative spherical and chromatic aberration coefficients, C_s/f_i and C_c/f_i,

respectively, for the electrostatic Einzel lens operating at zero magnification at various values of k (since the voltage ratio changes only with the changing the constant k). According to this figure, as k increases, or as the ratio U_i/U_0 increases, so do the relative spherical and chromatic aberration coefficients.

In Fig. (6), the object side C_s/f_o and C_c/f_o were computed for a range of the voltage ratio U_i/U_0 at various values of k. Figure (6) shows that C_s/f_o and C_c/f_o increase with increasing U_i/U_0. From the last to figures one can concludes that low values of C_s/f_o, C_c/f_o, C_s/f_i and C_c/f_i are achieved at low values of k.

Table (1) shows the image and object side's relative chromatic and spherical aberration coefficients for different values of k at constant a=0.025 and V_0=1V, from this table, one may see that the relative chromatic and spherical aberration coefficients increase with increasing the values of k as shown in the figures (5) and (6).

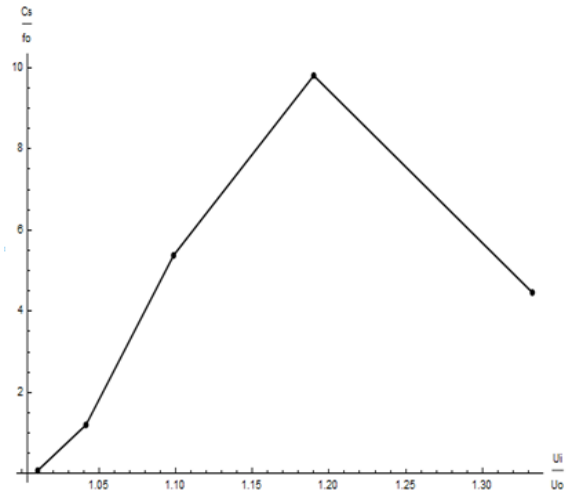

(a)

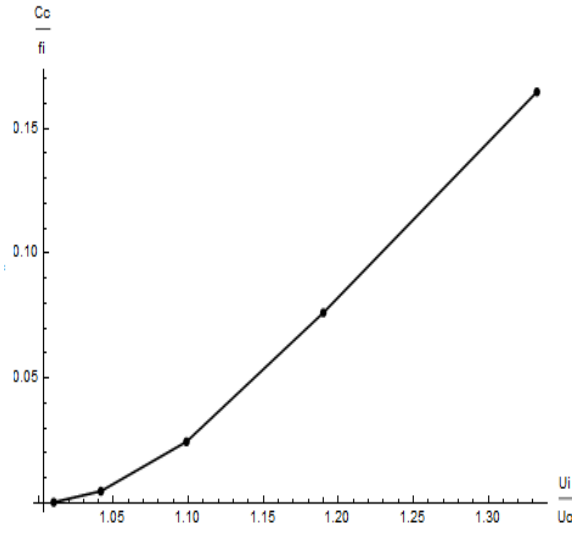

(b)

Fig. (6) The relative (a) Spherical and (b) Chromatic aberration coefficients respectively, versus U_i/U_0 at diverse values of k under infinite magnification conditions with a=0.025 and V_0=1V

Table (1) The image and object side relative chromatic and spherical aberration coefficients for diverse values of k

k	f	U_i/U_0	C_s/f_i	C_c/f_i	C_s/f_0	C_c/f_0
0.1	1.000	1.010	0.075	0.0003	0.075	0.0002
0.2	1.004	1.040	1.243	0.0046	1.200	0.0047
0.3	1.026	1.090	6.582	0.0221	5.830	0.0245
0.4	1.102	1.190	20.172	0.0524	9.812	0.0762
0.5	1.349	1.333	37.323	0.0569	4.463	0.1650

The electrode shapes are determined using the synthesis method, i.e., the shape of the electrodes corresponds to the axial potential distribution was calculated with the aid of Eq. (5). Figure (7) depicts the two-dimensional electrostatic forms that represent the einzel lens. From this figure, we can recognize the shape of the electrodes by rotating these shapes around the optical axis with the boor diameter of the central electrode equal to 2.8 mm.

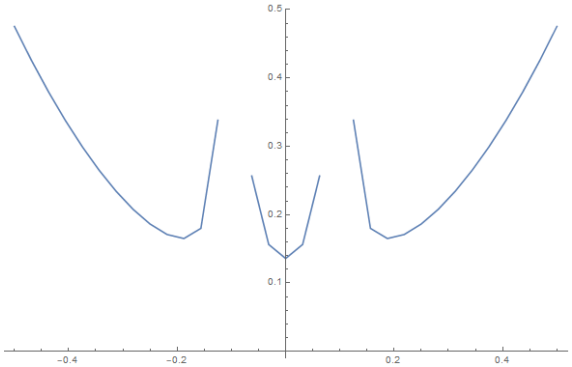

Fig. (7) The Einzel lens's three-electrodes correspond to the axial distribution of the constant (V_0=1V and a=0.025, k=0.3 and L=10mm)

3. Conclusion

The current study demonstrates that several types of electrostatic lenses with tiny aberrations can be designed and operated at varied potential ratios. It has been discovered that utilizing the invers Schiske's model, which can be utilized to solve the paraxial ray equation of charged particles, it is possible to create an Einzel lens with low aberration and the shortest course of the electron trajectory. The results show that the aberration coefficient decreases as the constant k decreases, where the best outcome occurs at the constant k are equal to 0.1 with constants (V_0=1V, a=0.025) for lens length equal to 10mm.

References

[1] B. Paszkcwski, **"Electron Optics"**, Itffe Book (London, 1968).

[2] R.R.A. Syms, L. Michelutti and M.M. Ahmad, "Two-dimensional microfabricated electrostatic einzel lens", *Sens. Actuat. A*, 107(3) (2003) 285-295.

[3] M.H. Rashid, "Simple analytical method to design electrostatic einzel lens", *Proc. DAE Symp. on Nucl. Phys.*, 56 (2011) 1132-1133.

[4] O. Sise, M. Ulu and M. Dogan, "Multi-element cylindrical electrostatic lens systems for focusing and controlling charged particles", *Nucl. Instrum. Meth. A*, 554 (2005) 114-131.
[5] K. Ho-Seob et al., "Arrayed microcolumn operation with a wafer-scale Einzel lens", *Microelectron. Eng.*, 7879 (2005) 55-61.
[6] S.N. Mazhir, "Generated and shifted of Ion beams By Electrostatic Lenses (Einzel lens)", *Baghdad Sci. J.*, 12(5) (2015) 814-821.
[7] A.K. Ahmad and B.F. Abd-Alghane, "Design and analysis of the optical properties of electrostatic unipotential lens (einzel lens)", *J. Opt.*, 52 (2023) 1704-1709.
[8] A. Amer and A.K. Ahmad, "Differential algebraic description for aberrations analysis of typical electrostatic einzel lens", *Optik*, 168 (2018) 112-117.
[9] Grivet, **"Electron Optics"**, 2nd ed., Elsevier Ltd. (1972).
[10] J. Szep and M. Szilagyi, "A novel approach to the synthesis of electrostatic lenses with minimized aberrations", *IEEE Trans. Electron Dev.*, 35(7) (1988) 1181-1183.
[11] M. Szilagyi and J. Szepa, "Optimum design of electrostatic lenses", *J. Vac. Sci. Technol. B*, 6(1) (1988) 953-957.
[12] A.K Ahmad, S.M. Juma and A.A. Al-Tabbakh, "Computer aided design of an electrostatic FIB system", *Indian J. Phys.*, 76B(6) (2002) 711-714.
[13] M. Szilagyi, "Reconstruction of electrodes and pole pieces from optimized axial field distributions of electron and ion optical systems", *Appl. Phys. Lett.*, 45(5) (1984) 499-501.
[14] A.K. Ahmad and F.A. Abdularhman, "Design of Einzel Electrostatic Lenses Using Schiske's Model", *AIP Conf. Proc.*, 2830 (2023) 040012.

$$C_{so} = \frac{U_o^{-1/2}}{16 r_o'^4} \int_{zo}^{zi} \left(\frac{5}{4}\left(\frac{U''}{U}\right)^2 + \frac{5}{24}\left(\frac{U'}{U}\right)^4 + \frac{14}{3}\left(\frac{U'}{U}\right)^3 \frac{r'}{r} - \frac{3}{2}\left(\frac{U'}{U}\right)^2 \frac{r'^2}{r^2} \right) \sqrt{U} r^4 dz \quad (3)$$

$$C_{co} = \frac{\sqrt{U_o}}{r_o'^2} \int_{zo}^{zi} \left(\frac{1}{2}\left(\frac{U'}{U}\right) r' + \frac{1}{4}\left(\frac{U''}{U}\right) r \right) \frac{r}{\sqrt{U}} dz \quad (4)$$

where C_{so} and C_{co} represent the spherical and chromatic aberration, respectively.

AMERICAN QUALITY FOR SCIENTIFIC PUBLISHING

About AQSP

American Quality for Scientific Publishing (AQSP) is a society-owned scientific publisher, providing impact, recognition and value for the scientific community. AQSP's portfolio includes several journals, which are published jointly with or on behalf of partner societies and research organizations. Our publishing portfolio reflects the growth of scientific research in core scientific fields, while recognizing the increasingly interdisciplinary nature of scientific research.

We work closely with researchers, librarians and partners worldwide to produce academic journals, books and conference proceedings. We also have a science news and media portfolio which includes trusted sources of science news.

Our aim is to publish the latest and best research in the sciences and beyond, and make that research available to as many people as possible. All our academic publications are specifically designed to help readers quickly and easily access the content we publish. We also provide a range of services to help the scientific community register, validate, edit, disseminate, preserve and maximize their research.

Making universal access to research a reality is a priority. We believe conducting science more openly can accelerate scientific discovery and we are committed to supporting the wider adoption of open practices across the sciences. We call this approach Open Science and we have developed a program of activities to make it a reality.

Board of Directors

AQSP's Board of Directors is composed of an experienced group of executive and non-executive directors who meet regularly throughout the year and oversee the management of the company.

Diversity, Equity and Inclusion at AQSP

We can only realize our commitment to open science with an equally strong commitment towards diversity, equity and inclusion in scientific publishing.

At its core, open science embraces transparency, collaboration and participation. We support these principles by:

- Committing to diversity, equity and inclusion
- Fostering a safe and inclusive publishing environment
- Reporting on diversity, equity and inclusion
- Actively reducing bias within peer review

AQSP publishes as a total or partial sponsor the following publications:

- American Journal of Remote Sensing
- American Journal of Numerical Analysis
- American Journal of Pathology
- American Journal of Organometallic Chemistry
- American Journal of Biotechnology
- American Journal of Signal Processing
- American Journal of Luminescence
- Applied Chemistry Letters
- Iraqi Journal of Applied Physics
- Iraqi Journal of Applied Physics Letters
- Iraqi Journal of Materials
- Iraqi Journal of Scientific and Industrial Research
- Journal of Applied and Physical Mathematics
- Journal of Applied and Practical Sciences
- Journal of Applied Chemical Physics
- Journal of Applied Modeling and Simulation
- Journal of Applied Spectroscopy and Spectral Analysis
- Journal of Atomic and Nuclear Physics
- Journal of Biophysics and Biotechnology
- Journal of Data and Signal Processing
- Journal of Environmental Physics and Technology
- Journal of Heat Transfer and Thermodynamics
- Journal of Hybrid and Remote Sensing
- Journal of Industrial Engineering and Sciences
- Journal of Laser Science and Engineering
- Journal of Magnetics: Materials and Applications
- Journal of Micro and Nano Electrooptomechanics
- Journal of Modeling and Optimization in Physics
- Journal of Nanomaterials and Nanodevices
- Journal of Optics and Laser Physics
- Journal of Optoelectronics and Photonics
- Journal of Photonics and Radiation Physics
- Journal of Physical Vapor Deposition Science and Technology
- Journal of Plasma Physics Letters
- Journal of Quantum Physics Research
- Journal of Recent Materials Technology
- Journal of Renewable Energy Science and Technology
- Journal of Spectroscopy and Molecular Physics
- Journal of Surface and Coating Science
- Journal of Theoretical and Computational Physics
- Nanophotonics Letters
- Optoelectronics Communications
- Photonic Spectra
- Renewable Energy Letters
- Spectral Physics Communications
- Thin Film Research and Technology

Noor Z. Alrawe [1]
Nathera A.A. AL Tememee [2]
Akram M. Ali [3]

[1] *Department of Physics, College of Education for Pure Sciences, University of Anbar, Rammadi, IRAQ*
[2] *Department of Physics, College of Science, University of Baghdad, Baghdad, IRAQ*
[3] *Department of Physics, College of Science, University of Anbar, Rammadi, IRAQ*

Effect of Solvent on Spectroscopic Characteristics and Energy Transfer Processes of Some Laser Dyes

This article summarizes recent progress and the authors work in the field of solvation effects on spectroscopic properties of some organic compound. For many aromatic molecules the position and the structure of the fluorescence spectrum are strongly dependent on the solvent. The wavelength displacement can often be correlated with changes in solvent dielectric constant and the solvent index of refraction. A general review for the effect of the solvent is presented including studying the relationship between energy transfer processes and quantum efficiency with different solvent types.

Keywords: Laser dyes; Organic molecules; Fluorescence; Energy transfer
Received: 22 September 2023; **Revised:** 19 February; **Accepted:** 26 February 2024

1. Introduction

The spectral properties of organic molecules are usually modified in solvation processes, Solvation refers to the reorientation of solvent molecules around a solute molecule, an effect which does not take place in rigid medium [1]. For many aromatic molecules the position and the structure of the absorption and fluorescence spectrum are strongly dependent on the used solvent properties. The wavelength displacement can often be correlated with changes in solvent dielectric constant and the solvent index of refraction. Usually prepared organic molecules solutions contain very small quantities of dye. Typical dye concentrations are 10-2 to 10-6 M. For this reason, the solvent in which the dye is dissolved plays an important role when defining physical properties. In moderate to higher polarity solvents the properties like Stokes' shifts, fluorescence quantum yields fluorescence lifetimes, radiative and non-radiative rate constants follow more or less linear correlation with the solvent polarity [2,3]. To determine if a molecule is polar it must be known two things, the polarity of the bonds in a molecule and how these bonds are arranged. So the molecule is considered polar if its center of negative and positive charge do not coincide this polar molecule have a dipole but if these dipoles are equally and in opposite to each other the dipoles cancel-out and the molecule considered nonpolar. Therefore, solvent polarity plays an important role in shifting the lasing wavelength of fluorescence and absorption spectrum of lasing compounds. In a majority of circumstances, increasing solvent polarity will shift the gain curve toward longer wavelength. In the case of more polar dyes, the shift can be as high as 20-60 nm [3]. Thus for many dyes which where use in optical, chemical, biomedical and technological field we must choose a suitable solvent coincide with the molecule properties and take on a count amount of a shift(increasing or decreasing the frequency) that including reaching to the required goals.

2. Materials and Methods

The existent theories on the intermolecular interaction in liquid express the supply of some type of interaction by different function of solvent parameters. Hence there are four types of interactions. The first one concerned the interaction between permanent dipoles of the solute and solvent. This contributes to the shift only if both molecules are polar. If the usual approximation is made, that the chromophore is a spherical particle of radius d, the following expression is obtained [1].

$$\Delta v_1 = v_1 - v_0 = D\left\{\frac{\varepsilon-1}{\varepsilon+2} - \frac{n^2-1}{n^2+2}\right\} \quad (1)$$

Here ε is the dielectric constant, n is the refractive index of the solvent, and

$$\frac{-2}{d^3}\{(\mu^0_{solute})\,(\mu^1_{solute}\,cos\,B - \mu^0_{solute})\} \quad (2)$$

Here μ^1_{solute} and μ^0_{solute} are magnitude of the permanent dipole moments of the excited and ground states of the chromophore, respectively, and B is the angle between them in the molecule coordinate system.

Secondly, interaction between the permanent solute dipole and induced solvent dipole: This term arises in second-order perturbation- theory treatment. Its value is zero if the chromophore is nonpolar. Otherwise, the shift is given by the following expression [1]

$$\Delta v_2 = c \left\{\frac{n^2-1}{2n^2+1}\right\} \quad (3)$$

Here

$$c = \frac{1}{d^3}\{(\mu^1_{solut})^2 - (\mu^0_{solut})^2\} \quad (4)$$

The third interaction is between induced solute dipole and permanent solvent dipole: Here, the solute in a particular electronic state is represented by a spherical volume of radius d and of electronic polarizability α that is imbedded in continuum of dielectric constant ϵ and of refractive index n. In the limit that the solute is approximately isotropic, the shift due to this interaction is given by the following expression [1, 4].

$$\Delta v_3 = B\left\{\frac{(\varepsilon-n^2)(2\varepsilon+n^2)}{\varepsilon(n+2)^2}\right\} \quad (5)$$

Here

$$B = -\left\{\frac{108ln^2\left(\frac{R}{d}\right)}{R^3}\, k_B T\,(\alpha_1 - \alpha_0)\right\} \quad (6)$$

Here kB is the Boltzmann constant, T the absolute temperature of the solution, R the radius of the spherical shell containing the molecule, and α_0 and α_1 are the electronic polarizabilities of the solute in the ground and excited electronic state, respectively

Finally, the interaction between naturally induced dipoles of solute and solvent: This interaction is present whether solvent and solute molecules are polar or non- polar. McRae found that the shift takes the following form [5,6]:

$$\Delta v_4 = A\left\{\frac{n^2-1}{2n^2+1}\right\} \quad (7)$$

where A is taken to be a solute, transition-dependent, parameter which is assumed to be solvent independent. It has the form [1]:

$$A = -\left(\frac{1}{d^3}\right)[\{\sum_{i\neq 1} A_{1i}\,(\mu^{1i}_{solute})^2\} - \{\sum_{i\neq 0} A_{0i}\,(\mu^{0i}_{solute})^2\}] \quad (8)$$

Here $\mu's$ are to represent the transition dipoles and A's some weighing factors. In the two cases, when the solvent and solute are such that one is polar and one is nonpolar, or if both are nonpolar, the frequency shifts in absorption and emission are predicted to be [7,8].

3. Experimental Work

Coumarin 334 dye (denoted as C334) ($C_{17}H_{17}NO_3$) with molecular weight of 283.33 g/cm^3, Rhodamine 590 dye (denoted as R590) ($C_{28}H_{31}N_2O_3Cl$) with molar mass of 479.02 g/mol supplied by Lambda Physic were used in this work. Also, ethyl alcohol (C_2H_5OH), DMSO (C_2H_8OS C_2H_8OS) with molar mass of 78.13 g/mol and Chloroform ($CHCl_3$) with molecular weight of 119.38 g/mol, were used as solvents.

The dye solutions were prepared by dissolving the required amount of the dye in the solvent. The required weight of the dye was measured using a Matter balance of 0.1mg sensitivity. This weight W (in g) was calculated using the following equation:

$$W = M_w V\, C/1000 \quad (9)$$

where M_w is the molecular weight of the dye (g/mol), V is the volume of the solvent (mL), and C is the dye concentration

To prepare a dilute solution, the following equation was used:

$$C_1\, V_1 = C_2\, V_2 \quad (10)$$

where C_1 is the high concentration ,V_1 is the volume before dilution (L), C_2 is the low concentration, and V_2 is the total volume after dilution [l]

4. Results and Discussion

Laser dyes have shown a significant influence throughout using solvent. The normalized absorption spectra of C334 and R590 dye solutions are shown in Fig. (1). A reasonable shift occurs in absorption spectrum as a result of mutual interaction between solute and solvent. This shift depends on the nature of this interaction, the solvent type, and the concentration of the dye. This figure clarifies the influence of the solvent on the position of absorption peaks. The spectra are shifted towards longer wavelength as the polarity of the solvent increases.

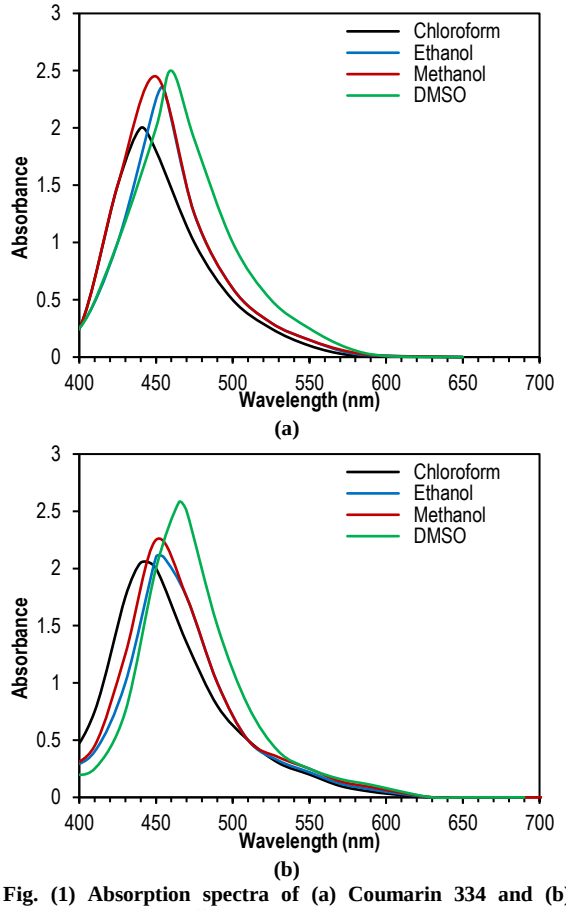

Fig. (1) Absorption spectra of (a) Coumarin 334 and (b) Rhodamine 590 in different solvents

Fluorescence spectra of these dyes had also been affected by solvent polarity, as can be seen in Fig. (2) and the peak positions are listed in table (1). The peaks of fluorescence bands are largely red-shifted when the solvent polarity increases as compared to absorption bands under the same conditions. This fact

indicates an increase in dipole moment of excited state compared to ground state [9]. It can be stated that the peak at lower wavelength of these spectra is corresponding to non-aggregated molecules and the peak at longer wavelength is caused by excimer emission of aggregated molecules.

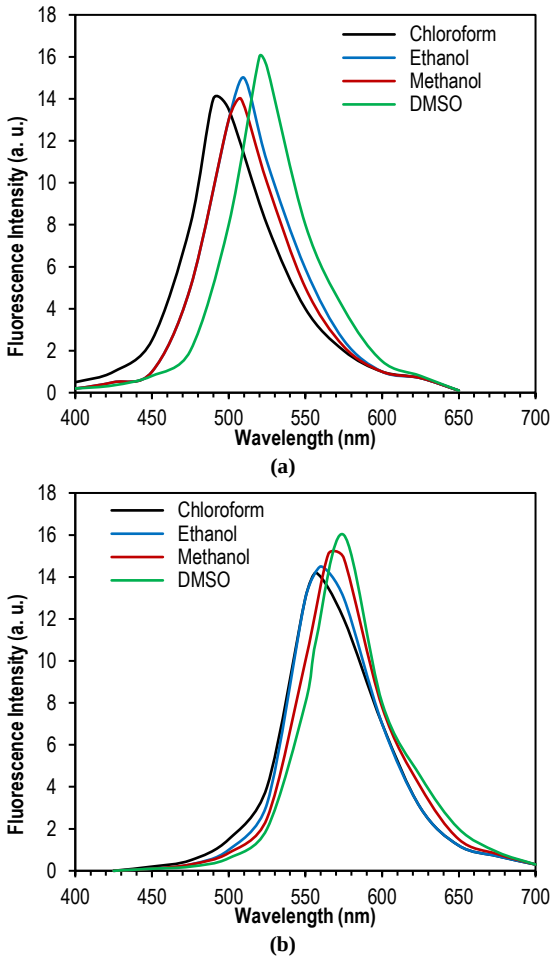

Fig. (2) Fluorescence spectra of (a) Coumarin 334 and (b) Rhodamine 590 in different solvents

Table (1) Peak wavelengths of absorption and fluorescence spectra of both dyes in different solvents

Solvent	Molecules	λ_{abs} (nm)	λ_{fluo} (nm)
DMSO	Coumarin	462	520
	Rhodamine	542	574
Methanol	Coumarin	453	508
	Rhodamine	534	570
Ethanol	Coumarin	451	506
	Rhodamine	530	563
Chloroform	Coumarin	442	494
	Rhodamine	523	558

Because the transfer of excitation energy between molecules be an effective and important phenomenon in extensive application [10], and particularly in the development of dye laser, the transfer of excitation energy between C334 and R590 was investigated to clarify the effect of solvent on this process. Figure (3) shows the effect of solvent on the efficiency of energy transfer process.

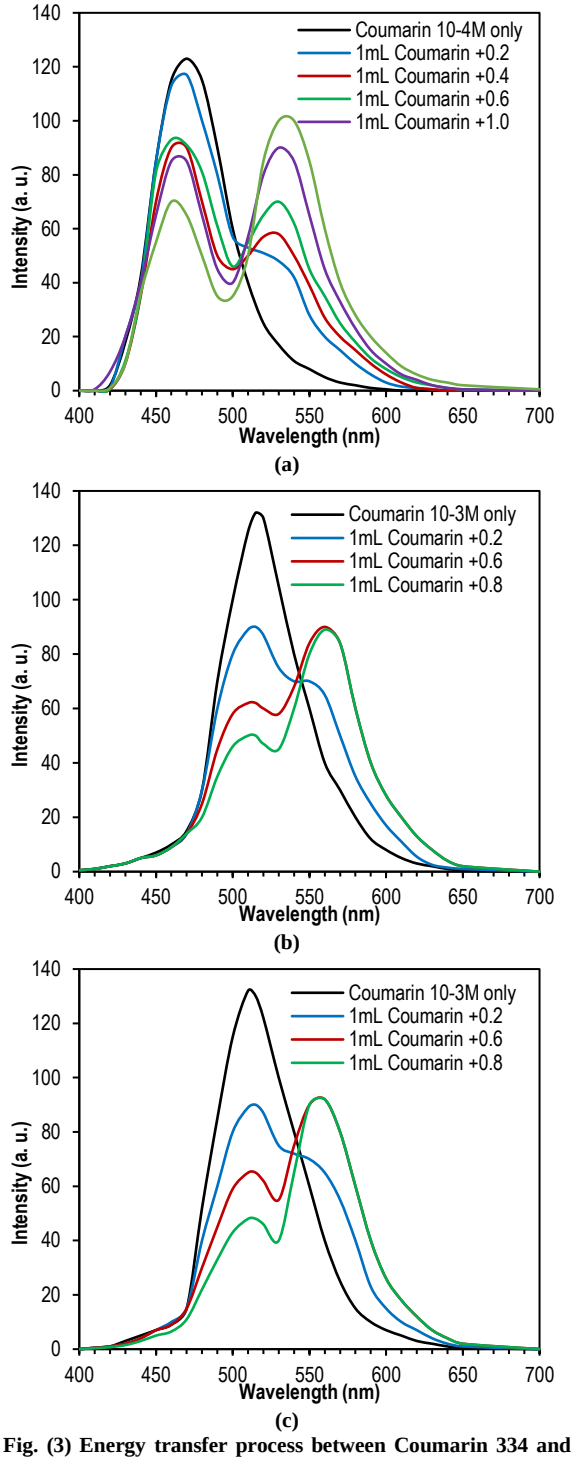

Fig. (3) Energy transfer process between Coumarin 334 and Rhodamine 590 (a) in DMSO, (b) in ethanol, and (c) in chloroform

There is a clear relation between the solvent polarity and quantum efficiency [11] and the quantum efficiency of energy transfer process had been calculated by the following relation to determine the optimal solvent for these processes:

$$E = 1 - \frac{\phi_D}{\phi_D^{\circ}} \qquad (11)$$

Here ϕ_D and $\phi_D{}^{o}$ are the quantum yield of donor fluorescence in the presence and absence of acceptor,

respectively. The value of E can thus be determined by experiment. The results were listed in table (2)

Throughout the calculation of quantum yield for dye solutions in different solvents and different concentrations, it was found that its value decreases with increasing the solvent polarity. In DMSO, for example, the quantum efficiency decreases due to the high polarity of the solvent, while in ethanol, it was found that the value of quantum efficiency reaches to its maximum value. This indicates that the efficiency of this processes can be improved by using a particular solvent.

5. Conclusion

The polarity of solvent plays an important role in shifting lasing wavelength in laser dyes as increasing the polarity of solvent causes a shift in gain curve toward longer wavelengths. It is clearly observed that using ethanol, which has refractive index of about 1.361 (lower than that of DMSO and chloroform), a homogeneous lasing spectrum is obtained at a low threshold pump beam intensity. So, this property makes ethanol one of the best solvents for laser dyes. Although, using DMSO as a solvent produces lasing spectrum with higher intensity.

References

[1] M.F. Nicol, "Solvent Effects on Electronic Spectra", *Appl. Spectro. Rev.*, 8 (1974) 183-227

[2] A. Barik, S. Nath and H. Pal, "Effect of solvent polarity on the photophysical properties of coumarin-1 dye", *The J. Chem. Phys.*, 119(19) (2003) 10202-10208.

[3] K.H.H Drexhage, "Structure and properties of laser dye", Topics in Applied Physics, Springer (1977).

[4] D.C Harris and M.D. Bertolucci, "Symmetry and spectroscopy: an introduction to vibrational and electronic spectroscopy (Dover Books on Chemistry)", Dover Publications (1989).

[5] U. Brackmann, "Lambdachrome Laser Dyes", 3rd ed., LambdaPhysics AG (Goettingen, 2000).

[6] M. Homcianu, A. Airinei and D. Ortansa Dorohoi, "Solvation effect on the electronic absorption and fluorescence spectra", *J. Adv. Res. Phys.*, 2(1) (2011) 011105.

[7] M.A Haidekker et al., "Effects of solvent polarity and solvent viscosity on the fluorescent properties of molecular rotors and related probes", *Bioorg.* Chem., 33(6) (2005) 415-425.

[8] C.H. Chen et al., "Lasing characteristics of new coumarin-analog dyes: broadband and narrow-linewidth performance", *Appl. Opt.*, 27(1) (1988) 443-445.

[9] E.G. McRae, "Solvation Effects in Molecular Spectroscopy", *J. Phys. Chem.*, 8 (1957) 562-572.

[10] J.R. Mannekutla, B.G. Mulimani and S.R. Inamdar, "Solvent effect on absorption and fluorescence spectra of coumarin laser dyes: evaluation of ground and excited state dipole moments", *Spectrochimica Acta A: Mol. Biomol. Spectro.*, 69(2) (2008) 419-426.

[11] E.A. Abdullah, "Energy Transfer for Some Organic Compounds Doped in Sol-gel Material", MSc thesis, University of Baghdad (2013).

[12] U.M. Nayf, "Spectroscopic study and competing processes in laser dyes (Coumarin 552 and rhodamine 101", *Eng. Technol. J.*, 26(5) (2008) 252-262.

Table (2) Quantum efficiency of energy transfer processes in different solvents

Donor Concentration [M]	Acceptor Concentration [M]	Q (Ethanol)	Q (DMSO)	Q (Chloroform)
0.5×10^{-4}	0.16	68.52	35.61	35.57
	0.28	69.16	34.14	34.10
	0.37	72.76	35.08	35.04
	0.44	78.58	33.52	33.48
	0.5	83.10	38.08	38.04
	0.54	87.51	49.63	49.57
	0.58	87.99	52.78	52.72
	0.61	88.55	63.32	63.25
	0.64	90.75	73.02	72.93

Esraa A. Al-Oubidy
Tawfiq S. Mahdi

Department of Physics, College of Science, University of Baghdad, Baghdad, IRAQ

Synthesis of Silicon Carbide Nanostructures from Carbon Sooted-Silicon Substrates Using Magnetron Sputtering Technique

In this work, a simple, inexpensive, and fast method to prepared silicon carbide from formation of carbon soot layer on silicon substrate by air laminar diffusion flames. This layer was 143 nm in thickness and formed at different exposure times. The carbon soot-silicon substrate was used to synthesize silicon carbide nanostructures by magnetron sputtering technique at optimum conditions. The structural characteristics of the prepared samples were investigated by using x-ray diffraction (XRD), scanning electron microscopy (SEM), and energy-dispersive x-ray (EDX) spectroscopy. The spectroscopic characteristics were determined by UV-visible and Fourier-transform infrared (FTIR) spectroscopy. As the formation of silicon carbide nanostructures was confirmed, the particle size of the final sample is the minimum found to be around 47.44 nm, with an absorption peak around 400 nm and energy band gap of 2.4 eV.

Keywords: Silicon carbide; Carbon Soot; Magnetron sputtering; Nanostructures
Received: 28 December 2023; **Revised:** 20 February; **Accepted:** 27 February 2024

1. Introduction

Silicon carbide (SiC) is a significant non-oxide ceramic with distinct properties such as high temperature, strength, oxidation resistance, high thermal shock resistance, high hardness and wear resistance, strong chemical resistance, low thermal expansion and high thermal conductivity, among other ceramic types [1-3]. These characteristics make silicon carbide an ideal contender for the production of fast, high temperature, and high voltage electrical device for abrasion and cutting applications. Furthermore, silicon carbide with present advanced technologies (e.g., MOSFETS, MEMS, sensors) can suit many practical applications; such as light-emitting diodes (LEDs) [4-6]. Silicon carbide crystallizes into a covalently linked structure that is tightly packed [7] in which the silicon and carbon atoms are linked by covalent bonds and produce polar constructions [6]. Several alternative production methods for high purity silicon (carbide, oxide, nitride) have emerged in recent years, including the carbo-thermal reduction method using binary systems, chemical vapor deposition (CVD), Acheson process, sol-gel, and physical vapor deposition (PVD) techniques such as the dc magnetron sputtering [7-11]. The latter technique has several benefits over other methods. First, any material may be deposited by magnetron sputtering with high adhesion of deposited films; second, coatings of alloys and compounds can be sputtering while retaining a composition identical to the parent material. In addition; pure and homogenous thin films can be obtained comfortably [12,13].

In the current work, soot layers were coated by allowing a flame to go over the silicon surface and use them as targets in the magnetron sputtering technique.

2. Experimental Part

The present work includes two parts: the production of carbon soot and the synthesis of silicon carbide nanostructures. The active management of soot required its production with particular features. This in turn necessitates a knowledge of physical and chemical methods; usually adopted to produce soot from fuel [14]. In most cases, soot is produced by partial rather than complete combustion. The fuel ought to be burnt at a lower temperature with a slight decrease in the oxygen supply [15]. This step is materialized to form soot in a wide and highly ventilated laminar diffusion flame by transmitting fuel through an oxidizer flowing in a cylindrical glass tube. The reaction area is formed between two opposing streams of fuel and oxidizer in order to ensure the entry of small oxygen amounts from the bottom of the glass tube to realized partial combustion and soot formation. When the fuel burns, it disintegrates into fine soot particles which settle as black powder deposits; shown in Fig. (1a).

High purity silicon wafer (99.99%) was heated on a burner flame for 2 minutes until a soot layer was deposited, as illustrated in Fig. (1b). To synthesize silicon carbide nanostructures, a dc magnetron sputtering system was utilized; with its stainless steel electrodes connected to a dc power supply that provides 150W power (50mA current and 3kV discharge voltage). The two electrodes were separated by 4cm, and the carbon soot-coated silicon wafer; representing the sputtering target, was mounted on the cathode. Plasma was generated by discharging an electric current through 0.07 mbar argon gas; Fig. (2a) shows the prepared sample after three hours of deposition time. The final samples were extracted as a powder from the thin film samples deposited on glass substrates using a conjunctional freezing-assisted ultrasonic extraction technique [16].

The final sample was a dark grey powder that is insoluble in water, alcohol, and acid, as seen in Fig. (2b).

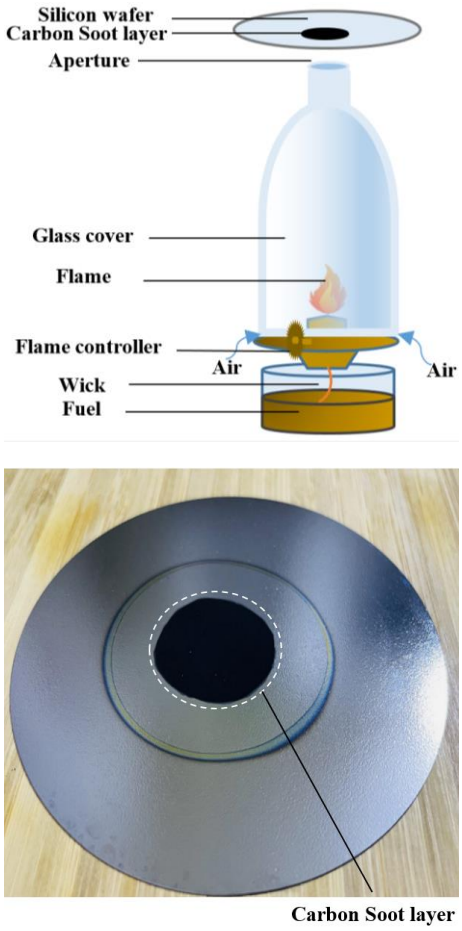

Fig. (1) Production of carbon soot layer on a silicon wafer (a) a silicon wafer is held in the flame for 2 min; (b) a carbon soot layer deposited on silicon wafer

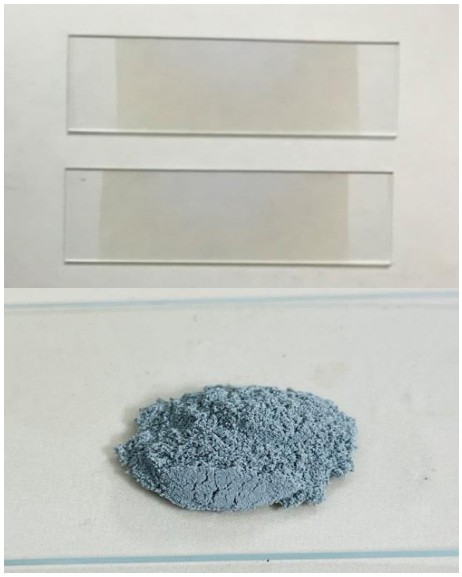

Fig. (2) The prepared samples (upper) SiC thin films, and (lower) extracted SiC nanopowder

3. Results and Discussion

Figure (3) shows the XRD pattern of final sample prepared after deposition time of 3 hours. Five most intense peaks are presumably observed on this pattern at 35.56°, 41.06°, 60.06°, 71.84° and 75.64° corresponding to lattice planes of (111), (200), (220), (311) and (222), respectively, according to JCPDS card no. 29-1129 [17].

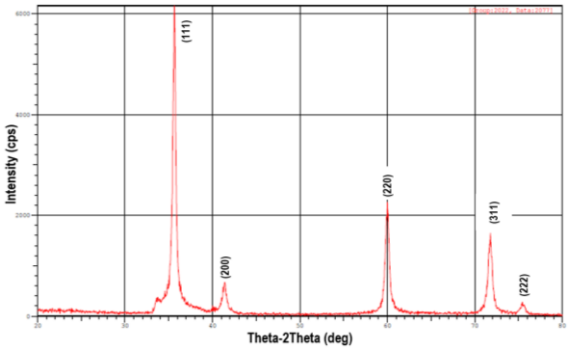

Fig. (3) The XRD pattern of SiC sample synthesized in this work

The diffraction pattern in Fig. (3) primarily confirms the production of SiC. Whereas each SiC molecule is a single-crystal grain that forms in a preferred crystallographic orientation, specifically, [111], since the (111) plane has the lowest surface energy of the SiC surface planes [18-21].

In general, the FTIR spectrum in Fig. (4) shows two peaks of Si-C bonds seen at 619 and 923 cm^{-1}, while the Si-O bond characteristic peaks are seen at 649 and 1045 cm^{-1}. Furthermore, the peaks observed at 1012, 1423 and 2400 cm^{-1} for the C-O bond adsorbed from the surrounding environment. Also, the distinctive peaks seen at 1573 and 3500 cm^{-1} are attributed to the stretching vibration bond of the O-H bonds. Depending on its surroundings, the prepared sample may differently adsorb water vapor or some gases [22-25].

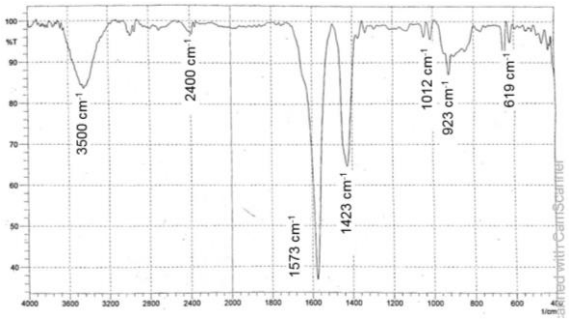

Fig. (4) The FTIR spectrum of the SiC sample synthesized in this work

Scanning electron microscopy (SEM) was used to introduce the surface morphology and determine the particle size of the deposited thin films, as shown in Fig. (5), which clearly shows that the particles are evenly dispersed, crack-free, homogenous in size,

and relatively tiny. The minimum particle size is about 47.44 nm. The EDX result and elemental analysis displayed in Fig. (6), validate the structural purity and stoichiometry of the synthesized SiC. Only peaks related to Si and C elements were observed. The origin of the oxygen peak is attributed to the fact that the prepared sample was exposed to the environment prior to the EDX test, and oxygen atoms adsorbed on SiC. As a result, the presence of such a trace quantity of oxygen in the final sample is unavoidable but ineffectual. The atomic ratio of [Si/C] obtained from EDX analysis, as shown in table (1), is around 1, indicating the formation of a stoichiometric SiC phase.

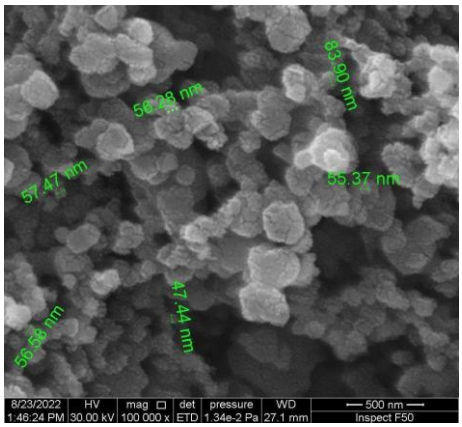

Fig. (5) SEM micrograph of the SiC layer grown in this work

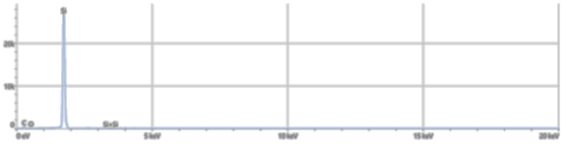

Element	Weight%	Atomic %
C	27.8	46.8
O	2.2	2.8
Si	69.9	50.3

Fig. (6) EDX result and elemental constitution analysis of the SiC layer grown in this work

The UV-visible spectrophotometry was used to record the absorption spectra of carbon soot when deposited as thin film on silicon substrate with different exposure times as shown in Fig. (7) and notice that an increase in the absorption peaks as a function of the deposition time. This is due to the increase in the number of atoms sputter from the target as the deposition time increases, thus increasing the quantum yield and increasing the absorption peaks. The absorption is increased with increasing exposure time of laminar diffusion flames. Also; the absorption spectrum of SiC, as a final product (Fig. 8), shows a significant absorption around the wavelength of 400 nm, while the energy band gap was determined by using Tauc's formula [26]:

$$\alpha\, h\nu = A\left(h\nu - E_g\right)^{1/2} \quad (1)$$

where α is the absorption coefficient, h is Planck's constant, A is constant, and E_g is the energy band gap

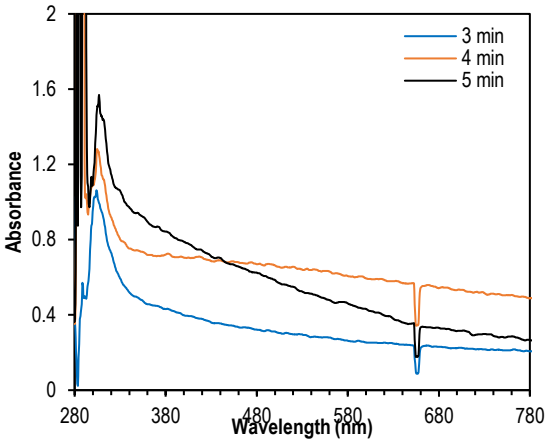

Fig. (7) Absorption spectra of the carbon soot layers prepared after different exposure times

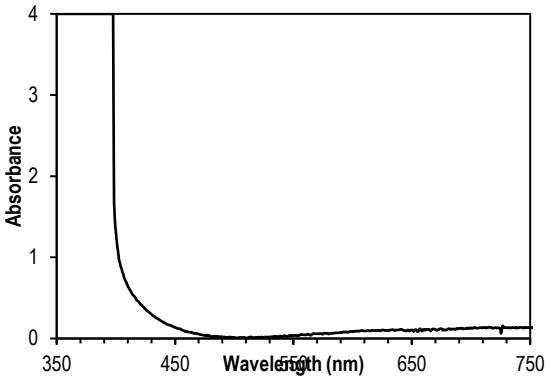

Fig. (8) Absorption spectrum of the SiC thin film sample prepared in this work

In Fig. (9), the optical energy band gap of SiC was determined to be 2.4 eV from the intercept of linear behavior of drawing the relationship between $(\alpha hv)^{1/2}$ and photon energy incident (hv) and its corresponds to the structural phase of SiC as a semi-conductor material.

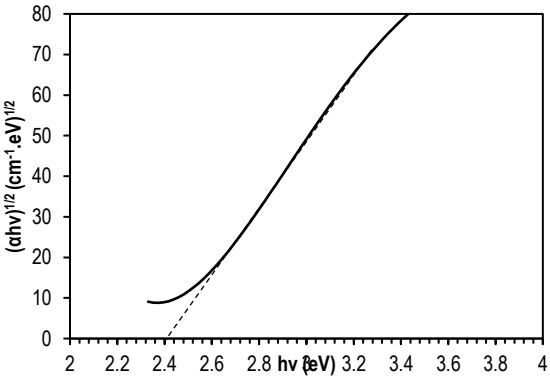

Fig. (9) Determination of optical energy band gap of SiC sample prepared in this work

4. Conclusion

In summary, the primary goal of this research is to provide a low-cost synthesis process to produce SiC nanostructures in two steps; first, production of carbon soot and deposit it on a silicon wafer, and second, using the carbon soot-coated silicon wafer is used a target in sputtering system to synthesize highly-homogenous nanostructured thin film samples of SiC, those finally were extracted as a black grey nano-powders.

References

[1] G. L. Harris, **"Properties of Silicon Carbide"**, INSPEC Publication (London, 1995).

[2] M. Mukherjee (ed.), **"Silicon Carbide - Materials, Processing and Applications in Electronic Devices"**, Intech Publications (Croatia, 2011).

[3] O.A. Hammadi, "Magnetically-supported electrically-induced formation of silicon carbide nanostructures on silicon substrate for optoelectronics applications", *Opt. Quant. Electron.*, 54 (2022) 427.

[4] G.L. Harris, **"Properties of Silicon Carbide"**, INSPEC (London, 1995), vol. 19, pp. 170-180.

[5] S. Somiya and Y. Inomata, **"Silicon Carbide Ceramics"**, Fundamental and Solid Reaction, Elsevier Science (Essex, 2012).

[6] O.A. Hammadi, Characterization of SiC/Si Heterojunction Fabricated by Plasma-Induced Growth of Nanostructured Silicon Carbide Layer on Silicon Surface, Iraqi J. Appl. Phys., 12(2) (2016) 9-13.

[7] D.A. Taher and M.A. Hameed, "Structural and Hardness Characteristics of Silicon Nitride Thin Films Deposited on Metallic Substrates by DC Reactive Sputtering Technique", *Silicon*, 15 (2023) 7855-7864.

[8] Y.R. Hathal et al., "Influence of DC Magnetron Sputtering Power on Structural, Topography, and Gas Sensor Properties of Nb_2O_5/Si Thin Films", *Iraqi J. Phys.*, 21(3) (2023) 41-54.

[9] K.A. Al-Hamdani, "Current–voltage and capacitance-voltage characteristics of Se/Si heterojunction prepared by DC planar magnetron sputtering technique", *Iraqi J. Phys.*, 8(13) (2010) 28-32.

[10] F.J. Kadhim and A.A. Anber, "Microhardness of Nanostructured Si_xN_{1-x} Thin Films Prepared by Reactive Magnetron Sputtering", *Iraqi J. Appl. Phys.*, 12(2) (2016) 15-19.

[11] O.A. Hammadi, "Plasma-Induced Growth of Silicon Carbide on Silicon Substrate for Heterojunction Fabrication", Iraqi J. Mater., 3(1) (2024) 19-24.

[12] K. Vaideki, S. Jayakumar and R. Rajendran, "Investigation on the effect of RF air plasma and neemleaf extract treatment on the surface modification and antimicrobial activity of cotton fabric", *Appl. Surf. Sci.*, 254 (2008) 2472-2478.

[13] C.H. Xue, R.L. Wang and J. Zhang, "Growth of ZnO nanorod forests and characterization of ZnO coated nylonfibers", *Mater. Lett.*, 64 (2010) 327-330.

[14] J. Du et al., "The effect of flame structure on soot particle inception in diffusion flames", *Combus. Flame*, 100(3) (1995) 367-375.

[15] Y. Wang and S.H. Chung, "Progress in Energy and Combustion Science Soot formation in laminar counter flow flames", *Prog. Ener. Combus. Sci.*, 74 (2019) 152-238.

[16] O.A. Hammadi, "Production of Nanopowders from Physical Vapor Deposited Films on Nonmetallic Substrates by Conjunctional Freezing-Assisted Ultrasonic Extraction Method", *Proc. IMechE, Part N, J. Nanomater. Nanoeng. Nanosys.*, 232(4) (2018) 135-140.

[17] L. Li et al., "Synthesis and characterization of 3C and 2H-SiC nanocrystals starting from SiO_2, C_2H_5OH and metallic Mg", *J. Alloys Comp.*, 484(1-2) (2009) 341-346.

[18] G.Y. Yang et al., "Direct observation of the growth process of silicon carbide nanowhiskers by vapor–solid process", *Physica E*, 39 (2007) 171-174.

[19] R.B. Wu et al., "Prism-shaped SiC nanowhiskers", *J. Alloys Comp.*, 453 (2008) 241-246.

[20] S. Dhage et al., "Formation of SiC nanowhiskers by carbothermic reduction of silica with activated carbon", *Mater. Lett.*, 63 (2009) 174-176.

[21] R. Dhiman, E. Johnson and P. Morgen, "Growth of SiC nanowhiskers from wooden precursors, separation, and characterization", *Ceram. Int.*, 37 (2011) 3759-3764.

[22] A. Popov, P. Savchyn and I. Karbovnyk, "Infrared Characterization of Silicon Carbide Nanowires", *Nanomater. Appl. Proper.*, 2 (2011) 134-136.

[23] A.B.D. Nandiyanto, R. Oktiani and R. Ragadhita, "How to Read and Interpret FTIR Spectroscope of Organic Material", *Indonesian J. Sci. Technol.*, 4(1) (2019) 97-118.

[24] E. Huseynov and A. Garibov, "Fourier transform infrared spectroscopic study of gamma irradiated SiO_2 nanoparticles", *Int. J. Mod. Phys. B*, 32(7) (2018) 1850074.

[25] Z.G. Sun et al., "Synthesis and microwave absorbing properties of SiC nanowires", *Appl. Phys. A*, 124 (2018) 802.

[26] Ł. Haryński et al., "A facile method for Tauc exponent and corresponding electronic transitions determination in semiconductors directly from UV–Vis spectroscopy data", *Opt. Mater.*, 127 (2022) 112205.

Orass A. Hussein
Omar F. Abdullah
Sara S. Tawfeek

Department of Physics, College of Education, University of Samarra, Samarra, IRAQ

Determination of Physical and Thermal Properties of Triiodosilane by Semi-empirical Approach

WINMOPAC 7.21 and the MNDO-PM3 software are two semi-experimental theoretical programs used in this work to analyze the thermal and physical properties of the SiI_3H molecule. After adjusting the Si-H bond's length to satisfy the minimal formation energy at standard temperature (298 K), Reaction characteristics such as electronegativity, molecular hardness, electronic affinity, and ionization potential – which equaled 6.912779 eV, 3.37808 eV, 3.534699 eV, and 10.290859 eV – as well as the HOMO-LUMO energy gap were estimated in order to better understand the nature and reactivity of the molecule. Furthermore, an estimate of the molecule's thermal properties was made.

Keywords: Triiodosilane; MNDO-PM 3; Physical properties; Thermal properties
Received: 05 January 2024; **Revised:** 24 March 2024; **Accepted:** 31 March 2024

1. Introduction

Due to their wide range of uses, semiconductor halide compounds are very important from a scientific and industrial standpoint. This has piqued scientists' interest in both theoretical and practical research on these compounds' features. Triiodosilane is a nonlinear silicon halide molecule that is significant because it can be used to deposit silicon atomic layers on a variety of microelectronic device structures. [1]. The molecule has nine vibrational modes, all of which are in the far- and mid-infrared spectrum [2,3]. In this study, the MNDO/PPM3 method was used with the WINMOPAC 7.21 program to calculate and study the thermal properties and some physical properties of the $SiHI_3$ molecule.

The theoretical treatment of molecular spectra for the calculation of thermodynamic properties and balanced geometry (obtaining the best balanced and stable shape of the molecule) and the energy of the molecular levels of the compounds was greatly impacted by the rapid development of software and the incredible speed at which computers could perform calculations. These methods and software were developed using the Schrödinger equation and approximations of its solutions, and they adopted two directions: one that did not rely on quantum mechanics, and the other that did. These treatments are commonly referred to as semi-experimental methods.

2. Approach

By using the molecule's geometrical advantage and altering it multiple times, the length of the Si-H bond at equilibrium can be found by computing the energy for each iteration. One can create a potential curve using this information. The non-harmonic version of true interatomic potential energy resembles the Morse potential [4].

$$V_m = D_e\left[1 - e^{-\alpha(r-r_e)}\right]^2 \quad (1)$$

Equation (1) indicates that the value of V_m approaches D_e as r approaches infinity, which is consistent with the actual behaviour of the diatomic particles. Where α is a constant for the electronic energy levels of the molecule, V_m represents the potential energy of the bond.

The vibrational energy levels are found by [5] when a Morse potential function is used in place of the potential energy in the Schrödinger equation:

$$g(v) = \left(v + \frac{1}{2}\right) w_e - \left(v + \frac{1}{2}\right)^2 w_e x_e \quad (2)$$

where g(v) represents the vibrational energy level, ω_e the vibrational frequency in an harmonic motion, x_e the an harmonic constant

When v = 0 the value of g (v) is equal to the zero point energy [6]:

$$g(v) = \frac{1}{2} w_e \left(1 - \frac{1}{2} x_e\right) cm^{-1} \quad (3)$$

The following relationship can also be used to calculate the molecule's dissociation energy [7]:

$$D_e \cong \frac{w_e^2}{4 w_e x_e} \quad (4)$$

Some physical parameters, such as ionization potential and electronic affinity, are computed using Koopmans' theory [8,9]:

$$IE(\text{Ionization potential}) = -E_{HOMO} \quad (5)$$

$$EA(\text{Electron affinity}) = -E_{LUMO} \quad (6)$$

In which LUMO is the lowest empty molecular orbital and HOMO is the highest occupied molecular orbital. The following formulas [10–15] are used to calculate the electronegativity (χ) and molecular hardness (η), which are vital interacting properties of matter that are defined as the resistance to electron cloud polarisation or deformation of chemical species and a measure of the stability and interactions of molecules, based on these values (IE and EA):

$$\chi \approx \frac{(IP+EA)}{2} \quad (7)$$

$$\eta \approx \frac{(IP-EA)}{2} \quad (8)$$

The statistical thermodynamic equations can also be used to calculate the thermal properties [16,17].

The statistical thermodynamics of ideal gas laws and the standard case were used to calculate the thermal properties using the following equations:

$$U^0_{total} = U^0_{trans} + U^0_{rot} + U^0_{vib} + U^0_{elec} + U^0_{nucl} \quad (9)$$

$$U^0_{trans} = U^0_{rot} = 1.5RT \quad (10)$$

$$U^0_{vib} = \sum_{i=1}^{3N-6} \frac{RTX_i}{e^{X_i}-1} \quad (11)$$

$$X_i = \frac{hc\bar{\upsilon}}{KT} = \frac{1.44\bar{\upsilon}}{T} \quad (12)$$

$$H^0 = U^0_{total} + RT \quad (13)$$

$$S^0_{total} = S^0_{trans} + S^0_{rot} + S^0_{vib} + S^0_{elec} + S^0_{nucl} \quad (14)$$

$$S^0_{trans} = R\left[\frac{5}{2} + \ln\frac{(2\pi mKT)^{\frac{3}{2}}RT}{N_0 h^2}\right] \quad (15)$$

$$S^0_{rot} = R\left[\frac{3}{2} + \ln\frac{8\pi^2(8\pi^2 I_X I_Y I_Z)^{\frac{1}{2}}(KT)^{\frac{3}{2}}}{\sigma\hbar^3}\right] \quad (16)$$

$$S^0_{vib} = R\sum_{i=1}^{3N-6}\left[\frac{X_i}{e^{X_i}-1} - \ln(1-e^{-X_i})\right] \quad (17)$$

$$G^0 = H^0 - TS^0 \quad (18)$$

$$A^0 = U^0 - TS^0 \quad (19)$$

3. Results and Discussion

The curve of potential When we reach the lowest energy level at which the molecule is stable at a specific distance, known as the equilibrium distance (re=1.4758 AO), the total energy starts to increase due to the repulsion (nucleus - nucleus), until the bond is broken, at which point it is known as the energy of dissociation (De=6.76785 eV). Figure (1) illustrates how the total energy decreases as the distance between the atoms (Si - H) increases due to the drop in potential energy, which is caused by the attraction (electron - nucleus).

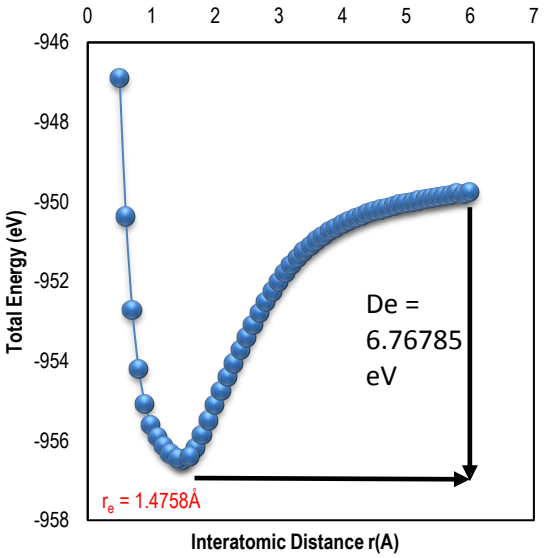

Fig. (1) Nonharmonic potential curve of $SiHI_3$ molecule calculated by Winmopac software (MNDO-PM3)

Some important physical properties of the studied molecule that were also calculated at equilibrium are shown in table (1).

Table (1) The physical properties of the Triiodosilane ($SiHI_3$) molecule calculated by MNDO-PM3

Quantity	Magnitude
Heat Of Formation Hf at 298K	-0.39257 eV
E_{LUMO}	-3.534699 eV
E_{HOMO}	-10.290859 eV
Ionization Potential (I.P.)	10.290859 eV
Electronic Affinity (E.A.)	3.534699 eV
electronegativity (χ)	6.912779 eV
molecular hardness η	3.37808 eV

SiI_3H's high ionization energy denotes the molecule's low reactivity. With an electronegativity of 6.912779 eV, the SiI_3H molecule has a notable capacity to draw electrons from neighboring molecules.

The HOMO–LUMO energy gap of SiI_3H is predicted by this study to be 6.75616 eV. It was discovered to be extremely high and, because of the enormous border orbital gap linked to high kinetic stability and minimal chemical interaction, results in more molecular stability and less polarization.

The investigated molecule's heat of production increases with temperature, as seen in Fig. (2).

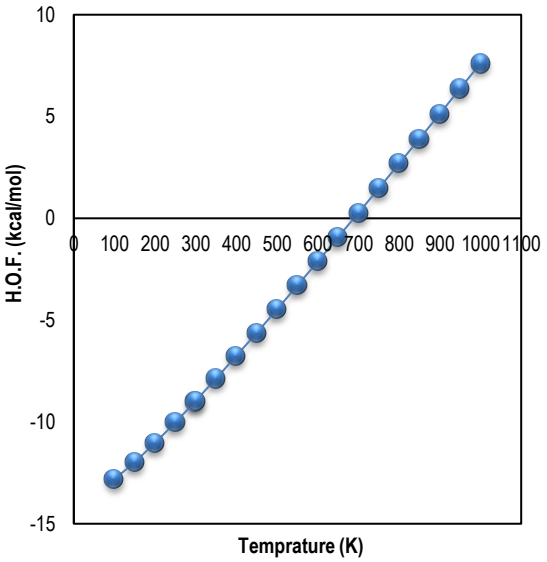

Fig. (2) Heat of formation of $SiHI_3$ molecule at different temperatures

In accordance with [18], figure (3) illustrates how the enthalpy change rises with temperature, suggesting that the reaction is endothermic.

Entropy rises with temperature because it measures how random the atoms that comprise molecules are, as seen in Fig. (4).

Figure (5) illustrates how the system's high thermal resistivity and great thermal stability are demonstrated by Gibbs free energy reductions in SiI_3H [19]. It's also clear that the computed values agree with the real values [18].

See Figure 6 for an illustration of how the heat capacity varies with temperature and rises as a result of an increase in the number of particles at various vibrational energy levels [18].

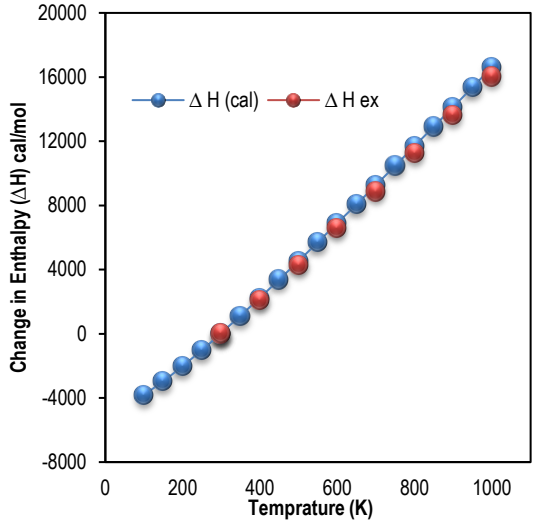

Fig. (3) Enthalpy change of $SiHI_3$ molecule at different temperatures

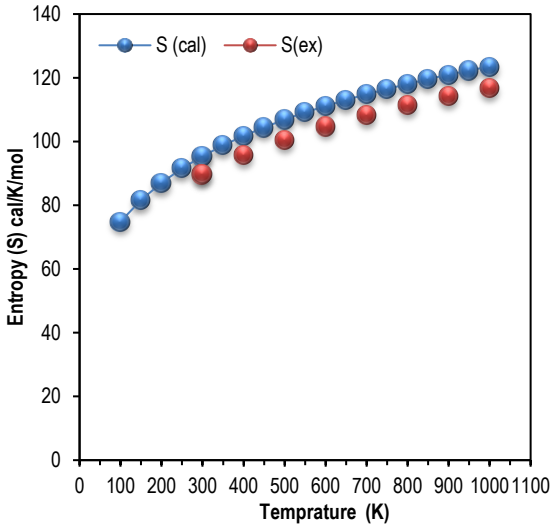

Fig. (4) Entropy of $SiHI_3$ molecule at different temperatures

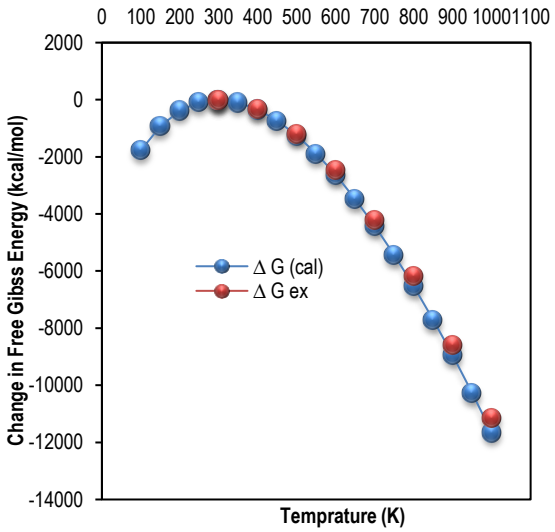

Fig. (5) Change in the Gibbs free energy of $SiHI_3$ at different temperatures

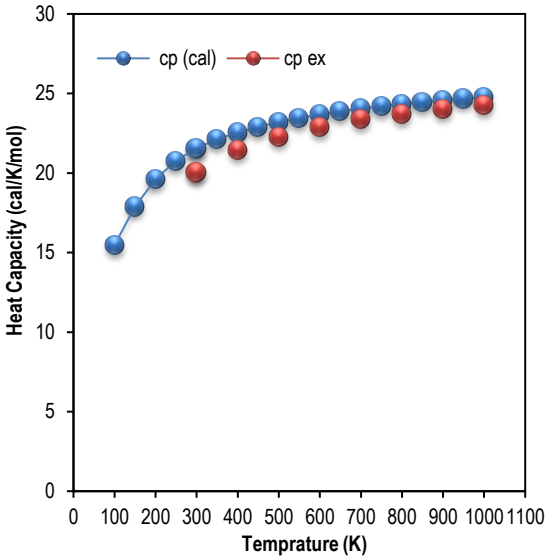

Fig. (6) Heat capacity of $SiHI_3$ molecule at different temperatures

4. Conclusion

A solid grasp of the nature, structure, electrical properties, and chemical reactivity is provided by this study. The molecule is one among those with strong heat resistance, with a bond length (Si-H) equal to r_e=1.4758Å and a dissociation energy of D_e=6.76785 eV. The number of molecules at different vibrational energy levels increases with temperature, which raises specific heat capacity. In addition, the procedure is endothermic.SiI_3H's high ionization energy denotes the molecule's low reactivity. With an electronegativity of 6.912779 eV, the SiI_3H molecule has a notable capacity to draw electrons from neighboring molecules.

According to this study, SiI_3H's HOMO–LUMO energy gap is predicted to be 6.75616 eV. which, since the border orbital gap is big and linked to high kinetic stability and low chemical interaction, was found to be extremely high and results in more molecular stability and less polarization.

In addition to the previously mentioned, the MNDO-PM3 approach results produced with Winmopac 7.21 closely matched the trial outcomes.

References

[1] D. Kuiper et al., "Preparation of Triiodosilanes", Patent No. 20200181178, USA (11 June 2020).

[2] O.A. Hussein, D.M. Khudhair and A.A.A.A. Aljbar, "IR Spectroscopic Study of Triiodosilane ($SiHI_3$) by Using Semi-empirical Quantum Program", *J. Phys.: Conf. Ser.*, 1818(1) (2021) 012014.

[3] www.NIST.gov/Chemistry NIST (2016)

[4] D.V. Shenai-Khatkhate et al., "Environment, health and safety issues for sources used in MOVPE growth of compound semiconductors", *J. Cryst. Growth*, 272(1-4) (2004) 816-821.

[5] J.R. Ferraro, "**Introductory Raman Spectroscopy**", Elsevier, 2003.
[6] G. Henderson, D. Neuville and R Downs, eds., **"Spectroscopic methods in mineralogy and material sciences",** vol. 78, Walter de Gruyter GmbH (2014).
[7] W.S. Struve, "**Fundamentals of molecular spectroscopy**", Wiley (NY, 1989).
[8] R.C. Bingham, M.J.S. Dewar and H.C. Lo, "The Chemistry of Heterocyclic Compounds, Thiophene and Its Derivatives", *J. Am. Chem. Soc.*, 97(6) (1975) 1285-1293.
[9] A. Hinchliffe and H.J. Soscun Machado, "Density Functional Studies of Molecular Polarizabilities. Anthracene and Phenanthrene", *Int. J. Mol. Sci.*, 1(1) (2000) 8-16.
[10] K.R.S. Chandrakumar and S. Pal, "The concept of density functional theory based descriptors and its relation with the reactivity of molecular systems: A semi-quantitative study", *Int. J. Mol. Sci.*, 3(4) (2002) 324-337.
[11] R.G. Parr et al., "Electronegativity: the density functional viewpoint", *The J. Chem. Phys.*, 68(8) (1978) 3801-3807.
[12] A. Rauk, **"Orbital Interaction Theory of Organic Chemistry"**, John Wiley & Sons (2004).
[13] S. Kaya and C. Kaya, "A new equation for calculation of chemical hardness of groups and molecules", *Mol. Phys.*, 113(11) (2015) 1311-1319.
[14] O.A. Hussein and O.F. Abdullah, "Effect of the flow rate of O_2 on SnO_2 thin film properties", *AIP Conf. Proc.*, 2394(1) (2022) 090035.
[15] O.F. Abdullah, O.A. Hussein and T.A. Aswad, "Effect of the Laser Surface Treatment on Properties of the Alloy (Ni-Cu-V) Nanoparticles Prepared by Powder Metallurgy Method", *NeuroQuantology*, 19(12) (2021) 1.
[16] N.A. Jasim, "Theoretical Study of Some Physical and Thermodynamic Properties for some Diclofenac Derivatives by using Semi-Empirical Calculations (PM3 Method)", *Syst. Rev. in Pharma.*, 11(12) (2020) 1294.
[17] K.O. Kzar, "Study the Effect of the Positive (+1,+2) and Negative (-1,-2) Charges on the Geometry and Vibrational Spectra of Bromofulvene Isomers with DFT model", M.Sc. thesis, University of Kerbala, Iraq (2013).
[18] M. Chase Jr., "NIST-JANAF Themochemical Tables", 4th ed., *J. Phys. Chem. Ref. Data*, Monog. 9 (1998) 1-1951.
[19] T. Mathavan et al., "A study on thermochemical properties of ZnS Nanomaterial: A computational Approach", *Int. J. Sci. Eng. Res.*, 5(3) (2014) 33-36.

Ghufran J. Matrood
Niveen J. Abdulkader
Nahedh M. Ali

University of Technology - IRAQ

Determination of Electrical Conductivity of Aluminum Nano Films prepared by Flame Thermal Spray

This study measured the electrical conductivity of the Al coating layer deposited on acrylonitrile butadiene styrene (ABS) by flame thermal spraying. The results showed that the electrical conductivity of aluminum coating on the ABS polymer substrate were good but lower than that in bulk aluminum, with values of 1.68×10^{4} – 2.17×10^{4} $\Omega^{-1}.cm^{-1}$. The scanning electron microscopy (SEM) also showed good adhesion force between the Al coating layer and the surface of the polymeric substrate; the results of the x-ray diffraction (XRD) showed no oxidation. The contact angle for the ABS substrate was 36.442°, meaning that the ABS surface is hydrophilic and has good surface energy and adhesiveness.

Keywords: Thermal spraying; Electrical conductivity; Metallization; Polymers
Received: 27 January 2024; **Revised:** 28 February 2024; **Accepted:** 06 March 2024

1. Introduction

Nanotechnology is considered to have a significant influence on nearly every aspect of human life. Nanotechnology possesses the capacity to profoundly impact many domains, including physical sciences, biotechnology, energy, communication technology, social psychology, manufacturing, cognitive sciences, catalysis, computational sciences, and transportation. It has the ability to revolutionize the future by increasing the durability and reactivity of existing materials [1,2].

Thermal spraying is a process where molten, or partially molten materials are applied to a surface to create a coating. The coating substance is applied with a high-velocity spray. When the coating particles come into contact with the surface of the substrate, they can experience permanent deformation, resulting in the creation of a coating layer. The coating material can be employed in either a powder or a wire form. Oxygen and acetylene are the usual gases used for generating heat. The flare induces rapid melting of the coating material, which is then violently ejected onto the substrate's surface [3].

Metallization refers to the process of depositing metal layers onto the polymeric substrate using thermal spraying. This technique is accomplished through the adhesion of the sprayed metal to the polymeric surface. Thermal spraying process factors, such as particle speed and temperature, influence the deposited plates. The deposited layer is also affected by the substrate's surface roughness and the angle between the substrate and the particle line [4,5].

Aluminum has a density of 2.7 g/cm^3, which is approximately one-third of the densities of steel and cast iron [6]. Aluminum alloys typically consist of silicon, copper, magnesium, zinc, and several additional alloying elements. They possess the benefits of being lightweight, exhibiting good electrical and thermal conductivities, and demonstrating exceptional mechanical qualities [7,8].

Acrylonitrile butadiene styrene (ABS) is a thermoplastic material that has several applications in engineering because to its beneficial qualities. These properties include chemical resistance, light weight, strong mechanical capabilities, and ease of processing [9]. Materials with thermal and electrical conductivities, corrosion resistance, and light weight can be obtained by coating a commercially available polymer with a thin layer of aluminum [10]. Voyer et al. [11,12] noted that polyester fabrics became electrically conductive after depositing a layer of aluminum on them by flame spraying, thus obtaining a coating layer with a thickness of 75-100 µm and an electrical resistance of about 0.002 Ω.cm because the aluminum coating did not affect the elasticity of the polyester fabric. Huonnic et al. [13] measured the electrical resistance of flame-sprayed glass and basalt tubes after a layer of aluminum coating was deposited on the surface, which was found to be 69×10^{7} and 89×10^{7} Ω.cm, respectively. Two flame sprayers were used to produce a uniform metal layer with electrical properties on a polymeric substrate. It was noted that the electrical resistance values of the coated materials were higher than that of annealed aluminum alloy. Affi et al. [14] analyzed the electrical resistance of Al coatings applied by cold and plasma spraying methods onto carbon-fiber-reinforced epoxy substrates. The resistance values of the aluminum deposits that were sprayed with plasma were significantly higher than those of the aluminum coatings that were sprayed with cold. This could be attributed to the increased oxidation of the sprayed particles at higher temperatures of the carrier gas.

The three significant motivations are behind the utilization of metallized polymer in the production of electronic devices is the reduction of costs, decrease

of weight, and enhancement of electrical conductivity.

The objective of this research is to modify ABS surface with a metallic coating to enhance electrical conductivity for electronic applications.

2. Experimental Work

Acrylonitrile butadiene styrene (ABS) with a dimension of 2×2 cm^2 was used as a substrate material, and 99.9% pure aluminium powder with a diameter of 61.8 nm was used as a coating material. The chemical composition of Al is shown in table (1).

Before spraying, the substrates were prepared for the coating procedure by cleaning them with NaOH and subsequently roughening them using sandpaper to improve the surface roughness. This step was performed to enhance the coating's ability to adhere to the substrate. Finally, a layer of aluminium coating was applied.

Table (1) Chemical Composition of Pure Al

Element	Ti %	Zn %	Cu %	Fe %	Mn %	Si %	V %	Mg %	Al %
Chemical Composition	0.024	0.033	0.026	0.15	0.045	0.052	0.008	0.028	Balance

The coating method utilised the thermal spraying approach, employing an oxyacetylene thermal spraying device on a two-dimensional table. The table was outfitted with spherical screws and a motor that facilitated the seamless movement of the spraying device in both right and left directions. The operational specimen was placed on a flat surface in front of the spraying apparatus. The screw sample fixture was equipped with a stepper motor, which allowed it to move in a spherical manner. The given sample fixture featured a spherical screw mechanism equipped with a motor that enabled vertical movement in both upward and downward directions [15]. The O_2 pressure was 0.5 bar, while the C_2H_2 pressure was 1 bar. Figure (1) and table (2) displays the thermal spraying device and the spraying parameters, respectively.

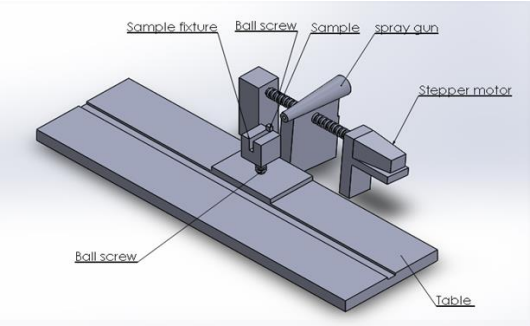

Fig. (1) Thermally spray device

Table (2) Process parameters and their levels

Parameters	Level 1	Level 2	Level 3
Distance mm	150	200	250
Powder feeding gl/min	15	30	45
Spray velocity m/min	100	200	300
Delay time min	4	6	8

3. Results and Discussion

Figure (2) shows the peaks obtained from the x-ray diffraction (XRD) analysis of the aluminum layer on a polymer substrate, and the apparent peaks seem to be very similar to those found in a standard sample. It seems that the intensity of the peaks may vary at angles of 38.36°, 44.67°, 65.12°, and 78.20°. The strong peaks with a narrow base give the impression that the crystal structure of the coating is regular, and the low peaks mean that the coating has a random or irregular structure.

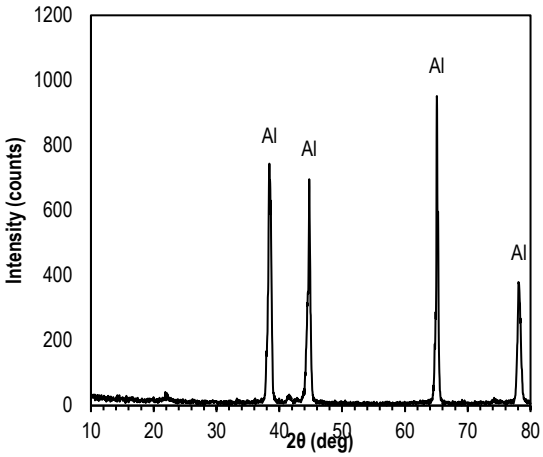

Fig. (2) XRD pattern for Al coating prepared in this work

The SEM of the coated samples was carried out using Inspect S50 SEM instrument to determine the coated layer and measure their thickness as well as the coating-substrate interface. Figure (3) shows the adhesion between the ABS polymer and the Al coating layer. The coating layer had a thickness of approximately 74.35 µm.

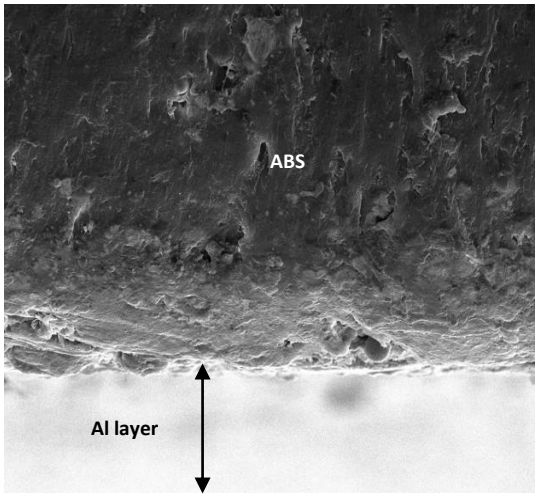

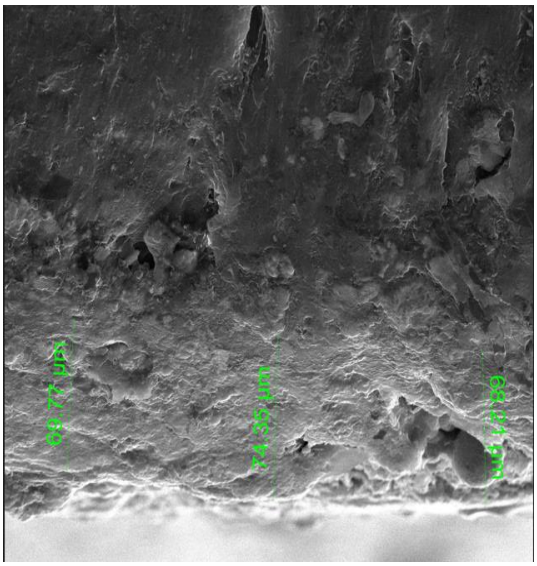

Fig. (3) SEM images showing the interface between polymer substrate and metallic coating

The contact angle is the angle at which the liquid–solid and liquid–vapour interfaces intersect [16]. As shown in Fig. (4), the contact angle test showed that the surface of ABS has a contact angle of 36.422°, which suggests that the surface is hydrophilic and thus, ABS has good wettability and adhesiveness.

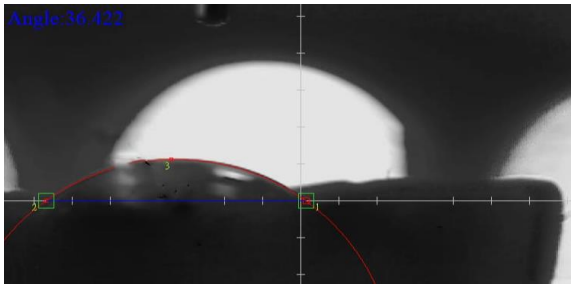

Fig. (4) The contact angle for ABS

Scratch testing is the predominant and preferred method for evaluating the adhesive strength of a coating-substrate system [17-19]. Taguchi orthogonal arrays are utilized to determine the effects that the values of the thermal spraying parameters have on the adhesion strength between the aluminum coating and the ABS substrate. The best adhesion between ABS polymer and Al coating can be obtained if the distance between the gun spray and substrate is 200mm, the powder feeding is 45 gL/min, the velocity of spray is 100 m/min, and the delay time is 6min as shown in table (3).

The electrical conductivity of the coated layer has been measured using an LCR-821 meter. Figure (5) shows that the electrical conductivity of the Al layer is significantly lower than that of bulk aluminum. This is because the nano-coating layer increased the resistance values due to an increase in grain boundaries. The electrical conductivity value of bulk aluminum was $3.77\times10^{7}\ \Omega^{-1}.m^{-1}$.

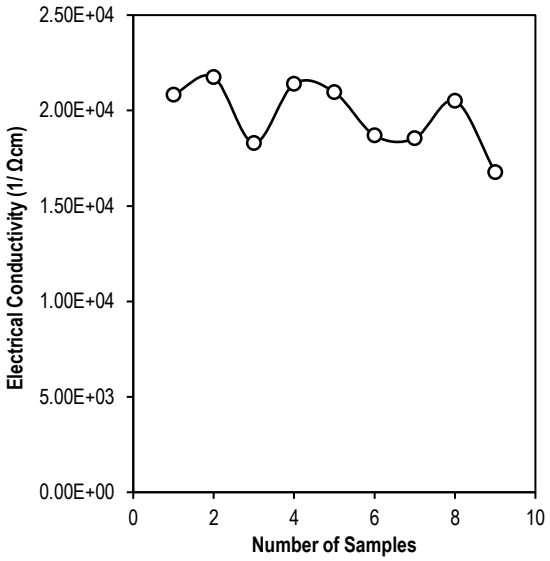

Fig. (5) Electrical conductivity of Al coating layer

4. Conclusion

In this study, aluminum coating layers were deposited on polymer substrates by flame thermal pyrolysis. It was found that the electrical conductivity of these layers are good but lower than the electrical conductivity of bulk aluminum. This is due to the fact that the coating deposited on the polymeric substrate is nano-sized, thus forming many crystalline boundaries. In addition, due to an increase in grain boundaries in the Al layer, the electrical conductivity decreased. The characterization shows that there is no oxidation on the coating layer. The contact angle was 36.224°, suggesting that the surface of ABS is hydrophilic and thus, ABS has good wettability and adhesiveness.

Acknowledgments

I would like to thank the Materials Engineering Department at the University of Technology for their support and encouragement to complete this work.

References

[1] A. Nouailhat, **"An introduction to nanoscience and nanotechnology"**, John Wiley & Sons (2010), p. 27.

[2] H.A. Akkar and S. Khalooq, "Characteristics and evaluation of nano electronic devices", *Eng. Technol. J.*, 32(3) (2014).

[3] G.J. Matrood, A.M. Al-Gaban and H.M. Yousif, "Studying the Erosion Corrosion Behavior of NiCrAlY Coating Layer Applied on AISI 446 Stainless Steel Using Thermal Spray Technique", *Eng. Technol. J.*, 38(11) (2020) 1676-1683.

[4] J.R. Davis, **"Handbook of thermal spray technology"**, ASM international (2004), pp. 109-110.

[5] P. Fauchais et al., "Knowledge concerning splat formation: an invited review", *J. Therm. Spray Technol.*, 13 (2004) 337-360.
[6] J. Davis, **"Alloying, Understanding the Basics"**, ASM International, Materials Park (OH, 2001), pp. 44073-0002.
[7] A. Association, **"Aluminum: properties and physical metallurgy"**, ASM international (1984), p. 1.
[8] R. Lumley, **"Fundamentals of aluminium metallurgy: production, processing and applications"**, Elsevier (2010), p. 2.
[9] S. Owen and J. Harper, "Mechanical, microscopical and fire retardant studies of ABS polymers", *Polym. Degrad. Stabil.*, 64(3) (1999) 449-455.
[10] B. Anand, "Thermal Spray Deposition of Metals on Polymer Substrates", University of Toronto, Canada (2019), p. 1.
[11] J. Voyer, P. Schulz and M. Schreiber, "Electrically conductive flame sprayed aluminum coatings on textile substrates", *J. Therm. Spray Technol.*, 17(5-6) (2008) 818-823.
[12] J. Voyer, P. Schulz and M. Schreiber, "Conducting flame-sprayed Al coatings on textile fabrics", *J. Therm. Spray Technol.*, 17 (2008) 583-588.
[13] N. Huonnic et al., "Deposition and characterization of flame-sprayed aluminum on cured glass and basalt fiber-reinforced epoxy tubes", *Surf. Coat. Technol.*, 205(3) (2010) 867-873.
[14] J. Affi et al., "Fabrication of aluminum coating onto CFRP substrate by cold spray", *Mater. Trans.*, 52(9) (2011) 1759-1763.
[15] A.N. Mohsin, H.M. Yousif and S.S. Ahmed, "Investigation of the Diffusion Depth of Ni-Cu Thermal Spray Coating for the Low Carbon Steel", *Eng. Technol. J.*, 39(11) (2021) 1734-1739.
[16] F.H. Edan, "Prediction of Contact Angle for Sintered Alloy for Solid Freeform Fabrication", *Eng. Technol. J.*, 34(8) (2016) 1666-1672.
[17] P. Benjamin and C. Weaver, "Measurement of adhesion of thin films", *Proc. Royal Soc. London. Ser. A: Math. Phys. Sci.*, 254(1277) (1960) 163-176.
[18] M. Laugier, "The development of the scratch test technique for the determination of the adhesion of coatings", *Thin Solid Films*, 76(3) (1981) 289-294.
[19] S. Bull and E. Berasetegui, "An overview of the potential of quantitative coating adhesion measurement by scratch testing", *Tribol. Int.*, 39(2) (2006) 99-114.

Table ()3 Taguchi orthogonal array results

No. of samples	Distance (mm)	Powder feeding (g/min)	Spray velocity (m/min)	Delay time (min)	Trial 1	Trial 2	Trial 3	Mean	S/N ratio
1	150	15	100	4	36.90	36.96	36.97	36.9433	31.35
2	150	30	200	6	37.65	37.66	37.67	37.6600	31.52
3	150	45	300	8	38.34	38.37	38.36	38.3567	31.68
4	200	15	200	8	38.41	38.44	38.42	38.4233	31.70
5	200	30	300	4	38.89	38.87	38.87	38.8767	31.80
6	200	45	100	6	43.99	43.95	43.97	43.9700	32.86
7	250	15	300	6	36.73	36.72	36.77	36.7400	31.30
8	250	30	100	8	41.99	42.21	42.22	42.1400	32.50
9	250	45	200	4	43.67	43.70	43.71	43.6933	32.81

Where Trial 1, Trial 2, and Trial 3 are adhesion forces (N)

Oday A. Hammadi

Department of Physics, College of Education, Al-Iraqia University, Baghdad, IRAQ

Effects of Extraction Parameters on Particle Size of Iron Oxide Nanopowders Prepared by Physical Vapor Deposition Technique

In this work, the effects of different extraction parameters on the particle size of the nanopowders extracted from iron oxide (FeO) thin film samples were studied. These films were deposited by the dc reactive magnetron sputtering, which is one of the physical vapor deposition (PVD) techniques. These nanopowders were obtained by the conjunctional freezing-assisted ultrasonic extraction method. Results showed that extraction parameters such as freezing temperature, ultrasonic frequency and application time are very effective in determining the nanoparticle size, which is very important for many applications and uses of highly-pure nanomaterials and nanostructures.

Keywords: Nanopowders; Nanoparticles; Physical vapor deposition; Iron oxide
Received: 19 December 2023; **Revised:** 30 January; **Accepted:** 06 February 2024

1. Introduction

Typical breakthroughs in spectroscopic and photonic applications are continuously satisfied when highly pure nanomaterials are employed. For example, titanium dioxide nanoparticles can be perfect nanophotocatalysts (NPCs) when no other material exists in the fabricated device as this quantum activity is individually attributed to the titanium dioxide [1,2]. Similarly, quantum dot photonic devices (QDPDs) are critically sensitive to the presence of any material with the active nanomaterial [2,3]. Hence, the small contribution may result in a big effect on the device operation. Accordingly, measurements and characterization tests should be carried out with as much as possible guarantee that the prepared nanomaterial is highly pure [4].

Minimizing the probability of existing substrate's material in the extracted material makes any method or technique with such advantage most preferred in nanomaterials and nanotechnology. Unfortunately, mechanical methods cannot overcome this problem for accurate structural and spectroscopic applications [5]. Thermal methods are obviously avoided because the consequent increase in nanoparticle size is not desired at all [6]. Chemical methods are also avoided because they definitely include some reactions with tiny particles forming very large area (nanosurfaces) [7].

A recently invented method – known as conjunctional freezing-assisted ultrasonic extraction method – submits a highly efficient tool to get nanopowders from thin film samples without any probability to detect residual from substrate's material in the final product. However, the operation parameters of this method can reasonably affect the nanoparticle size. Therefore, further more typical jumps can be made in nanomaterials and nanotechnology as the nanoparticle size is sufficiently controlled [8].

In this work, the effects of some operation parameters of conjunctional freezing-assisted ultrasonic extraction method, such as freezing temperature, ultrasonic frequency and application time, on the particle size of extracted nanopowders are studied.

2. Experimental Part

A homemade dc reactive sputtering system employing a closed-field unbalanced dual magnetrons (CFUBDM) assembly was used to deposit nanostructured thin films on nonmetallic substrates. This system was used to prepare thin films from several compound materials, such as nickel oxide (NiO), silicon nitride (Si_3N_4), silicon dioxide (SiO_2), and titanium dioxide (TiO_2) [9-13]. The operation parameters and preparation conditions of these samples were separately optimized. More details on the specifications and operation of this system can be found elsewhere [14,15].

Highly-pure (99.99%) iron sheet was used as a sputter target to be maintained on the cathode of the discharge system. Argon gas is used to generate discharge plasma while the oxygen is used as reactive gas to form iron oxide (FeO) molecules. The mixing ratio of argon and oxygen could be precisely controlled in a gas mixer before pumped into the deposition chamber. The discharge electrodes could be cooled using a cooling system employing water as a coolant. The crystalline phase of iron oxide nanostructures could be determined by controlling the operation parameters of magnetron sputtering system, especially gas mixing ratio, oxygen content in the gas mixture, and anode temperature. Iron oxide nanostructures were prepared using $Ar:O_2$ gas mixture of 50:50 and a heat sink under the substrate on which the thin film is deposited. Without cooling,

the anode temperature might reach 150-180°C. Using electrical heater on the anode can raise its temperature to 400 °C, which sufficiently induces the anatase structures to convert into rutile completely.

As the deposition time is varied, the thickness of the prepared film is proportionally varied. Film thickness was measured by laser-fringes method. The nanopowder was extracted from thin film samples by the conjunctional freezing-assisted ultrasonic extraction method. Full description and specifications of this method can be introduced in reference [8] and schematically shown in Fig. (1). The structural properties of the extracted nanopowders were determined by x-ray diffraction (XRD), Fourier-transform infrared (FTIR) spectroscopy, field-emission scanning electron microscopy (FE-SEM), and atomic force microscopy (AFM).

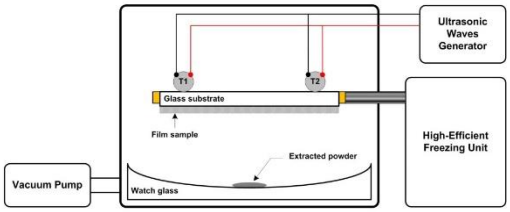

Fig. (1) Schematic diagram of the experimental setup of the conjunctional freezing-assisted ultrasonic extraction method used in this work [8]

3. Results and Discussion

Figure (2) shows the variation of nanoparticle size of the three different samples prepared in this work with the deposition time, which determines film thickness. As the deposition time is increased, the film thickness is increased and hence the layers of the thin film are further grown. This growth results the grains to get larger as observed in this figure.

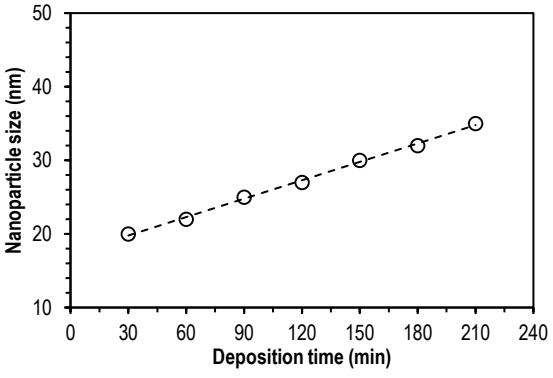

Fig. (2) Variation of nanoparticle size with deposition time for the iron oxide nanostructures prepared in this work

As the nanopowders were extracted from the thin film samples using the conjunctional freezing-assisted ultrasonic extraction method, the effect of freezing temperature on the value of ultrasonic frequency at which the nanopowder was completely extracted is shown in Fig. (3). As the freezing temperature is decreased, lower frequency is required to extract the nanopowder because lower freezing temperature lead to further shrinkage of the nonmetallic substrate and hence the adhesion of the film to the substrate gets lower.

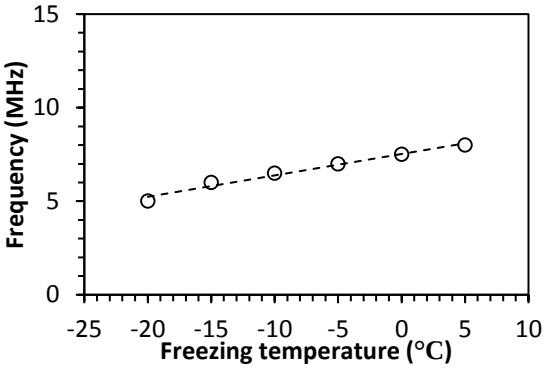

Fig. (3) Variation of ultrasonic frequency with freezing temperature for the iron oxide nanostructures prepared in this work

It is clear that the values of ultrasonic frequencies required for the extraction of nanopowders are relatively convergent regardless the grown phase of iron oxide.

The variation of nanoparticle size with the ultrasonic frequency at which the nanopowder was extracted for the iron oxide structures prepared in this work is shown in Fig. (4). As the thin film is typically composed of at least several layers of iron oxide particles, higher ultrasonic frequency can vibrate atoms in different layers and hence extract larger particles.

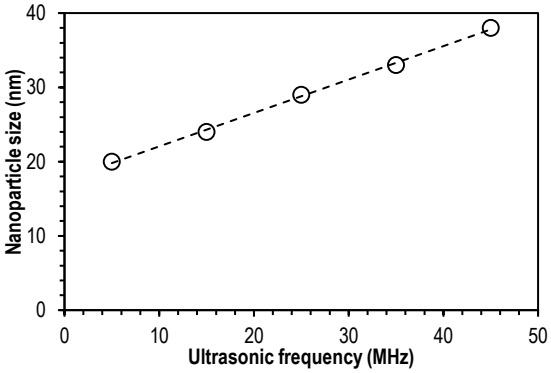

Fig. (4) Variation of nanoparticle size with the ultrasonic frequency for the iron oxide nanostructures prepared in this work

The time taken to apply the ultrasonic waves to the thin films sample before the extraction of nanopowder was completed is an effective parameter. Accordingly, the variation of nanoparticle size with application time at frequency of 5 MHz is shown in Fig. (5) for the iron oxide thin films. It is clearly observed that the particle size of the extracted

nanopowder does not show large differences for application times from 30 to 210 minutes. This is attributed to the fact that particles of certain size are extracted by ultrasonic waves of given frequency regardless the application time. Extraction of particles containing molecules from different layers within the thin film is carried out at certain range of sizes as a function of ultrasonic frequency. Larger particles are extracted due to their further growth within the deposited film.

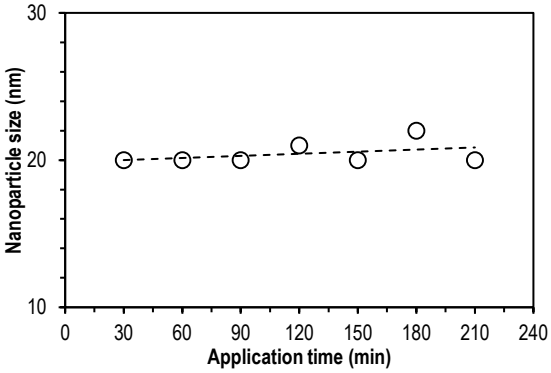

Fig. (5) Variation of nanoparticle size with the application time of ultrasonic waves for the iron oxide nanostructures prepared in this work

As the extraction method mainly depends on the freezing stage, the freezing temperature may be very effective in determining the particle size of the extracted nanopowder. Figure (6) shows the variation of nanoparticle size with freezing temperature for the iron oxide samples prepared in this work.

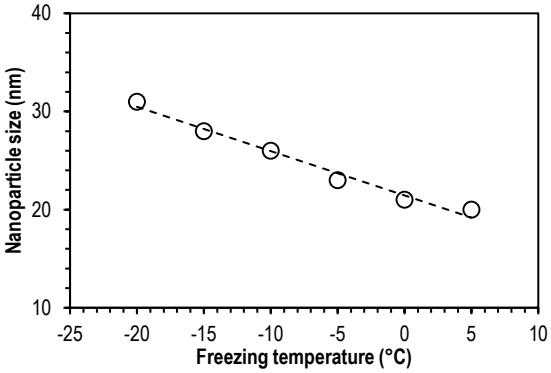

Fig. (6) Variation of nanoparticle size with the freezing temperature for the iron oxide nanostructures prepared in this work

It was mentioned before that the lower freezing temperature leads to larger shrinkage in the substrate on which the thin film is deposited and hence the adhesion between the film and the substrate gets lower and the film surface breaks earlier at the same value of ultrasonic frequency. Accordingly, larger particles can be extracted from the thin film before partitioning into smaller ones. In contrast, freezing to relatively higher temperatures leads to smaller shrinkage in the substrate and the adhesion between the film and the substrate gets higher. Therefore, the application of ultrasonic waves can extract titanium dioxide particles from the upper surface layer of the thin film, which means smaller particles. Layer-by-layer extraction at higher freezing temperatures produces smaller nanoparticles when compared to the case of lower temperatures.

According to the results obtained from this work, the principle of the conjunctional freezing-assisted ultrasonic extraction method can be shown in Fig. (7).

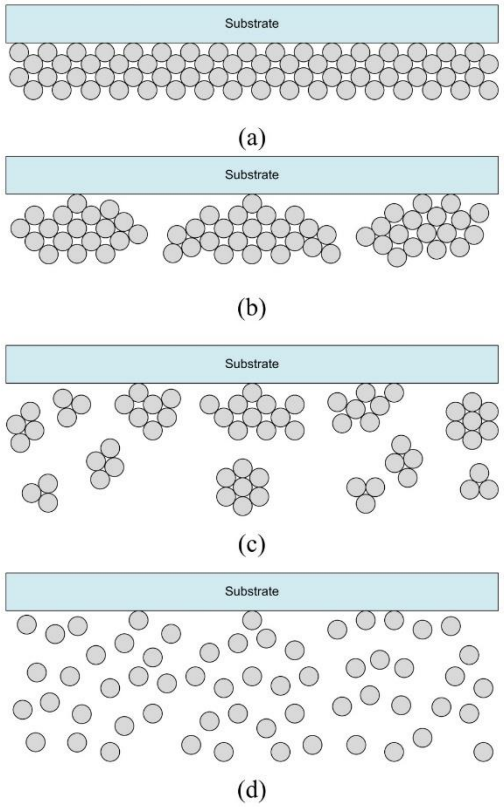

Fig. (7) Schematic representation of the conjunctional freezing-assisted ultrasonic extraction method

The thin film layers are typically deposited on the substrate as shown in Fig. (7a) as each single layer may contain nanoparticles or molecules of the thin film material. Freezing of the prepared sample causes the nonmetallic substrate to shrink faster than the thin film and as soon as the temperature of the sample rises, the substrate again expands faster than the thin film. Therefore, their dimensions get different and the film surface is broken to form islands over the surface of the substrate. These islands keep adhered to the substrate surface at some points with loosen terminals, as shown in Fig. (7b). Strong vibration of these islands may soon extract large parts, as shown in Fig. (7c), while the weak vibration may extract smaller parts over relatively long time of application ultrasonic waves, as shown in Fig. (7d).

4. Conclusion

As conclusions, freezing temperature, ultrasonic frequency and the time taken to apply ultrasonic waves on nanostructured thin films deposited on nonmetallic substrates are very effective to determine the nanoparticle size of nanopowders extracted from these thin film samples. The conjunctional freezing-assisted ultrasonic extraction method can be successfully used to extract highly-pure nanoparticles with approximately the same size of nanoparticles in the thin films deposited by physical vapor deposition methods and techniques. This technique is reliable, efficient and low cost to produce highly-pure nanomaterials with as low as possible particle sizes.

References

[1] S. Shen, J. Chen, M. Wang, X. Sheng, X. Chen, X. Feng and S.S. Mao, "Titanium dioxide nanostructures for photoelectrochemical applications", *Prog. In Mater. Sci.*, 98 (2018) 299-385.

[2] E.A. Al-Oubidy and F.J. Kadhim, "Photocatalytic activity of anatase titanium dioxide nanostructures prepared by reactive magnetron sputtering technique", *Opt. Quantum Electron.*, 51(1) (2019) 23.

[3] K. Vidhya, M. Saravanan, G. Bhoopathi, V.P. Devarajan and S. Subanya, "Structural and optical characterization of pure and starch-capped ZnO quantum dots and their photocatalytic activity", *Appl. Nanosci.*, 5 (2015) 235-243.

[4] K. Kim, M.-J. Kim, S.-I. Kim and J.-H. Jang, "Towards visible light hydrogen generation: quantum dot-sensitization via efficient light harvesting of hybrid-TiO_2", *Sci. Rep.*, 3 (2013) 1-8.

[5] D. Wu, S. Zhang, S. Jiang, J. He and K. Jiang, "Anatase TiO_2 hierarchical structures composed of ultra-thin nano-sheets exposing high percentage {001} facets and their application in quantum-dot sensitized solar cells", *J. Alloys Compd.*, 624 (2015) 94-99.

[6] H.A. Alhadrami, A. Baqasi, J. Iqbal, R.A.M. Shoudri, A.M. Ashshi, E.I. Azhar, F. Al-Hazmi, A. Al-Ghamdi and S. Wageh, "Antibacterial Applications of Anatase TiO_2 Nanoparticle", *Am. J. Nanomater.*, 5(1) (2017) 31-42.

[7] M.T. Noman, M.A. Ashraf and A. Ali, "Synthesis and applications of nano-TiO_2: a review", *Environ. Sci. Pollut. Res.*, 26 (2019) 3262-3291.

[8] O.A. Hammadi, "Production of Nanopowders from Physical Vapor Deposited Films on Nonmetallic Substrates by Conjunctional Freezing-Assisted Ultrasonic Extraction Method", *Proc. IMechE, Part N, J. Nanomater. Nanoeng. Nanosys.*, 232(4) (2018) 135-140.

[9] O.A. Hammadi, M.K. Khalaf, F.J. Kadhim, "Fabrication of UV Photodetector from Nickel Oxide Nanoparticles Deposited on Silicon Substrate by Closed-Field Unbalanced Dual Magnetron Sputtering Techniques", *Opt. Quantum Electron.*, 47(12) (2015) 3805-3813.

[10] O.A. Hammadi, M.K. Khalaf, F.J. Kadhim, "Silicon Nitride Nanostructures Prepared by Reactive Sputtering Using Closed-Field Unbalanced Dual Magnetrons", *Proc. IMechE, Part L, J. Mater.: Design and Applications*, 231(5) (2017) 479-487.

[11] M.A. Hameed and Z.M. Jabbar, "Optimization of Preparation Conditions to Control Structural Characteristics of Silicon Dioxide Nanostructures Prepared by Magnetron Plasma Sputtering", *Silicon*, 10(4) (2018) 1411-1418.

[12] F.J. Al-Maliki, O.A. Hammadi and E.A. Al-Oubidy, "Optimization of Rutile/Anatase Ratio in Titanium Dioxide Nanostructures prepared by DC Magnetron Sputtering Technique", *Iraqi J. Sci.*, 60 (2019) 91-98.

[13] O.A. Hammadi, F.J. Al-Maliki and E.A. Al-Oubidy, "Photocatalytic Activity of Nitrogen-Doped Titanium Dioxide Nanostructures Synthesized by DC Reactive Magnetron Sputtering Technique", *Nonlinear Opt. Quantum Opt.*, 51 (1-2) (2019) 67-78.

[14] O.A. Hammadi, M.K. Khalaf, F.J. Kadhim, B.T. Chiad, "Operation Characteristics of a Closed-Field Unbalanced Dual-Magnetrons Plasma Sputtering System", *Bulg. J. Phys.*, 41(1) (2014) 24-33.

[15] O.A. Hammadi, M.K. Khalaf, F.J. Kadhim, "Fabrication and Characterization of UV Photodetectors Based on Silicon Nitride Nanostructures Prepared by Magnetron Sputtering", *Proc. IMechE, Part N, J. Nanoeng. Nanosys.*, 230(1) (2016) 32-36.

Atyaf S.F. Alrubaie

Branch of Basic Sciences, College of Dentistry, AL-Qadisiyah University, AL-Qadisiyah, IRAQ

Preparation and Characterization of Copper Nanoparticles by Pulsed-Laser Deposition

In this work nanostructured copper thin films were deposited on glass and silicon substrates by the pulsed-laser deposition (PLD) technique utilizing a Nd:YAG laser operating with a pulse energy of 480mJ, a repetition frequency of 6Hz, and 500 pulses. The results of characterizations showed clear peaks that indicated plasmonic absorption at a wavelength of 220nm. The predominance of the anatase Cu phase was revealed. The presence of spherical particles that were dispersed in clusters were also revealed. The average size of these clusters ranged from 66.2 to 90.7 nanometers.

Keywords: Nanoparticles; Copper; Pulsed-laser deposition; Structural characterization
Received: 06 January 2024; **Revised:** 29 February 2024; **Accepted:** 07 March 2024

1. Introduction

There has been an increasing fascination with creating and designing metal nanoparticles that have well-defined structures. This is because these materials possess distinct and auspicious characteristics. Copper (Cu) is a metal that has attracted considerable interest at the nanoscale. It is a versatile metal that finds extensive usage in electrical conductivity, catalysis, and antibacterial applications. Copper nanoparticles have distinctive optical characteristics, such as adjustable bandgaps and effective light absorption [1]. Copper (Cu) is a highly regarded metal known for its excellent qualities, which make it indispensable in numerous sectors. Substantial research and utilization of its unusual mix of physical, chemical, electrical, and thermal properties have been observed in varied domains [2]. Copper is highly recognized for its exceptional electrical conductivity. It possesses the most significant electrical conductivity compared to other commonly found metals, except superconductors at extremely low temperatures. Copper's characteristic of facilitating efficient current flow with minimal energy loss makes it a highly suitable material for electrical wiring, power transmission, and electronics. Copper also demonstrates exceptional heat conductivity. Due to its remarkable thermal conductivity, it is highly favored as a material for heat sinks, cooling systems, and heat exchangers. Its exceptional thermal conductivity facilitates efficient heat dissipation, making it indispensable for electronics, power generation, and thermal management. Copper exhibits superior ductility, malleability, and excellent electrical and thermal conductivity. It has excellent malleability, allowing it to be easily manipulated and molded into intricate shapes without any breaking risk, making it appropriate for manufacturing techniques, including rolling, extrusion, and forging. These characteristics facilitate the manufacturing complex copper parts used in plumbing, architecture, and industrial machinery. Nanotechnology is an interdisciplinary domain that includes scientific and technological endeavors focused on manipulating and regulating matter at the nanoscale, typically ranging from 1 to 100 nm in size. It encompasses the comprehension, creation, and production of materials, technologies, and systems having unique features and functionalities at a minuscule scale. At the nanoscale, the characteristics of materials can vary considerably compared to their larger forms. Nanotechnology harnesses these distinctive characteristics to create novel materials, devices, and procedures that find utility in diverse domains such as electronics, medicine, energy, materials research, and environmental science [2,3].

Copper exhibits excellent corrosion resistance, especially in both air and aquatic conditions. The metal develops a patina, a protective oxide layer on its surface that effectively inhibits additional corrosion. Copper's exceptional corrosion resistance makes it suitable for outdoor applications, architectural structures, and plumbing systems. In addition, copper demonstrates antibacterial capabilities, referred to as the "oligodynamic effect." Studies have shown that it possesses inherent antibacterial properties, which make it valuable for usage in healthcare facilities, antimicrobial coatings, and water purification systems [3].

2. Experimental Part

Copper exhibits exceptional electrical conductivity, second only to silver. Its efficient conductivity makes it popular for electrical wiring, power transmission, and electronics. Copper's exceptional thermal conductivity makes it an optimal selection for heat transfer applications. It is frequently employed in heat sinks, heat exchangers, and cooling systems. Copper exhibits exceptional ductility and malleability, allowing it to undergo extensive

elongation into wires or be effortlessly molded into diverse shapes without experiencing fracture. This feature enables the fabrication of complicated copper components using techniques such as rolling, drawing, and forging. Copper exhibits excellent corrosion resistance, especially in both air and aquatic conditions. The metal develops a defensive oxide layer, known as patina, on its surface, inhibiting additional corrosion. Its characteristics render it appropriate for use in outdoor applications and plumbing systems. Copper has natural antibacterial capabilities, referred to as the "oligodynamic effect." It demonstrates the capacity to eradicate or impede the proliferation of bacteria, viruses, and fungi on its surface. Copper's inherent characteristics have resulted in its use in healthcare environments, antimicrobial coatings, and water purification systems.

The pulsed-laser deposition (PLD) system schematically shown in Fig. (1) has been used to deposit thin films on different substrates. This system comprises the following components: a laser device, a deposition chamber, a rotary vacuum pump, a vacuum pressure monitoring device, a target holder, and an electronic thermometer. A Diamond-288 Pattern EPS Nd:YAG laser used was supplied by Huafei Tongda Technology. The laser energy may reach to 1900 mJ at wavelength of 1064nm, and the operation frequency ranges from 1 to 6 Hz. The pulse duration is 10ns. The laser system was water-cooled by flowing cool water to replace the heated water as a result of laser operation. This system also contains the deposition chamber made from Pyrex glass with a height of 30 cm, a diameter of 20 cm, and a thickness of 5 mm. The chamber is mounted on an aluminum base with a diameter of 30 centimeters and a thickness of 20 mm. A circular groove, measuring 2 cm in width and 5 mm in depth, was formed on the upper surface of this base. An O-ring is placed inside this groove to prevent the leak of the deposition chamber. The vacuum of 10^{-3} mbar inside the deposition chamber was created by using a rotary vacuum pump (Varian Rotary Pump DC 302 949-9325 s 006 W/Leroy L 080 BR type). To reach 10^{-6} mbar vacuum level, a diffusion pump supplied by Mancha Vacuum Technologies was used.

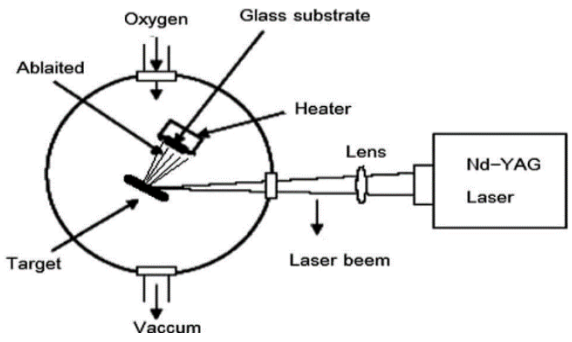

Fig. (1) Scheme of the PLD system used in this work

The target holder is made from stainless steel with a diameter of 2 cm and a depth of 3 mm. A tiny rotary motor was employed to rotate the holder at a speed of 10 r.p.m. The rotation of the holder is done consistently to ensure that the laser energy is evenly distributed on the compressed material (target), resulting in a uniform deposition of prepared films. The temperature of elements inside the chamber was monitored using a thermocouple. Precise measurement of the substrate temperature is crucial in thin film growth. A 250W halogen lamp was used to warm the substrate up to 400°C.

The system's interior was cleaned with alcohol to prevent the contamination by any residue from previously deposited substances. The material to be deposited is placed in a tungsten boat, which has a high melting point that is significantly higher than the melting point of the material to be deposited. The substance being used is pure copper. The boat is linked to a pair of electrodes connected to an internal electric current source within the system to be electrically heated. As the substance melts, we gradually raise the electric current provided to the electrodes, therefore, the material undergoes a process of glowing, which involves the evaporation of the material and the deposition of a film on the substrate. Once the material is entirely deposited, the current is gradually decreased. The sample oxidation is prevented because the system is left for 30 minutes after the deposition process is completed. The copper film deposition process includes the following stages:
- The interaction between the laser beam and the copper target
- The generation and enlargement of plasma within the deposition chamber, directed towards the glass slide where the deposition occurs, is induced by laser beams. The film was deposited onto a glass substrate (slide) at room temperature and under 10^{-3} mbar vacuum pressure. The laser energy was 600 mJ, with a frequency of 6 Hz. The incident laser beam was directed at an angle of 45° to the target surface, and the slide was positioned 10 cm above the target.

The film thickness (t) was determined by the weight method as follows:

$$t = \frac{M}{\pi \rho L^2} \qquad (1)$$

where M is the mass of the substance (g), ρ is the density of the substance (g/cm^3), and L is the distance between the crucible and the substrate stand (cm)

The structure, surface morphology, and optical properties of the deposited films were determined by x-ray diffraction (XRD), field-emission scanning electron microscopy (FE-SEM), energy-dispersive x-ray spectroscopy (EDX), and UV-visible spectrophotmetry.

3. Results and Discussion

The x-ray diffraction used for the diagnosis of structure of the prepared films is based on Bragg's law to determine the inter-planar distance (d_{hkl}) as [10]

$$n\lambda=2d_{hkl}\,sin\theta \quad (2)$$

where n represents the diffraction order, θ represents the diffraction angle, and λ is the x-ray wavelength, which is pertained by the metal target used to produce the x-ray radiation

The Scherrer's formula shown below was used to determine the crystallite size, which is inversely proportional to the full-width at half maximum (FWHM) of diffraction peaks [11]:

$$C.S=\frac{0.9\,\lambda}{\beta.cos\theta} \quad (3)$$

where β is the FWHM

The XRD pattern of the prepared nanoparticles is depicted in Fig. (2). It displays diffraction peaks at 2θ of 27.34°, 29.99°, 31.89°, 35.69°, 39.89°, 45.59°, and 53.14°, which are assigned to crystal planes of (111), (110), (200), (210), (211), (220), and (311), respectively, belonging to the crystal structure of copper. The presence of these peaks confirms the formation of nanomaterial with a high degree of crystallinity. Also, the Cu nanoparticles can be inferred to be in the anatase phase, as indicated by the Joint Committee on Powder Diffraction Standard (JCPDS) (card no. 00-0333-0492).

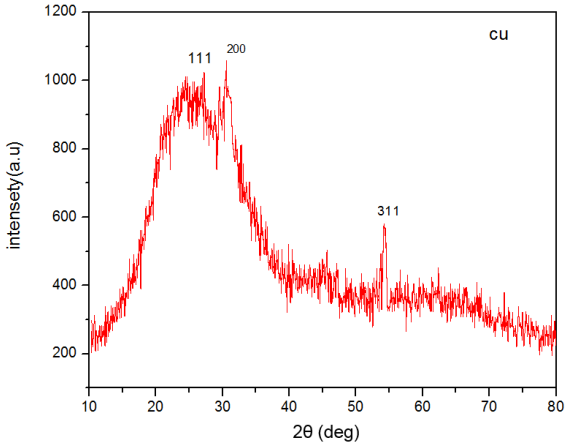

Fig. (2) XRD pattern of Cu NPs prepared in this work by PLD

The diffraction peaks of the processed samples exhibit distinct domain peaks at (111), (200), and (311) orientations, occurring at approximately 2θ = 27.34°, 31.89º, and 53.14°, respectively, ascribed to a cubic structure of Cu anatase phase with lattice constants a=b=c=3.615nm and angles α=β=γ=90°. The XRD pattern does not show peaks of other materials, indicating the samples were prepared with high purity, as illustrated in table (1). It was observed that there were minor variations in the match due to a slight increase in thickness, contaminants, or voids in the film. The granularity level is directly proportional to the thickness and inversely proportional to the width of the center peak observed in XRD pattern [12,13].

The absorption spectrum of Cu nanoparticles prepared using laser energy of 480mJ is shown in Fig. (3). It shows that the absorbance is high within the range of 190-300nm, with a prominent peak at 220nm. The transmittance of Cu nanoparticles shown in Fig. (4) reaches its minimum at the same wavelength. The absorbance decreases at wavelengths longer than 220nm. The appearance of these peaks can be attributed to the quantum size effect. The plasmon peaks' intensity and width were shown to depend on both laser energy and the number of laser pulses. The aggregation of the prepared Cu nanoparticles within a few days, which agrees with the observations of Anikin et al. [14].

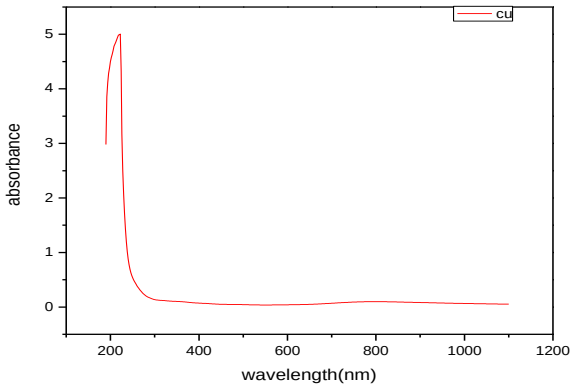

Fig. (3) UV-visible absorption spectrum of of Cu NPs prepared in this work by PLD

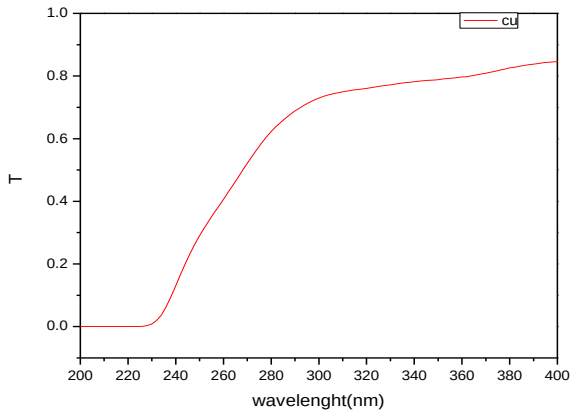

Fig. (4) UV-visible transmission spectrum of Cu NPs prepared in this work by PLD

The surface morphology of the produced samples was examined using FE-SEM, as depicted in Fig. (5). The FE-SEM image reveals that the sample prepared using 480 mJ laser energy have a nanostructure characterized by a distribution of spherical particles. The spherical clusters are spread in various places with an average diameter of 7.72 nm, as indicated in table (2). It was observed that the sample had a rough surface and large pore size, resulting in a high specific surface area.

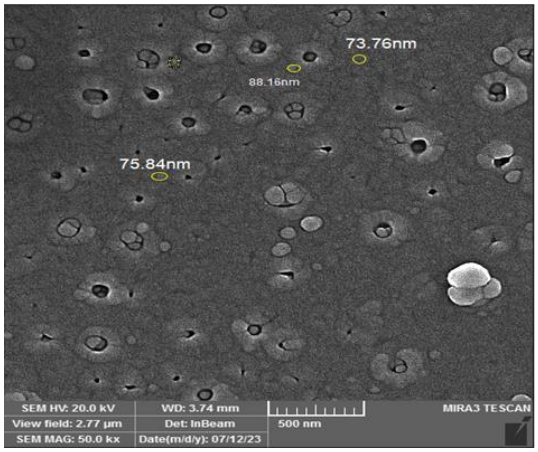

Fig. (5) FE-SEM image of Cu NPs prepared in this work by PLD

Table (2) FE-SEM results of of of Cu NPs prepared in this work by PLD

Label (Cu)	Area	Particle Size (nm)		
		Mean	Min	Max
1	0.016	88.167	43.000	141.000
2	0.019	73.769	40.000	109.000
3	0.019	73.769	40.000	109.000
4	0.018	75.844	28.000	120.000
5	0.006	73.344	49.000	100.000
6	0.011	82.083	41.000	121.000
7	0.006	66.656	42.000	109.000
8	0.016	76.841	47.000	114.000
9	0.018	70.742	38.000	115.000
10	0.016	92.333	44.000	146.000

4. Conclusion

The study showed the one-step preparation process of spherical-shaped copper nanoparticles using PLD technique. The prepared Cu nanoparticles have a single-phase cubic structure (anatase Cu). The laser fluence determines the form and size of the nanoparticles. The presence of extensively clustered Cu particles measuring 41–77 nm was verfieid depending on the laser fluence.

References

[1] J.D. Smith and A.B. Johnson, "Selection of Copper (Cu), Cadmium Sulfide (CdS), Zinc (Zn), and Tin (Sn) for Nanomaterial Fabrication: Characteristics and Applications", *J. Adv. Mater.*, 10(2) (2022) 45-60.

[2] Y. Huang et al., "Decorated Cu NPs on Lignin Coated magnetic Nanoparticles: Its Performance in The reduction of Nitroarenes and Investigation of Its Anticancer Activity in A549 Lung Cancer Cells", *Arabian J. Chem.*, 14 (2021) 103299.

[3] R. Hultgren and P.D. Desai, "Selected Thermodynamic Values and Phase Diagrams for Copper and Some of Its Binary Alloys, Incra Monograph I", International Copper Research Association Inc. (NY, 1971).

[4] C.T. Avedisian et al., "Nanoparticles for Cancer Treatment: Role of Heat Transfer", *Annals New York Acad. Sci.*, 1161(1) (2009) 62–73.

[5] R.K. Swarnkar, S.C. Singh and R. Gopal, "Effect of Aging on Copper Nanoparticles Synthesized by Pulsed Laser Ablation in Water: Structural and Optical Characterizations", *Bull. Mater. Sci.*, 34(7) (2011) 1363-1369.

[6] A.V. Simakin et al., "Nanoparticles Produced by Laser ablation of Solids in Liquid Environment", *Appl. Phys. A: Mater. Sci. Process.*, 79 (2004) 1127-1132.

[7] D.M. Mattox, **"Handbook of Physical Vapor Deposition (PVD) Processing: Film Formation, Adhesion, Surface"**, William Andrew Inc. (NY, 1998).

[8] T. Ctvrtnickova et al., "Laser Deposition of Powdered Samples and Analysis by Means of Laser-Induced Breakdown Spectroscopy", *Appl. Surf. Sci.*, 255 (2009) 5329-5333.

[9] M. Kim et al., "Synthesis of Nanoparticles by Laser Ablation", *KONA Powder Particle J.*, 34 (2017) 80–90.

[10] R. Herrero-Vanrell et al., "Self-assembled Particles of an elastin-like polymer as vehicles for controlled drug release", *J. Control. Rel.*, 102 (2005) 113–122.

[11] R.L. Siegel, K.D. Miller and A. Jemal, "Cancer statistics", *CA Cancer J. Clin.*, 70 (2020) 7–30.

[12] A.H.O. Alkhayatt et al., "Characterization of CuO/n–Si pn junction synthesized by successive ionic layer adsorption and reaction method", *Opt. Quantum Electron.*, 51(7) (2019) 233.

[13] L. Madler et al., "Controlled synthesis of nanos-tructured particles by flame spray pyrolysis", *J. Aerosol. Sci.*, 33(2) (2002) 369–389.

[14] K. Anikin et al., "Formation of ZnSe and CdS quantum dots via laser ablation in liquids", *Chem. Phys. Lett.*, 366(3-4) (2002) 357-360.

Table (1) XRD results for the Cu nanoparticles prepared by pulsed-laser deposition

Sample	2θ (deg) standard	2θ (deg) Observed	d(Å) Standard	d(Å) Observed	(hkl)	Standard Card
Cu	27.4202	27.3442	3.2500	3.2422	(111)	00-0333-0492
	29.9808	29.9940	2.9780	2.9848	(110)	00-034-1354
	31.8193	31.8940	2.8100	2.8688	(200)	00-0333-0492
	35.4512	35.694	2.5300	2.5881	(210)	00-0333-0492
	39.1866	39.8940	2.2970	2.8865	(211)	00-0333-0492
	45.4729	45.5940	1.9930	1.6518	(220)	00-0333-0492

Tabarak A. Al-Mashhadani [1]
Firas J. Kadhim [2]
Noor Alhuda H. Hashim [3]

[1] *Al-Farabi University College, Baghdad, IRAQ*
[2] *Department of Physics, College of Science, University of Baghdad, Baghdad, IRAQ*
[3] *College of Pharmacy, Uruk University, Baghdad, IRAQ*

Optimization of Surface Plasmon Resonance Band of Copper Nanoparticles Doping in Silica Xerogels

Copper nanoparticles were synthesized via chemical reduction method. Copper nitrate aqueous precursor using trisodium citrate as a reducing agent at boiling temperature. Structural and optical characteristics were determined as a function of copper nitrite concentration. The effect of concentration on the characteristics of the surface plasmon absorption band was determined and studied at 790 nm. The broadening of the surface plasmon resonance (SPR) band indicated the existence of larger particles in the solution. Silica xerogel doped with Copper nanoparticles by sol-gel route at specific preparation parameters. The absorption intensity reasonably increased for bulk samples (Cu NPs in xerogels) as compared to Cu NPs solution.

Keywords: Silica xerogel; Chemical reduction; Nanoparticles; Concentration
Received: 20 December 2023; **Revised:** 05 March; **Accepted:** 12 March 2024

1. Introduction

Nanomaterials are investigated widely at the present time because of their distinct optical, electronic and mechanical characteristics [1]. Noble metal nanoparticles, such as copper nanoparticles (Cu NPs), have been a source of great interest to their unusual physical features, particularly their strong Plasmon absorption peak in the visible region [2]. The resonance frequencies are determined by the particle form and size, and remain stable for months. Nobel metal nanoparticles show brilliant colors due to the surface plasmon resonance absorption [3]. The examination of the surface plasmon resonance absorption is part of a large ongoing research field to investigate properties on the nanometer scale [4]. The color of metal nanoparticles depends on the shape and size of the nanoparticles and dielectric constant of the surrounding medium, leading to many studies on their synthesis and applications [5]. Copper is a relatively rare element with an estimate of copper atoms comprising 22 parts per million (ppm) of the Earth's crust (68 ppm by weight); making it the eighth most abundant metal. Bulk copper has good conductive properties, but not when synthesized as nanoparticles. Despite that, Cu NPs have superior antibacterial, deodorant, catalysis, lubricant and conductive links [6-9]. In the past few years, the synthesis of Cu NPs has attracted much attention because of its huge potential for replacing expensive nano silver inks used in conductive printing. If a suitable protective coating is applied on copper nanoparticles, they can withstand oxidation in the environment [6]. An organic polymer, alkene chains, graphene or amorphous carbon, inorganic substances like silica, or an inert metal could all be present in this layer. By directly printing conductive patterns, such coated copper nanoparticles allow for the achievement of high conductivities. By employing copper-based inkjet inks to create solar cells, RFID tags, and electroluminescence devices, among other gadgets, this method creates new opportunities in printed electronics [8-10]. To develop nanoparticles, ultrasonic irradiation, electrochemical synthesis, thermal decomposition, radiolysis, and chemical reduction of metal salts had been used [11,12]. Chemical reduction is one of the most important technique for preparing Ag, Au and Cu colloids [7]. In the present study, copper nanoparticles were synthesized from copper nitrate salt solution with trisodium citrate as a reducing agent. This approach allows regulating particle size and form by varying the molar concentration of reactants. Metal salt precursor, reducing agent, and stabilizing/surfactants/capping agent are the three key components used in this procedure. The two stages of the copper reduction process are nucleation and particle growth [13]. When compared to the physical approach, the chemical method is characterized by high yield, cost-effective and easy particle size control [14]. Despite numerous attempts, preparing NPs with a well-defined size remains difficult, necessitating a second procedure to prevent particle aggregation [15]. Synthesis of NPs utilizing stabilizers, surfactants, and capping agents has been evaluated and reported to prevent aggregation [16]. A metal alkoxide and an organic alkoxysilane precursor are combined with water and a solvent in the presence of an acid or base catalyst to hydrolyze and condense to create sol-gel materials, which are inorganic/organic hybrid compounds [17]. It can

create extremely porous, stiff membranes that are useful for a variety of purposes, including the entrapment or immobilization of biomolecules like proteins and enzymes that maintain their biological function and may be released from fouling. [18]. In order to optimize the surface plasmon resonance band of Cu NPs, the later was doped in silica xerogel for the development of future anti - bacteria agent.

2. Experimental Part

The synthesis of $CuNO_3$ NPs was carried out using chemical reduction method. At first, a solution of 6.7×10^{-3}, 5×10^{-3}, c= 5×10^{-1} , d=8.5 $\times$ 10^{-1} , e =9×10^{-1} & f= 1 $mol\backslash L$ $CuNO_3$ were prepared by dissolving the copper nitrate precursor in water. Besides; 0.5g sodium citrate was dissolved in 50mL of H_2O to obtain 5% solution. Copper nanoparticles were synthesized by heating the diluted solution of $CuNO_3$ until it begins to boil, then 2.5 mL of 0.5% sodium citrate solution was added drop by drop, as soon as boiling commences. The heating process continued until a pale blue color change was seen. 3 minutes after the boiling point, heating was seized but stirring the solution continued until reaching room temperature as shown in Fig. (1). Drop casting method was used to coat glass substrates with the prepared colloidal copper nanoparticles in order to characterize the samples [19].

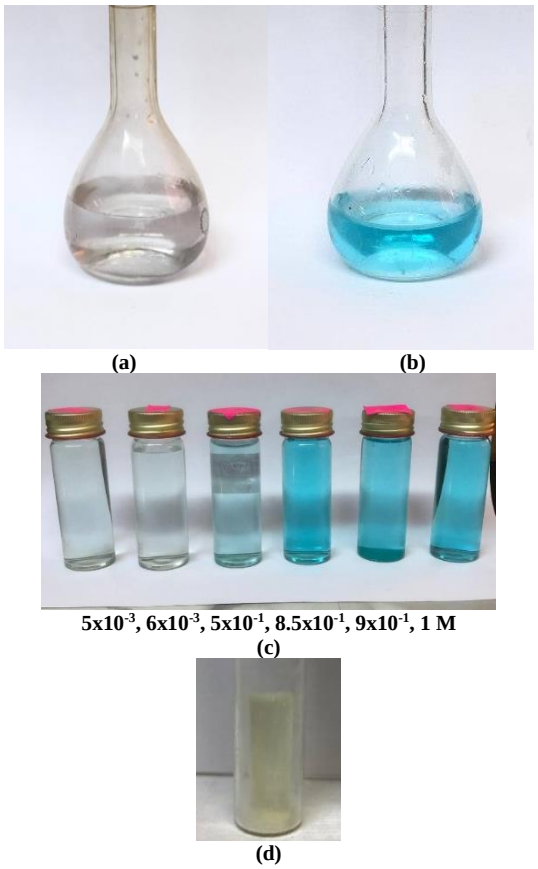

Fig. (1) (a) $CuNO_3$ solution (b) Cu NPs solution (c) Copper NPs prepared by chemical reduction at different concentrations (d) Cu NPs doped silica xerogel

The silica xerogel sol-gel rod samples were prepared under selected reaction conditions in order to prepare a suitable transparent host for Cu, TEOS and absolute EthOH after mixing them 1:5:10 volume ratio and pH of 1.5. For Cu doping, 1 ml of CuNPs solution, at different Cu concentrations, was added to the mixture of TEOS and absolute EthOH before the hydrolysis and this was denoted as sol (I). This was homogenized by stirring it obtained for 15 min by a magnetic stirrer. A mixture of 0.6 ml deionized water and 1.2 ml absolute EthOH was prepared and denoted as sol (Π) which was slowly added to the sol (I) for the hydrolysis process. The final solution was left for (30 min) under magnetic stirrer, and this was followed by adding 0.5 ml of N,N-dimethylformamide. The solution was poured in a closed glass tube and kept under 80 ºC reaction temperature. After aging and drying, the xerogel bulk rod samples was sintered by increasing the temperature from 110 to 250°C within 48 hours [20].

3. Results and discussions

In order to investigate the phase structure of the synthesized Cu nanoparticles (NPs), the XRD pattern in Fig. (2) shows three peaks with their corresponding planes; obtained at diffraction angles 35.55° (111), 41.40° (200), 72.73° (220) Bragg's reflections planes which represent (111), (200), and (220) planes of FCC crystal structure of metal copper. No extra/impurity peaks are observed in XRD pattern and this means there is no impurity present in the prepared samples. The sharp and strong peaks reveal that Cu nanocrystals are highly oriented. The patterns reveal that all the diffraction peaks are indexed to the characterization of metal copper, which are similar to the prepared pure copper samples. The analysis reveals that the as prepared samples have a crystallite size of 26.86 nm; calculated by using Debye-Scherrer's equation [21].

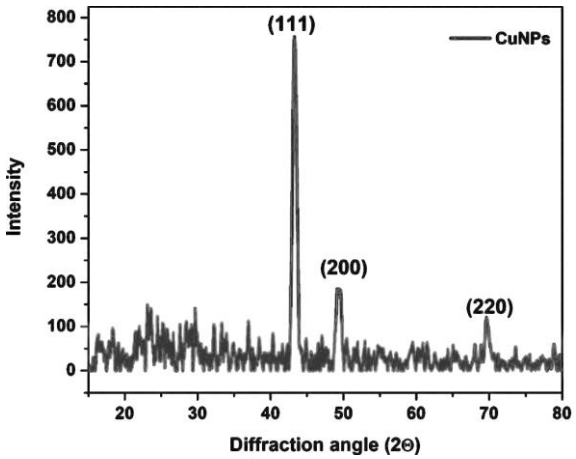

Fig. (2) The XRD pattern of Cu NPs were prepared by chemical reduction method

In order to explore the influence of preparations conditions on the characterization of such nanostructures, the absorption of Cu colloidal was

recorded as a function of $CuNO_3$ concentrations. Figure (3) shows that the absorption intensity increases with concentration while the maximum peak surface absorption of plasmon copper nanoparticles (at 1 $mol\backslash l$ as a concentration) occurred at 797 nm and for $9\times 10^{-1}, 8.5\times 10^{-1} mol\backslash l$ & $0.5\times 10^{-1} mol\backslash l$ concentration, it occurred at 790, 793 and 781 nm, respectively. At low concentration (0.5×10^{-3}& 6.7×10^{-3} 1 $mol\backslash l$) no absorption peak was observed. Figure (4) represents the absorbance as a function of concentrations which increased with concentration; a result that agrees well with Beer-Lambert laws.

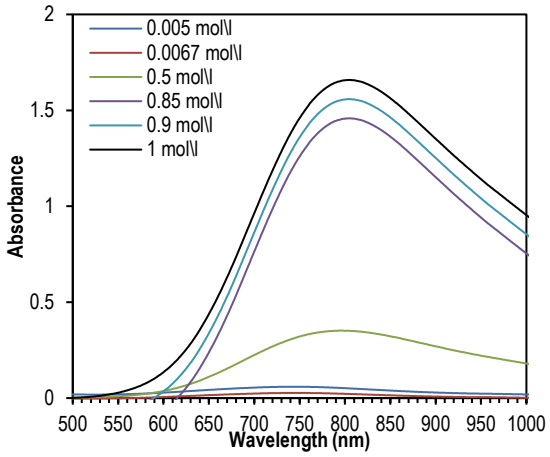

Fig. (3) The absorption spectra of Cu colloidal were prepared by chemical for different concentrations

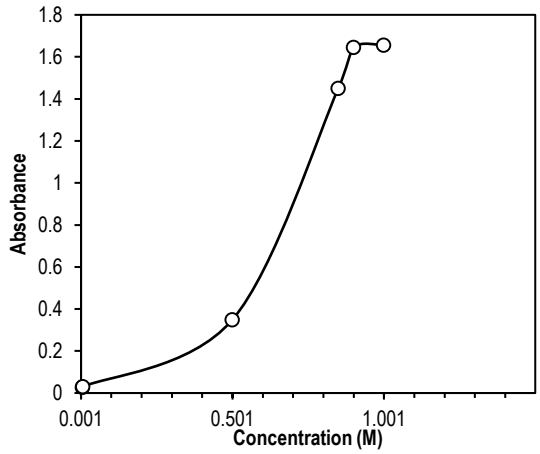

Fig. (4) The absorption spectra of Cu colloidal were prepared by chemical for different concentrations

To prevent decomposing the Cu-NPs, the liquid colloidal must be incorporated into a solid host by caging it into solid network; such as polymer or sol-gel host whereas its stability in liquid phase is a global problem. Cu-NPs dopant has been added to increase absorbance of silica xerogel. Figure (5) shows the absorption coefficient against the wavelength of the silica xerogels doped with different Cu-NPs concentrations. It shows the peak absorption coefficient α (λ), of each band increases steadily with Cu concentration.

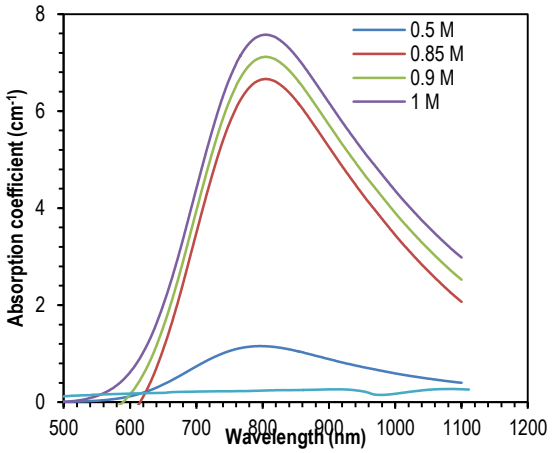

Fig. (5) The absorption spectra of silica xerogels doped with different concentrations of Cu NPs

The characteristic vibrational bands of silica were located in the FTIR spectra of silica xerogel and Cu-NPs doped silica xerogel samples as shown in Fig. (6). These samples were prepared at pH 1.5, 1:5:10 volume ratio and 80°C temperature. They were dried at 110°C and sintered at 250°C. The bending vibrations of Si-O-Si groups facilitate centering the absorption band at 460.2 cm^{-1}. The symmetric stretching Si-O-Si groups caused the absorption band peaking at 810.1 cm^{-1}. Lastly, the wide band round 1103.8 cm^{-1} is the distinctive Si-O-Si asymmetric stretching vibrations.

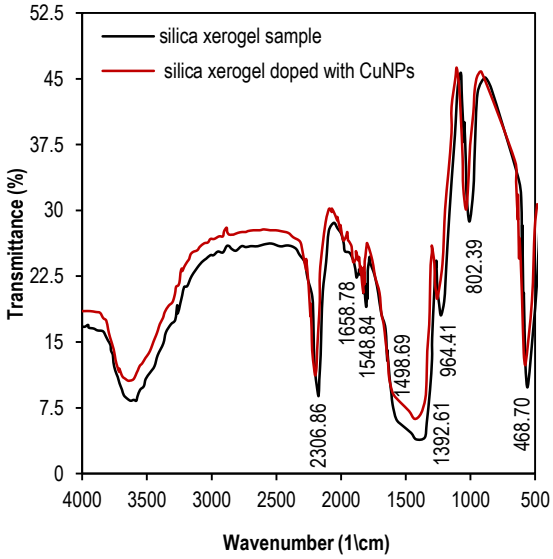

Fig. (6) FTIR transmission spectra of silica Xerogel and silica xerogel doped with CuNPs

The weak band at 964.8 cm^{-1}, attributed to stretching vibrations of silanol (Si-OH) groups which suggests a limited number of these groups in the silica network and implies a complete condensation reaction. The incomplete trapped water molecules in the pores of silica xerogel during the drying process at 110°C, two absorption bands appeared: 1640.7 cm^{-1} and 3440 cm^{-1}. The first band is caused by the bending vibrations of the O-H bond in the H_2O

molecules, whereas the second band is caused by stretching vibrations of the link. For glass sample sintered at 250°C, the first band became very weak and the second band vanished; indicating the driving out of most H_2O molecules as explained in Fig. (6).

4. Conclusions

It was found that the Copper nanoparticles were successfully prepared using a chemical reduction method based on varying the concentration of copper nitrate and studying its effect on the plasmon resonance band specification. In order to use such nanoparticles, they are embedded in a transparent host medium, silica xerogel. It turns out that these particles are concentrated within the pores that characterize the media prepared by the sol-gel method also, the absorption intensity reasonably increased for bulk samples (Cu NPs in xerogels) as compared to Cu NPs solution. Thus the possibility of using them in various applications.

References

[1] Mohd. Arshad et al., "Band gap engineering and enhanced photoluminescence of Mg doped ZnO nanoparticles synthesized by wet chemical route", *J. Lumin.*, 161 (2015) 275-280.

[2] J.K. Majhi and P.K. Kuiri, "Enhancement of spectral shift of plasmon resonances in bimetallic noble metal nanoparticles in core–shell structure", *J. Nanopart. Res.*, (22) (2020) 546-551.

[3] A. Moores and F. Goettmann, "The plasmon band in noble metal nanoparticles: an introduction to theory and applications", *New J. Chem.*, 30(8) (2006) 1121-1132.

[4] A. Pyatenko, M. Yamaguchi and M. Suzuki, "Synthesis of Spherical Silver Nanoparticles with Controllable Sizes in Aqueous Solutions", *J. Phys. Chem. C*, 111(2) (2007) 7910-7917.

[5] K.M.M.A. El-nour, A. Al-warthan and R.A.A. Ammar, "Synthesis and application of silver nanoparticles", *Arab. J. Chem.*, 3(3) (2010) 135-140.

[6] M. Ansari, M. Arshad and P. Tripathi, "Study of ZnO and Mg doped ZnO nanoparticles by sol-gel process", *AIP Conf. Proc.*, 1665 (2015) 050123.

[7] R. Bushra et al., "Electrical and Optical Properties of Synthesized Composite Material Polyaniline-Ti(IV) Arsenophosphate", *Asian J. Chem.*, 27(3) (2015) 1121-1124.

[8] A. Eychmuller, "Structure and Photophysics of Semiconductor Nanocrystals", *J. Phys. Chem. B*, 104 (2000) 6514.

[9] T.P. Chou et al., "Hierarchically Structured ZnO Film for Dye-Sensitized Solar Cells with Enhanced Energy Conversion Efficiency", *Adv. Mater.*, 19 (2007) 2588–2592.

[10] S.J. Pearton et al., "Advances in wide bandgap materials for semiconductor spintronics", *Mater. Sci. Eng. R*, 40(4) (2003) 137-168.

[11] T. Ghodselahi, T. Neishaboory and M.A. Vesaghi, "Localized surface plasmon resonance of Cu_2O core shell nanoparticles: absorption scattering and luminescence", *Biosensors*, 2 (2011) 59-61.

[12] L. Mahmudin et al., "The effect of the concentration of the stabilizer in the formation of a silver nanoparticle on the phenomenon of Surface Plasmon Resonance (SPR) as an active material for biosensor", *J. Phys.: Conf. Ser.*, 1763 (2021) 012064.

[13] T.K. Nguyen et al., "Mechanisms of Nucleation and Growth of Nanoparticles in Solution", *Chem. Rev.*, 114(15) (2014) 7610-7630.

[14] N. Baig, I. Kammakakam and W. Falath, "Nanomaterials: a review of synthesis methods, properties, recent progress, and challenges", *Mater. Adv.*, 2 (2021) 1821-1871.

[15] M. Zahoor et al., "A Review on Silver Nanoparticles: Classification, Various Methods of Synthesis, and Their Potential Roles in Biomedical Applications and Water Treatment", *Water*, 13(16) (2021) 2216.

[16] M.Z. Hossain et al., "Synthesis of Spherical Silver Nanoparticles by Chemical Reduction Method", *J. Bangladesh Chem. Soc.*, 30(20) (2021) 42-47.

[17] J.Y. Wen and G.L. Wilkes, "Organic/inorganic hybrid network materials by the sol–gel approach", *Chem. Mater.*, 8 (1996) 1667-1681.

[18] S. Smith et al., "A Comprehensive Review of the Covalent Immobilization of Biomolecules onto Electrospun Nanofibers", *Nanomater.*, 10 (2020) 2142.

[19] T.A. Al-Mashhadni and F.J. Al-Maliki, "Effect of Silver Colloidal Concentration on Morphology of Silver Nanostructures Prepared by Chemical Reduction Method", *Iraqi J. Appl. Phys. Lett.*, 6(1) (2023) 3-6.

[20] T.A. Al-Mashhadni and F.J. Al-Maliki, "Optimized Characteristics of Silver Nanoparticles Synthesized by Chemical Reduction and Embedded in Silica Xerogels", *Iraqi J. Appl. Phys.*, 18(3) (2022) 25-30.

[21] M.M. Ansari, M. Shahid and A.S. Ansari, "Synthesis and Characterization of Cu Nanoparticles by Chemical Reduction Method", *AIP Conf. Proc.*, 1953(1) (2018) 030006.

IRAQI JOURNAL OF APPLIED PHYSICS

Volume (20) Issue (2B) May 2024

CONTENTS

Contents